



Norwegian University of  
Science and Technology

# Numerical Study on a Floating Wind Turbine in Intermediate Depth

**Even Sandøy Nærum**

Marine Technology

Submission date: June 2017

Supervisor: Marilena Greco, IMT

Co-supervisor: Erin Bachynski, IMT  
Håkon S. Andersen, Dr. Techn. Olav Olsen

Norwegian University of Science and Technology  
Department of Marine Technology



## MASTER THESIS IN MARINE TECHNOLOGY

Spring 2017

FOR

**Even Sandøy Nærum**

### **Numerical Study on a Floating Wind turbine in Intermediate Depth**

(Numerisk studie på en flytende vindturbin i middels dybde)

Offshore wind energy is an attractive renewable resource due to high and consistent wind speeds. At present, the majority of installed turbines are on bottom-fixed support structures, while floating platforms have been applied for relatively deep (> 200 m) water. There is some evidence that floating platforms may be economically feasible in intermediate water depths (50 – 200 m), although there remain technical challenges and uncertainties.

The project thesis identified a Floating Wind Turbine (FWT) concept, OO Star 6MW concept, and an available numerical solution strategy for investigating the behavior of the FWT in intermediate water-depths. The master thesis represents the logical continuation. It will examine the behavior of the selected FWT concept at different water depths in relevant environmental conditions. Challenges for the system as a whole and for the mooring-line arrangement will be analyzed. Importance of coupling and nonlinear effects in the fluid-body interactions will be examined, as well as the sensitivity of the results to the chosen numerical modelling. Attention will be given to the damping effect of the plates adopted for the selected FWT concept.

#### **Objective**

The present master thesis aims to contribute to enhancing the knowledge of the behaviour of FWT concepts in intermediate water-depth sites. This includes an attempt to assess sensitivity to adopted theoretical/numerical modelling and relevant features of concept design.

The work should be carried out in steps as follows:

1. Summarize major findings/outcomes from the project thesis. Summarize the numerical modelling selected for the investigations on the OO Star 6MW FWT concept and discuss assumptions and limitations.
2. Complement the literature study initiated in the project thesis with focus on the state-of-the-art research and activities involving FWT concepts, as well as on the damping effects of plates in the selected concept. As the OO Star 6MW is a semi-submersible, compare this type of FWT's to other offshore wind turbine concepts.
3. Update the numerical model based on the results of the project thesis. Check the rigid body motions through free decay tests. Verify the turbine model (independent of the floating platform) against specifications.
4. Using studies from the project thesis in terms of relevant intermediate water-depth sites and environmental conditions, examine numerically the behaviour of the FWT in three different water-depths. Examine the influence of water depth and identify critical conditions for extreme response analysis, in addition to relevant operational conditions for the turbine. Study the influence of coupling and possibly nonlinear effects.

5. Perform parametric studies on the design of the heave damping plates of the FWT concept. Simplified CFD simulations and/or findings from the literature studies in step 2 should be used to quantify the damping and added-mass effect of the plates.
6. Perform global time domain analysis with the different plate designs and water depths and examine the effect in terms of ULS and relevant operational states.

The work may show to be more extensive than anticipated. Some topics may therefore be left out after discussion with the supervisor without any negative influence on the grading.

The candidate should in his report give a personal contribution to the solution of the problem formulated in this text. All assumptions and conclusions must be supported by mathematical models and/or references to physical effects in a logical manner.

The candidate should apply all available sources to find relevant literature and information on the actual problem.

The thesis should be organised in a rational manner to give a clear presentation of the work in terms of exposition of results, assessments, and conclusions. It is important that the text is well written and that tables and figures are used to support the verbal presentation. The thesis should be complete, but still as short as possible. In particular, the text should be brief and to the point, with a clear language. Telegraphic language should be avoided.

The thesis must contain the following elements: the text defining the scope (i.e. this text), preface (outlining project-work steps and acknowledgements), abstract (providing the summary), table of contents, main body of thesis, conclusions with recommendations for further work, list of symbols and acronyms, references and (optional) appendices. All figures, tables and equations shall be numerated.

The supervisor may require that the candidate, in an early stage of the work, present a written plan for the completion of the work. The plan should include budget for the use of computer and laboratory resources that will be charged to the department. Overruns shall be reported to the supervisor.

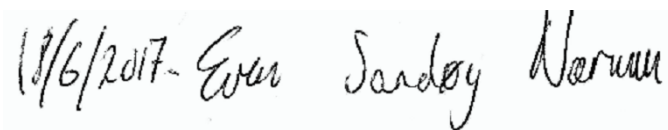
From the thesis it should be possible to identify the work carried out by the candidate and what has been found in the available literature. It is important to give references to the original source for theories and experimental results.

Supervisor : Marilena Greco  
Submitted : January 13<sup>th</sup> 2017  
Deadline : June 18<sup>th</sup> 2017

Marilena Greco  
Supervisor

## Preface

The master thesis herein constitutes the 5-year Master of Science program in Marine Technology with a specialization in hydrodynamics at the Norwegian University of Science and Technology (NTNU). The thesis presents the work done over the course of the spring semester of 2017. The studies have been based on numerical analysis on the floating wind turbine concept OO-Star Wind Floater, patented by Dr. Techn. Olav Olsen AS. The company has provided information on the design and participated in defining the early scope of this thesis.

A handwritten signature in black ink on a light-colored background. The signature reads "18/6/2017 - Even Sandøy Nærum".

Even Sandøy Nærum  
Asker, June 18, 2017



## Acknowledgments

First and foremost, I would like to express my sincere gratitude to my supervisor, professor Marilena Greco. Throughout the thesis work, our weekly meetings have provided a stable progress and fruitful discussions. I would especially like to thank her for allowing me to identify and pursue my own topics, and for her constructive feedback and opinions on the thesis scope.

A special recognition is more than due to co-supervisor Erin Bachynski. Her experience and knowledge in numerical modelling of floating wind turbines have been of great help. She has been available and devoted time on short notice when I encountered problems in the software. I would also like to thank her for invaluable advice in the writing process of this thesis.

My supervisor in Dr. Techn. Olav Olsen AS, Håkon S. Andersen, deserves a recognition for providing structural drawings on the concept. I would also like to thank both him and his colleague Simen K. Rasmussen for helping define the early scope of the thesis.

I would also like to thank my colleagues and friends at office C.1.062 for creating an energetic and fun atmosphere to work in.

Finally, I would like to express a special thanks to my parents, as their support have been priceless throughout the thesis work. They have also been helpful by giving me constructive criticism on the thesis writing, and offering a different perspective on the subject.





## Abstract

Floating wind turbines are considered to be a promising source for renewable energy. Offshore wind power production is moving towards larger turbines and deeper water, and FWT's can unlock areas of rich wind resources currently unavailable due to large water depths. The application of FWT's do, however, come with engineering challenges, especially in the intermediate water range. This thesis aims to map out the added hydrodynamic implications of a semi-submersible FWT concept in intermediate water by numerical analysis. Viscous effects have been given a particular consideration in the numerical modelling, and consequently it was also decided to investigate the damping effects due to heave plates.

The North Sea is considered viable for floating wind production due to high average wind speeds. 3 locations in this area, with water depths of 50, 80 and 110 metres, were therefore selected to investigate the FWT behaviour in the intermediate water range. Joint distribution models for wind and waves were used to establish extreme state and operational environmental cases for analysis.

Previous studies have indicated that slow drift excitation forces are particularly important in shallow and intermediate water. Experiments have shown that this force contribution increases in this range, and that it can be underestimated by numerical methods in such conditions. Past studies have also indicated that the relative wave velocity at the structure can significantly change viscous damping and flow separation due to sharp edges. Heave plates are often designed for semi-submersibles to take advantage of this effect, as high damping coefficients and flow separation can cause favourable damping on the structure. Due to past experiments, second-order potential theory was used to establish slow drift excitation forces in the intermediate range. Additionally, 3 alternative heave plate configurations were proposed for the 6 MW OO-Star Wind Floater, to possibly uncover parameters with better heave stability.

The numerical modelling was based on the 6 MW OO-Star Wind Floater, which is a semi-submersible FWT concept developed by Dr. Techn. Olav Olsen AS. Coupled aero-hydro-servo-elastic analysis were carried out by *SIMO/RIFLEX*-coupling in *SIMA*. An iterative procedure was proposed to obtain reasonable estimates for the viscous forces in each environmental case. In this procedure, the KC-numbers of the OO Star hull components were obtained through a statistical consideration for each sea state, and KC-dependent viscous force coefficients were established based on a literature study. A separate catenary mooring configuration was designed for each water depth.

The global time domain analysis confirmed that difference-frequency excitation forces had a considerable contribution to the FWT response. This force contribution also increased with decreasing water depth, and it was especially governing for high wave periods. In extreme conditions, the OO-Star Wind Floater response in surge and pitch was directly affected by this, and it was concluded that depth effects will change the design parameters for the OO-Star Wind Floater in the intermediate water range.

Additionally, the first order excitation forces also experienced depth effects. This load contribution was consistently lower for the 50 meter model. As a consequence, the heave response in this depth was smaller than for the other depths.

A design with an extra heave plate, in the same material and geometry as the original plate,

improved the heave response. In extreme conditions, the response in this degree of freedom was 8.7 % lower than the response of the original plate. The new design also experienced a lower response in surge. However, further studies are needed to determine whether the reduced response will increase the lifetime of the OO Star enough to defend a higher cost of material.





## Sammendrag

Flytende vindturbiner anses å være en lovende kilde for fornybar energi. Utaskjærs vindkraftproduksjon har de siste årene beveget seg mot større turbiner og dypere vann, og flytende vindturbiner kan utnytte store vindressurser som har vært utilgjengelige. Anvendelsen av flytende vindturbiner i mellomgrunt vann kommer imidlertid med tekniske utfordringer på grunn av den begrensede vanddybden. Denne oppgaven tar sikte på å kartlegge de ekstra hydrodynamiske implikasjonene av en halvt nedsenkbar flytende vindturbin i mellomgrunt vann ved hjelp av numerisk analyse. Viskøse effekter har blitt studert grundig i den numeriske modelleringen, og oppgaven tar også sikte på å undersøke dempingeffekter på grunn av hivplater.

Nordsjøen anses å være et levedyktig område for flytende vindproduksjon ettersom det er et område med høye gjennomsnittlige vindhastigheter. 3 lokasjoner i dette området, med vanddybder på 50, 80 og 110 meter, ble derfor valgt for å undersøke oppførselen til den flytende vindturbinen i mellomgrunt vann. Fellesfordelingsmodeller for vind og bølger ble brukt til å etablere ekstremtilstanden og operative lasttilstander for numerisk analyse.

Tidligere studier tyder på at kraftbidraget grunnet differansen mellom to bølgekomponenter kan være spesielt viktig i grunt og mellomgrunt vann. Eksperimenter har vist at dette kraftbidraget øker i grunt vann, og at det kan undervurderes ved numeriske metoder under slike forhold. Både numeriske og eksperimentelle studier viser at den relative bølgehastigheten ved strukturen kan forandre viskøs demping og strømningsavløsning grunnet skarpe kanter. Hivplater er ofte brukt på halvt nedskenkbare plattformer for å utnytte denne effekten, da høye dempingskoeffisienter og strømningsavløsning kan forårsake gunstig demping for strukturen. På grunn av tidligere eksperimenter ble 2. ordens potensialteori brukt til å etablere kraftbidraget fra den nevnte bølgedifferansen. I tillegg ble det foreslått 3 alternative hivplatekonfigurasjoner for konseptet OO-Star Wind Floater, med formål å avdekke en struktur med bedre hivstabilitet.

Den numeriske modelleringen var basert på 6 MW OO-Star Wind Floater, som er et halvt nedsenkbart flytende vindturbin-konsept utviklet av Dr. Techn. Olav Olsen AS. Koblet aero-hydro-servo-elastisk analyse ble utført ved hjelp av *SIMO/RIFLEX*-kobling i *SIMA*. Det ble foreslått en iterativ prosedyre for å oppnå rimelige estimater for de viskøse kreftene for hver lasttilstand. I denne prosedyren ble KC-tallene til vindturbinens skrogkomponenter bestemt gjennom en statistisk vurdering for hver sjøtilstand, og KC-avhengige viskøse kraftkoeffisienter ble etablert basert på et litteraturstudie. En separat forankringskonfigurasjon ble utformet for hvert vanddyb.

Den globale tidsdomenanalysen bekreftet at 2. ordens eksitasjonskrefter hadde et betydelig bidrag til den flytende vindturbinens respons. Dette kraftbidraget økte for redusert vanddybde, og var spesielt styrende for høye bølgeperioder. I ekstreme forhold ble OO-Star Wind Floater-responsen i jag og stamp direkte påvirket av dette, og det ble konkludert med at dybdeeffekter vil endre designparametrene for OO-Star Wind Floater i grunnere vann.

I tillegg ble det også observert en dybdeeffekt for første ordens eksitasjonskrefter. Dette belastningsbidraget var konsekvent lavere for modellen på 50 meters dyp. Som en følge av dette var hivresponsen i denne dybden mindre enn for de andre dybdene.

Et design med en ekstra hivplate, i samme materiale og geometri som originalplaten, forbedret hivresponsen. I ekstreme forhold var standardavviket i denne frihetsgraden 8,7 % lavere enn

responsen til den opprinnelige platen. Det nye designet opplevde også en lavere respons i jag. Imidlertid er det behov for ytterligere studier for å avgjøre om den reduserte respons vil øke levetiden til OO Star nok til å forsvare en høyere materialkostnad.







# Nomenclature

## Abbreviations

BEM	Blade Element Momentum
CFD	Computational Fluid Dynamics
COB	Centre of Buoyancy
COG	Centre of Gravity
DOF	Degree of Freedom
FE	Finite Element
FEM	Finite Element Method
FLS	Fatigue Limit State
FWT	Floating wind turbine
GDW	Generalized Dynamic Wake
HSWL	Highest water level
IEA	International Energy Association
JR	Jacobi Ratio
KC	Keulan-Carpenter
LCOE	Levelized cost of energy
MSL	Mean water level
MW	Mega-Watt
N	Newton
NREL	National Renewable Energy Laboratory
PSD	Power Spectral Density

QTF Quadratic Transfer Function

RANS Reynolds-Averaged Navier Stokes

TLP Tension-Leg Platform

ULS Ultimate Limit State

W Watt

WADAM Wave Analysis by Diffraction and Morison Theory

### Letters

$A_{33}$  Added mass in heave

$A_{33}^{corr}$  Correction to added mass in time-domain simulations

$C_A$  Added-mass coefficient

$C_D$  Drag coefficient

$C_M$  Mass coefficient

$D$  Diameter

$g$  Acceleration of gravity

$h$  Water depth

$H_S$  Significant wave height

$k$  Wave number

$K_I$  Integral speed-error gain

$K_P$  Proportional speed-error gain

$T_P$  Peak period

$T_{Hi}$  Pretension in mooring line i

$T_{ni}$  Natural period in DOF i

$U_c$  Current speed

$U_w$  Wind speed

### Symbols

$\eta_k$  Body motion

$\lambda$	Wave Length
$\omega$	Circular wave frequency
$\phi$	Velocity potential
$\rho$	Density of water
$\sigma_v$	Standard deviation of velocity
$\theta$	Wave direction
$\zeta$	Surface elevation
$\zeta_a$	Amplitude of regular wave



# Contents

Preface . . . . .	iii
Acknowledgements . . . . .	iv
Abstract . . . . .	v
Sammendrag . . . . .	vi
<b>List of Figures</b>	<b>xvi</b>
<b>List of Tables</b>	<b>xx</b>
<b>1 Introduction</b>	<b>1</b>
1.1 Background . . . . .	2
1.1.1 Project Thesis . . . . .	2
1.1.2 Current State of Offshore Wind Industry . . . . .	4
1.2 Feasibility of Floating Wind Turbines . . . . .	6
1.3 Objectives . . . . .	8
1.4 Structure . . . . .	9
<b>2 Literature</b>	<b>11</b>
2.1 Added-Mass and Drag of Heave Plate . . . . .	11
2.2 Selection of Viscous Coefficients . . . . .	15
2.3 Numerical software for FWT design . . . . .	19
2.4 Intermediate Water Effects . . . . .	20
<b>3 Theory</b>	<b>23</b>
3.1 Hydrodynamic Theory . . . . .	23
3.1.1 Linear Theory . . . . .	23
3.1.2 Short Term Wave Statistics . . . . .	24
3.1.3 Wave Spectrum . . . . .	25
3.1.4 Response in Regular Waves . . . . .	26
3.1.5 Non-Linear Effects . . . . .	27
3.2 Aerodynamic Theory . . . . .	30
3.2.1 Blade Element/Momentum . . . . .	30
3.2.2 Corrections of BEM . . . . .	31
3.2.3 Wind Profile . . . . .	34
3.3 Coupled Time-Domain Analysis . . . . .	34

3.3.1	Non-Linear Finite Element Method	35
3.3.2	Time-Domain Solution	35
3.4	Catenary Equations	37
<b>4</b>	<b>Environmental Conditions</b>	<b>41</b>
4.1	Locations	41
4.2	Joint Distribution of Wind and Waves	43
4.3	Wind Distribution Models	44
4.4	Currents	45
4.5	Water Levels	46
4.6	Load Cases	47
<b>5</b>	<b>Methodology</b>	<b>49</b>
5.1	OO-Star Wind Floater	49
5.2	Programming	50
5.2.1	GeniE	51
5.2.2	HydroD	51
5.2.3	TurbSim	51
5.2.4	SIMA Workbench	52
5.3	FE Panel Model	52
5.4	Frequency-Domain Hydrodynamic Analysis	56
5.4.1	Frequency Domain	56
5.4.2	Second Order Frequency Domain	57
5.5	Coupled Model	59
5.5.1	FWT Hull Corrections	59
5.5.2	Wind Turbine Dimensions	60
5.5.3	Wind Input	61
5.5.4	Control System	61
5.6	Viscous Forces in Time-Domain	64
5.6.1	Heave Plate Modelling	64
5.6.2	Non-Linear Viscous Drag	65
5.6.3	Iterative Scheme	65
5.7	Design of Mooring System	67
5.7.1	Design Challenges	67
5.7.2	Material	67
5.7.3	Design procedure	68
5.7.4	Final Design	69
5.7.5	Design verification	69
5.8	Conceptual Heave Plate Study	70
<b>6</b>	<b>Verification of Numerical Model</b>	<b>73</b>
6.1	Potential Theory from HydroD	73
6.2	Free Decay	73
6.3	Mooring Line Static Tension	76

6.4	Wind Turbine Performance	77
<b>7</b>	<b>Intermediate Water Depth Study</b>	<b>81</b>
7.1	Quadratic Transfer Function	81
7.2	Viscous Force Coefficients	82
7.3	Time Series	83
7.4	Model Behaviour in Intermediate Water Range	88
7.5	Loads in Intermediate Water Range	93
7.6	Global FWT Response Spectrum	99
7.6.1	Case E	100
7.6.2	Case O1	106
7.6.3	Case O2	109
7.6.4	Case M1	113
7.6.5	Case M2	117
<b>8</b>	<b>Parametric Heave Plate Study</b>	<b>121</b>
8.1	HydroD Natural Periods	121
8.2	KC	122
8.3	Standard Deviations of Different Heave Plate Parameters	123
8.4	Power Spectral Densities for Heave Plate Configurations	126
8.4.1	Case M1	126
8.4.2	Case O1	132
8.4.3	Case E.1	138
<b>9</b>	<b>Conclusion</b>	<b>147</b>
	<b>Bibliography</b>	<b>151</b>
<b>A</b>	<b>Free Decay</b>	<b>I</b>
A.1	Surge	I
A.2	Sway	II
A.3	Heave	III
A.4	Pitch	IV
A.5	Roll	V
A.6	Yaw	V
<b>B</b>	<b>Difference-Frequency Excitation Forces</b>	<b>VII</b>
B.1	50 m	VIII
B.1.1	Surge	VIII
B.1.2	Heave	IX
B.1.3	Pitch	X
B.1.4	Yaw	XI
B.2	80 m	XII
B.2.1	Surge	XII

B.2.2	Heave	XIII
B.2.3	Pitch	XIV
B.2.4	Yaw	XV
B.3	110 m	XVI
B.3.1	Surge	XVI
B.3.2	Heave	XVII
B.3.3	Pitch	XVIII
B.3.4	Yaw	XIX
<b>C</b>	<b>FWT Time-Series and Spectrums</b>	<b>XXI</b>
C.1	Global FWT Motion Spectrum	XXI
C.1.1	Case O1	XXI
C.1.2	Case O2	XXII
C.1.3	Case M1	XXIII
C.1.4	Case M2	XXIV
C.2	Wave Loads in Time-Domain Simulation	XXV
C.2.1	Case O1	XXV
C.2.2	Case O2	XXVI
C.2.3	Case M1	XXVII
C.2.4	Case M2	XXVIII
C.3	Heave Plate Parametric Study	XXIX
C.3.1	Case M1	XXIX
C.3.2	Case O1	XXIX
C.4	Wave Loads in Time-Domain Simulation	XXXI
C.4.1	Case M1	XXXI
C.4.2	Case O1	XXXII
<b>D</b>	<b>Structural Drawing 6 MW OO Star</b>	<b>XXXIII</b>



# List of Figures

1.1	Body motions due to superposition of environmental loads and coupled analysis. (Nærum, 2016)	3
1.2	Cumulative and annual offshore wind turbine capacity (Ho and Mbistrova, 2016)	4
1.3	Sea depth in Europe (Ho et al., 2016)	5
1.4	Bottom-fixed and floating wind turbine foundations (Bailey et al., 2014)	6
2.1	Non-dimensional added mass for different depth/diameter-ratios as a function of wave number $k$ and disc diameter $a$ ( $b = \text{depth}/\text{diameter}$ ), (Martin and Farina, 1997)	12
2.2	Added mass and damping coefficients from Lopez-Pavon and Souto-Iglesias (2015)	13
2.3	Dependence of spacing and $KC$ on added mass (Tao et al., 2007)	14
2.4	$KC$ -dependence of added mass and damping of column with heave-plates (Lopez-Pavon and Souto-Iglesias, 2015),(Tao et al., 2007),(Moreno et al., 2015),(Tao and Cai, 2004).	16
2.5	Added mass dependency on $KC$ , $KC_w$ (Moreno et al., 2015)	17
2.6	Damping dependency on $KC$ , $KC_w$ (Moreno et al., 2015)	17
2.7	Drag Coefficients for different $KC$ (Li and Lin, 2010)	18
3.1	Relative importance of mass, viscous drag and diffraction forces on marine structures Faltinsen (1993)	30
3.2	Forces acting on a 2-D foil section (Glauert, 1983)	31
3.3	Relative velocity on a foil section (Glauert, 1983)	32
3.4	Upwind tower effect including drag correction (Bachynski, 2016)	33
3.5	Simplified illustration of mooring line configuration	37
3.6	Catenary mooring line (Faltinsen, 1993)	38
4.1	Bathymetry contours in the North Sea (Neill et al., 2014)	42
4.2	100-year $H_S$ in the North Sea (Williams et al., 2008)	42
4.3	Water level components (DNV, 2016)	46
5.1	6 MW OO-Star Wind Floater (Dr. Techn. Olav Olsen, 2016)	50
5.2	Overview of software used to build the numerical model	51
5.3	Flow chart for the aero-hydro-servo-elastic coupling in <i>SIMA Workbench</i>	52
5.4	Illustration of free surface model	55

5.5	Comparison of Newman approximation and second-order potential theory with fine and coarse frequency resolution . . . . .	58
5.6	Pitch motion with different speed-error gains . . . . .	63
5.7	Conceptual design cases . . . . .	71
6.1	Static horizontal mooring line tension for surge displacement of FWT . . . . .	76
6.2	Rated power, rotor speed and thrust for 6 MW OO Star . . . . .	78
6.3	Generator torque, rotor speed and blade pitch for 6 MW OO Star . . . . .	78
6.4	Rotor thrust, steady-state surge position and pitch angle for 6 MW OO Star . . . . .	79
7.1	Quadratic transfer function in surge and pitch . . . . .	81
7.2	Surge response time-series for load case O.1 . . . . .	84
7.3	Surge response time-series for load case M.1 . . . . .	85
7.4	Pitch response time-series for load case O.1 . . . . .	86
7.5	Pitch response time-series for load case M.1 . . . . .	87
7.6	Power output for load cases O.1 and M.1 . . . . .	88
7.7	Surge response PSD, load case E.1/E.2 . . . . .	100
7.8	Heave and pitch response PSD, load case E.1/E.2 . . . . .	101
7.9	Surge first order, mean drift and difference Frequency loads, PSD for load case E.1/E.2 . . . . .	102
7.10	Heave and pitch first order and difference-frequency loads, PSD for load case E.1/E.2	103
7.11	Aerodynamic pitch moment PSD, load case E.1/E.2 . . . . .	104
7.12	Heave and pitch response PSD, load case O.1 . . . . .	106
7.13	Pitch and heave first order and difference-frequency loads, PSD for load case O.1 .	107
7.14	Aerodynamic pitch moment PSD, load case O.1 . . . . .	108
7.15	Heave and pitch response PSD, load case O.2 . . . . .	109
7.16	Pitch and heave first order and difference-frequency loads, PSD for load case O.2 .	110
7.17	Aerodynamic pitch moment PSD, load case O.2 . . . . .	111
7.18	Heave and pitch response PSD, load case M.1 . . . . .	113
7.19	Pitch and heave first order and difference-frequency loads, PSD for load case M.1 .	114
7.20	Aerodynamic pitch moment PSD, load case M.1 . . . . .	115
7.21	Heave and pitch response PSD, load case M.2 . . . . .	117
7.22	Pitch and heave first order and difference-frequency loads, PSD for load case M.2 .	118
7.23	Aerodynamic pitch moment PSD, load case M.2 . . . . .	119
8.1	Heave PSD for different heave plate parameters, load case M.1 . . . . .	126
8.2	Pitch PSD for different heave plate parameters, load case M.1 . . . . .	127
8.3	Heave first order excitation forces PSD - load case M.1 . . . . .	128
8.4	Pitch first order excitation forces PSD - load case M.1 . . . . .	129
8.5	Aerodynamic pitch moment PSD - Case M.1 . . . . .	130
8.6	Heave PSD for different heave plate parameters, load case O.1 . . . . .	132
8.7	Pitch PSD for different heave plate parameters, load case M.1 . . . . .	133
8.8	Heave first order excitation forces PSD - load case O.1 . . . . .	134
8.9	Pitch first order excitation forces PSD - load case M.1 . . . . .	135

8.10	Aerodynamic pitch moment PSD - Case O.1	136
8.11	Surge PSD for different heave plate parameters, load case E.1	138
8.12	Heave PSD for different heave plate parameters, load case E.1	139
8.13	Pitch PSD for different heave plate parameters, load case M.1	140
8.14	Surge first order excitation forces and mean wave drift PSD - load case E.1	141
8.15	Heave first order excitation forces PSD - load case E.1	142
8.16	Pitch first order excitation forces PSD - load case E.1	143
8.17	Aerodynamic pitch moment PSD - Case E.1	144
A.1	Free decay tests in surge	I
A.2	Free decay tests in sway	II
A.3	Free decay tests in heave	III
A.4	Free decay tests in pitch	IV
A.5	Free decay test in roll	V
A.6	Free decay test in yaw	V
B.1	Contour plots of surge difference-frequency excitation force at first-order wave frequencies	VIII
B.2	Contour plots of heave difference-frequency excitation force at first-order wave frequencies	IX
B.3	Contour plots of pitch difference-frequency excitation force at first-order wave frequencies	X
B.4	Contour plots of yaw difference-frequency excitation force at first-order wave frequencies	XI
B.5	Contour plots of surge difference-frequency excitation force at first-order wave frequencies	XII
B.6	Contour plots of heave difference-frequency excitation force at first-order wave frequencies	XIII
B.7	Contour plots of pitch difference-frequency excitation force at first-order wave frequencies	XIV
B.8	Contour plots of yaw difference-frequency excitation force at first-order wave frequencies	XV
B.9	Contour plots of surge difference-frequency excitation force at first-order wave frequencies	XVI
B.10	Contour plots of heave difference-frequency excitation force at first-order wave frequencies	XVII
B.11	Contour plots of pitch difference-frequency excitation force at first-order wave frequencies	XVIII
B.12	Contour plots of yaw difference-frequency excitation force at first-order wave frequencies	XIX
C.1	FWT Surge response spectrum	XXI
C.2	FWT Surge response spectrum	XXII
C.3	FWT Surge response spectrum	XXIII

C.4 FWT Surge response spectrum . . . . . XXIV

C.5 FWT Surge First Order, Mean Drift and Difference Frequency Loads . . . . . XXV

C.6 FWT Surge First Order, Mean Drift and Difference Frequency Loads . . . . . XXVI

C.7 FWT Surge First Order, Mean Drift and Difference Frequency Loads . . . . . XXVII

C.8 FWT Surge First Order, Mean Drift and Difference Frequency Loads . . . . . XXVIII

C.9 FWT Surge response spectrum . . . . . XXIX

C.10 FWT Surge response spectrum . . . . . XXX

C.11 FWT Surge First Order, Mean Drift Loads . . . . . XXXI

C.12 FWT Surge First Order and Mean Drift Loads . . . . . XXXII

# List of Tables

1.1	Natural periods, linear and quadratic damping coefficients (Nærum, 2016) . . . . .	2
4.1	Deep water wave length . . . . .	41
4.2	Parameters for joint distribution of wind and waves (Johannessen et al., 2001), (Li et al., 2013) . . . . .	43
4.3	Variations of environmental conditions . . . . .	44
4.4	Wind profile parameters (IEC et al., 2009) . . . . .	45
4.5	Ocean current parameters . . . . .	46
4.6	Variations of environmental conditions . . . . .	47
4.7	Environmental cases . . . . .	47
5.1	OO Star Wind Floater data in operational state (Dr. Techn. Olav Olsen, 2016) . . . . .	49
5.2	Mesh quality of FE panel model . . . . .	53
5.3	Difference periods for second-order <i>WADAM</i> -analysis . . . . .	58
5.4	Hydrostatic parameters . . . . .	60
5.5	Upscaling of NREL 5MW rotor to 6MW . . . . .	61
5.6	Speed-Error Gains . . . . .	63
5.7	Slender elements in <i>SIMA</i> . . . . .	66
5.8	Stud Chain Properties (Veritas, 2015) . . . . .	68
5.9	Properties of cross section design . . . . .	69
5.10	Tabulated values of catenary design . . . . .	70
5.11	GeniE-values in conceptual heave plate designs . . . . .	72
6.1	Natural periods from <i>HydroD</i> . . . . .	73
6.2	Natural periods and damping for coupled models . . . . .	74
7.1	KC-numbers, $A_{33}^{corr}$ and drag coefficients for load case O.1 . . . . .	82
7.2	KC-numbers, $A_{33}^{corr}$ and drag coefficients for load case O.2 . . . . .	82
7.3	KC-numbers, $A_{33}^{corr}$ and drag coefficients for load case M.1 . . . . .	83
7.4	KC-numbers, $A_{33}^{corr}$ and drag coefficients for load case M.2 . . . . .	83
7.5	KC-numbers, $A_{33}^{corr}$ and drag coefficients for load case E.1 and E.2 . . . . .	83
7.6	Standard deviation of FWT response . . . . .	89
7.7	Extreme values of FWT response . . . . .	91
7.8	Standard deviation of FWT loads - Case 0.1 . . . . .	94

7.9	Standard deviation of FWT loads - Case 0.2	95
7.10	Standard deviation of FWT loads - Case M.1	96
7.11	Standard deviation of FWT loads - Case M.2	97
7.12	Standard deviation of FWT loads - Case E.1/E.2	97
8.1	Natural periods for heave plate designs	121
8.2	Kc-numbers $A_{33}^{corr}$ and drag coefficients for load case O.1	122
8.3	KC-numbers $A_{33}^{corr}$ and drag coefficients for load case M.1	122
8.4	KC-numbers $A_{33}^{corr}$ and drag coefficients for load case E.1	122
8.5	Standard deviations for different heave plate parameters	123
8.6	Extreme values for different heave plate parameters	125

# Chapter 1

## Introduction

An important topic for engineers today is the development of sustainable energy sources for the future. Due a growing population worldwide and economic growth in developing countries, the International Energy Association (IEA) expects the global demand for energy to increase by 48% between 2012 and 2040. At the same time, the threat of global warming due to the burning of fossil fuels remain a threat. In order to meet the future energy demands while overcoming the challenges presented by climate change, developing new and renewable energy sources are a necessity.

Floating wind turbines (FWT's) are a promising technology when it comes to delivering renewable energy. This technology would allow for harvesting of wind energy at deep water sites, where such resources could be rich and consistent. However, as with most developing technologies, engineering and economical challenges need to be solved. One important challenge is to reduce the motions of a floating substructure and ensure the stability of the floater. The economic feasibility of FWT power production depend on several unknown quantities, with development costs, material costs, size of wind farm and distance from shore being important factors.

One of the concepts that aim to overcome these issues is the 6 MW OO-Star Wind Floater concept. It is a semi-submersible FWT designed by the company Dr. Techn. Olav Olsen AS. It is designed with a concrete floating structure, which could possibly reduce the material costs. One of the uncertain engineering aspects is its behaviour in intermediate water. This could be an important area of application in order to unlock areas of high wind close to shore, where the water depth is too large for fixed wind turbine foundations. This thesis aims to map out the challenges in such conditions. It also aims to investigate the importance of viscous effects to reduce global motions, for configurations of the original OO-Star Wind Floater design.

## 1.1 Background

### 1.1.1 Project Thesis

A project thesis was carried out as a preparation for this master study in the fall of 2016. In this preliminary study, a numerical model of the 6 MW OO-Star Wind Floater design was proposed. The proposed model was based on structural drawings provided by Dr. Techn. Olav Olsen AS, and the simulation platform was selected in view of the current state-of-the-art in FWT design software. A North Sea location with a water depth of 70 metres was selected, and environmental conditions based on this location was implemented in a coupled analysis. The hydrodynamic performance of the numerical model was assessed through free decay tests.

Some simplifications and assumptions were made during the project thesis. Simple modifications were made to the structural design of the OO-Star Wind Floater, in order to make for an easier modelling process. However, free decay tests revealed that the symmetric qualities of the original design were not sufficiently preserved in time-domain analysis. This can be seen in table 1.1, where the natural periods in surge-sway and roll-pitch deviate with 0.23 and 0.14 seconds, respectively. Because of this, improving the finite element (FE) panel model to reduce these numerical errors was proposed as a recommendation for further work.

Another important discovery was that the natural period in heave was lower than expected.

Table 1.1: Natural periods, linear and quadratic damping coefficients (Nærum, 2016)

Degree of Freedom	$T_n$ [s]	$b_l$ [ $\cdot 10^3$ ]	$b_q$ [ $\cdot 10^3$ ]
Surge	107.47	0.40	56.9
Sway	107.24	0.62	48.8
Heave	19.56	4.026	27.81
Roll	29.83	1.282	7.2
Pitch	29.69	1.278	3.6
Yaw	110.1	4.380	42.098

Semi-submersibles are generally designed with this value being above 20 seconds, in order to avoid resonance behaviour in normal waves (Faltinsen, 1993). However, the free decay tests on the numerical model of the OO-Star Wind Floater concept yielded a natural period of 19.56 seconds in heave. The reasons for this behaviour were discussed, and it was proposed that incorrect implementation of second-order drag forces in time-domain could be an important factor. However, correspondence with supervisors in the wake of the thesis uncovered that the effect of drag on added mass would be more important in shifting the natural periods.

Besides second-order drag forces, no higher-order hydrodynamics was included in the analysis. Especially slow-drift excitation forces could be important for moored structures, and the the assessment of higher-order hydrodynamics for the OO-Star Wind Floater were proposed for further work.



In general, the modelling approach utilized in the project thesis was determined to be adequate. A simple catenary mooring design was implemented and assessed to be adequate for the purposes of the project thesis. The performance curves of a 6 MW rotor and control system was validated, and its performance in a coupled wind, wave and current environment was verified. A coupling effect between wind, wave and current loads were observed (Figure 1.1).

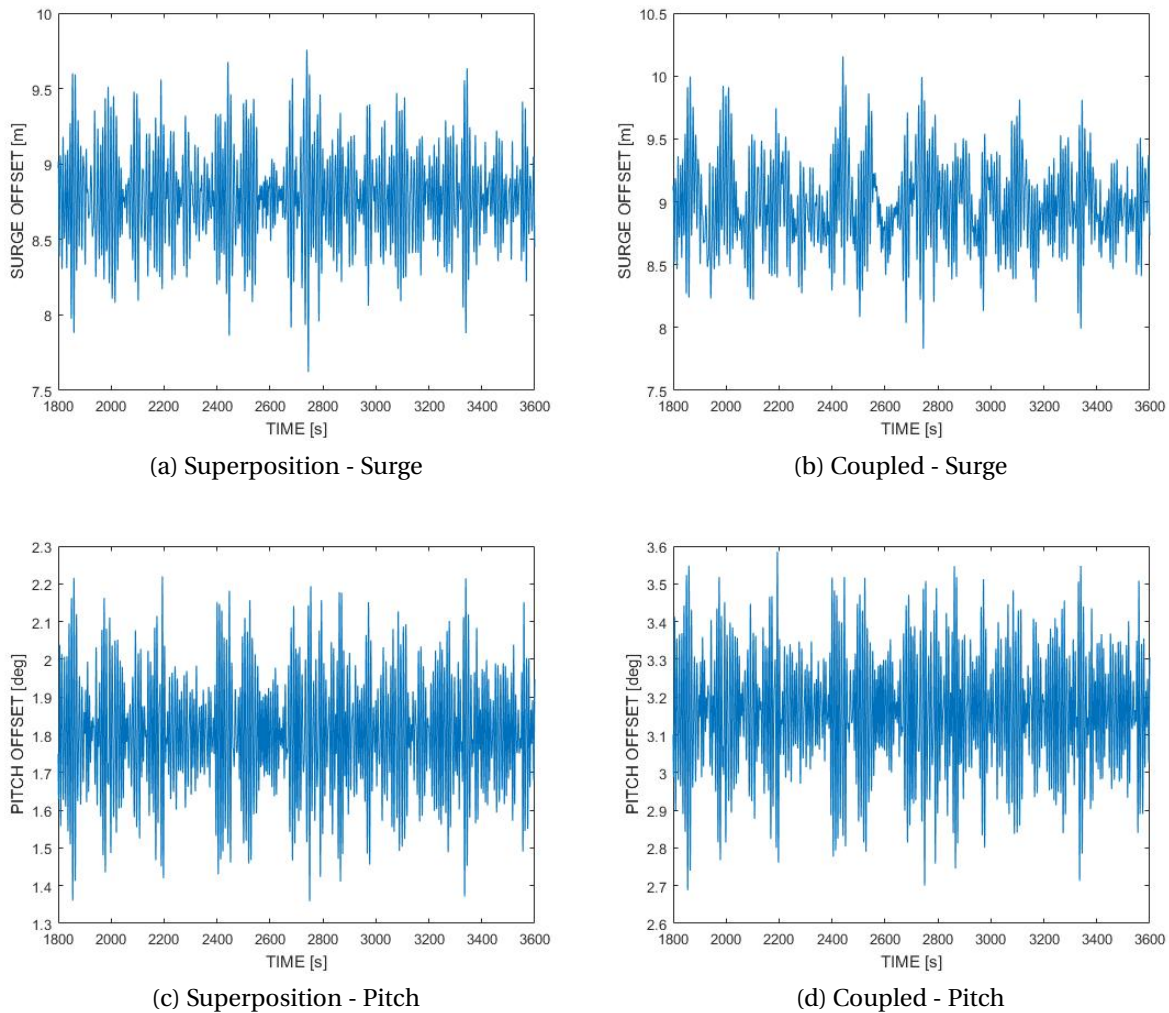


Figure 1.1: Body motions due to superposition of environmental loads and coupled analysis. (Nærum, 2016)

The preliminary studies in the project thesis laid the foundation for this master thesis. The general procedure was followed also in this report, with some changes due to the discoveries in the preliminary studies.

### 1.1.2 Current State of Offshore Wind Industry

Offshore wind turbines have had a growing contribution to the worldwide energy consumption since the first offshore wind turbines were built off the coast of Denmark in 1991 (Strahan, 2014). Today, offshore wind is an established energy source, contributing to 2,96 % of the global wind energy capacity (14.384 out of 486.749 MW)(Council, 2017). Most of the offshore wind installations are situated off the coast of Europe, with a total capacity of 12.631 MW in 2016 (Ho and Mbistrova, 2016).

The outlook for the offshore wind industry in Europe is generally positive. The industry saw a

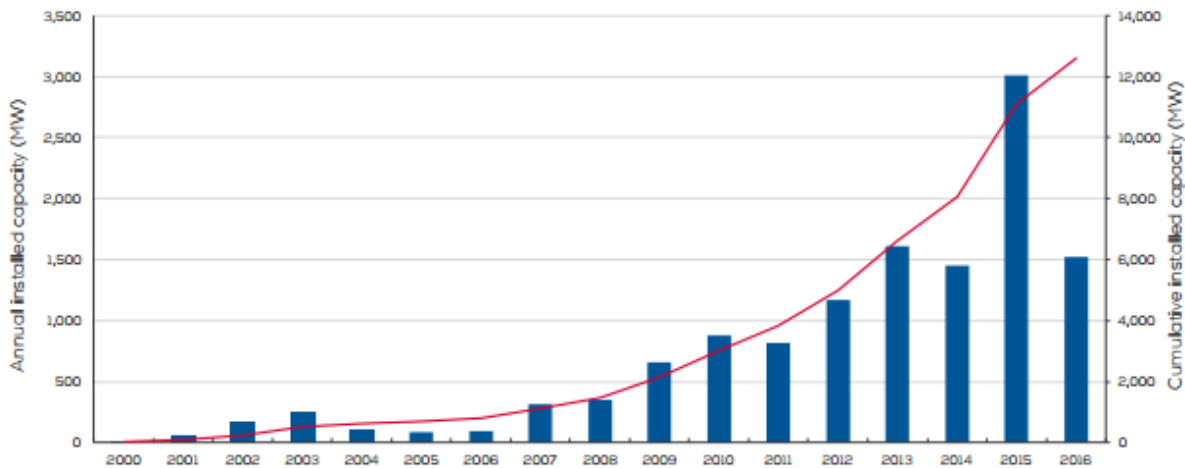


Figure 1.2: Cumulative and annual offshore wind turbine capacity (Ho and Mbistrova, 2016)

big increase in the annual commissioning of new installations between 2006 and 2015 (Figure 1.2). However, the huge increase of new capacity in 2015 is seen as somewhat uncharacteristic. Due to factors like a more conservative prediction for power demand in Europe and the 2008 financial crisis the growth of annual installations are expected to decline somewhat (Moccia, 2014)(Corbetta, 2015). It should be noted that it is still a growing industry, and the cumulative offshore wind power capacity is expected to reach a capacity of 66 GW in 2030 (Corbetta, 2015). This trend is also expected worldwide, where China, South Korea and the United States all had large increases in their offshore wind capacity in 2016 (Council, 2017).

The offshore wind industry largely utilizes substructures fixed to the seabed. The dominating fixed substructures are monopile and jacket foundations (illustrated in Figure 1.4). Due to structural and economical restrictions these bottom-fixed foundations are limited to water depths below 50 meters (Arapogianni et al., 2013). In order to generate wind energy at water depths greater than 50 meters, floating foundations are necessary. In Europe, large portions of coastal areas have a water depth of over 50 meters (Figure 1.3). This includes the majority of the North Sea, which is generally considered to be a geographic area with large wind resources (Carlington, 2014). As the offshore wind industry is predicted to move into deeper waters over the coming years (Corbetta, 2015), it can be assumed that there is a commercial desire for FWT's.

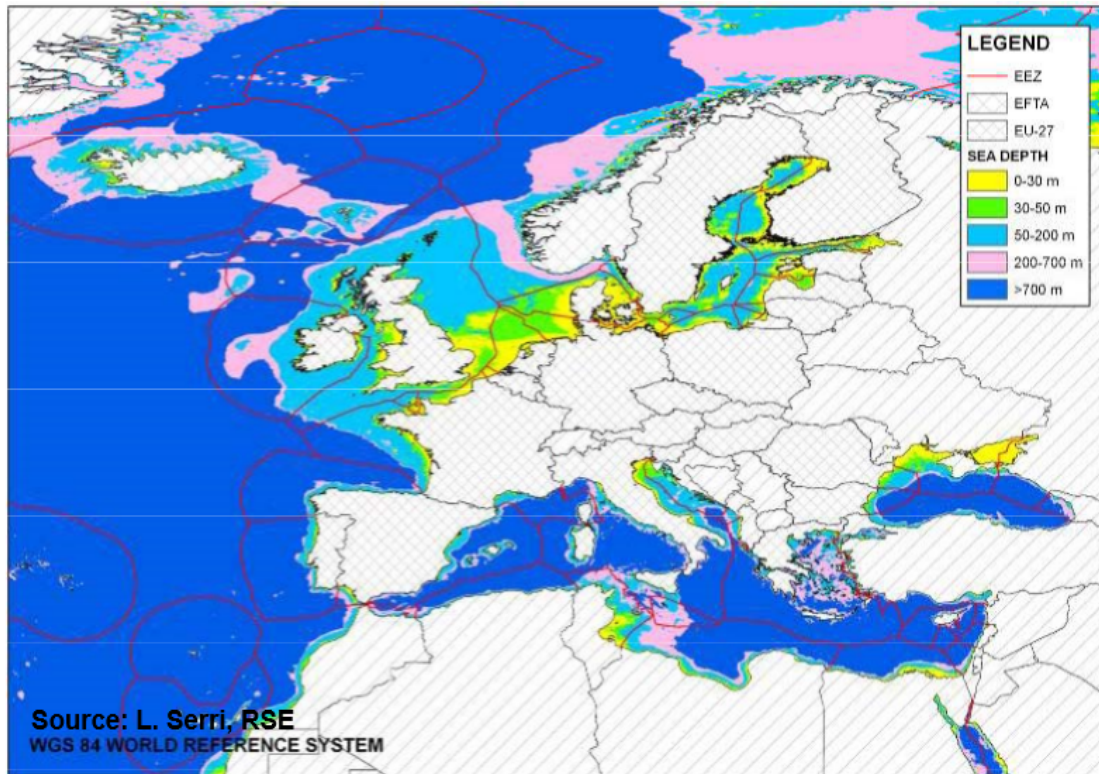


Figure 1.3: Sea depth in Europe (Ho et al., 2016)

The development of FWT's began in the early 2000's, but there are still relatively few installations worldwide. It should still be considered a developing market, as the first floating offshore wind farm in Europe is planned for commissioning this year. According to Richard (2016), there are currently over 40 FWT projects under development on a world wide basis. However, many of these are far from commissioning. The milestones in FWT development over the past years are summarized in the following:

- In 2008, the world's first floating wind turbine prototype was installed off the coast of Puglia in southern Italy. The structure consisted of a tension-leg platform (TLP) supporting a 80 kW turbine (Patel, 2009). It was installed by Dutch engineering company Blue H Technologies, who specializes in FWT technology (Blue H Engineering, 2016).
- In 2009, the worlds first large scale, operational floating wind turbine was installed in a water depth of 220 m of the coast of Haugesund, Norway. The installation, which was developed by Statoil, consisted of a 2.3 MW turbine supported by a spar buoy structure. Originally thought of as a prototype, it was as of April 2016 still delivering power to the mainland grid (Larsen Hirth, 2016), and was as of this date Norway's only offshore wind turbine. Statoil is currently in the process of moving the turbine to an offshore oil field, hoping to replace one of the gas turbines delivering power to the platforms *Kvitebjørn* and *Valemon* (Larsen Hirth, 2016).
- The first operational semi-submersible FWT concept was installed and grid connected in

2012. It supports a 2MW turbine, and is designed by the US company Principle Power (Carrington, 2014). Principle Power also had plans of constructing a wind farm off the coast of Oregon, US consisting of five 6 MW turbines. However, the future of this project is at best uncertain as the lease request for the proposed site was withdrawn in September, 2016 (Offshore Wind, 2016).

- In the aftermath of the 2011 Fukushima nuclear disaster, the energy politics in Japan shifted its focus from nuclear power to alternative renewable energy sources. This sparked the Fukushima offshore wind project, which eventually developed into the first FWT farm. It was inaugurated in 2013, when the first 2MW turbine was installed, an installation that was accompanied by a 7MW FWT in 2015. As of September 2016, a third 5MW turbine is currently being installed.
- In 2017, Statoil is planning the final commissioning of Europe's first floating wind turbine farm. This pilot farm is set to be installed 25-30 km off the coast of Aberdeenshire in Scotland, and will consist of 5 6MW Hywind turbines (Statoil, 2016).

## 1.2 Feasibility of Floating Wind Turbines

By looking into the milestones of FWT technology, it is clear that the developments in floating wind turbine technology have been concentrated around three different types of concepts: spar buoys, tension-leg platforms (TLP's) and semi-submersibles. As illustrated by figure 1.4, these concepts allow for offshore wind power production at larger water depths than traditional, bottom-fixed structures. However, there still remain engineering and economic challenges connected to floating wind power production, despite the commissioning of such wind farms off the coast of Japan and Scotland. In a study conducted by Robertson et al. (2011), the engineer-

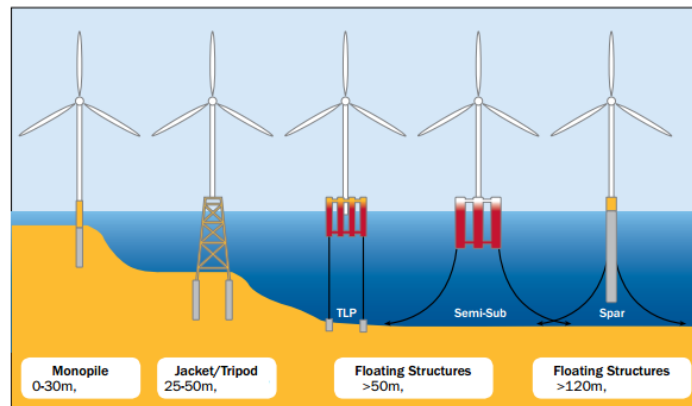


Figure 1.4: Bottom-fixed and floating wind turbine foundations (Bailey et al., 2014)

ing trade-offs between different offshore wind concepts were analyzed. The study compared the structural qualities of two spar buoys, a semi-submersible, two TLPs and a barge foundation in wind, wave and current conditions. It concluded that the barge concept experienced significantly higher loads in all areas of concern. The study concluded that the TLP, semi-submersible

and spar buoy concepts experienced roughly the same maximum loads, with smaller trade-offs between the concepts. This relation can explain why these concepts have been at the center of FWT developments. The main difference was that the semi-submersible and spar buoy concepts were considerably more prone to high tower base bending stresses. These stresses were the result of pitch and roll motions.

In [Robertson et al. \(2011\)](#), bending moments at exposed elements in several floating wind turbine concepts were compared to the corresponding values for a land-based turbine. It was found that bending stresses in the turbine rotor blades were of the same order as the land-based concept. However, the tower base bending moments due to roll and pitch were significantly higher in the floating concepts. In extreme conditions, the sea-to-land ratio was as high as 1.7 and 2.5 for the semi-submersible and spar buoys, respectively. From these results, it seems evident that a reduction in pitch and roll motions should be an emphasis in semi-submersible and spar buoys FWT design.

A FWT can experience reduced electric output due to inclinations of the wind turbine rotor. [Karimirad and Michailides \(2015\)](#) investigated output of a 5 MW semi-submersible wind turbine concept through numerical analysis. It was found that pitch inclinations were below 5.5 degrees, which corresponded to a reduction in rotor swept area of 0.4 %. Other motions also confirmed the feasibility of this semi-submersible FWT-concept for deep waters. For the 6 MW concept reviewed in this thesis, the allowed pitch angle in operational conditions is 6 degrees. Consequently, the power output of the OO-Star Wind Floater is considered feasible if pitch motions are below this angle. However, the behaviour in intermediate water depths remain to be analyzed.

Floating wind power production is considered a developing technology. Thus, the full economic feasibility of the structures is still uncertain, but some work has been done to map the cost of this energy source. [Myhr et al. \(2014\)](#) looked into the costs of a full life cycle of several offshore wind concepts, including both floating and fixed foundations. The costs were measured in levelized cost of energy (LCOE) for each concept. This parameter is a measure of the full life cycle cost per MWh produced. The study concluded that the considered TLP concepts had a lower LCOE than the bottom-fixed monopile structures. Other floating concepts were also competitive, including the Statoil *Hywind* concept now being realized. The semi-submersible FWT *Windfloat* was considered a much more expensive concept. This was mainly due to high material and manufacturing costs. As *Windfloat* is a steel structure, traditionally being a more expensive material than concrete, the concrete OO-Star Wind Floater-concept reviewed in this thesis could potentially be more competitive.

A more recent study on the economic feasibility of an offshore wind farm was carried out by [Castro-Santos et al. \(2016\)](#). This study reviewed a semi-submersible, a spar and a TLP concept. The study contradicts the findings of [Myhr et al. \(2014\)](#), as it calculates the semi-submersible and spar concepts reviewed to be more economically favourable. Both studies seem to indicate that floating wind are feasible from an economic standpoint, but their contradictions under-

line the uncertainties currently involved. Additionally, offshore wind energy in general is still far from being as cheap as e.g. land-based wind or power plants (Richard, 2016).

This is supported by James and Ros (2015), who argue that a large offshore wind farm (above 20 GW) should be more economically favourable than bottom-fixed. However, the uncertainties involved, with no large-scale data available and high up-front investments needed, makes investors cautious. The review argues that despite the potential of floating wind production, the outlook for the near future is uncertain at best. The reasons for this skepticism is uncertain political awareness on environmental matters, perception of the technology being immature and the large investment needed for large-scale production. Additionally, recent history has shown ambitious FWT developments to be more difficult than initially thought. The Fukushima Forward project in Japan is delivering electricity at twice the projected price, while a projected 5-turbine floating wind farm off the coast of Oregon was abandoned after failing to find utility customers for electricity it was supposed to deliver (Richard, 2016). The pending commissioning of Statoil's Hywind Pilot Farm should for these reasons be a highly important milestone for the floating wind business.

### 1.3 Objectives

Some economic and engineering challenges for FWT technology have been outlined in the previous section. It was found that floating wind farms could be economically competitive to fixed offshore wind farms, especially close to shore. In such cases, FWT technology can unlock economically favorable areas with water depths greater than the limit of fixed turbines. The goal of this thesis is consequently to map out hydrodynamic challenges for FWT modelling in intermediate water. In the wake of the project thesis, it was discovered that additional added mass due to flow separation and viscous damping could affect the FWT behaviour. A particular emphasis was made on prediction of these hydrodynamic forces, and it was subsequently decided to investigate how the heave plate configuration could impact the global FWT behaviour. The full project description is presented on the first page of this thesis. This section is considered a supplement, with the intention of further explaining the thesis work with regards to the structure of this report. The work on the master thesis was carried out in the following steps:

1. Carry out a literature study on FWT behaviour in the intermediate water depths. Identify important load factors, and perform a study on the damping effect of heave plates.
2. Update the numerical model based on results from the project thesis. Carry out free decay tests to investigate the model behaviour, and verify the turbine performance in constant uniform wind tests.
3. Identify a relevant location and environmental data for three different water depths. Use data to define relevant operational load cases for the FWT, as well as extreme environmental values for Ultimate Limit State (ULS) analysis.

4. Use the findings of the literature study to propose alternative heave plate configurations on the 6 MW OO-Star Wind Floater. Base viscous coefficients of the heave plate configurations on previous numerical or experimental analysis.
5. Carry out time-domain analysis on the FWT behaviour. Examine the influence of water depth in extreme conditions and relevant operational conditions, and investigate the influence of coupling and non-linear effects. Study the effect of different heave plate design on the response in extreme and operating conditions.

## 1.4 Structure

In order to address the objectives, the structure of this master thesis is as follows:

- Chapter 2 contains a literature study, where the state-of-the art in numerical modelling and the subjects laid out in the objectives are discussed.
- An introduction to the theoretical background of the numerical analysis in this thesis is given in chapter 3.
- The chosen locations and subsequent environmental data are discussed in chapter 4.
- The methodology and decisions made in the modelling phase are explained in chapter 5.
- In chapter 6, the performance of the numerical model is documented through free decay tests and constant uniform wind tests.
- Chapter 7 contain results of time-domain analysis, where the FWT behaviour in the intermediate water range is discussed.
- A parametric heave plate study was carried out, and the results are presented and assessed in Chapter 8.
- The final conclusion and recommendations for further work are given in chapter 9.





# Chapter 2

## Literature

### 2.1 Added-Mass and Drag of Heave Plate

In the design of floating structures such as spar buoys and semi-submersibles, a common approach to reduce the heave response is to implement thin, flat and submerged plates that are perpendicular to the this degree of freedom (DOF). Such plates are referred to as "heave plates". The use of heave plates can increase the natural period in heave as the component induces additional added mass in as well as viscous damping effects in the axial direction. The need for a good prediction of viscous damping is underlined by [Lopez-Pavon and Souto-Iglesias \(2015\)](#), who writes: "[...], in a seakeeping analysis, having an accurate estimation of viscous damping is crucial when predicting the platform behavior in survival conditions with time domain simulations, often coupled with the aeroelastic code FAST". However, accurate estimations of viscous damping are difficult to obtain, as both added-mass and damping depend strongly on both geometry and the motion of the floating structure.

Most of the previous studies on heave plates were carried out for simple geometrical shapes such as circles, rectangles and squares. Thus, a computational fluid dynamics (CFD) analysis of heave plate structure for the OO Star 6 MW concept would be valuable, as its geometry is that of a circle segment. However, this was left as further work, and the added mass and damping of heave plates in this thesis was based on previous studies. In the development of other semi-submersible FWT concepts, experimental and numerical analysis have been carried out to determine these effects in somewhat similar heave plate designs.

In a numerical study conducted by [Tao and Cai \(2004\)](#), the parametric dependency of added-mass and damping on the heave plate of a spar buoy was investigated. The results indicated that the added-mass of the heave plate in water was strongly dependent on the diameter ratio between the heave plate and the spar cylinder. Thus, the results indicate that the natural period in heave are higher for plates with high diameter-to-cylinder ratios. It was also found that the damping effects of the heave plate are more effective for a thin plate. Based on this paper, a wide

and thin heave plate will provide a higher added mass and damping.

In [Martin and Farina \(1997\)](#), it was shown that the relative submergence of a flat plate will have a strong effect on its hydrodynamic behaviour. When the submergence of the plate was small, it was shown that the added mass of the plate can be negative for higher wave numbers. The findings of [Martin and Farina \(1997\)](#) give a strong indication that the depth/radius ratio of the heave plate will affect viscous coefficients. However, the results given in figure 2.1 are only presented for depth/radius-ratios smaller than the configuration in the OO Star design (which are of approximately 2.0). [Antonutti et al. \(2014\)](#) goes further into detail on the subject of surface effects

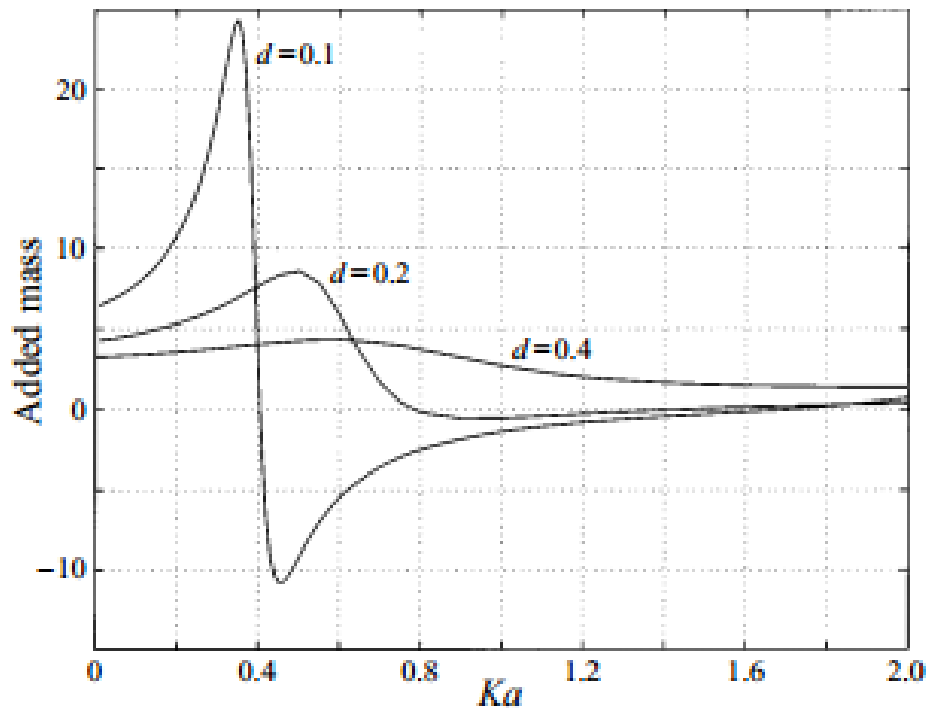


Figure 2.1: Non-dimensional added mass for different depth/diameter-ratios as a function of wave number  $k$  and disc diameter  $a$  ( $b = \text{depth/diameter}$ ), ([Martin and Farina, 1997](#))

on the hydrodynamic behaviour. Here, it was found that proximity to the surface considerably affects the discs radiation/diffraction for depth/radius-ratios below 1. The OO Star heave plates are as mentioned designed with a draft/diameter ratio  $\approx 2$ . Thus, proximity to the surface is not considered to significantly alter the hydrodynamics of the OO Star heave plates.

Most of the studies on heave plate design has been conducted on spar buoy and cylinder designs. For the use in semi-submersible FWT concepts, an elaborate investigation was conducted by [Lopez-Pavon et al. \(2015\)](#). This authors conducted a comparison study for a FWT design consisting of three vertical cylinders which were held together by a braced structure. However, the studies were isolated for one cylinder with an attached heave plate at the base, and any coupling with the braced structure were consequently neglected. The study compared the results

from a CFD analysis, experimental results and a first-order WAMIT analysis for a wide range of frequencies and KC-numbers. The results are shown in figure 2.2. In this figure, the change in heave added mass and damping for different  $KC$  and  $\omega$  are given by the coefficients  $A'_{33}$  and  $B'_{33}$ . These denote the **change added-mass and damping in reference to the theoretical added mass given by the cylinder+plate structure**.

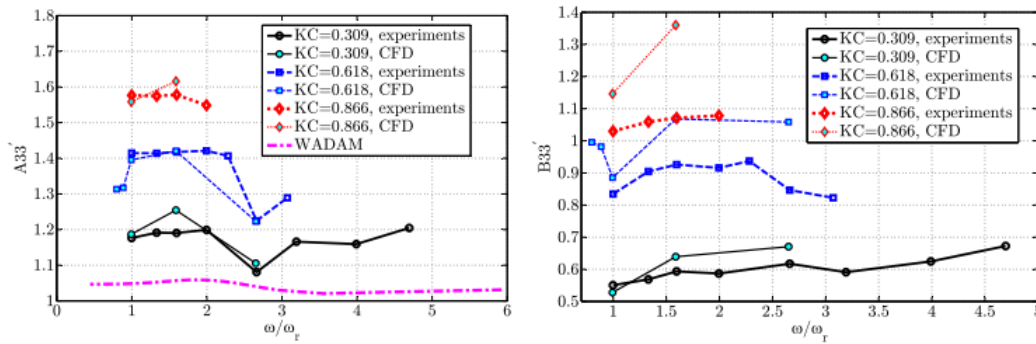


Figure 2.2: Added mass and damping coefficients from Lopez-Pavon and Souto-Iglesias (2015)

The study showed that the results from a first-order WAMIT calculation strongly underestimates the added mass of the heave plate. Furthermore, it was observed that the added-mass and viscous damping effects are more sensitive to the amplitude of the motions (i.e. the KC-number) than the frequency. This observation is supported by other studies, including Tao and Cai (2004), Tao et al. (2007) and Moreno et al. (2015).

There have also been carried out studies on the effect of having multiple heave plates on the same floating structure. Tao et al. (2007) carried out a numerical analysis on a cylinder with two heave plates. Here, the dependence of spacing between the two plates was determined. The study concluded that due to coupling between the two plates, the added mass and damping would be higher with large separation between the two plates. However, the studies also showed promising results for relatively small spacing, as can be seen in Figure 2.3. Due to the promising prospect of using two separate heave plates on each pontoon, it was decided to investigate this configuration in the parametric heave plate study.

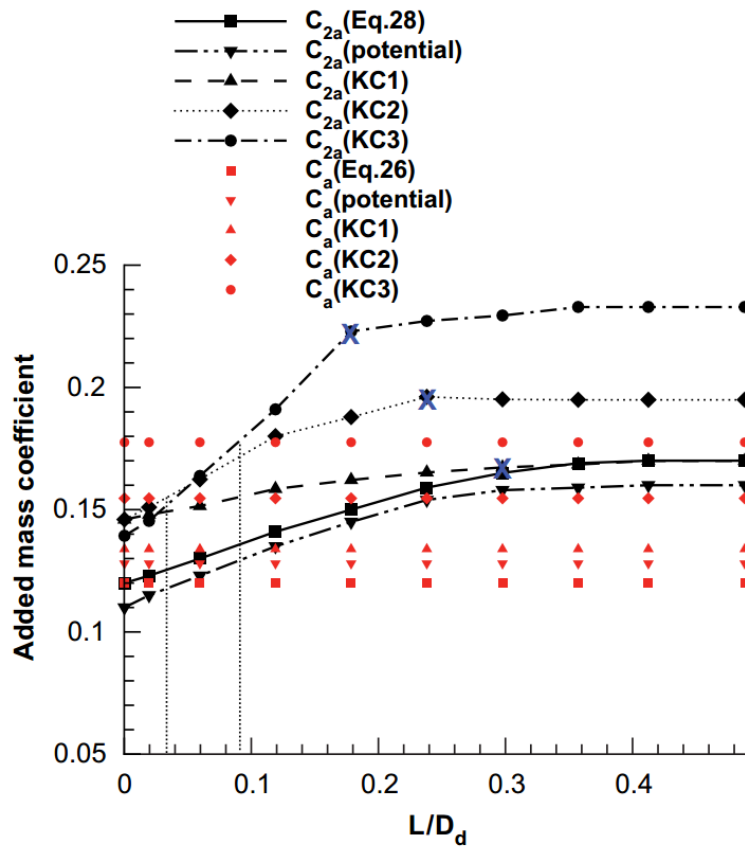


Figure 2.3: Dependence of spacing and KC on added mass (Tao et al., 2007)

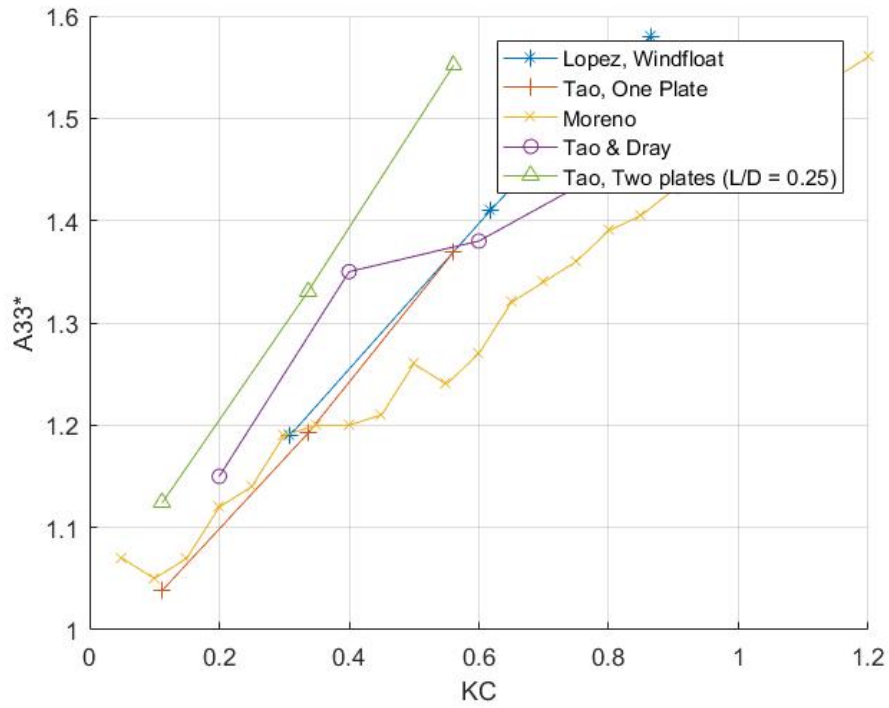
## 2.2 Selection of Viscous Coefficients

In order to determine added mass and damping for time-domain simulations, it was decided to lean on previous studies. Based on the discussion above, it was also decided to neglect frequency dependence to reduce the variables defining viscous coefficients. This was done as some frequency-dependence of added mass are maintained in first order potential theory analysis, which is illustrated in Figure 2.2. The discussion above also outlined the importance of the thickness/diameter-ratio and depth/diameter ratio on the hydrodynamic performance of the heave plate.

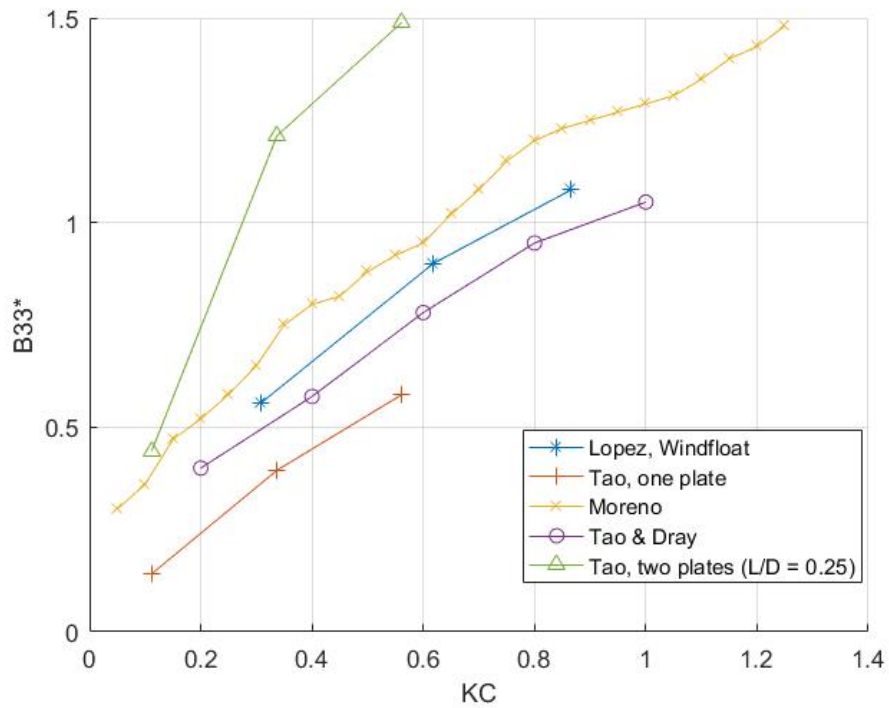
A summary of the  $KC$ -dependence on the added mass and damping of heave plates are illustrated in figure 2.4. It was discovered some varying results between the different studies. Therefore, the parameters outlined in the above were used to determine the most relevant set-up for this thesis. Based on this, the experimental results of [Moreno et al. \(2015\)](#) were chosen. This study considered a model with similar draft/plate diameter- and thickness/plate diameter-ratios. Due to limited availability of experimental studies on multiple heave plates, the numerical study of [Tao et al. \(2007\)](#) was chosen to investigate the additional added mass and damping of two heave plates. The results in this study, with a similar length scale between the two plates, are shown in figure 2.4. This figure also illustrates the similarity in  $KC$ -dependence for one plate between the numerical studies in [Tao et al. \(2007\)](#) and the experimental results for still water in [Moreno et al. \(2015\)](#). This similarity contributed to increase the confidence on this selection.

[Moreno et al. \(2015\)](#) also discussed the relevance of waves on the hydrodynamic performance of the heave plates. As shown in figure 2.5 and 2.6, waves were shown to have a strong effect on the radiation/diffraction effects of the plates. However, it was chosen to proceed with the still water results, as the relative velocity of the heave plates were already implemented in the definition of  $KC$ . Additionally, it was preferred to keep the variables included in the definition of  $A_{33}$  and  $B_{33}$  at a minimum at this stage, seeing that the regular wave results were only given for a minimum of wave combinations. In future work, it is recommended that more work should be carried out in determining the right  $KC$ -dependence on waves and body motions. Further explanation on the determination of  $KC$ ,  $A_{33}$  and  $B_{33}$  for the 6 MW OO Star are given in section 5.6.1.

In order to accurately predict the viscous terms in time-domain analysis, the contributions of the whole submerged body has to be considered. This contribution is added by the use of slender elements in *SIMA*. A simplified model, based on rectangular and cylindrical elements, was proposed in [Nærum \(2016\)](#). The hydrodynamic coefficients for such elements also have to be determined. [Arai et al. \(1995\)](#), who measured the forces on rectangular cylinders in waves, proved a strong dependency on the  $KC$ -number for the drag coefficients of such elements. However, he also observed a relatively small  $KC$ -dependency for inertia forces. These relations were supported by experiments carried out by [Vengatesan et al. \(1999\)](#). However, the latter experiments provided larger values for  $C_d$ , as can be seen in figure 2.7. [Li and Lin \(2010\)](#) compared



(a) Added mass



(b) Damping

Figure 2.4: KC-dependence of added mass and damping of column with heave-plates (Lopez-Pavon and Souto-Iglesias, 2015), (Tao et al., 2007), (Moreno et al., 2015), (Tao and Cai, 2004).

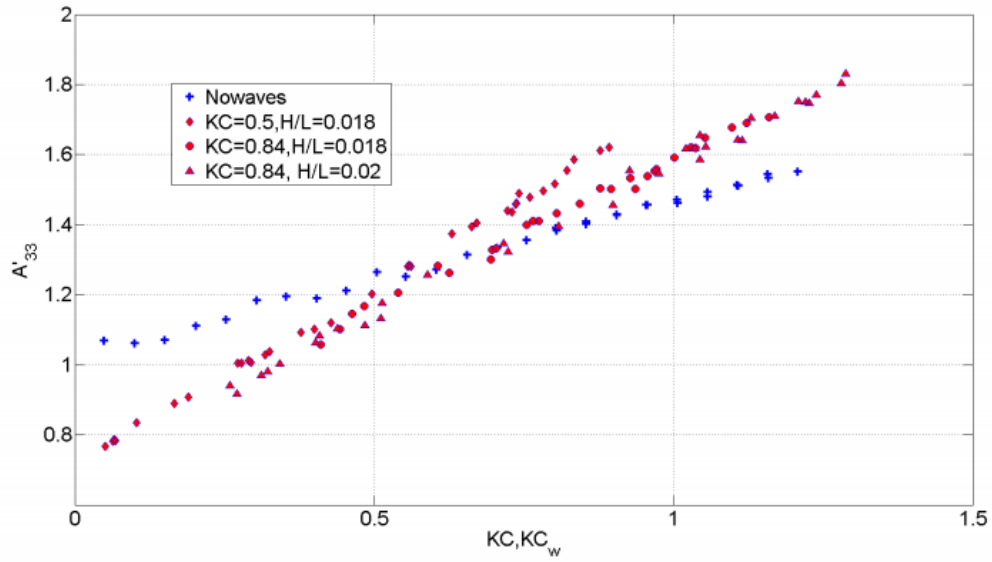


Figure 2.5: Added mass dependency on  $KC$ ,  $KC_w$  (Moreno et al., 2015)

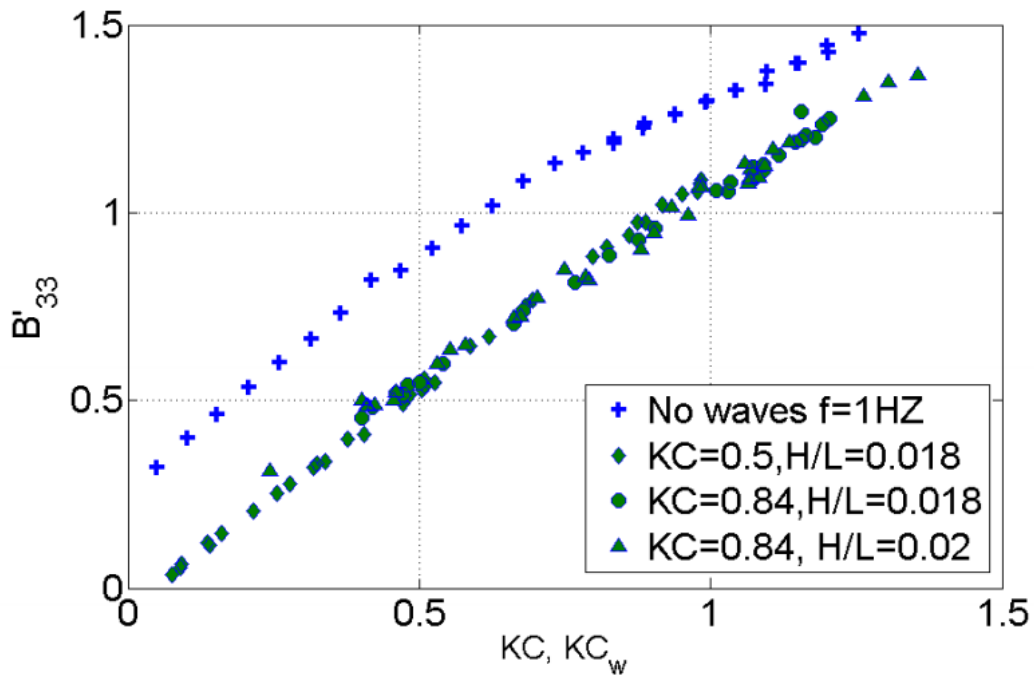
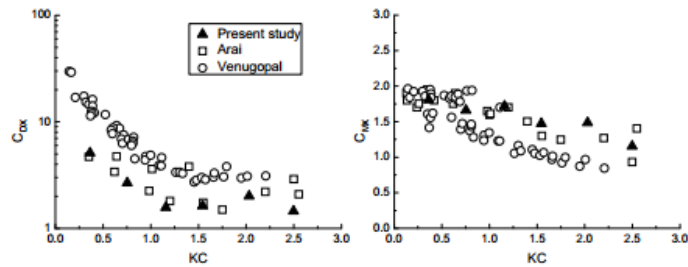


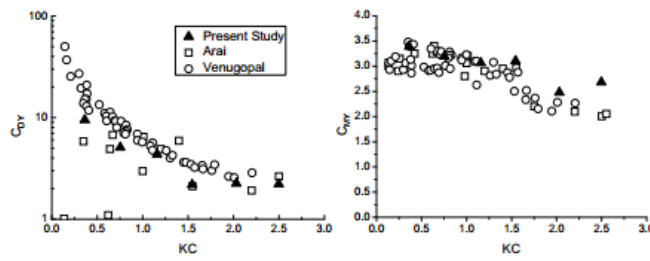
Figure 2.6: Damping dependency on  $KC$ ,  $KC_w$  (Moreno et al., 2015)

both experiments to the results of a CFD analysis, which also included an analysis of circular cylinders in waves.

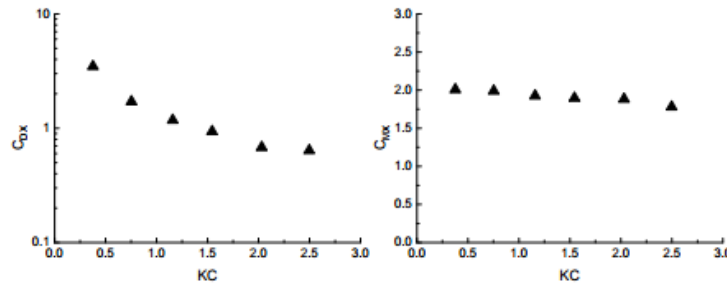
The experiments carried out by [Arai et al. \(1995\)](#) and the CFD analysis presented in [Li and](#)



(a) Horizontal drag and inertia coefficient for rectangular cylinder with aspect ratio 0.5



(b) Vertical drag and inertia coefficient for rectangular cylinder with aspect ratio 0.5



(c) Horizontal drag and inertia coefficient for circular cylinder

Figure 2.7: Drag Coefficients for different KC ([Li and Lin, 2010](#))

[Lin \(2010\)](#) showed a strong correlation. Because of this, these results were later used for the drag coefficients in time-domain analysis. Drag coefficients for cylindrical cylinders were also based on [Li and Lin \(2010\)](#), and used to define the quadratic force contribution from the FWT upper columns. Because of the small change in inertia forces for varying KC, additional added-mass for all components except heave plates are considered to be negligible in time-domain analysis.



## 2.3 Numerical software for FWT design

The state-of-the-art in numerical modelling of FWT's was discussed in the project thesis. The topic is important to verify the modelling procedure in this thesis. However, the available modelling tools have been consistent over the last 10 months. Because of this, the following section was taken directly from [Nærum \(2016\)](#), with minor alterations and corrections to the text.

The numerical modelling and analysis of FWT's was initially (early 2000s) based on frequency-domain analysis. This type of analysis is often deployed in the offshore oil & gas industry to analyze the response of floating structure ([Cordle et al., 2011](#)). However, there are important coupling effects between the controller, tower and hydrodynamics that are not accounted for in the frequency-domain ([Matha, 2010](#)). Thus, the design of offshore FWT's have to be carried out time-domain ([Cordle et al., 2011](#)), and state-of-the-art in numerical modelling includes different approaches to this problem.

In general, there are 5 components that need to be analyzed and coupled in the numerical analysis. These are turbine aerodynamics, loads from the controller, hydrodynamics, structural dynamics and mooring line effects ([Borg et al., 2015](#)). There are currently a number of different numerical methods that are used to model these effects. [Borg et al. \(2015\)](#) presents 13 different types of software used for FWT design and verification, based on a study within the the MARINTEK-led consortium LIFES50+. This is an international consortium where Dr. Techn. Olav Olsen, MARINTEK and DNV GL are members, and the results are considered to be representative for the industry as a whole.

The most common approach in LIFES50+ are *FAST*, which is an open-source code developed by National Renewable Energy Laboratory (NREL). It is a code originally developed for the design of onshore turbines, but was modified to include hydrodynamic models ([Cordle et al., 2011](#)), ([Borg et al., 2015](#)). This approach did not as of 2015 allow for FEM analysis, but according to [Borg et al. \(2015\)](#), this was under development at the time. Most companies that employ *FAST* for the coupled analysis use *ANSYS AQWA* to solve for potential flow and import frequency-domain hydrodynamic properties. Dynamic mooring properties can also be included in this analysis. The aerodynamics in this code are solved by either BEM or GDW (Generalized Dynamic Wake) in *FAST* ([Borg et al., 2015](#)).

In this master thesis, *SIMA(SIMO/Riflex)* have been used to perform coupled time-domain analysis. This was the other main approach in LIFE50+, and it is utilized by both Dr. Techn. Olav Olsen and MARINTEK. As was done in *FAST*, *SIMA* imports frequency-domain hydrodynamic analysis from an external software [Borg et al. \(2015\)](#). Frequency domain analysis in this thesis was carried out using the *WADAM*-package in *HydroD*. Aerodynamics are modelled by BEM, while the coupled dynamics was be calculated through a non-linear FEM analysis in *RIFLEX*. As can be seen by the methods mentioned above, the main differences are the ability to perform a GDW aerodynamic analysis in *FAST*, while *SIMA* allows for FEM structural analysis. However,

the latter utilize a correction for dynamic wake in the BEM, which is considered to give similar results. In general, the methods used in the *LIFES50+* consortium were utilizing a similar approach in the design and analysis of FWTs (Borg et al., 2015).

Although a relatively new field, some validation efforts have been made to verify the numerical models above. According to Borg et al. (2015), the hydrodynamic numerical models mentioned have been validated and tested against experimental data from model testing. However, there are still concerns about accuracy, which is a problem particularly in extreme conditions Borg et al. (2015).

There does not exist much data for the verification and validation of the mooring analysis models. Most developments in FWT mooring are based on the offshore oil and gas industry (Borg et al., 2015), and these are subsequently verified and validated for the much larger structures needed in this sector. As for the aerodynamics and structural dynamics analysis, *LIFES50+* has verified the numerical models through testing of a spar- and semi-submersible type of FWT (Robertson et al., 2013), (Sandner et al., 2015). However, some concerns of aero-elastic bending still remain, and need to be validated according to Borg et al. (2015).

Although the separate modules of the current numerical model are validated individually, there still remain uncertainties about the coupled analysis (Borg et al., 2015). The models were originally developed separately, and the focus area in the development of wind turbines is to develop a verified and validated code for coupled analysis (Borg et al., 2015). Finally, it should be noted that although CFD is developing as computational power is increased, it was as of 2011 far away from being computationally effective enough to perform a full 3-D RANS (Reynolds-Averaged Navier-Stokes) solution of the coupled model (Matha et al., 2011). However, isolated cases can be modelled effectively to determine special corrections to the coupled numerical model.

## 2.4 Intermediate Water Effects

The hydrodynamic analysis carried out in *WADAM* is based on the WAMIT panel method developed at MIT. Past experimental and numerical result comparisons have been reviewed in order to consider its validity in this project. This includes a consideration of which second-order effects that should be included in the analysis at intermediate water depths. Both the *FAST* and *SIMO/RIFLEX* coupled models utilize potential flow calculations for frequency domain hydrodynamic analysis. Past experimental verification of both models have therefore been included in the following.

Kimball et al. (2012) compared *FAST* data to model tests for a TLP, Spar and Semi-submersible FWT concept. Their findings suggested that the potential flow model are in good agreement with experimental results for the semi-submersible concept. However, the work clearly stated that second order wave diffraction effects must be accounted for. The reason for this was the

large response at low frequencies for the moored semi-submersible structure. This is likely to be the result of slow-drift excitation forces, which induces resonant conditions in surge and sway if the excitation frequency coincide with the low natural frequency of the moored structure.

[Bayati et al. \(2014\)](#) suggests that difference-frequency effects will be present in both surge, pitch and heave for a semi-submersible FWT. Therefore, these second-order effects have to be incorporated in the numerical model. Comparisons in [Gueydon et al. \(2014\)](#) show that sum-frequency effects are negligible, which is to be expected with the relatively high natural periods in all DOF for a moored semi-submersible structure.

*WADAM* utilize direct pressure integration to calculate slow-drift excitation forces and mean wave drift ([Veritas, 2010](#)). [Lopez-Pavon et al. \(2015\)](#) suggested that this approximation of second-order forces should be considered "adequate for engineering purposes". However, it was also identified that the current numerical analysis tools for time-domain design showed a clear tendency to under-predict this second-order effect for a FWT semi-submersible design. The reason for this was due to the relatively stiff mooring system and small water depth usually experienced by such concepts. The paper suggested a cautious approach during the design phase, due to the fact that the current state-of-the-art numerical analysis tools can only provide an "adequate" approach to slow-drift excitation force calculation.

[Lopez-Pavon et al. \(2015\)](#) suggest that the validity of direct pressure integration of slow-drift forces can be sensitive to water depth. However, little work has, to this authors knowledge, been carried out to investigate this phenomena. As reference, the results of [You \(2012\)](#) has been used to predict the validity of first and second order forces computed by the WAMIT-model in different water depths. Here, the first order, mean wave drift and slow-drift excitations on a truncated cylinder are compared to experimental results. The predictions of first order and mean wave drift forces compared well to experimental results for the intermediate range investigated. However, there is a tendency of under-estimation of difference-frequency effects in both heave and surge in limited water depth. The effect was stronger as the water depth got smaller. According to [You \(2012\)](#), experimental results also had a tendency to show rapid variations as a function of the wave period. Thus, it must be considered that the numerical predictions obtained in this thesis will under-predict the slow-drift excitation forces. This effect will be stronger for more shallow water depth.

In order to predict the FWT response in time-domain, viscous forces have to be accounted for. Common practise in FWT design is to include this effect based on the Morison drag model, where the quadratic damping is predicted by a consideration of the drag coefficients of the wet body. A consideration of this model was carried out by [Ishihara et al. \(2007\)](#), who suggested that it shows a good validity at higher frequencies. Slow-drift excitation forces are not included in this study, which could be a reason for the discrepancies between the experimental and numerical results at low frequencies. [Ishihara et al. \(2007\)](#) suggests that a combination of Newman approximation for slow-drift effects and Morison model for quadratic damping should give a reasonable prediction of hydrodynamic forces. An important note from the study is that the

inertia effects due to the heave plates have to be included in time-domain simulations. These inertia effects can not be predicted by the Morison model. Instead, the effects of the heave plates are investigated by assuming a damping proportional to the floater motion in heave. The damping coefficient utilized in [Ishihara et al. \(2007\)](#) is based on the heave added mass a vertical column with a plate.

Due to the previous studies discussed above, a first order potential theory with corrections for mean wave drift forces and slow-drift excitation forces have been used for analysis in this thesis. Based on studies summarized above, this model can be considered to have an adequate accuracy. It must be clearly pointed out that the method is expected to under-estimate slow-drift excitations. The deficiency in the numerical results is thought to be worse for more shallow water. The results have to be analyzed in light of this phenomenon.

# Chapter 3

## Theory

This section is based on the project thesis carried out by this author in the fall of 2016 (Nærum, 2016). This includes the derivation of the first order potential theory and wave statistics, which are only slightly modified. Aerodynamic theory and the explanation of coupled time-domain analysis are revised based on feedback from supervisor Marilena Greco and co-supervisor Erin Bachynski. In addition to this, the section is modified based on changes in the modelling procedure.

### 3.1 Hydrodynamic Theory

The purpose of this section is to give a broad view of the theory used in the numerical model. This is done to sufficiently address possible deficiencies in the model. Certain elements of the theory will consequently not be explicitly discussed. This section is in general based on Faltinsen (1993).

#### 3.1.1 Linear Theory

The calculation of hydrodynamic coefficients in *HydroD* is based on first order potential theory. The scope of the project is to determine a numerical model for investigation of shallow and intermediate water effects. In order to assume infinite water depth, a rule of thumb is that the water depth  $h$  must be according to 3.1, where  $\lambda$  is the wave length.

$$h > \frac{\lambda}{2} \quad (3.1)$$

$$\lambda = \frac{T^2 g}{2\pi} \quad (3.2)$$

For a water depth of 70 metres, it follows from 3.1 and the deep water dispersion relation 3.2 that we cannot have periods ( $T$ ) over 9.47 seconds. This is expected to occur in most sea states

in the Northern Sea. Thus, the full expression for the velocity potential has to be included. The wave elevation ( $\zeta$ ) for individual waves is given in 3.3. Here,  $\zeta_a$  is the wave amplitude, while  $k$  is the wave number and  $\omega$  the circular frequency of the wave.

$$\zeta = \zeta_a \sin(\omega t - kx) \quad (3.3)$$

$$\phi = \frac{g\zeta_a}{\omega} \frac{\cosh k(z+h)}{\cosh kh} \cos(\omega t - kx) \quad (3.4)$$

In linear wave theory, water is assumed to be incompressible and irrotational. Furthermore, the waves are assumed to be linear at all times, also in the boundaries (on the free surface). Thus, nonlinear problems like breaking waves are not accounted for in the linear wave theory. The boundary conditions that are implemented to obtain the velocity potential are the kinematic and dynamic boundary conditions. The former require the motion at the surface to be preserved. Consequently, it requires a fluid particle at the surface to remain there at all times. The dynamic boundary condition require the pressure at the surface to be equal to the atmospheric pressure. In first order potential theory, this error is small for low waves, and subsequently larger for bigger wave heights. In extreme North Sea conditions, with amplitudes close to 10 metres, this introduce an error that could possibly be of importance. The presented equations are based on the derivation of the velocity potential equation done in [Faltinsen \(1993\)](#).

### 3.1.2 Short Term Wave Statistics

The response of the floating wind turbine concept will be analyzed by time-domain analysis in *SIMA*. In order to represent a sea state, the individual, linear waves explained in the previous section can be linearly superimposed to represent to wave elevation at a given time and place. Thus, the wave elevation is given by 3.5. Here, components  $\zeta_j$ ,  $\omega_j$ ,  $k_j$  and  $\epsilon_j$  represent the amplitude, circular frequency, wave number and random phase angle of wave component  $j$  [Faltinsen \(1993\)](#).

$$\zeta(x, t) = \sum_{j=1}^N \zeta_j \sin(\omega_j t - k_j x + \epsilon_j) \quad (3.5)$$

The wave elevation in 3.5 describe an irregular and long-crested wave. Irregular as it is described by several amplitudes, frequencies, wave numbers and phase angles (as opposed to the single values describing the wave in 3.3) and long-crested as it only propagates in x-direction. The variables  $k_j$  and  $\omega_j$  are related through the dispersion relation in finite and infinite water depth, while  $\epsilon_j$  is a random phase angle between 0 and  $2\pi$ . In order to represent the sea state in the frequency domain, the wave amplitude  $\zeta_j$  is often represented by a wave spectrum  $S(\omega_j)$ .

$$\frac{1}{2} \zeta^2 = S(\omega_j) \Delta\omega \quad (3.6)$$

The instantaneous wave distribution is Gaussian distributed with zero mean. The variance is given by 3.7. In order to have a good representation of the wave field, a relevant wave spectrum

have to be defined. When  $\Delta\omega \rightarrow 0$ , the sum of all wave amplitudes can be found from 3.8.

$$\sigma = \int_0^{\infty} S(\omega) d\omega \quad (3.7)$$

$$\sum_{j=1}^N \frac{1}{2} \zeta_j^2 = \int_0^{\infty} S(\omega) d\omega \quad (3.8)$$

In reality, a sea state dominated by wind-generated waves will have waves propagating in more than one direction. As a consequence, it has to be represented by short-crested waves, with a two-dimensional wave spectrum representing the sea state. However, for the analysis in this thesis, the waves have been assumed to be uni-directional. Thus, only the long-crested waves are explained in this section.

### 3.1.3 Wave Spectrum

In this section, the basis for choosing a representation for the sea states in this project will be discussed. As the selected location of the wind turbines is in the North Sea, it is subsequently determined that the JONSWAP (Joint North Sea Wave Project) type spectrum will give the best representation of the wave conditions. A further explanation on this assumption is presented in this section. The JONSWAP spectrum is a correction of the Pierson-Moskowitz type spectre in 3.9, which was a result of a multinational project obtaining wave data in the southern North Sea in the period of 1968-69 (Hasselmann et al., 1973).

$$S(\omega) = \frac{A}{\omega^5} \exp\left(-\frac{B}{\omega^4}\right) \quad (3.9)$$

The main difference between the PM type spectra, developed on the basis of data from the North Atlantic, and the JONSWAP spectrum, is that the constant B is dependent on the wind speed for the former, and the peak frequency for the latter. Furthermore, the JONSWAP spectrum includes a peak enhancement factor  $\gamma$ . Thus, the JONSWAP wave spectrum representing the north sea represent waves with larger energy density around the peak period.

$$A = 0.0081 g^2 \quad (3.10)$$

$$B = \frac{5}{4} \omega_p^4 \quad (3.11)$$

This gives the full expression for the JONSWAP spectra as defined in 3.15. The parameters  $\sigma$ ,  $\alpha$  and the peak correction factor  $\gamma$  are taken as the values used in Eik and Nygaard (2003), as these parametric values represent a representable location for the wind turbine concept.

$$\alpha = (1 - 0.287 \ln(\gamma)) \frac{5}{16} \frac{H_S^2}{g^2} \quad (3.12)$$

$$\gamma = \exp(5.75 - 1.15 \frac{T_p}{\sqrt{H_S}}) \quad (3.13)$$

$$\sigma = \begin{cases} 0.07 & \text{for } \omega \leq \omega_p \\ 0.09 & \text{for } \omega > \omega_p \end{cases} \quad (3.14)$$

$$S(\omega) = \frac{A}{\omega^5} \exp(-\frac{B}{\omega^4}) \gamma^{\exp(-\frac{1}{2}(\frac{\omega - \omega_p}{\sigma \omega_p})^2)} \quad (3.15)$$

The JONSWAP spectra physically represent a purely wind-generated sea. However, this is not always the case. For swell-dominated sea, a two-peaked spectral model has been developed by [Torsethaugen et al. \(2004\)](#). The method was originally created by combining two JONSWAP-type spectra. In [Eik and Nygaard \(2003\)](#), the boundary between swell- or wind-dominated sea states were given as

$$T_p = 6.6 H_S^{0.333} \quad (3.16)$$

[Eik and Nygaard \(2003\)](#) suggest that a JONSWAP spectrum can be used for the wave distribution of  $T_p$  in the sea state is within a  $\pm 2s$  of the  $T_p$ -value for equation 3.16. This is the case for all but one of the environmental cases later defined in Table 4.7. Further discussion on the subject of wind- and swell-dominated sea was presented in [Nærum \(2016\)](#), and will therefore not be assessed here.

### 3.1.4 Response in Regular Waves

In first order wave theory, the response of a large-volume body subjected to hydrodynamic waves can be linearly superposed as the sum of the response due to separate wave components. Hydrodynamic problems in regular waves are commonly subdivided into two sub-problems. From [Faltinsen \(1993\)](#), these are defined as:

- *A: The forces and moments on the body when the structure is restrained from oscillating and there are incident regular waves. The hydrodynamic loads are called wave excitation loads and composed of so-called Froude-Kriloff and diffraction forces and moments.*
- *B: The forces and moment on the body when the structure is forced to oscillate with the wave excitation frequency in any rigid-body motion mode. There are no incident waves. The hydrodynamic loads are defined as added mass, damping and restoring terms.*

The excitation forces, added mass, damping and restoring moments are found as a function of the pressure distribution on the body. By requiring equilibrium between the two isolated problems, and considering the excitation forces and moments in direction  $j$  as the real part of the complex load function  $F_j e^{-i\omega t}$ , the hydrodynamic problem can be written as in equation 3.17. This formulation constitutes the 6-DOF equation of motion for a rigid body in water.

$$F_j e^{-i\omega t} = \sum_{k=1}^6 [(M_{jk} + A_{jk})\ddot{\eta}_k + B_{jk}\dot{\eta}_k + C_{jk}\eta_k] \quad (3.17)$$



The response of the floating wind turbine concept considered in this thesis is calculated by numerical simulations in *HydroD* (*WADAM*) and *SIMA* (*SIMO*), as explained in Section 5.2.

### Panel Method

The first order excitation forces, including added mass, damping and restoring terms, are solved for a user-defined frequency and directional domain in *WADAM*. The wave-body interaction problem is solved in line with the theory derived above (Veritas, 2010). The total potential is thus defined as the sum of diffraction and radiation potential (3.18). The radiation problem is the sum the potential from the freely oscillating body, while the diffraction forces is the sum of the incident wave potential  $\phi_0$  (equation 3.4) and the disturbance of the incident wave from the fixed body (here noted as  $\phi_7$ ).

$$\phi = \phi_D + \phi_R \quad (3.18)$$

$$\phi_R = i\omega \sum_{j=1}^6 \phi_j \quad (3.19)$$

$$\phi_D = \phi_0 + \phi_7 \quad (3.20)$$

The boundary conditions are defined by

$$\phi_{jn} = n_j \quad (3.21)$$

$$\frac{\partial \phi_j}{\partial n} = 0 \quad (3.22)$$

By solving the above equations, the equation of motion (Equation 3.17) is established for the frequency and directional domain according to equation 3.23. Here, a complex translation vector  $\mathbf{X}(\omega, \theta)$  is determined in six degrees of freedom. The six-by-six matrices  $\mathbf{M}$  and  $\mathbf{C}$  represent the mass matrix and restoring coefficients. The six-by-six matrices  $\mathbf{A}(\omega)$  and  $\mathbf{B}(\omega)$  represent the frequency-dependent added mass and damping.

$$\mathbf{F}(\omega, \theta) = [\omega^2(\mathbf{M} + \mathbf{A}(\omega)) - i\omega\mathbf{B}(\omega) + \mathbf{C}]\mathbf{X}(\omega, \theta) \quad (3.23)$$

### 3.1.5 Non-Linear Effects

The panel method based on first order linear potential theory requires corrections for second-order effects. In order to obtain better computational efficiency, the relevant corrections were identified through the literature survey (Chapter 2). It was explained that difference-frequency excitation forces are important for a semi-submersible FWT concept. Additionally, mean wave forces are included in the calculation in order to obtain a higher order of accuracy. Hence, both of these are included in the hydrodynamic analysis.

### Mean Wave Force

According to [Faltinsen \(1993\)](#), mean wave drift forces in the potential flow model are "due to a structure's ability to cause waves". For a surface piercing structure in regular waves, the surface of the structure will have areas that will be in and out of water due to the oscillating waves. This phenomena causes a mean pressure difference in this area, which results in a mean wave force. In this thesis, the mean wave force are approximated by momentum conservation in *WADAM*. The horizontal force component averaged over one oscillation period is found according to equation 3.24 ([Faltinsen, 1993](#)).

$$\bar{F}_i = - \overline{\iint_{S_\infty} [pn_i + \rho V_i V_n] ds} \quad (3.24)$$

$V_i$  is the velocity in surge or sway, while  $V_n$  is the normal component of the fluid velocity at the surface of the structure.  $S_\infty$  is the time-dependent wetted-surface of a non-moving cylindrical control surface away from the body,  $\rho$  is the density of water and  $p$  is the wave pressure normal to  $S_\infty$ . Equation 3.24 is also valid for yaw moment ( $i = 6$ ) if properly defined (see ([Faltinsen, 1993](#)) for explanation). When using equation 3.24, only first order potential theory is needed. The result is that it is possible to establish the mean wave drift in surge, sway and yaw without losing much computational efficiency.

The relative importance of this force will strongly depend on the structures ability to cause radiation waves. The response of a semi-submersible FWT concept, which has a relatively low water-plane area, will therefore not be strongly dominated by mean wave forces. However, the scope of this thesis is to investigate the effects of water depth. According to [You \(2012\)](#), the mean wave force will be affected by limited water depth. Additionally, the mean wave forces are in approximately the same order as the aerodynamic thrust. This is proved by the standard deviations of the FWT loads, presented in chapter 7. In order to carry out a full analysis, the horizontal mean wave forces is therefore included.

### Difference-Frequency Effects

As mentioned in the literature study, the semi-submersible FWT is susceptible to slowly varying forces. This is due to the high natural periods in surge, sway and yaw for the moored structure. Additionally, it was shown in Chapter 2 that slowly varying excitation forces will also have a contribution in heave, roll and pitch as well. From [Faltinsen \(1993\)](#), it is found that the quadratic velocity term in Bernoulli's equation for fluid pressure can be written as in equation 3.25.

$$-\frac{\rho}{2}(V_1^2 + V_2^2 + V_3^2) = -\frac{\rho}{2}|\nabla\phi|^2 \quad (3.25)$$

Here,  $V_1$ ,  $V_2$  and  $V_3$  are the fluid velocity components in three dimensions. The quadratic Bernoulli velocity term is neglected in first order potential theory. By considering only the x-component of the velocity and two wave components of circular frequencies  $\omega_1$  and  $\omega_2$ , equation 3.25 can

be written as

$$-\frac{\rho}{2}V_1^2 = -\frac{\rho}{2}\left[\frac{\zeta_1^2}{2} + \frac{\zeta_2^2}{2} + \frac{\zeta_1^2}{2}\cos(2\omega_1 t + 2\epsilon_1) + \frac{\zeta_2^2}{2}\cos(2\omega_2 t + 2\epsilon_2)\right. \\ \left. + \zeta_1\zeta_2\cos[(\omega_1 - \omega_2)t + \epsilon_1 - \epsilon_2] + \zeta_1\zeta_2\cos[(\omega_1 + \omega_2)t + \epsilon_1 + \epsilon_2]\right] \quad (3.26)$$

Here, the first term is a constant pressure term depending on the amplitudes of two incident waves, while the difference-frequency excitation forces are induced by the term including  $\omega_1 - \omega_2$ . For irregular sea calculations, the contributions from all wave components are summed up, as shown in equation 3.27.

$$F_i^{SV} = \sum_{j=1}^N \sum_{k=1}^N \zeta_j \zeta_k [T_{jk}^{ic} \cos(\omega_k - \omega_j)t + (\epsilon_k - \epsilon_j) + T_{kj}^{is} \sin(\omega_k - \omega_j)t + (\epsilon_k - \epsilon_j)] \quad (3.27)$$

$T_{kj}^{ic}$  and  $T_{kj}^{is}$  are second-order transfer functions for the difference frequency-loads. These are dependent on frequency, and are found from direct pressure integration in WADAM.

The terms in 3.26 consisting the sum of two frequencies ( $2\omega_1$ ,  $2\omega_2$  and  $\omega_1 + \omega_2$ ) induce sum-frequency excitation forces on the structure. Due to the high natural periods of the moored structure in all 6 DOFs, these are unlikely to be of importance under resonance conditions and are neglected in this thesis.

### Viscous Drag Effects

The hydrodynamic properties of the floating body is calculated by first order potential theory. This analysis does not account for viscous forces, which is pressure forces due to separated flow. As seen by figure 3.1, these forces could dominate for thin structures, especially when exposed to the large wave amplitudes occurring in extreme conditions. For this structure, viscous forces are not considered negligible. This was explained in Chapter 2. The contribution to the viscous forces from the body geometry are included by Morison's equation (equation 3.28).

$$dF_k = \rho\pi \frac{D^2}{4} C_M a_k + \frac{\rho}{2} C_D D |(u - \dot{\eta}_k)|(u - \dot{\eta}_k) \quad (3.28)$$

$$dF_k = \rho\pi \frac{D^2}{4} C_M a_k + \frac{\rho}{2} C_D D |(u - \dot{\eta}_k)|(u - \dot{\eta}_k) - \rho(C_M - 1) \frac{\pi D^2}{4} dz \ddot{\eta} \quad (3.29)$$

Morison's equation consists of two terms: a mass term and a drag term. The mass forces on the floating structure are calculated as explained previously in this chapter. However, due to flow separation, the added mass of the structure will differ from the theoretical calculations from first order theory. This is especially dominant for the effect of the heave plates. This difference is added as a correction of the added mass coefficient ( $C_A$ ), which is correlated to the mass

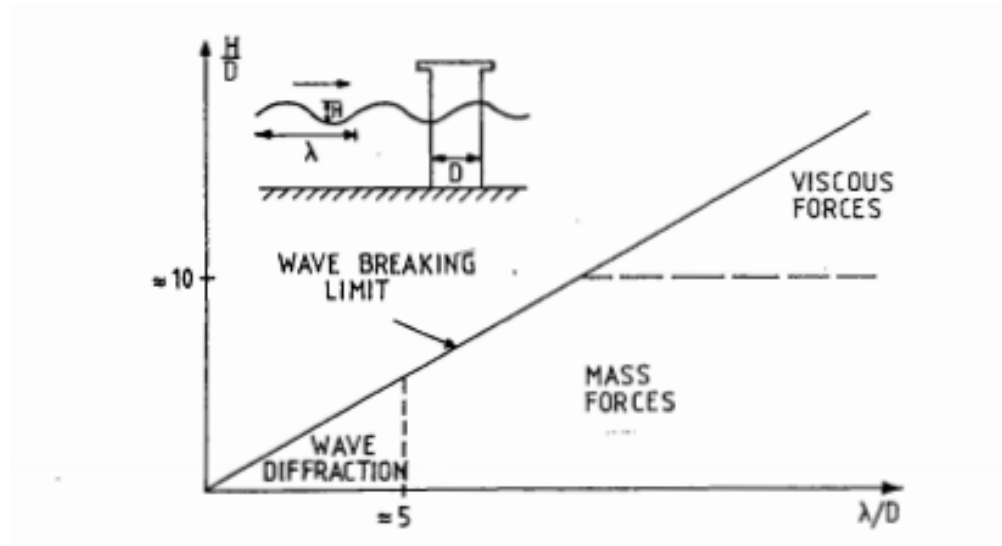


Figure 3.1: Relative importance of mass, viscous drag and diffraction forces on marine structures [Faltinsen \(1993\)](#)

coefficient according to the following equation

$$C_M = 1 - C_A \quad (3.30)$$

The second term of Morison's equation are not accounted for in first order potential theory. It is therefore added during time-domain integration. As shown in equation 3.28, the drag force is added as a function of the relative velocity of the floating structure ( $u$  notes the wave particle velocity in  $k$ -direction and  $\eta_k$  is the velocity of the body).

The added-mass and drag coefficient ( $C_M$  and  $C_D$ ) are strongly dependent on Reynolds Number and the Keulan-Carpenter number. In the current state-of-the-art in numerical design tools for offshore wind, it is not possible to include these variables as changing parameters. Thus, a decision has to be made on these values in order to optimize the accuracy of the simulations. The establishment of these coefficients is explained in section 5.6.1.

## 3.2 Aerodynamic Theory

### 3.2.1 Blade Element/Momentum

The aerodynamics in SIMA is based on the Blade Element/Momentum (BEM)-theory ([Cruz and Atcheson, 2016](#)). Therefore, an introduction to this theory will be given in this section. The following derivation will be mostly based on [Glauert \(1983\)](#). BEM is based on the 1-D Momentum Theory. This theory is based on the assumption that the rotor is frictionless and that there are no rotational velocity components in the wake (actuator disc theory). However, in BEM the

rotational speed in the wake is also introduced. In the following, this factor is noted by  $a'$ .

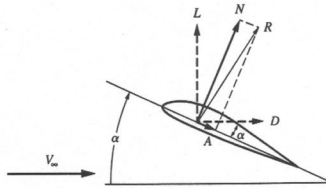


Figure 3.2: Forces acting on a 2-D foil section (Glauert, 1983)

A BEM model is defined by discretization of the stream tube considered in the 1-D control theory. It is discretized into a finite number of elements, where each element has a thickness of  $dr$ . Thus, by assuming that there are no coupling effects between the elements and an infinite number of blades, thrust and momentum contributions from each element (3.31 and 3.32) can be integrated to obtain the total thrust and momentum. For each 2-D foil section (figure 3.2),  $dT$  and  $dQ$  can consequently be established if foil data are known. In the following,  $V_0$  is the incoming velocity according to Figure 3.2.

$$dT = 4\pi r \rho_a V_0^2 a(1-a) dr \quad (3.31)$$

$$dQ = 4\pi r^3 \rho_a V_0 \omega (1-a) a' dr \quad (3.32)$$

Determination of the correct induction factor  $a$  and rotational velocity  $a'$  for each element is based on an iteration scheme. This scheme is thoroughly explained in literature, and will not be explained in detail here. The general purpose of the iteration scheme is to make  $a$  and  $a'$  correspond with normal and tangential force coefficients at the given angle of attack.

### 3.2.2 Corrections of BEM

Several corrections have to be made to the BEM to give a good physical representation of the aerodynamics of a wind turbine. The purpose of this section is to give a short and concise representation of the aerodynamic theory implemented in SIMA. Therefore, the exact mathematical formulations of these corrections will not be included in this thesis.

#### Prandtl's Tip Loss Factor

The BEM assumption of an infinite number of blades is incorrect. In order to correct for this assumption, Prandtl's tip loss factor is commonly applied to rotors with a finite number of blades. To correct for the finite number of blades in the rotor, a correction to the relative velocity  $V_{Rel}$  (Figure 3.3) is added to the equations for the normal and tangential force (equation 3.31 and 3.32, respectively) (Glauert, 1983). The tip-loss factor is thus a function of the angle of attack

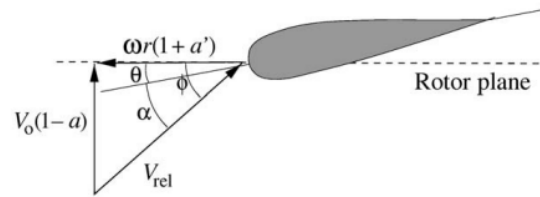


Figure 3.3: Relative velocity on a foil section (Glauert, 1983)

( $\alpha$ ), flow angle ( $\phi_a$ ) and blade pitch ( $\theta_a$ ) of each rotor blade, as well as the number of blades and chord distribution. A full derivation of the tip-loss factor is commonly available in literature such as Glauert (1983).

### Dynamic Wake

In the BEM model derived above, the wake experiences an instantaneous effect of the incoming velocity on the rotor. Thus, the induction factor will be immediately updated if the incoming velocity changes. In reality, the wake can be shown to change with a time scale proportional to  $D/U$ , where  $D$  is the rotor diameter and  $U$  is the inflow velocity (Glauert, 1983). Dynamic wake effects will have a bigger influence for high induction factors, and are in SIMA modelled by the Stig Øye Dynamic Inflow Model (Bachynski, 2016). The model can be explained as a numerical iteration scheme. An induced velocity vector from the dynamic wake is determined by the derivative of the incoming velocity and scheme-specific values. Thus, the induced velocity vector smooths over the instantaneous wake change to create a more physical wake change.

### Dynamic Stall

Dynamic stall accounts for a dynamic incoming flow. The drag and lift coefficient input in BEM are typically variables governed only by the angle of attack. Due to sudden flow attachment and re-attachment, these coefficients could differ from their input values. The dynamic stall is included in SIMA by the Øye model (Bachynski, 2016), (Glauert, 1983). In this model, the dynamic stall is included by assuming that the rate of flow separation will always approach a certain value which correspond with static aerofoil data. Thus, the modification to the drag and lift coefficient can be found from a numerical integration scheme between each time-step based on previous values.

### Glauert Correction

Glauert Correction is a correction factor that is used for the axial induction factor when  $a > 0.4$ . The reason for this is that the BEM model is not valid for  $a > 0.5$ , as the far-field wave would

be negative. Thus, a correction factor have to be applied for large induction factors. An exact representation of the mathematical formulation can be found in (Glauert, 1983).

### Tower Shadow Effects

The tower shadow effects are implemented to model the effect of the tower on the incoming flow. The turbine shadow effect is usually not neglected in wind turbine analysis, as the thrust will experience a variation every time a blade passes the region where the inflow is affected by the tower. Thus, there will be a resulting load variation at the  $3p$ -frequency (3 times the rotational frequency) which can be important for fatigue analysis (Bachynski, 2016). In SIMA, the tower shadow effect can be modelled for both upwind and downwind turbines.

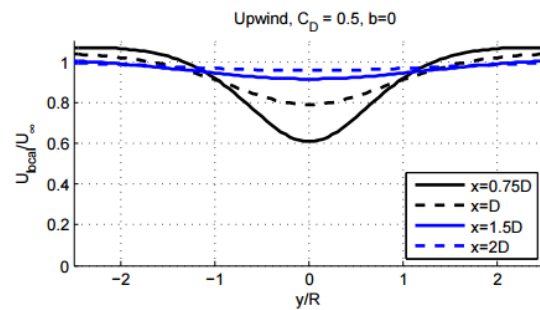


Figure 3.4: Upwind tower effect including drag correction (Bachynski, 2016)

Figure 3.4 show how the incoming flow can be influenced by the tower. The variable  $y$  in this case indicate the transverse coordinate of the incoming flow, with the tower positioned in  $y = 0$ . The figure illustrate a decreased incoming velocity in this position. The theory behind the tower shadow effect will not be further derived in this thesis, as structural fatigue assessments are not carried out.

### Other correction factors

In addition to the previously mentioned corrections, the aerodynamic calculations in SIMA includes corrections for hub loss and skewed wake corrections. Hub losses are implemented to correct for the presence and geometry of the hub. Skewed wake corrections are done to account for the possible yaw tilt of the turbine, and the resulting change of wake orientation (Chaney et al., 2001).

### 3.2.3 Wind Profile

#### Vertical Wind Profile

The average wind speed will deviate with height over the rotor disc diameter. This is due to shear effects between the atmosphere and earth surface. The shear ratio depend on the surface roughness at the turbine location. In the wind models used in this thesis, the power law distribution is recommended to describe the vertical distribution of average wind speed. This model is given in equation 3.33. In the power-law model, the wind speed  $U_0$  in a reference height  $z_0$  is distributed vertically by the power coefficient  $p$ . This a commonly used approach in offshore engineering, as the model has proved to be relatively accurate for offshore wind modelling (Panofsky and Dutton, 1984).

$$u_1 = u_0 \left( \frac{z_1}{z_0} \right)^p \quad (3.33)$$

The establishment of  $u_0$  is to be based on long-term statistics and will be further explained in section 4.3. In this thesis,  $u_0$  is taken as the one-hour-mean value at reference height  $z_0 = 10m$ . The values for the power-law coefficient are based on IEC et al. (2009), and further discussion on the topic is continued in section 4.3.

#### Turbulent wind profile

Based on the work carried out during preliminary studies (Nærum, 2016), it is clear that wind loads will have a large contribution on the motions of a FWT. In order to correctly take these loads into account, it is important to factor in deviations in wind speed. Thus, turbulent wind have to be implemented. Turbulence can be described as a deviation to the mean wind speed, and several models have been developed to represent the velocity deviations in x-, y- and z-direction. The rate of turbulence  $I$  can be described as in equation 3.34, where  $\sigma_p$  is the standard deviation of wind speed and  $U$  is the wind velocity.

$$I = \frac{\sigma_p}{U} \quad (3.34)$$

The result is a deviating wind profile, which will be statistically determined over a period of time based on a turbulence model and environmental site data for average wind speed. As with the vertical wind profile, the values for  $I$  and  $\sigma_p$  are take from IEC et al. (2009).

## 3.3 Coupled Time-Domain Analysis

This section will broadly explain the coupled time-domain analysis performed in *SIMA*. The iteration procedure in the *SIMO/RIFLEX* coupled analysis is explained in section 5.2.



### 3.3.1 Non-Linear Finite Element Method

The response of the FWT is solved for each time-step in time-domain. The external loads are defined in *Simo*, while aerodynamic and hydrodynamic loads on flexible elements are computed in *RIFLEX*. The latter is done by the non-linear FEM, which is able to account for large deformations and displacements. It can also compute accurate solutions for cases with boundary condition changes. In FWT analysis these characteristics are useful. This is due to the non-linearities introduced by large deformations in turbine rotor blades, as well as the quadratic behaviour of thrust and drag forces (Kvittem, 2014).

In the non-linear FEM, the global system is discretized according to the position of each node and element. The mass, damping and stiffness properties of each element are assembled into global matrices according to equation 3.35. In this thesis, the turbine tower is assumed as a stiff structure, and the global mass, damping and stiffness matrices contain information on the floating body (computed in *HydroD*), rotor blades, rotor hub and mooring elements. The external force contributions are assembled in the global matrix  $R_{ext}$ .

$$\mathbf{M}_g \ddot{\mathbf{D}} + \mathbf{B}_g \dot{\mathbf{D}} + \mathbf{R}_{int} = \mathbf{R}_{ext} \quad (3.35)$$

### 3.3.2 Time-Domain Solution

Equation 3.35 is solved by step-by-step numerical integration in *RIFLEX* (Fylling et al., 1995). This calculations are carried out using the Newmark  $\beta$ -approach, where equilibrium is obtained for each time-step. Thus, the time-domain solution is obtained by numerical integration, according to

$$\dot{\mathbf{D}}_{k+1} = \dot{\mathbf{D}}_k + (1 - \lambda_n) \Delta_n \ddot{\mathbf{D}}_k + \lambda_n \Delta_n \ddot{\mathbf{D}}_{k+1} \quad (3.36)$$

$$\mathbf{D}_{k+1} = \mathbf{D}_k + \Delta_n \dot{\mathbf{D}}_k + \left(\frac{1}{2} - \beta_n\right) \Delta_n^2 \ddot{\mathbf{D}}_k + \beta_n \Delta_n^2 \ddot{\mathbf{D}}_{k+1} \quad (3.37)$$

The numerical integration scheme utilized in this thesis was the same as in the preliminary studies. As written in the project thesis, the Newmark  $\beta$ -method is implicit and gives no artificial damping if  $\beta_n = \frac{1}{4}$  and  $\lambda_n = \frac{1}{2}$ . The default approach in *RIFLEX* is to use  $\beta_n = \frac{1}{3.905}$  and  $\lambda_n = 0.505$ , in order to remove high-frequent numerical noise (Fylling et al., 1995). This is also the approach used in this thesis. The starting point of the dynamic analysis was the static analysis of the structure. Thus, the dynamic analysis' starting point was the results of the static analysis, i.e.  $\mathbf{D}_0 = \mathbf{D}_{static}$ ,  $\dot{\mathbf{D}}_0 = 0$  and  $\ddot{\mathbf{D}}_0 = 0$ .

### Coupled Equation

A FWT will be subject to several load and response contributions. Wind, wave and current loads will each contribute to the response, in addition to the structural dynamics of the mooring lines and rotor and the hydrodynamic characteristics of the floating body. When these loads inter-

act, they could lead to coupling effects that are important for the FWT behaviour. According to [Kvittem \(2014\)](#), some of these effects include:

- Aerodynamic damping on the FWT global motions.
- The wind force is influence due FWT motions.
- The mean platform position is affected by the mooring dynamics, turbine performance and aerodynamic forces.
- The mooring dynamics have an effect on the FWT global motions.

Due to its importance of the FWT behaviour, a short introduction to the theoretical background of *SIMO/RIFLEX*-coupling will be given in this section.

The hydrodynamics of the floating body are established through a frequency-domain analysis. The 6-DOF equation of motion for the floating body is established for a rigid body in the frequency-domain (equation 3.23). For the coupled analysis, this data is transformed to the time-domain by the Cummins-equation ([Cummins, 1962](#)). This equation includes an impulse-response function to introduce a radiation memory to the response. By the introduction of this term, the wave radiation of the floating body depend on the history of motion. Thus, frequency-domain added mass and damping can be included in time-domain analysis. The frequency-dependent wave excitation loads are transformed to time-domain by a Fourier-transform. Consequently, time-domain 6-DOF can be represented as in equation 3.38. The terms are added to the global mass, damping and stiffness matrices and load vector in equation 3.35.

$$(M + A_{jk}^{\infty})\ddot{\eta}_k + \int_0^t K_{jk}(t-s)\dot{\eta}(s)ds + C_{jk}\eta = F_j \quad (3.38)$$

The interaction with mooring loads and restoring forces and the rigid floating body have to be accounted for at every timestep. Thus, *SIMO/RIFLEX* calculates the dynamic equilibrium between these components at every time-step, before implementing this input into a fully coupled equation. The load vector of the coupled non-linear equation contains the following load contributions:

$$\mathbf{F}(t) = \mathbf{F}^{wave}(t) + \mathbf{F}^{moor}(t) + \mathbf{F}^{visc}(t) + \mathbf{F}^{wind}(t) + \mathbf{F}^{turb}(t) \quad (3.39)$$

The elements in the load vector can be summarized as

- $\mathbf{F}^{wave}(t)$  contain the fourier-transformed frequency domain excitation forces, in accordance with the hydrodynamic theory outlined in this chapter.
- $\mathbf{F}^{moor}(t)$  contain the wave and current forces on the mooring elements.
- $\mathbf{F}^{visc}(t)$  contain the additional added mass due to flow separation and the quadratic damping of the floating structure. The viscous forces are explained in section 3.1.5.

- $\mathbf{F}^{wind}(t)$  contain the wind loads, as derived in the aerodynamic theory described in this chapter.
- $\mathbf{F}^{turb}(t)$  contain the structural force contributions from the turbine and controller.

### 3.4 Catenary Equations

Because of the geometry of the FWT concept, a spread catenary system with three mooring lines was proposed. A spread catenary mooring system induces horizontal stiffness on the FWT by the use of pre-tensioned cable lines. The material of the lines are typically chains, ropes or a combination of both (Faltinsen, 1993). When the FWT moves, the cables will experience a change in geometry, which in return will induce horizontal forces on the FWT. Because of this, the response will depend heavily on the characteristics of the mooring line. The angle between each mooring line where designed to be equal, with a angle of  $120^\circ$  separating the lines.

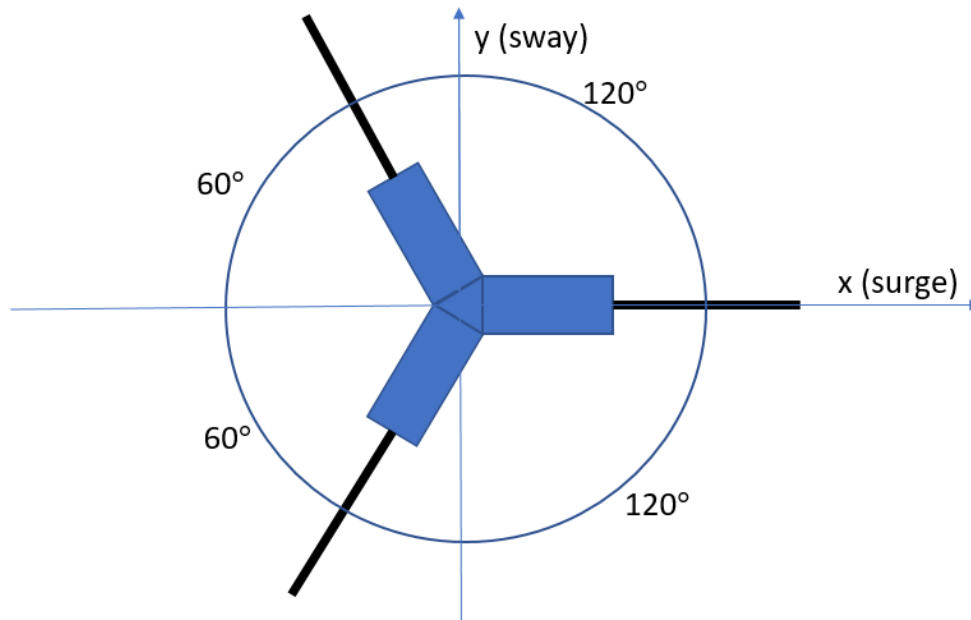


Figure 3.5: Simplified illustration of mooring line configuration

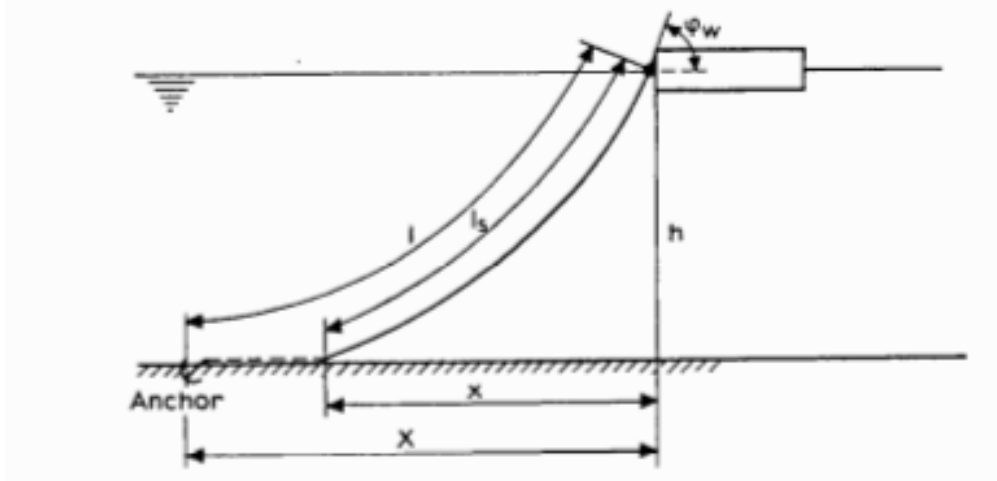


Figure 3.6: Catenary mooring line (Faltinsen, 1993)

$l$ : Length of mooring line from anchor to fairlead

$l_s$ : Suspended mooring line

$x$ : Horizontal distance from sea-bottom to fairlead under static configuration

$X$ : Anchor radius

$h$ : Vertical distance from fairlead to sea-bottom

$T_H$ : Horizontal Pretension

In this thesis, the mooring design is designed by aiming for a specific natural period in surge. This value is determined by the horizontal restoring coefficient  $C_{11}$ , the infinite-frequency added mass  $A_{11}$  and the mass of the structure, as seen in equation 3.40.

$$T_1 = 2\pi \sqrt{\frac{M + A_{11}}{C_{11}}} \quad (3.40)$$

The horizontal restoring coefficient is determined by the shape and weight of the mooring system. In order to find the pretension corresponding to the selected natural period in surge,  $T_H$  for each water depth was found analytically from equation 3.41.

$$C_{11} = \frac{dT_H}{dX} = \omega \left[ \frac{-2}{\sqrt{1 + 2\frac{a}{h}}} + \cosh^{-1}\left(1 + \frac{h}{a}\right) \right]^{-1} \quad (3.41)$$

$$a = \frac{T_H}{\omega_m} \quad (3.42)$$

When  $T_H$  was established, all parameters needed to define the mooring system could be determined using the catenary equations presented in Faltinsen (1993). The anchor radius  $X$  was

defined at a constant value at all water depths. This was done to obtain a sufficient offset margin and easier calculation. Thus, the length of each mooring line can be found according to equation 3.43. The margin to the horizontal position in which the line was fully stretched, measured from the fairlead, is given by equation 3.44.

$$l = X - x + l_s \quad (3.43)$$

$$x_{lim} = \sqrt{l^2 - X^2} \quad (3.44)$$



# Chapter 4

## Environmental Conditions

### 4.1 Locations

In the project thesis, the North Sea was chosen as the location for the FWT concept (Nærum, 2016). It was considered a viable location for a FWT due to the high wind speeds in the area and availability of environmental data. Another important factor behind the decision was the bathymetry of the North Sea, as two-thirds of the North Sea have a depth between 50 and 220 metres. Two generic northern North Sea locations, with depths of 70 and 120 metres, were presented. Mean and 100-year wind and sea states were presented based on the work done by Johannessen et al. (2001). These values were validated against measurements from the Stafjord oil field in the northern North Sea.

For this thesis, some parameters have been updated. First of all, it was decided to propose three different water depths to investigate the effects of intermediate water. FWT applications are considered for depths larger than 50 metres, which is currently the upper limit for fixed foundations. Thus, this was taken as the water depth for the most shallow location. It was also determined that the difference between each depth should be equal, and that all data points should be within the intermediate range.

Based on the deep water dispersion relation, the peak period of the expected sea state were found to be 155.5 metres. Three locations with water depths of  $h = 50m$ ,  $h = 80m$  and  $h = 110m$  were considered to confidently be in the intermediate water depth range, and were consequently chosen for further analysis.

Table 4.1: Deep water wave length

Case	$H_S$ [m]	$T_p$ [s]	$\lambda$ [m]
1	2.69	9.98	155.5

Although two-thirds of the North Sea has a water depth of 50-220 metres, the depths are not

randomly distributed. This can be seen from figure 4.1. By comparing this figure to the 100-year extreme values of  $H_S$ , it was observed that applying the same environmental conditions at all three water depths is not realistic. This was also supported by Li et al. (2013), which includes extreme values for  $H_S$  and wind speed for several North Sea locations. However, it was an advantage to perform analysis in the same environmental conditions at each depth to be able to compare the FWT response.

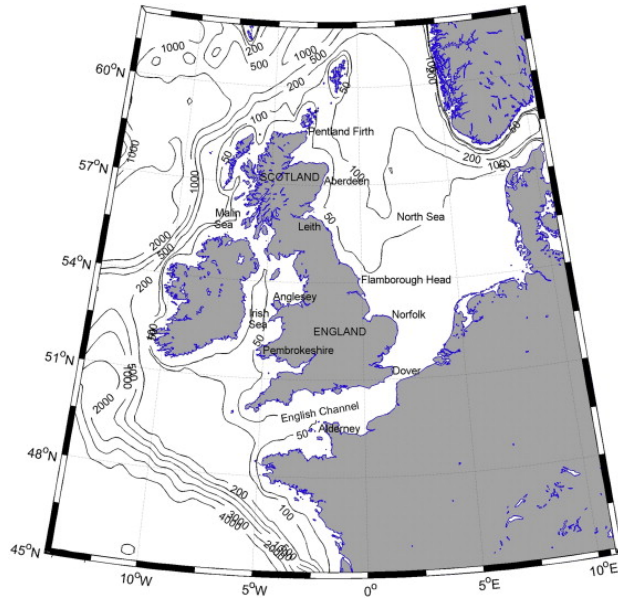


Figure 4.1: Bathymetry contours in the North Sea (Neill et al., 2014)

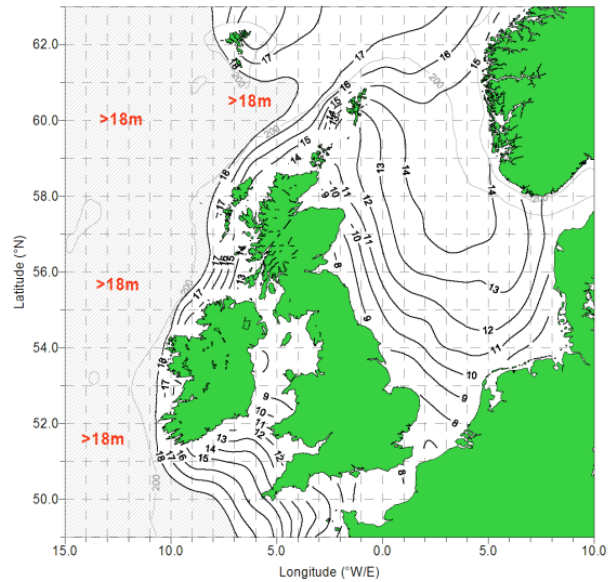


Figure 4.2: 100-year  $H_S$  in the North Sea (Williams et al., 2008)

By considering the bathymetry of the North Sea, it was determined that the joint distribution parameters proposed by Johannessen et al. (2001) was a good fit for the FWT at  $h = 80$  and  $100$  m. The parameters proposed for a central North Sea location in Li et al. (2013) was considered a better fit at  $h = 50$  m. However, the scope of this thesis was to evaluate the global behaviour of the FWT in different water depths. Therefore Johannessen et al. (2001) will be used for analysis in operational state for all water depths. The probability for these environmental cases to occur at  $h = 50$  metres are lower than at the other depths, however they were still considered to represent a possible load state. For case sensitive analysis such as ULS, the most fitting joint distribution model should be used for each location.



## 4.2 Joint Distribution of Wind and Waves

The joint distribution of wind, significant wave heights and peak periods was represented by the same models in both [Johannessen et al. \(2001\)](#) and [Li et al. \(2013\)](#). The measurements at the test sites are not equal, producing different parameters for the distribution model. The procedure was explained in [Nærum \(2016\)](#), but a general explanation will also be given here.

The distribution of average wind speed is represented by a two-parameter Weibull distribution (equation 4.1). The distribution was determined on the basis of one-hour mean wind speed measurements at a reference height of 10 metres. In the following equation,  $\alpha_w$  and  $\beta_w$  are site-dependent variables.

$$f(w) = \frac{\alpha_w}{\beta_w} \left( \frac{w}{\beta_w} \right)^{\alpha_w} e^{-\frac{w}{\beta_w} \alpha_w} \quad (4.1)$$

The distribution of  $H_S$  is determined by the same equation as the one-hour mean wind speed. The parameters  $\alpha_h$  and  $\beta_s$  are dependent on the wind speed. They are given in Table 4.2, along with environmental data for mean and extreme wind speeds at both sites. The latter values are calculated along the procedure outlined in [Nærum \(2016\)](#).

As explained in [Nærum \(2016\)](#), the peak period given a one-hour mean wind speed and  $H_S$  is distributed by a log-normal model. The value of the peak period for each sea state is determined mainly by  $H_S$ , but variations in wind speed also contributes to shifting the periods. In [Johannessen et al. \(2001\)](#) a parametric distribution of  $T_p$  was suggested. This distribution is governed by equation 4.2, where  $T_p^*(H_S)$  and  $W^*(H_S)$  are site dependent parameters varying with  $H_S$ . These site dependent parameters are also used to investigate the expected wind and period for a suggested  $H_S$ .  $\theta$  is a site dependent constant ([Johannessen et al., 2001](#)).

$$T_p(H_S, w) = T_p^*(H_S) \left[ 1 + \theta \frac{w - W^*(H_S)}{W^*(H_S)} \right] \quad (4.2)$$

Table 4.2: Parameters for joint distribution of wind and waves ([Johannessen et al., 2001](#)), ([Li et al., 2013](#))

Site	1	2
$\alpha_w$	1.708	2.299
$\beta_w$	8.426	8.920
$\alpha_{H_S}$	$2.000 + 0.135w$	$1.755 + 0.184w$
$\beta_{H_S}$	$1.800 + 0.10w^{1.322}$	$0.534 + 0.07w^{1.435}$
$T_p^*(H_S)$	$4.883 + 2.680H_S^{0.52}$	$5.563 + 0.798H_S^{1.00}$
$W^*(H_S)$	$1.764 + 3.426H_S^{0.780}$	$3.500 + 3.592H_S^{0.735}$
$\theta$	-0.190	-0.477

Values for  $H_S$ ,  $w$  and  $T_p$  in different scenarios are tabulated in table 4.3. The table also presents the probability for a  $w$ - $H_S$ -combination (noted as  $P(H_S)$ ). It was proposed that the joint

Table 4.3: Variations of environmental conditions

Condition	Value at Site 1	Value at Site 2
Conditions during 100-year one-hour mean wind extreme		
$w$ [m/s]	38.979	27.834
$H_S$ [m]	13.57	8.1032
$T_P$ [s]	14.37	10.04
Environmental conditions given expected one-hour mean wind		
$w$ [m/s]	7.516	7.902
$H_S$ [m]	2.89	1.69
$T_P$ [s]	9.98	7.25
Peak period and probability of j.d. of $H_S = 2.89$ and $w = 7.516$		
$T_P$ [s]	9.98	9.14
$P(H_S)$	0.491	0.0118

distribution model based on site 1 should be used for all three water depths. For some combinations of  $w$ ,  $H_S$  and  $T_P$ , this also represent a possible load case for  $h = 50m$ , even though its probability of occurrence is small. To define the environmental case for a ULS analysis the joint distribution parameters at site 1 were used at the 80 meter and 110 meter depth, while parameters from site 2 were used to define the extreme case at 50 meter depth.

### 4.3 Wind Distribution Models

In order to extrapolate the average wind velocities deduced in the previous section, relevant variables for vertical distribution and turbulence of wind speed have to be chosen. In this thesis, the IEC (International Electrotechnical Commission) standard *61400 - Part 3: Design Requirements for Offshore Wind Turbines* has been used. In this standard, several wind models are presented. Based on [Jonkman and Buhl Jr \(2007\)](#), it was decided to utilize the Normal Turbulence Model (NTM) for operating conditions and the Extreme Turbulence Model (ETM) in damage conditions ([IEC et al., 2009](#)).

In NTM, the standard deviation in wind speed is the 90 % quantile of the hub height wind speed. It consists of full field, 3-dimensional speed deviations. This is also the case in the ETM, where the standard deviation consists of stochastic wind distribution and increases with wind speed. Both wind models utilize the power law distribution for the vertical distribution of the average wind speed, as explained in chapter 3. The power-law coefficient  $\alpha$ , turbulence intensity  $I$  and standard deviation  $\sigma_t$  are all taken according to [IEC et al. \(2009\)](#). The standard operates with three models of turbulence intensity per wind case, A, B and C, where A is the highest and C the lowest. The choice of model within the wind case depends on the turbine class and the local wind conditions, and is in this case chosen according to [Jonkman and Buhl Jr \(2007\)](#). All parameters included are stated in table 4.4.

Table 4.4: Wind profile parameters (IEC et al., 2009)

Model	$\alpha$	$I_{ref}$	$\sigma_1$
NTM	0.14	0.14	$I_{ref}(0.75U_{hub} + 5.6)$
ETM	0.14	0.14	$2I_{ref}(0.072(\frac{V_{ave}}{2} + 3)(\frac{V_{hub}}{2} - 4) + 10)$

Here,  $V_{ave}$  is the annual average wind speed at hub height. The longitudinal standard deviation  $\sigma_1$  is also used to find the transverse and vertical standard deviation according to  $0.7\sigma_1 \leq \sigma_2$  and  $0.5\sigma_1 \leq \sigma_2$ .

## 4.4 Currents

Ocean currents can be described as a continuous movement of water in one direction. Strong currents can interact with waves to change the wave height and period. They can also induce slow-drift motions and drag forces on submerged structures. Currents can be considered as a sum of many contributions, with wind- and tidal-currents being the largest factors (DNV, 2010).

The joint distribution of wind and waves explained in the previous section does not include the distribution of currents (Johannessen et al., 2001). Furthermore, the discrete measurements of current contributions were difficult to obtain for a realistic scenario. When detailed measurements are not available, DNV-GL regulations recommend current to be modelled according to equations 4.3-4.5 (DNV, 2016).

$$U_c(z) = U_{tide}(z) + U_{wind}(z) \quad (4.3)$$

where

$$U_{tide}(z) = U_0 \left( \frac{h+z}{h} \right)^{\frac{1}{7}} \quad (4.4)$$

$$U_{wind}(z) = kw_{10} \left( \frac{50+z}{50} \right) \quad (4.5)$$

In the above equations,  $U_0$  is the tidal current at still water level. The 10-year current is used along with the joint distribution of the 100-year wind speed and sea state in ULS analysis. Because of this,  $k$  is taken as the value that gives the 10-year extreme current speed and the mean current at their respective wind speeds, as presented in Nærum (2016) and Eik and Nygaard (2003). Thus,  $k = 0.0308$ , which is between the interval of 0.016 and 0.033 suggested in DNV (2016). Finally, it should be noted that this method was proposed by this writer, in an effort to scale the current load between the extreme and expected values. Thus, the current can not be considered jointly distributed, but rather a suggested load for a given wind case.

Table 4.5: Ocean current parameters

$U_0$ [m/s]	0.2
$k$	0.0308
$w_{10}^*$	$w - 7.516$

## 4.5 Water Levels

The water depth is defined by a mean water level, as well as a tidal-varying component and a storm-induced surge. This is illustrated in Figure 4.3, where *MSL* is the mean water level. *HAT* and *LAT* refer to the highest and lowest astronomical tide, respectively. *HSWL* is the highest water level and occur when *HAT* coincide with a positive storm surge. *LSWL* denotes the opposite phenomena.

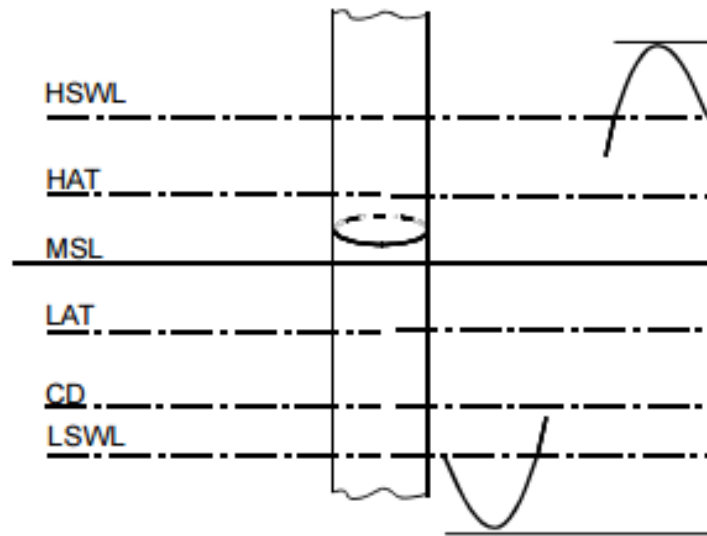


Figure 4.3: Water level components (DNV, 2016)

As this thesis discussed depth effects in the intermediate range, where the changes in water level will have a larger relative value than in deep water, the water level and its influence at the three locations was considered. Tidal ranges and extreme values for storm surge are presented for both sites in table 4.6. The values for site 1 was taken from Eik and Nygaard (2003), while Sündermann and Pohlmann (2011) was the reference for site 2. Due to the relatively low tidal amplitudes in the North Sea, the change in water depth will only be taken into account in ULS.

Table 4.6: Variations of environmental conditions

	Site 1	Site 2
Tidal Range [m]	1.0	1.0
Extreme Storm Surge [m]	0.9	1.5

## 4.6 Load Cases

Two joint distribution models have been presented. For operational state analysis, it was decided to use parameters based on measurements from the Veslefrikk oil field. For the ULS case, parameters from the central North Sea were used for  $h = 50\text{m}$ . The current speeds were based on [Eik and Nygaard \(2003\)](#), and a power-law distribution model was proposed based on DNV-GL regulations. A wind-speed dependent current model was proposed, in order to suggest relevant current speeds at different wind speeds. Finally, the extreme water level changes were discussed.

In order to analyze the FWT global motions in the intermediate water range, 5 different environmental cases were selected. The intention behind the selection was to get an indication of the hydrodynamic behaviour in relevant joint wind and wave cases. Therefore, it was selected to investigate the behaviour at the expected wind speed, upper operational mean wind speed (25 m/s at the hub height) and the 100-year extreme wind speed. The joint distribution was used to determine the corresponding values of  $H_S$  and  $T_p$ . Additionally, the 5<sup>th</sup> percentile significant wave height and peak period given expected and upper operational wind speed were investigated. This was done in order to determine the hydrodynamic behaviour in wave-dominated seas. The selections were loosely based on the cases presented in [Jonkman and Buhl Jr \(2007\)](#). As the power performance of the turbine was not a large focus in this thesis, the normal turbulence model was considered in operational wind speeds, while turbine fault was neglected. For the extreme load case, the turbulent extreme wind model was chosen. As previously explained, the parameters for the central North Sea were used for the extreme case at  $h = 50\text{m}$  (case E.2). The current profile was chosen according to the model explained above.

Table 4.7: Environmental cases

Case	Wind			Waves			Current		Water L.
	Model	$U_{w,z=10}$	Dir	$H_S$	$T_p$	Dir	$U_{c,z=0}$	Dir	
M.1	NTM	7.516 [m/s]	0 [°]	2.89 [m]	9.98 [s]	0 [°]	0.200 [m/s]	0 [°]	MSL
M.2	NTM	7.516 [m/s]	0 [°]	4.66 [m]	11.82 [s]	0 [°]	0.200 [m/s]	0 [°]	MSL
O.1	NTM	18.167 [m/s]	0 [°]	5.86 [m]	11.30 [s]	0 [°]	0.528 [m/s]	0 [°]	MSL
O.2	NTM	18.167 [m/s]	0 [°]	8.22 [m]	13.21 [s]	0 [°]	0.528 [m/s]	0 [°]	MSL
E.1	EWM	38.979 [m/s]	0 [°]	13.57 [m]	14.37 [s]	0 [°]	1.170 [m/s]	0 [°]	HSWL
E.2	EWM	27.830 [m/s]	0 [°]	8.23 [m]	10.04 [s]	0 [°]	1.170 [m/s]	0 [°]	HSWL



# Chapter 5

## Methodology

### 5.1 OO-Star Wind Floater

The numerical FWT model analyzed in this thesis is based on the OO-Star Wind Floater (pat.), which is developed by Dr. Techn. Olav Olsen AS. It is constructed to be able to support large wind turbine in rough conditions, and can be delivered with a concrete hull, steel hull or a combination of the two materials (Dr. Techn. Olav Olsen, 2016). In this thesis, the concept considered is a concrete hull supporting a 6 MW turbine. The cheap material costs of concrete compared to steel and the possibility of full quayside installation (Dr. Techn. Olav Olsen, 2016) are two factors that should increase the economic feasibility of the concept, reducing the lifetime cost of energy. However, neither a prototype nor a operational turbine have been installed as of this writing. To this authors knowledge, no full-scale installations are under construction either. Thus, the OO-Star Wind Floater concept should be considered to be in a developmental stage. The initial numerical model is fully based on structural drawings provided by co-supervisor Håkon S. Andersen. Relevant variables from these structural drawings are presented in table 5.1.

Table 5.1: OO Star Wind Floater data in operational state (Dr. Techn. Olav Olsen, 2016)

Draft	20 m
Displacement [tonnes]	16242
GM [m]	5.64
Mass contribution from rotor, hub & nacelle [tonnes]	320
Mass contribution from mooring [tonnes]	240
Natural period heave [s]	21.5
Natural period roll & pitch [s]	≈ 29
Max static tilt from wind load [deg]	6

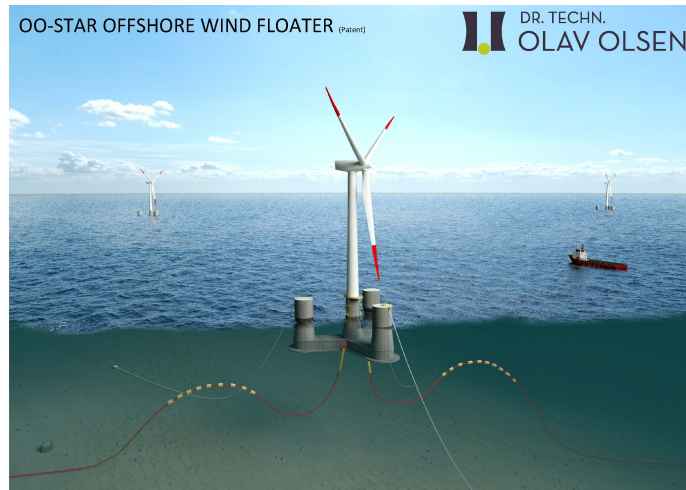


Figure 5.1: 6 MW OO-Star Wind Floater (Dr. Techn. Olav Olsen, 2016)

## 5.2 Programming

The goal of the numerical model was to set up a coupled aero-hydro-servo-elastic analysis in line with the state-of-the-art in FWT modelling. In order to do so, different software had to be utilized. These will be given an introduction in this section. In short, the numerical analysis was conducted in the following steps:

- Definition of a finite element panel model in *GeniE*.
- The panel model generated in *GeniE* was imported to a *HydroD*-workbench. Here, a relevant period-domain was defined for a subsequent frequency-domain hydrodynamic analysis performed in *WADAM*.
- Time-domain wind data was generated in *TurbSim*, using turbulence wind models and reference wind velocities identified in chapter 4.
- Coupled time-domain aero-hydro-servo-elastic analysis is carried out in *SIMA* using *SIMO/RIFLEX*-coupling.



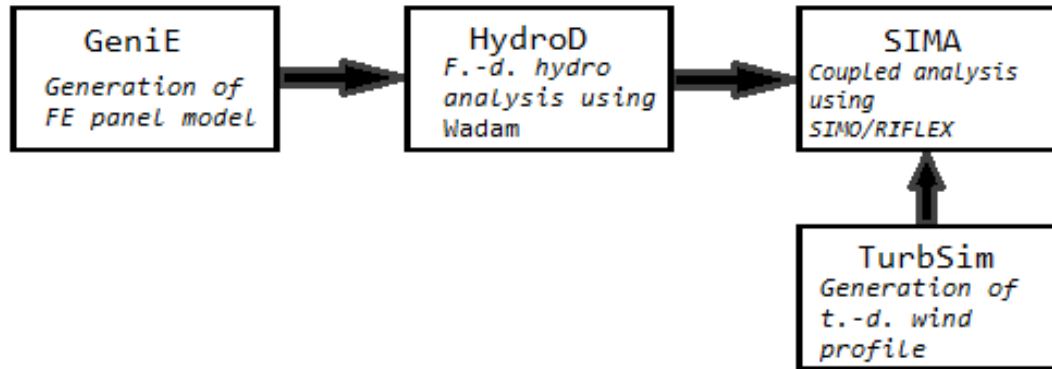


Figure 5.2: Overview of software used to build the numerical model

### 5.2.1 GeniE

*GeniE* is a design analysis tool that is part of the *SESAM* software package, developed and licensed by DNV-GL. The software is able to perform finite element mesh generation, analysis, results visualization and load calculation. Thus, it can be utilized as a stand-alone design tool. In this thesis, *GeniE* was used to model the geometry of the submerged parts of the 6 MW OO Star hull. It was also utilized to generate a finite element panel model for subsequent *WADAM* analysis, as well as to create a hydro pressure load case.

### 5.2.2 HydroD

*WADAM* (Wave Analysis by Diffraction and Morison Theory) has been used to carry out frequency-domain hydrodynamic analysis. The program is executed from *HydroD*, where wave periods for analysis and a rigid body structure was defined. The program is, like *GeniE*, part of the DNV-GL software tool *SESAM*. In *WADAM*, hydrodynamic analysis are carried out for slender elements by Morison's equation, or for large volume structure using the 3D panel method. The latter feature has been utilized in this thesis. For structures with a combination of slender and large volume elements, hydrodynamic analysis are carried out by combining the two theories. The numerical panel method analysis is based directly on the *WAMIT* code developed at *Massachusetts Institute of Technology* (Veritas, 2010).

### 5.2.3 TurbSim

*TurbSim* is an open source code developed by NREL. It produces 3-D stochastic turbulence deviations for time-domain analysis, by a FFT-transformation of frequency-domain statistical parameters. The deviations is implemented as a series of two-dimensional slices, with the interval and slice size being user-defined. The *TurbSim*-output is used as input in *AeroDyn*-based simulations (Jonkman, 2009).

### 5.2.4 SIMA Workbench

The *SIMA*-workbench is a software developed by Marintek for simulation and engineering analysis of marine operations and floating systems. In FWT-applications, it enables the user to perform a coupled aero-hydro-servo-elastic analysis. The coupled analysis is carried out in *SIMO*, a software for simulation of motions and station-keeping behaviour of floating systems, and *RIFLEX*, a tool for structural and dynamic analysis of slender marine structures. Here, non-linear FEM analysis are employed for time-domain analysis. The wind turbine aerodynamics are calculated in a separate Aerodynamics module in *RIFLEX*, where the turbine output is calculated from the BEM-theory outlined in this report. The *SIMO/RIFLEX*-coupling is illustrated in figures 5.3 (Bachynski, 2016).

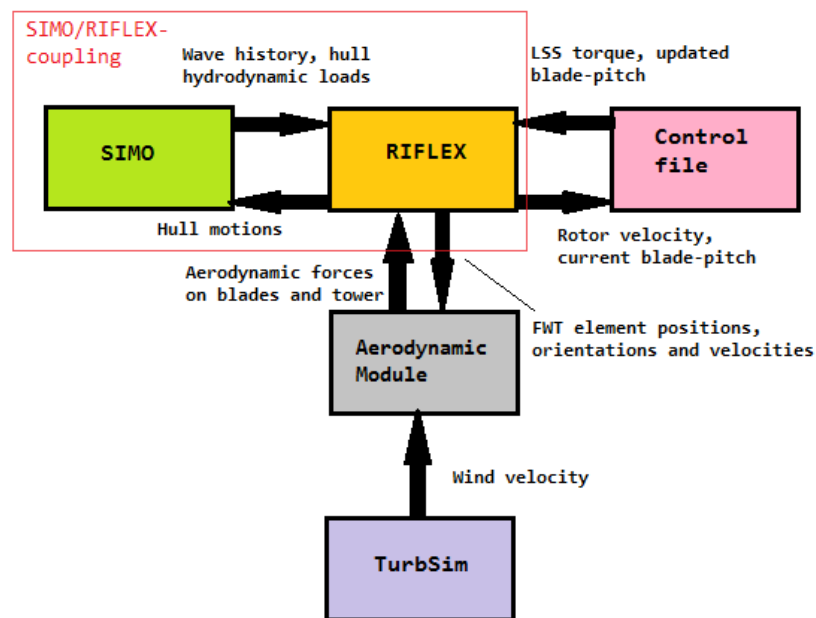


Figure 5.3: Flow chart for the aero-hydro-servo-elastic coupling in *SIMA Workbench*

## 5.3 FE Panel Model

All hydrodynamic models in this thesis have been generated in the design analysis tool *GeniE*. The original design was generated as 3-dimensional structures using structural drawings provided by Dr. Techn. Olav Olsen AS. After defining the geometry, the body was discretized into a finite element panel model using a wet surface loading condition. This FE model was subsequently imported into *HydroD* for frequency-domain analysis. Appropriate changes were made in the original parametric file to generate new models with different heave plate configurations. All models considered were generated as symmetric bodies, with the XZ-plane as the symmetry plane. This was done in an effort to increase the computational efficiency. The FE panel model

utilized for the calculation of difference-frequency excitation forces were subject to a different criteria, due to requirements in *HydroD*:

- Only the submerged parts of the structure had to be evaluated in the hydrodynamic analysis using first order potential theory. Thus, the model generated for these calculations was the submerged body in still water.
- In order to define a panel model for second-order potential theory, some alterations were needed. As this type of analysis does not neglect the changing wave elevation, a surface piercing body had to be generated. Additionally, second-order analysis in *HydroD* require a finite element model of the free surface. Thus, this model had to be generated separately. An example of a surface-piercing body and free surface model in *HydroD* is presented in Figure 5.3 .

### Mesh Quality

From the work during the project thesis, it was observed that the eigenperiod calculation in *HydroD* was not a satisfying indicator of the mesh quality. Most importantly, the eigenperiods did not show a significant rate of change or a clear convergence for the different configurations. Furthermore, it was computationally ineffective to use an extensive hydrodynamic analysis to review the mesh sensitivity. Therefore, based on the findings in the project thesis, it was decided that a panel model consisting of at least 4156 elements would provide sufficient accuracy for the *Wadam* eigenperiods. In order to analyze the mesh quality for configurations above this limit, the built-in mesh analysis tools in *GeniE* was utilized. Additionally, the design was reviewed with regards to symmetry. In the project thesis, it was discovered that the centre of buoyancy had an error of 0.007 m in the x-coordinate. It was therefore focused on reducing this error, in order to preserve the symmetric behaviour of the FWT. The x-coordinate of the COB for the models considered in this thesis can be seen in table 5.2.

The mesh quality was reviewed by considering the Jacobian Ratio of each panel. This is a

Table 5.2: Mesh quality of FE panel model

Design	Panels	JR violations	COB(x) [mm]	$\nabla$ [t]
Original	6638	0	0.4	16.124

measure of the global element distortion, measured at each node. The Jacobian matrix governs the mapping of global coordinates to the local shape functions. An example of this is shown for a 2-dimensional coordinate system in equation 5.1, where  $x$  and  $y$  are global coordinates and  $\xi$  and  $\eta$  are local element coordinates.

$$J = \begin{bmatrix} \frac{\partial x}{\partial \xi} & \frac{\partial y}{\partial \eta} \\ \frac{\partial x}{\partial \eta} & \frac{\partial y}{\partial \xi} \end{bmatrix} \quad (5.1)$$

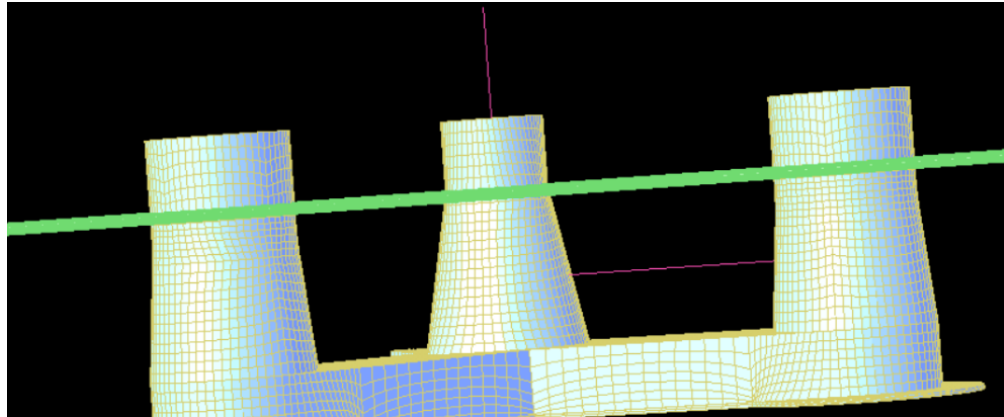
$$JR = \frac{|J|_{max}}{|J|_{min}} \quad (5.2)$$

In order to determine the Jacobian Ratio, the determinant of this matrix is defined at each element node. The Jacobian Ratio is determined for each element as the ratio between the highest and lowest Jacobian determinant (DNV-GL, 2013). A perfect quadratic mesh would return a Jacobian Ratio of 1 for each element, meaning that there is a linear mapping between the local element coordinates and the global coordinates. Due to the designs considered in this thesis, a perfect JR proved impossible to obtain. Therefore, the limit of the Jacobian Ratio was taken as  $JR \leq 4.5$ .

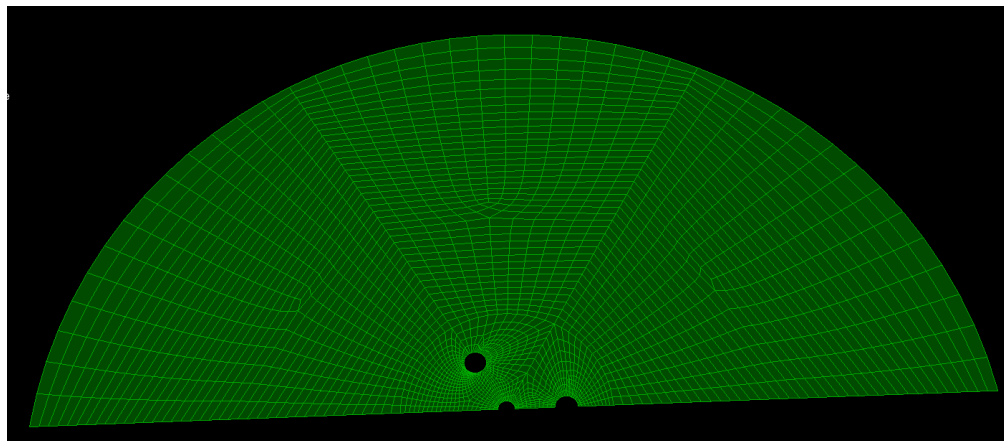
### Free Surface

In order to perform a second-order hydrodynamic analysis *HydroD*, a finite element model of the free surface had to be defined. This was done in compliance with Veritas (2010). Thus, the free surface-model was designed and discretized in *GeniE* with a hydro pressure load case in the negative z-direction. The model consisted of 4-noded elements, and the external boundary described a perfect circle. The free surface was also designed with the same symmetry properties as the FWT, meaning that the design consisted of a half-circle with circles corresponding to the surface-piercing elements of the FWT (figure 5.3). In order to investigate the quality of the finite element model of the free surface, three parameters were considered:

- The total number of elements had to be below 3000 panels, as this was the *HydroD* upper limit for such a loading condition.
- the Relative Jacobi was considered, with a criterion of  $JR \leq 3$ . This criterion was lower for the free surface than for the FWT, as the former had a less complex shape. Thus, it was easier to obtain a mesh with small distortions.
- The radius of the outer boundaries had to be sufficiently large. According to Veritas (2010), the radius of the free surface model should be at least larger than the depth in shallow water, or the wavelength in deep water. The largest depth considered in this thesis is 110 m. By using the assumption for deep water explained in 3.1, the consequence of this criterion was that the free surface model had to at least have a radius of 220 metres. For wavelengths above 220 m, shallow water was assumed (as  $h < \frac{\lambda}{2}$ ). Additionally, a security factor of 1.1 was used, and the radius of the outer boundary was rounded up to 250 m.
- It was focused on obtaining a fine grid interval close to the structure (Figure 5.3), but little consideration was given to the total number of elements. Although a mesh refinement study could have been carried out to increase computational efficiency, the above constraints made it a challenge to even construct a valid mesh beneath 3000 elements. Further work could be carried out to verify the numerical accuracy of the free surface panel model.



(a) Modified panel model with free surface in *HydroD*



(b) Free surface model in *GeniE*

Figure 5.4: Illustration of free surface model

## 5.4 Frequency-Domain Hydrodynamic Analysis

The finite element panel model generated in *GeniE* was imported to a *HydroD*-workbench, where input to the frequency-domain analysis was also defined. Subsequently, a frequency-domain hydrodynamic analysis was performed in *Wadam* by the panel method for large volume structures, utilizing first and second order potential theory. The output of the frequency-domain hydrodynamic analysis in *Wadam* consisted of the following:

- Mass matrix and hydrostatic stiffness for the floating body.
- Frequency-dependent added mass and damping
- Linear damping in heave, roll, pitch and sway
- First order motion transfer function
- Wave drift force in surge, sway and yaw
- Retardation function
- Quadratic transfer function for difference-frequency forces

The mass matrix and hydrostatic stiffness function was based on the displacement of the FWT, and thus had to be altered in the *SIMA*-workbench to account for the distributed weight of the wind turbine rotor and mooring lines. This will be discussed below. In order to define a mass distribution consistent with the FWT, the centre of gravity was manually defined in *HydroD*. COG was therefore determined in an iterative procedure, where this value was altered until the GM in roll and pitch converged against the value obtained from supervisor Håkon S. Andersen in Dr. Techn. Olav Olsen AS.

### 5.4.1 Frequency Domain

A well-defined frequency domain was necessary to accurately simulate the hydrodynamic behaviour of the FWT. An emphasis was made on capturing the response at common wave periods, as well as the response around the natural periods in all DOFs. In the projet thesis, the period range and intervals for hydrodynamic analysis was defined using an iterative approach. Due to the similarity of the design, it was decided to proceed with the same periods for first order analysis in this thesis. This also included a calculation of horizontal wave drift forces from momentum conservation, a procedure explained in chapter 3. Additionally, a period of 100 s was added to the analysis. This was done to get a more accurate calculation of the added mass at this period, a value utilized in the mooring design procedure explained in Section 5.7.

### 5.4.2 Second Order Frequency Domain

Difference-frequency excitation forces was calculated using second order potential theory. This effect occur due to the difference of two frequencies, meaning that all valid combinations of the frequency input were subject for analysis. Implementing the same frequency range for second order analysis would have resulted in a costly analysis, and it was therefore decided to define a new set of periods for a second order analysis. The difference-frequency excitation forces were calculated for 8 different wave headings, with a grid size of 45 deg. This was a computationally expensive procedure, and the computational resources were unable to automatically generate the input-file for *SIMA* due to a large file size. A *Matlab*-script was therefore used to write the results from *WAMIT*-analysis text-output into a *SIMO*-compatible text-file. The *Matlab*-script was modified from a similar script distributed by co-supervisor Erin Bachynski.

When selecting wave periods for the establishment of difference frequency quadratic transfer functions (QTF's), it was considered important that the QTF's were well-defined around the FWT natural periods. An emphasis was also made on defining periods corresponding to the most occurring wave periods. Additionally, it was prioritized to include wave periods close to the natural heave periods in heave and pitch from the project thesis (19.56 and 29.69, respectively). Finally, the periods subject for analysis was altered to ensure that the difference-frequency QTF's was well-defined around the natural periods from the project thesis in all DOF's.

As the second-order analysis for different wave headings were an expensive procedure, relatively few periods could be included in the analysis. Therefore, a refinement study was conducted on the periods, in order to obtain a good approximation of the difference-frequency effect at each wave heading. The quadratic transfer functions (QTF) for the selected periods, with wave heading  $0^\circ$ , was compared to the same functions from an analysis with a fine refinement of the frequency domain. The latter study could only be carried out at one wave heading, due to computational expenses. Figure 5.4.2 illustrate that the coarse frequency domain used for analysis in this thesis over-predict the difference-frequency forces in pitch at high wave periods (14 s-18 s). The opposite is observed for lower periods. Although the later results should be seen in light of these deviances, the coarse frequency domain was generally considered to reflect the physical behaviour. For reference, the Newman approximation grossly under-predicted the slow drift forces in pitch. In surge the deviances are smaller, and it was also observed that a Newman approximation would have been adequate in this DOE.

In table 5.3, the periods corresponding to the difference-frequencies of the second-order analysis can be seen. These difference periods was deemed to give a well-defined picture of the response, and the analysis proved computationally effective enough to complete. Consequently, the periods listed in table 5.3 was analysed in the second-order analysis.

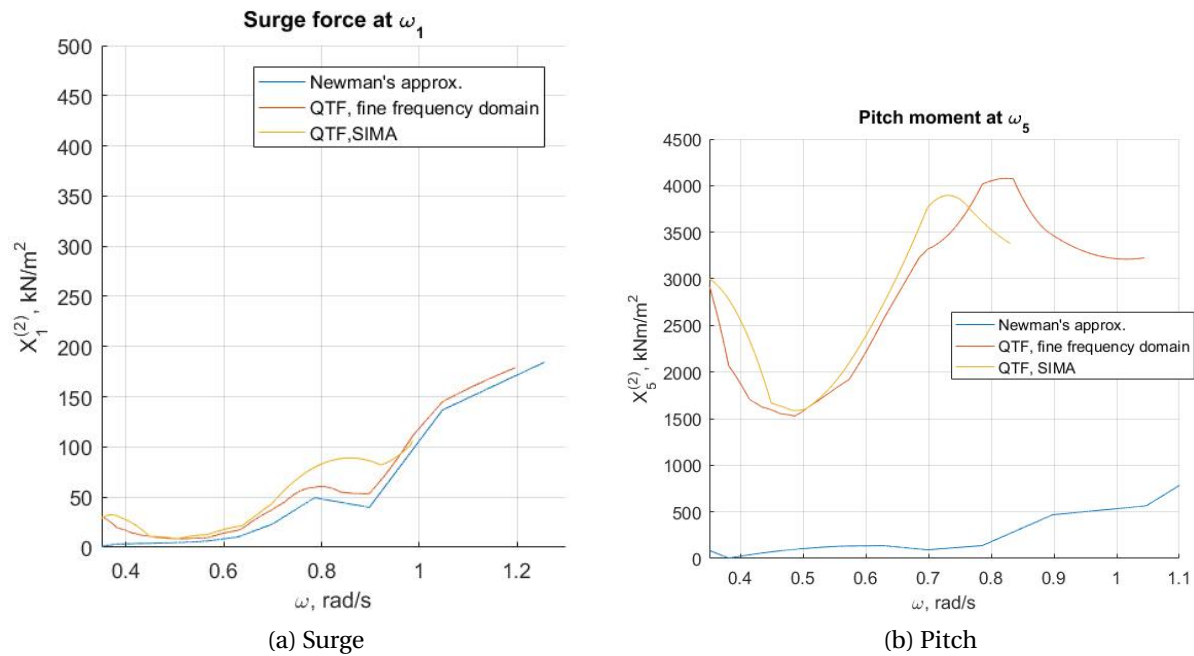


Figure 5.5: Comparison of Newman approximation and second-order potential theory with fine and coarse frequency resolution

Table 5.3: Difference periods for second-order WADAM-analysis

T [s]	5	6.4	9	11.1	12.5	14.2	18	20	24.5	29.5
5	$\infty$	22.86	11.25	9.10	8.33	7.72	6.92	6.67	6.28	6.02
6.4	-	$\infty$	22.15	15.11	13.11	11.65	9.93	9.41	8.66	8.17
9	-	-	$\infty$	47.57	32.14	24.58	18.00	16.36	14.23	12.95
11.1	-	-	-	$\infty$	99.11	50.84	28.96	24.94	20.29	17.80
12.5	-	-	-	-	$\infty$	104.41	40.91	33.33	25.52	21.69
14.2	-	-	-	-	-	$\infty$	67.26	48.97	33.78	27.38
18.0	-	-	-	-	-	-	$\infty$	180.00	67.85	46.17
20	-	-	-	-	-	-	-	$\infty$	108.89	62.11
24.5	-	-	-	-	-	-	-	-	$\infty$	144.55
29.5	-	-	-	-	-	-	-	-	-	$\infty$



## 5.5 Coupled Model

The model for hydro-aero-servo-elastic analysis was completed in the *SIMA*-workbench. Here, frequency-domain hydrodynamic data was imported as a *SIMO*-body. From this, it follows that the output of the *WADAM*-analysis, given in the above, was imported as a nodal component in a dynamic analysis. Furthermore, the floating body was connected to a rotor and a catenary mooring design by the master-slave technique. This was done by defining the mooring fairleads and the top of the tower as slaved nodes, with the floating body as their master. Subsequently, after importing the frequency-domain hydrodynamics from *WADAM*, the following had to be defined in the *SIMA*-workbench to complete a model for time-domain analysis. All steps are further explained later in this chapter.

- Implement a 6 MW wind turbine rotor and define a control system for the wind turbine.
- Model the load contribution from viscous forces.
- Design a catenary mooring system for stationkeeping.
- Correct the hull mass and hydrostatic data for the weight distribution of a catenary mooring system and the rotor.

### 5.5.1 FWT Hull Corrections

The frequency-domain hydrostatic data was calculated for the submerged parts of the FWT hull. The displacement of the hull therefore corresponded to the total weight of the FWT structure, including the rotor, hub, nacelle, tower and mooring lines. As these elements were accounted for in the coupled analysis, the FWT hull mass properties and hydrostatic coefficients in roll and pitch had to be modified. A quick explanation of the hull modifications will be given in this section, as the procedure was explained in [Nærum \(2016\)](#).

As the structural integrity of the FWT tower was not considered for analysis in this thesis, this component was modelled as an infinitely stiff line connecting the hull and the turbine. Because of this, the tower mass was included in the mass of the FWT hull. Accounting for the other weight components, the hull mass  $M_h$  (including the tower) was found according to

$$M_h = \Delta_f - M_{rotor} - M_{hub} - M_{nac} - M_{moor} \quad (5.3)$$

$M_{rotor}$ ,  $M_{hub}$  and  $M_{nac}$  denotes the mass of the rotor, hub and nacelle, respectively, while  $M_{moor}$  is the effective mass of the mooring lines in water.

Due to the new weight, the FWT hull CoG and hydrostatic restoring coefficients had to be modified. This modification was done according to equations 5.4 and 5.5. Due to the  $xz$ -

symmetry of the hull, the restoring coefficients in roll and pitch are equal (Faltinsen, 1993).

$$z_{G,f} = \frac{\sum_{i=1}^N M_i \cdot z_{G,i} - (M_{rot} \cdot z_{G,rot} + M_{hub} \cdot z_{G,hub} + M_{nac} \cdot z_{G,nac} + M_m \cdot z_{G,m})}{M_f} \quad (5.4)$$

$$C_{55} = \rho_w g I_{wp} + g \Delta_f (z_B - z_{G,f}) \quad (5.5)$$

A correction to the FWT buoyancy also had to be implemented. *SIMO* automatically assign buoyancy based on the weight of a floating body, meaning that the buoyancy assigned to the modified hull weight will be too low. This was accounted for by adding a constant vertical force equal to the difference between the hull displacement and hull weight. One of the steps in the installation of the semi-submersible OO-Star Wind Floater is filling the pontoons with water. It was considered that small changes in the hull mass could be within reason, as this could be obtained simply by flooding different amounts of water in the hull.

Table 5.4: Hydrostatic parameters

	HydroD	SIMA, 50 m	Sima, 80 m	Sima, 110 m
$M_h$ [tonnes]	16124	15474	15538	15541
$F_{aB}$ [kN]	0	6378	5745	5716
$z_{G,f}$ [m]	-7.9832	-10.239	-10.258	-10.259
$z_B$ [m]	-12.88	-12.88	-12.88	-12.88
$C_{55}$ [kNm]	$8.903 \cdot 10^8$	$1.2542 \cdot 10^9$	$1.2574 \cdot 10^9$	$1.2575 \cdot 10^9$
$C_{44}$ [kNm]	$8.903 \cdot 10^8$	$1.2542 \cdot 10^9$	$1.2574 \cdot 10^9$	$1.2575 \cdot 10^9$
$M_m$ [tonnes]	0	300.4	235.9	232.8
$M_{rot}$ [tonnes]	0	74.64		
$M_{hub}$ [tonnes]	0	70.98		
$M_{nac}$ [tonnes]	0	205.38		

## 5.5.2 Wind Turbine Dimensions

The FWT analyzed in this thesis is the 6 MW OO Star. Subsequently, this concept was designed with a 6 MW rotor. Due to available data, it was decided to use a scaled model of the open code 5 MW NREL turbine (Jonkman et al., 2009) for design during project thesis work. The model was scaled and modelled in *SIMA* by co-supervisor Eryn Bachynski, and the same data has been utilized in this master thesis. The model was scaled on the basis of the length-scale factor for wind turbines, where  $k_r$  is the scaling parameter for each component. This method was explained in Nærum (2016). The main dimensions of the implemented rotor are tabulated in table 5.5.

Table 5.5: Upscaling of NREL 5MW rotor to 6MW

	NREL	Scaled Model	Ratio
Rated Power	5 MW	6 MW	$k_r^2$
Tip Radius	63 m	69 m	$k_r$
Hub radius	1.5 m	1.64 m	$k_r$
Rated rotor speed	12.1 rpm	11.05 rpm	$k_r^{-1}$
Hub mass	56780 kg	73531 kg	$k_r^3$
Torque at rated speed	43093 Nm	56647 Nm	$k_r^3$
Hub Height	-	97.8 m	-

### 5.5.3 Wind Input

The wind input in time-domain analysis is generated in the NREL licensed code *TurbSim*. The wind data was generated based on the environmental data and wind profile given in chapter 4. Thus, a separate file containing wind velocities is written for each load case, and this file was subsequently imported to the *SIMA-Workbench* for time-domain analysis.

In *TurbSim*, the wind profile is generated as a box containing 2-D slices of the instantaneous velocities of the incoming wind. Because of this, the 2-D slices have to contain the area swept by the wind turbine rotor. The hub height is defined as the centre of each rectangular slice. In order to confidently contain the rotor-swept area, each box was defined to be a 180m · 180m square (the tip radius of the 6 MW turbine is 69m). Each slice was defined to include 32 · 32 matrix points, all containing a 3-D velocity vector. This grid size of 5.625m correspond to 12.27 data points along each rotor blade, and was considered sufficiently small after consulting with co-supervisor Erin Bachynski.

### 5.5.4 Control System

Wind turbines require a control system to control the operation of the turbine. The main purposes of the control system are:

- Regulate the power output, in order to ensure efficient operation.
- Limit the rotational speed, as noise restrictions limits the speed to around 80 m/s.
- Restrict the loads experienced by the turbine.

The control system used in the upscaled NREL rotor is a variable speed, pitch-to-feather turbine (Jonkman and Buhl Jr, 2007). This implies that the system governing the operation is based on two independent control systems: a generator torque controller and a pitch-controller controlling the collective pitch of the rotor. These control systems are implemented in the Aerodynamic module in *RIFLEX*.

The generator torque controller is designed to optimize the power output of the turbine. Thus, it restricts the torque at rated speed to the value given in table 5.5. As a consequence the controller also limit the loads experienced by the turbine. In order to sufficiently limit the turbine loads, a fault control system is usually implemented as well. This system typically shuts down the turbine when the wind speeds are above the operational limit. In this thesis, fault is not adjusted for, and analysis are carried out with a pre-defined operational or parked turbine.

The full-span, rotor-collective blade-pitch angle is computed by controlling the speed error between the filtered generator speed and the rated generator speed. The speed error  $\dot{\varphi}$  is in Jonkman et al. (2009) represented by the following equation of motion:

$$\left[ I_{DT} + \frac{1}{\Omega_0} \left( -\frac{\partial P}{\partial \theta} \right) N_{gear} K_D \right] \ddot{\varphi} + \left[ \frac{1}{\Omega_0} \left( -\frac{\partial P}{\partial \theta} \right) N_{gear} K_P - \frac{P_0}{\Omega_0^2} \right] \dot{\varphi} + \left[ \frac{1}{\Omega_0} \left( -\frac{\partial P}{\partial \theta} \right) N_{gear} K_I \right] \varphi = 0 \quad (5.6)$$

In the above equation,  $I_{DT}$  is the drivetrain inertia to the low speed shaft,  $\frac{\partial P}{\partial \theta}$  is the sensitivity of aerodynamic power to the blade-pitch angle,  $\Omega_0$  is the rated low-speed shaft rotational speed,  $N_{Gear}$  is the high- to low-speed gearbox ratio and  $P_0$  is the rated mechanical power of the wind turbine.  $K_D$ ,  $K_P$  and  $K_I$  is the derivative, proportional and integral speed-error gains, respectively.

When defining the control system coefficients  $K_D$ ,  $K_P$  and  $K_I$ , Hansen et al. (2005) recommends the derivative gains to be neglected. Additionally, it is recommended to ignore the term  $\frac{P_0}{\Omega_0^2}$ , which represents negative damping induced by the generator torque controller. From equation 5.6, it is implied that the controlled rotor speed error will respond as a second-order system, with a natural frequency of  $\omega_{\varphi n}$  and damping ratio  $\zeta_{\varphi}$ . Neglecting the derivative gain and the negative damping from the generator-torque controller, the system response characteristics are given by

$$\omega_{\varphi n} = \sqrt{\frac{K_{\varphi}}{M_{\varphi}}} = \frac{\left( -\frac{\partial P}{\partial \theta} \right) N_{gear} K_I}{\Omega_0 I_{DT}} \quad (5.7)$$

and

$$\zeta_{\varphi} = \frac{C_{\varphi}}{2M_{\varphi}\omega_{\varphi n}} = \frac{\left( -\frac{\partial P}{\partial \theta} \right) N_{gear} K_P}{2I_{DT}\Omega_0\omega_{\varphi n}} \quad (5.8)$$

In Hansen et al. (2005), it is recommended to aim for a natural frequency of 0.6 [rad/s] and a damping ratio of 0.6 to 0.7 for the definition of  $K_P$  and  $K_I$ . These values, with a damping ratio of 0.7, were implemented by co-supervisor Erin Bachynski in the definition of an upscaled 6 MW turbine. However, the low natural frequency of the FWT pitch motion ( $\omega_n = 0.21$  [rad/s]) makes such an approach problematic. The fast reaction of the control system induces a harmonic oscillating pitch motion on the FWT, as can be seen in figure 5.6. In order to obtain

stable behaviour of the FWT,  $\omega_{\varphi n}$  was therefore determined to be lower than the FWT natural frequency in pitch. As a consequence of this,  $K_P$  and  $K_I$  were modified to obtain a speed-error characterized by  $\omega_{\varphi n} = 0.20$  [rad/s], while the damping ratio where kept constant at 0.7.

Table 5.6: Speed-Error Gains

$\omega_{\varphi}$ [rad/s]	$K_P$	$K_I$
0.6	0.0225921	0.0096823
0.2	0.0075310	0.0010758

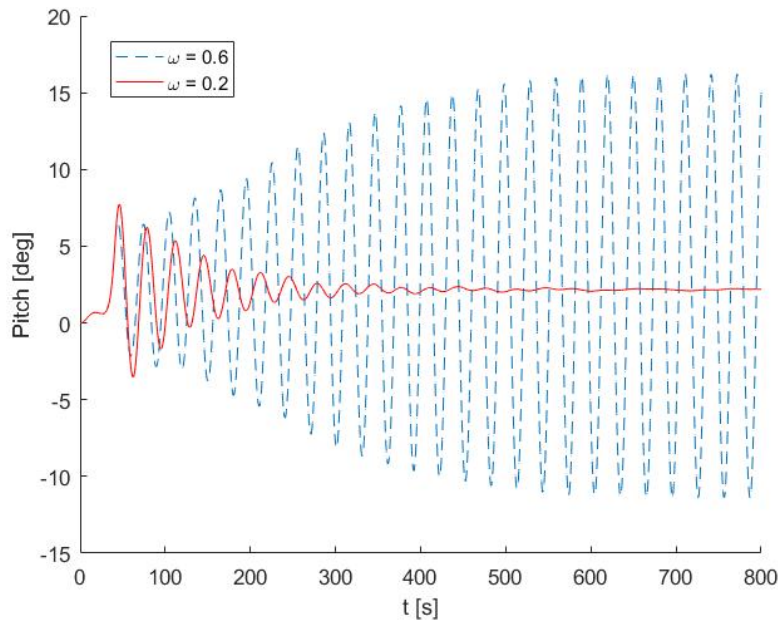


Figure 5.6: Pitch motion with different speed-error gains

In order to illustrate the effect on the FWT behaviour, constant uniform wind tests at 13 [m/s] where performed with the different coefficients. The results are illustrated in figure 5.6. As can be seen by the figure, the original blade pitch control system induces negative aerodynamic damping on the FWT, resulting in large harmonic pitch oscillations. With the modified system, on the other hand, the FWT pitch motions reach steady-state. Thus, the updated  $K_P$  and  $K_I$  was used in the numerical model of the 6 MW OO-Star Wind Floater.

## 5.6 Viscous Forces in Time-Domain

### 5.6.1 Heave Plate Modelling

As previously explained, a correction have to be implemented in the numerical model to adjust for viscous forces. The magnitude of this correction is strongly dependent on the KC-number (equation 5.9). The KC-number is a function of the flow velocity at the structure and the diameter, and this size will differ from wave to wave in an irregular sea state. This constitutes a problem for time-domain analysis, as it is not possible to define such coefficients as changing variables in a *SIMA*-workbench. As a consequence, the quadratic drag term in 3.28 will be under-predicted at in small waves, and over-predicted in large waves. The opposite is the case for added mass.

$$KC = \frac{2\pi\eta_0}{D} \quad (5.9)$$

In order to obtain a good approximation of the KC-number, it was decided to use a statistical approach. DNV-GL's recommended practise for marine operations was therefore used to establish a sea state-dependent KC-number for time-domain analysis. In Veritas (2011), the KC-number in irregular waves is given as

$$KC = \frac{\sqrt{2}\sigma_v T_z}{D}, \quad (5.10)$$

where  $\sigma_v$  is the standard deviation of the relative velocity at the plate,  $T_z$  is the zero-upcrossing period and  $D$  is the plate diameter.

In order to establish the added-mass contribution from viscous damping, it has been relied on previous research. A summary of this research was presented in section 2.2. The previous studies presented the change in added mass due to viscous effects as a relative number according to equation 5.11, while the damping coefficient for the heave plate was found from equations 5.12 and 5.13:

$$A'_{33} = \frac{A_{33}}{A_{33}^{th}} \quad (5.11)$$

$$B'_{33} = \frac{B_{33}}{\omega A_{33}^{th}} \quad (5.12)$$

$$B_{33} = \frac{1}{3}\rho D_p^3 f(KC)C_d \quad (5.13)$$

As explained in section 2.2, the experimental results of Moreno et al. (2015) have been used to define the rate of change in added mass and drag coefficients for the OO-Star Wind Floater heave plates. The parameter  $A_{33}^{th}$ , which is decisive in defining hydrodynamic coefficients according to 5.11 and 5.12, was established using potential theory frequency domain analysis in *WADAM*. Here, a model without heave plates was defined and analyzed, and  $A_{33}^{th}$  was found according in the following steps

- The difference in heave added mass for the numerical model with and without heave plates was established. The values for  $A_{33}$  at the wave period of  $T = 20s$  was used, in order to reflect the value at resonance conditions.
- This difference was divided by three, to obtain  $A_{33}^{pot}$  (added mass for each heave plate according to potential theory) for each separate plate.
- Potential theory values for  $A_{33}$  are higher than the theoretical values (figure 2.2). In order to account for this,  $A_{33}^{th}$  was found by scaling down the potential theory difference by a factor of 1.04.

In the coupled time-domain analysis,  $A_{33}^{pot}$  is already accounted for through frequency-domain hydrodynamic analysis. Thus, the correction in added mass implemented in *SIMA* should be found according to

$$A_{33}^{corr} = A_{33}^{th} \cdot A'_{33} - A_{33}^{pot}, \quad (5.14)$$

where  $A_{33}^{th}$  is the theoretical added mass as explained above,  $A'_{33}$  is the scaling factor according to [Moreno et al. \(2015\)](#) and  $A_{33}^{pot}$  is the added mass difference from *WADAM*.

### 5.6.2 Non-Linear Viscous Drag

The contribution to the quadratic drag term in equation 3.28 was accounted for. Due to the shape of the OO Star concept, the submerged structure was discretized into 10 slender elements in *SIMA*. The slender elements was modelled as three horizontal rectangular cylinders corresponding to the pontoons, three vertical circular cylinders corresponding to the surface-piercing corner columns, three vertical cylinders plates to model the heave plates and one vertical cylinder corresponding to the surface-piercing tower shaft. The contributions from each element are added together by strip theory in *SIMA*. For reference, a non-dimensional structural drawing of the OO-Star Wind Floater is included in [Appendix D](#)

The drag term depends on the KC-number for all sections. However, the fluid motion in waves depend on the depth. Therefore, the quadratic drag term for vertical slender elements are scaled accordingly, and implemented as depth-dependent coefficients in *SIMA*. The depth dependent coefficients also account for the changing diameter of the vertical cross-sections, while the KC-number for each strip was found according to equation 5.10. The drag-coefficient was based on previous measurements and CFD-analysis of a rectangular submerged cylinder in waves ([Figure 2.7](#)).

### 5.6.3 Iterative Scheme

An iterative scheme was established to define the viscous forces for each sea state. This scheme was followed for every simulation case. Tabulated values for KC-number, correction in added mass and drag coefficients for each load case and water depth are presented in [section 7.2](#).

Table 5.7: Slender elements in *SIMA*

Pontoons		
L [m]	B [m]	H [m]
38	14	6
Corner Columns		
Location	D	z
Free surface	12	0
Top of conical shape	12	-5
Bottom of conical shape	14	-14
Tower Shaft		
Location	D	z
Top of conical shape	8.892	0
Bottom of conical shape	14.212	-14
Heave Plates		
Part of element	D	z
Top of plate	21	-19.6
Bottom of plate	21	-20

The iterative scheme established the KC-number along one pontoon, one bottom cross-section and on one heave plate. The damping coefficients (and added mass correction for the heave plates) were implemented in the corresponding slender elements. Based on the methodology in this section, the iterative scheme can be summarized in the following steps:

1. Assumed values for added mass and damping was implemented in *SIMA*.
2. Time-domain analysis with environmental conditions according to chapter 4 was carried out for a 1-hour simulation.
3. The standard deviation of relative water particle velocity, in addition to the zero up-crossing period, was found through post-processing in *MATLAB* and *SIMA*.
4. The KC-numbers was calculated in *MATLAB* according to equation 5.10.
5. New KC-dependent added mass corrections and drag coefficients were established in line with the procedure explained in the above. This was done in *MATLAB*.
6. Iteration was aborted when all KC-numbers stabilized within a sensitivity of 0.001.



## 5.7 Design of Mooring System

### 5.7.1 Design Challenges

The main purpose of this thesis was to investigate the effects of intermediate depth on the behaviour of the chosen FWT concept. Thus, a spread catenary mooring design was proposed for each water depth. The design process built on the experiences from the preliminary studies of the project thesis, where a mooring design was suggested for depths of 70 metres and 120 metres. It was observed that the submerged weight of the mooring lines would be 50 % higher at 120 metres with the proposed material, indicating that different water depths would present varying design parameters.

There are several important design parameters for the stationkeeping system of a semi-submersible FWT. The mooring system should limit the maximum platform motions, to avoid high bending moments and stresses in the power cable. The power cable for a FWT is usually designed for each concept after the design of the mooring system. Large FWT motions would thus come with the implication of complex and expensive power cable designs.

The natural period in surge and sway have to be sufficiently large in order to avoid resonance conditions for regular frequencies. Mooring lines are also subject to large non-linear tension at large offsets. This could lead to high loads, possibly exceeding the structural capabilities of the mooring line material (Xu, 2015).

Thus, mooring design needs to be sufficiently soft to allow for large natural periods in horizontal motions, and sufficiently stiff to make for easier power cable design. The material have to be strong enough to withstand both extreme conditions and fatigue damage, as mooring line failure could lead to a substantial economic loss (Chen et al., 2008).

Mooring design for intermediate water is particularly challenging. Due to the limited water depth, the suspended mooring line becomes short. As seen in equation 3.41, this affect the ability to induce horizontal stiffness. Consequently, additional weight elements known as clump weights are commonly applied in intermediate water to restrict the FWT horizontal motions. The weight of the suspended mooring line also affect the horizontal offset requirement, as a shorter line is needed to obtain the desired pretension. Therefore, the mooring lines experience non-linear tension at smaller offsets in limited water depth, which could lead to failure in harsh conditions.

### 5.7.2 Material

In order to meet the requirements mentioned in the above, it was decided to utilize different types of mooring line material and/or dimensions for each water depth. Thus, the horizontal and vertical forces induced by the mooring line can be kept somewhat similar. The most com-

mon types of material are chain, wire ropes and synthetic fiber rope (Vryhof Anchors, 2010). Due to available data on the former two, these were considered for this thesis.

Chains are commonly used in catenary mooring. The material used in chain links are usually steel, which gives the line a high weight and better ability to keep its catenary shape. There are two main configurations of chain: stud-link and stud. The former is strengthened by a horizontal link in the chain opening and can resist higher breaking loads. However, the fatigue properties of stud configurations are typically higher and are frequently used in permanent mooring systems. Chain systems are terminated at the fairlead by the use of an endlink (Vryhof Anchors, 2010). Steel chain material for offshore mooring come with different grades of strength, as indicated in table 5.8. Empirical values for proof load and breaking load also exist and can be found in supplier catalogues, such as Global Maritimes Anchor Manual (Maritime, 2015).

Due to the high weight and ability to keep a catenary configuration, stud chains were chosen for all water depths. The end-link and enlarged link has largely similar geometric and material properties as the overall chain segment. Thus, the entire mooring line is modelled with similar properties in SIMA. .

Table 5.8: Stud Chain Properties (Veritas, 2015)

Grade	R3	R3S	R4	R4S	R5
Yield Strength [MPa]	410	490	580	700	760
Tensile Strength [MPa]	690	770	860	960	1000
Axial Stiffness [N]	$90000d^2$				
Breaking load [kN]	$0.0223d^2$ ( $44 - 0.08d$ )	$0.0249d^2$ ( $44 - 0.08d$ )	$0.0274d^2$ ( $44 - 0.08d$ )	$0.0304d^2$ ( $44 - 0.08d$ )	$0.0320d^2$ ( $44 - 0.08d$ )

### 5.7.3 Design procedure

The main challenge during the design was to allow a sufficiently large offset for each water depth, while maintaining roughly the same horizontal stiffness and weight in the mooring lines. As the scope of this thesis revolves around a hydrodynamic comparison of the concepts at different water depths, it was decided to focus on obtaining the same undamped natural periods, while maintaining roughly the same mooring line weight. In order to meet the offset requirements of the FWT, it was decided to incorporate a offset margin  $X_{lim}$  of roughly 20 % of the water depth. This is a common approach in early mooring design phases (Xu, 2015).

It was decided to aim for a natural period of 105s in surge for each water depth, in order to avoid resonance behaviour. Furthermore, the anchor radius was maintained at 750 metres, based on conversations with co-supervisor Håkon S. Andersen during the project thesis work.

Based on the above design challenges and parameters, the mooring lines were modelling using the following approach:

1. Choose material and dimensions of mooring cables for each water depth.
2. Calculate needed horizontal tension for each water depth according to equations 3.40 and 3.41 in Section 3.4.
3. Calculate  $l$  and  $l_s$  based on equations for catenary mooring (Section 3.4), (Faltinsen, 1993).
4. Control that the offset margin  $X_{lim}$  was around 20 %.
5. Assess difference in total weight of mooring line and horizontal tension for each mooring line. Iteration was aborted when these properties were considered roughly similar.

Due to the low length of the submerged line at  $h = 50$ , it was challenging to obtain a satisfying horizontal stiffness with sufficient margin for horizontal displacement of the floater. Thus, it was decided to incorporate clump weights in this design. This made for a more intricate design procedure, as the catenary shape was predicted in the *Matlab*-script before iteration in *SIMA* to obtain the same natural period.

At  $h = 80m$  and  $h = 110m$ , an ordinary steel stud chain configuration was chosen. In order to ensure a sufficiently large breaking strength, R5 material was chosen for the largest water depth. In the two other configurations, R4 was deemed sufficient.

#### 5.7.4 Final Design

The final mooring designs for the three water depths is presented in tables 5.9 and 5.10. The design for the 50 meter location is considerably heavier than the other designs, which could have implications for the hydrodynamics of the FWT. This directly effects the calculated restoring coefficient in pitch, which is lower for the location at 50 metres 5.4.

Table 5.9: Properties of cross section design

Nominal Diameter [mm]	185	180	137
Grade	R4	R4	R5
Axial Stiffness [N]	695	648	375
$C_D$ Longitudal [-]	2.4	2.4	2.4
$C_D$ Transverse [-]	1.15	1.15	1.15
Breaking load [kN]	27383	26277	19844

#### 5.7.5 Design verification

It was decided to implement a simple approach to the verification of the mooring designs, as the design was not viewed as a central part of this thesis. Free decay tests were used as a measure of the horizontal stiffness. In addition to this, the mooring lines capability to carry loads was analyzed. This was done through static analysis in *SIMO/RIFLEX*, where the mooring line

Table 5.10: Tabulated values of catenary design

Depth	50 m	80 m	110 m
d [mm]	185	180	137
Mass [kg/m]	695	648	375
$T_{Hi}$ [kN]	576.1	601.2	769.8
$l$ [m]	761.98	771.85	776.62
$l_s$ [m]	73.5	135.54	234.02
$M_{line}$ [tonnes]	135.41	235.85	232.82
$M_{cl}$ [tonnes]	55	-	-
$M_{moor}$ [tonnes]	300.41	235.85	232.82
$T_{n1}$ [s]	104.89	104.27	104.11
EA [MN]	1682	2510	3080
$X_{lim}$ [m]	15.18	19.10	20.79

tension at different horizontal orientations of the floater were measured. An ULS consideration was made by comparing the static mooring line tension at the maximum surge position in Load Case E.1 to figure 6.1. Both the surge natural period and the breaking load of the mooring lines will be discussed in the subsequent chapters.

For a full verification of the mooring line configuration, the fatigue life-time and dynamic line tension should also be considered. However, as this thesis revolves around the hydrodynamic capabilities of the OO Star design, the procedure outlined above was deemed adequate for this purpose.

It should be noted that all the tests carried out in this thesis have been carried out with a wind, wave and current direction of  $\theta = 0^\circ$  to the surge-motion. In Figure 6.1, the loads are taken for mooringline 2 and 3, which are oriented with a  $60^\circ$  angle to the surge-motion. Thus, the x-axis in Figure 6.1 does not reflect the actual offset of the mooring line.

## 5.8 Conceptual Heave Plate Study

In line with the scope, additional heave plate configurations were proposed for a conceptual study. In the literature study the effects of having multiple heave plates were discussed. Due to this, three different configurations with two heave plates were proposed, in addition to the original design:

- Two heave plates with a diameter/cylinder-ratio of 1.25
- Two heave plates with a diameter/cylinder-ratio of 1.5
- One lower heave plate with a diameter/cylinder-ratio of 1.5, and a higher plate with a diameter/cylinder-ratio of 1.25.

The four different concepts are illustrated in figure 5.8. As discussed in section 2.2, the added-mass increases as the plate thickness decreases. In order to not under-predict the potential damping of the smaller plates, it was also decided to reduce the thickness of the smaller plates to maintain the aspect ratio (thickness/diameter). With the scope of this thesis being the hydrodynamic behaviour of the FWT, it was assumed that this would also maintain the structural integrity of the small plate. Further work should be carried out to optimize the aspect ratio of the new plate configurations.

It was decided to investigate the different heave plate configurations at a water depth of 80

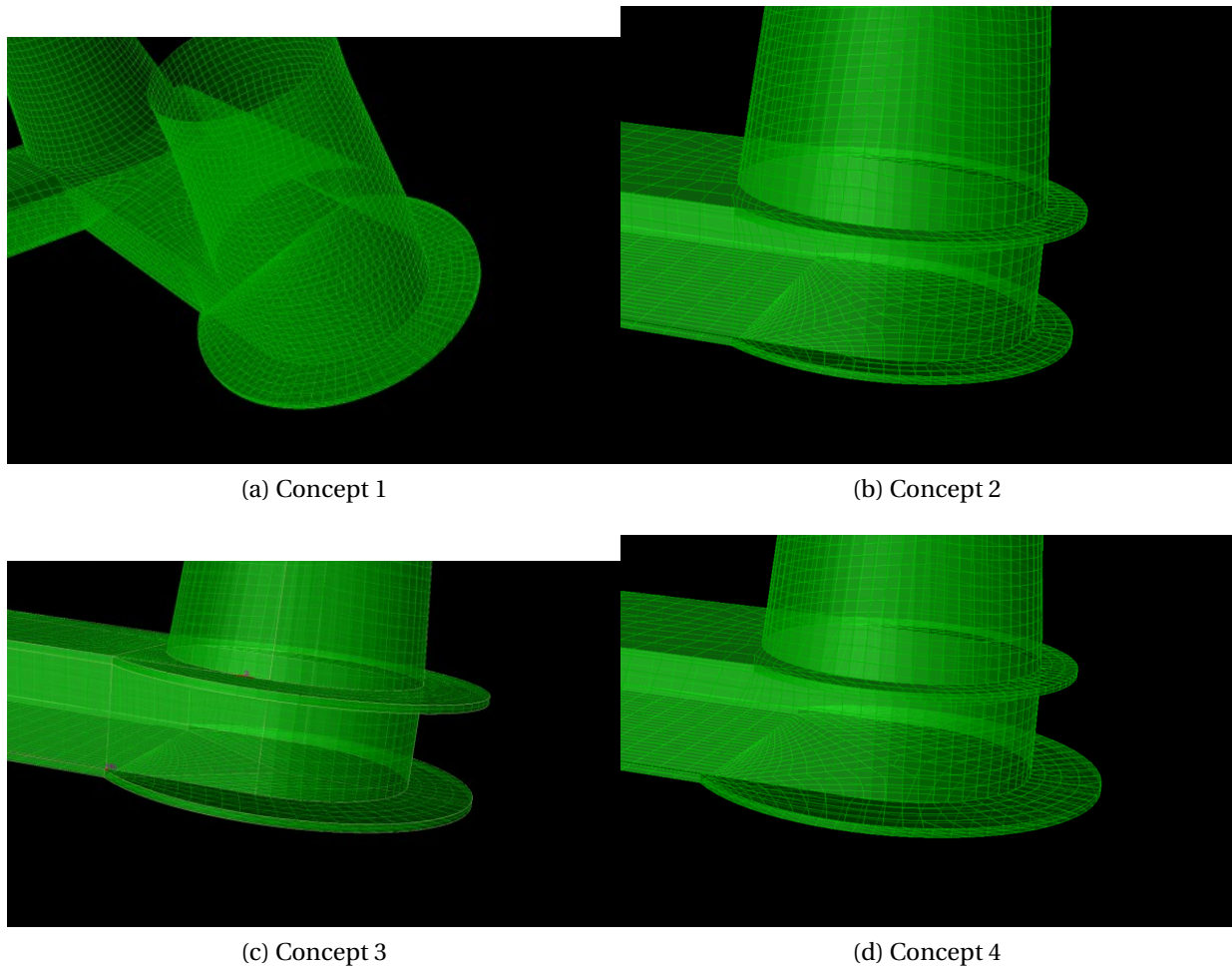


Figure 5.7: Conceptual design cases

m. Additionally, it was decided to not implement second-order difference-frequency excitation forces in the calculation. Only a single water depth was chosen in order to investigate the behaviour in identical load cases, keeping possible depth effects out of the conceptual study. The modelling process of the new designs was similar to the original design, where the only changes were due to the different weight and heave plate configuration of the conceptual models.

All three models were generated using a parametric code in *GeniE*. Due to the increased complexity in the geometry, a higher number of elements were needed for the new designs. Additionally, it proved difficult to obtain the same mesh quality, with certain elements having a high Jacobi-Ratio for each concept. The total number of panel and elements that failed the Jacobi-criterion and the new weight of the structure are found in table 5.11.

Table 5.11: GeniE-values in conceptual heave plate designs

Configuration	Case	Panels	JR	CoB, x [mm]	$\nabla$ [t]
Original	1	6638	0	0.4	16.124
Two-plates, D/C = 1.25	3	7596	2	0.6	16.075
Two plates, D/C = 1.5	2	8300	3	0.75	16.287
Two Plates, D/C = 1.5 and 1.25	4	7335	2	0.74	16.181

Upon implementation of the three new models in *SIMA Workbench*, the mass of the floating body, hydrostatic restoring coefficients in roll and pitch and the added buoyancy were all changed to account for the new weight of each concept. Additionally, the implementation of two heave plates for each pontoon were done by adding a slender element with a spacing according to the new design parameters.

Additional added mass and quadratic damping coefficients in heave was gathered from [Tao et al. \(2007\)](#). This selection was discussed in section 5.6.1. The study was performed in still water conditions, meaning that the KC-number was defined by the amplitude of the oscillating cylinder-plate structure. In waves, the KC-number depending on the relative velocity between the floating body and waves decrease with depth. Therefore, it was decided to use the average relative velocity of the two plates to define the added mass and damping coefficients. Subsequently, the KC-dependent added mass and damping coefficients were evenly distributed to the two plates, according to:

- The added mass and damping coefficient of the two plates were evenly distributed at the two slender elements in case 2 and 3.
- Due to the uncertain contribution from a smaller plate in combination with a larger, the added mass and damping coefficients were obtained using experimental studies for one plate. However, the average relative velocity was used to obtain the KC-coefficient, and the added mass and damping were evenly distributed. Due to these assumptions, the results for the case 4 concept should be considered a first approximation and should be further investigated.

# Chapter 6

## Verification of Numerical Model

### 6.1 Potential Theory from HydroD

*HydroD* is able to calculate the natural periods for the FWT without the influence of mooring lines. However, the horizontal stiffness for the semi-submersible concept was induced by this stationkeeping system, which were only defined for the coupled model. Thus, *HydroD* could only calculate the uncoupled natural periods in heave, roll and pitch. The added-mass changes with the frequency, yielding different natural period results for different first order waves. In Table 6.1,  $T_{n3}$  is presented as the results of a first order wave with  $T = 20$  seconds, while  $T_{n4}$  and  $T_{n5}$  are the natural periods for a first order wave at 28.5 seconds. The results in Table 6.1

Table 6.1: Natural periods from *HydroD*

h	$T_{n3}$	$T_{n4}$	$T_{n5}$
50	19.720	28.724	28.722
80	19.652	28.707	28.705
110	19.643	28.706	28.704

increase as the water depth get smaller. This indicate that the wave kinematics will be different in the intermediate water range, which could reflect in the response of the coupled system at different water depths. The symmetry properties was considered to be adequately preserved, with a 0.002 s difference between roll and pitch natural periods in all water depths.

### 6.2 Free Decay

As previously explained, it was decided to set up numerical models at water depths of 50 m, 80 m and 110 m for analysis. In the project thesis, it was found that the symmetric behaviour in the numerical model was not sufficiently preserved. It was also discovered that heave, roll and pitch natural periods from potential theory analysis would change with water depth. In addition to

possible discrepancies in hydrodynamic loads, the models will be subject to different mooring requirements. To map out how these factors will govern the FWT behaviour at different water depths, it was decided to carry out free decay tests. These tests will serve as a validation for the mooring design requirement of horizontal stiffness, and will present a foundation for the analysis of FWT behaviour at different water depths.

The free decay tests proved that the numerical model developed for the master thesis did a

Table 6.2: Natural periods and damping for coupled models

Depth	$T_n$	$b_1$	$b_2$
Surge			
50 m	104.89	0.0002	0.0571
80 m	104.27	0.0006	0.0698
110 m	104.11		
Sway			
50 m	104.80	0.0002	0.0541
Heave			
50 m	19.774	0.0030	0.0183
80 m	19.770	0.0034	0.0193
110 m	19.764	0.0023	0.0210
Roll			
110 m	30.69	0.0134	0.0034
Pitch			
50 m	29.94	0.0135	0.0033
80 m	30.59	0.0131	0.0034
110 m	30.66	0.0131	0.0041
Yaw			
110 m	87.49	0.0030	0.0340

better job in maintaining the 6 MW OO-Star Wind Floater symmetry. The biggest difference in surge-sway natural periods was 0.08 percent for the  $h = 50m$  location, while the largest deviation for roll-pitch natural periods was 0.1 percent. In the numerical model considered in the project thesis, the same values deviated with 0.3 % and 0.47 %, respectively. Thus, it was concluded that the numerical accuracy was improved, and that the decision to use the CoB x-coordinate as a parameter for mesh quality was reasonable. A deviation of less than 0.1 % in natural periods in surge-sway and roll-pitch was deemed acceptable, and it was considered that the symmetry in the numerical model was preserved within a reasonable degree.

The horizontal stiffness in surge is higher for the 50 meter water depth. As mentioned in Section 5.7, it was necessary to incorporate clump weights in this mooring configuration. This made it difficult to obtain the same pretension and offset limit as in the other concepts. It was decided to proceed when the natural periods in surge were within one second. The decision was made based on a consideration of the maximum allowable offsets. In order to keep the offset limit high in all water depths, a compromise was allowed for the natural period in surge. The



horizontal stiffness in all three water depths were therefore considered to be adequately similar.

More concerning was the low natural period in pitch at 50 metres. This contradicted the natural periods in pitch from the frequency-domain hydrodynamic analysis (Table 6.1). This indicated that the added mass in pitch was not the cause for the natural period differences in the coupled numerical models. Additionally, both the hull mass and  $C_{55}$  were smaller for the 50 meter model. Based on equation 6.1, the hull weight or restoring coefficient were not considered the governing factors in the natural period difference.

$$T_{n5} = 2\pi \sqrt{\frac{Mr_{55}^2 + A_{55}}{C_{55}}} \quad (6.1)$$

The differences in hull mass were not considered large enough to obtain a difference of  $\approx 0.6$  seconds in  $T_{n5}$ . Coupling with the mooring line stiffness and damping was therefore considered the main contribution to the different  $T_{n5}$ . However, stationkeeping in intermediate water is a big challenge for FWT's, and it was decided that the differences in pitch behaviour could be representative for these challenges. Because of this, it was decided to proceed with the numerical models as they were.

### 6.3 Mooring Line Static Tension

Figure 6.1 show the static tension in mooring line 2 and 3 for a fixed surge displacement of the FWT. The figure also displays the breaking loads of the three mooring configurations, as explained in section 5.7. The x-axis in figure 6.1 is not 1:1 with the actual offset of the mooring lines analyzed, as these are oriented with a 60° angle to the surge axis. However, due to the wind orientation in later simulations this was deemed the most relevant displacement for the FWT.

The static analysis was aborted when the mooring line was fully stretched, or the static horizontal tension reached the breaking load of the material. As seen by figure 6.1, the 50 m-configuration was fully stretched out at a displacement of 37 metres. The 80 m-configuration reached the material breaking load at 51 metres, while the same incident occurred for a surge position of 56 metres for the 110 m-configuration. These values were later compared to the maximum surge position during the extreme load case, in order to do a simple ULS assessment on the mooring line configuration.

The figure below clearly show how the offset margin get smaller as the water depths decreases. The non-linear behaviour of the mooring line occur at a smaller surge position for 50 metres, with the 110 meter configuration allowing the largest offsets. Thus, figure 6.1 underline the challenges of mooring in shallow water, which were explained in section 5.7.

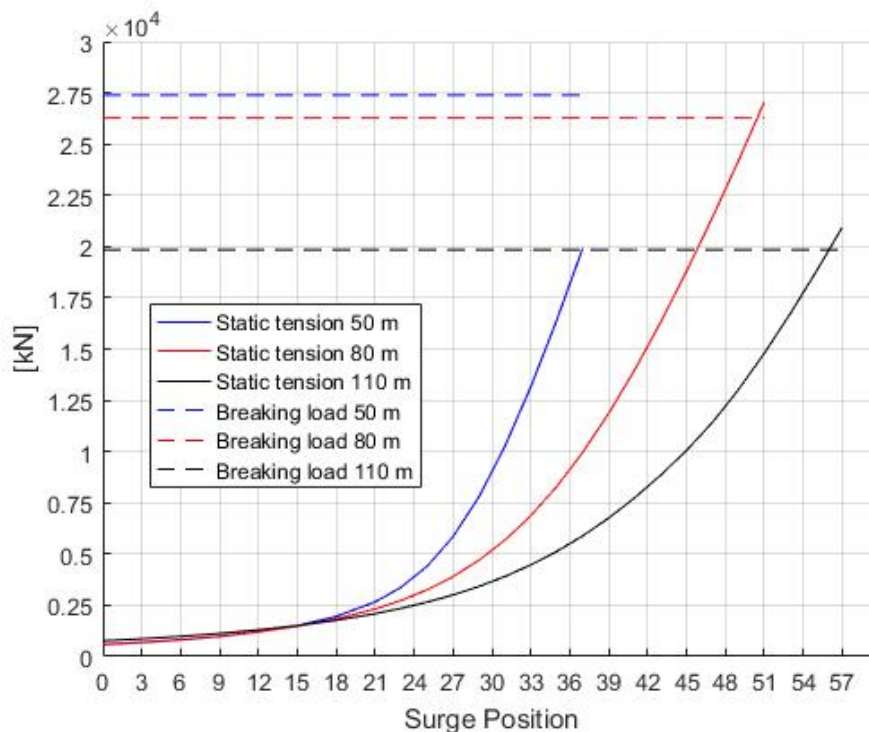


Figure 6.1: Static horizontal mooring line tension for surge displacement of FWT

## 6.4 Wind Turbine Performance

The 6 MW turbine modelled in this master thesis is an upscaled version of the open-source, 5 MW NREL turbine. In order to validate the performance of the 6 MW turbine and its controller, uniform wind tests were carried out. The tests were carried out by subjecting the FWT to constant wind speeds ranging from 2 m/s to 25 m/s, which is the range of wind speeds in which the turbine is operational. The uniform wind tests are carried out in calm sea, with zero current speed and minimum wave force contribution ( $H_S = 0.001$  m,  $T_p = 20$  s,  $U_C = 0$ ).

The performance curves compared well against the performance curves of a 5 MW-turbine (Jonkman et al., 2009). The rated power output, torque, generator speed and rotor speed corresponded to the predicted values in table 5.5. The 6 MW turbine reaches rated torque at a constant wind speed of 11.05 [m/s], and the blade-pitch controller reduces the rotor thrust by changing the blade-pitch in wind speeds above this value. Thus, the turbine and controller were considered to be validated, based on the performance curves in figure 6.2 and 6.3.

From figure 6.4, it was observed that the steady-state surge and pitch motion of the FWT reaches their highest values at the rated speed. In wind speeds above this value, the blade-to-feather pitch control system reduces the aerodynamic loads. Consequently, the surge and pitch motion decay proportionally to the rotor thrust. This characteristic is favorable for the FWT response, as it keeps the tilt-angle within the operational limits ( $\pm 6^\circ$ ) and reduces mooring line tension. These results implicate that optimized controllers for floating wind applications potentially can damp the global FWT motions favorably. However, there are also negative implications connected to FWT controllers in fault mode, e.g. Bachynski et al. (2013) showed that a FWT can experience large pitch and yaw motions due to blade seize and shutdown. The conclusion is that the wind turbine control systems will have an effect on the FWT motions, and that the development of FWT-specific controllers is recommended in future work.

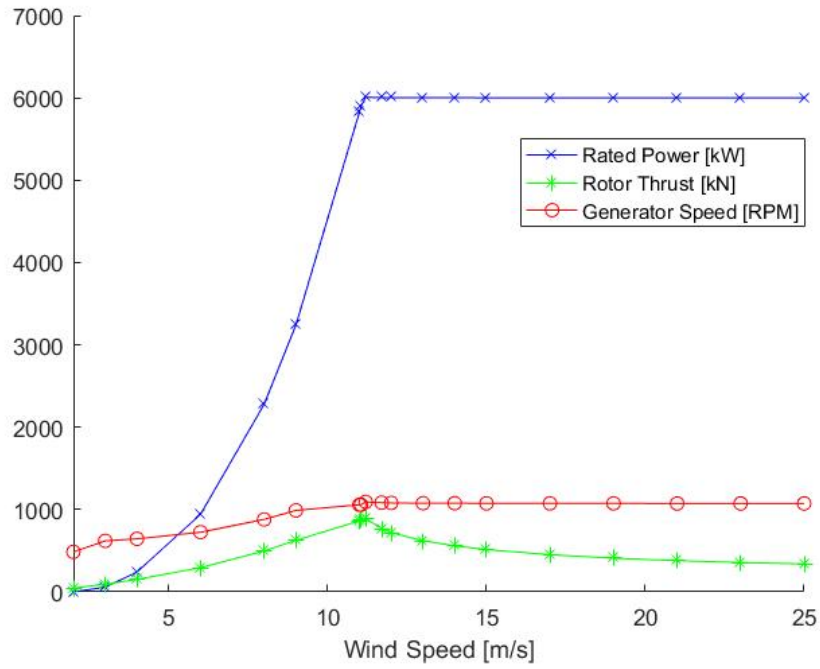


Figure 6.2: Rated power, rotor speed and thrust for 6 MW OO Star

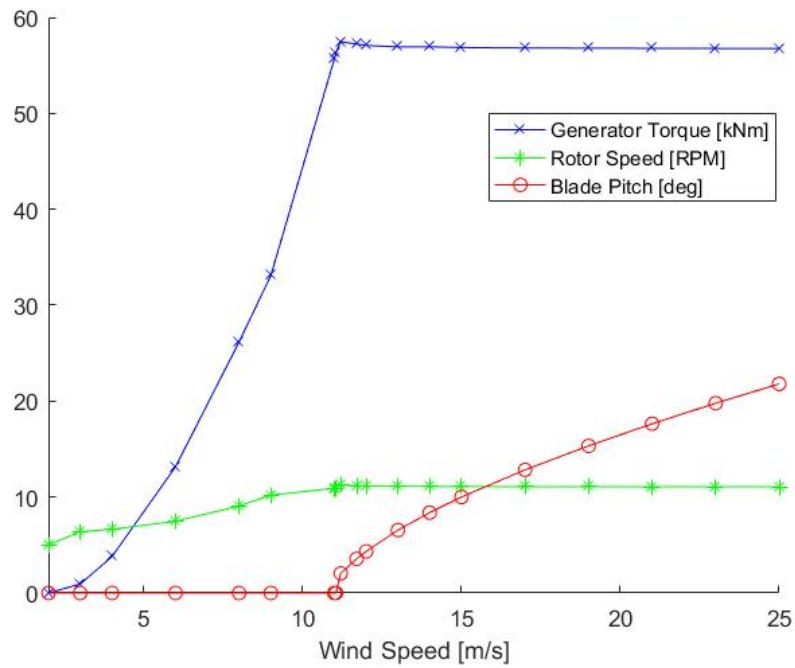


Figure 6.3: Generator torque, rotor speed and blade pitch for 6 MW OO Star

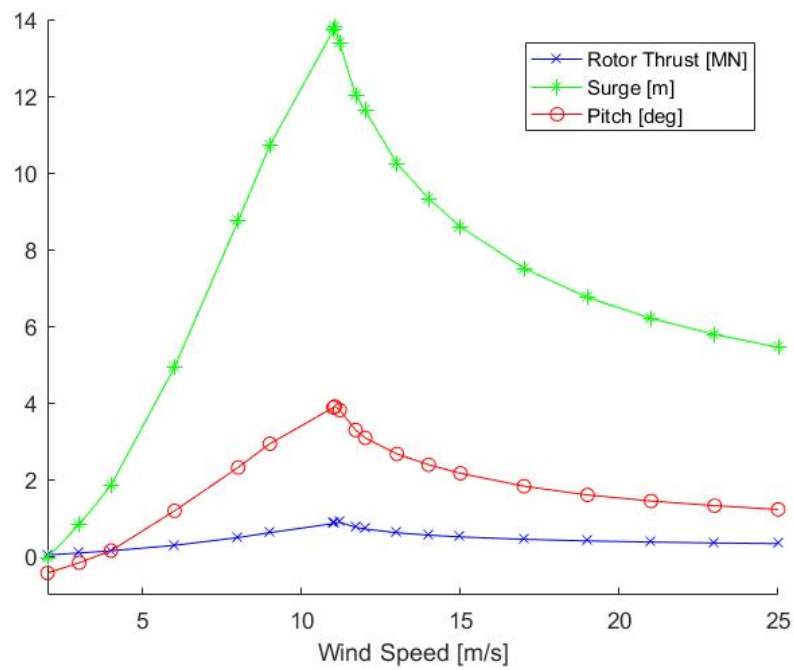


Figure 6.4: Rotor thrust, steady-state surge position and pitch angle for 6 MW OO Star



# Chapter 7

## Intermediate Water Depth Study

In this chapter, the response at three different intermediate water depth locations will be assessed and discussed.

### 7.1 Quadratic Transfer Function

The difference frequency quadratic transfer functions in surge and pitch are presented in 7.1. The full difference frequency excitation forces at different water depths and wave frequencies are presented as contour plots in Appendix B. The second-order forces are generally higher

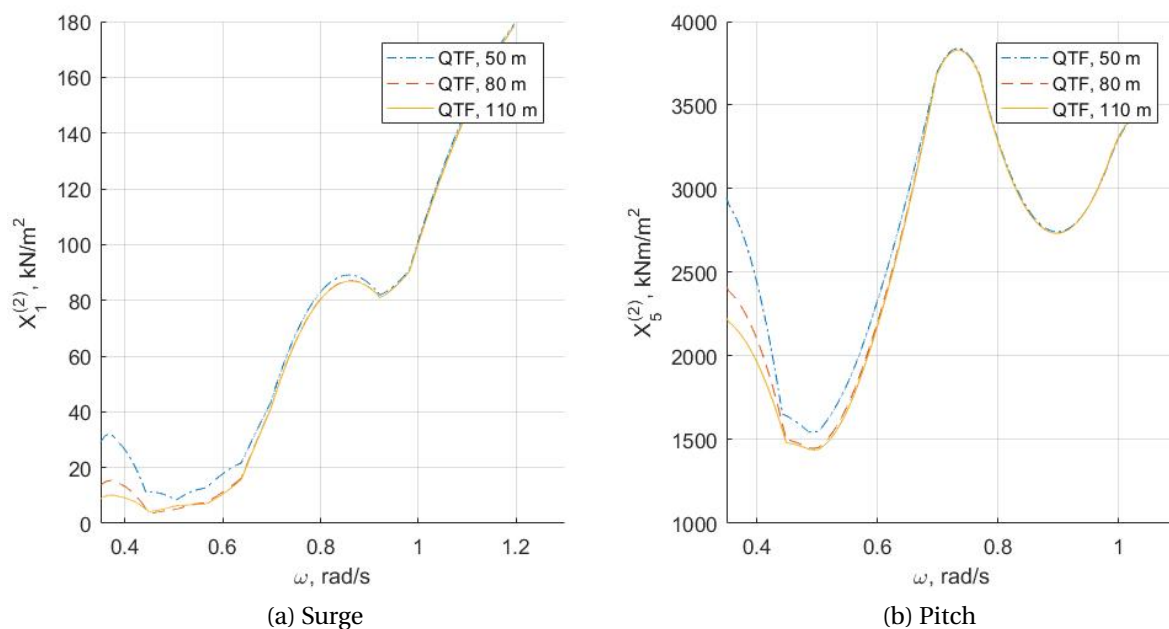


Figure 7.1: Quadratic transfer function in surge and pitch

for 50 metres in both surge and pitch. The difference is most obvious for low first order wave frequencies, but the depth differences are present for frequencies below  $\omega = 0.9$  in surge and  $\omega = 0.7$  in pitch. This corresponds to wave periods of 6.98 and 8.96 seconds, respectively. Thus, the depth are considered to affect the difference frequency excitation forces for all load cases in this thesis-

## 7.2 Viscous Force Coefficients

As explained in section 2.2, an iterative procedure was followed to establish the viscous force contribution in time-domain simulations. These forces were identified to be a correction to the potential theory  $A_{33}$  due to the presence of heave plates, as well as quadratic drag forces for the FWT hull and heave plates. Selected KC-numbers and their corresponding drag coefficients will therefore be presented in this section. In the following tabulated values, the KC-number according to equation 5.10 is presented for the FWT heave plates, pontoons and corner columns. The heave plate KC-number are found by using the standard deviation of the difference between the vertical velocity of the FWT and vertical wave particle velocity at  $z = 19.6$ . This depth correspond to the draft of the upper side of the heave plates. Similarly, the KC-number of the pontoon cross-section are defined by the standard deviation of the difference between FWT vertical velocity and the vertical wave particle velocity at  $z = 17$ . This is the wave particle velocity in the middle of the pontoon's cross-section. Finally, the surge KC-number at the water plane of the corner columns is presented. In the establishment of FWT quadratic drag coefficients, this value is found at different drafts of the corner column and central shaft. However, in order to make for a simple presentation, only one corner column KC-number and drag coefficient at  $z = 0$  is presented.

Table 7.1: KC-numbers,  $A_{33}^{corr}$  and drag coefficients for load case O.1

Depth	Heave Plate			Corner Column		Pontoon	
	KC	$A_{33}^{corr}$ [kg]	$C_D$	KC	$C_D$	KC	$C_D$
50 m	0.1572	141830	8.576	1.231	1.06	1.251	7.20
80 m	0.1580	142990	8.562	1.242	1.04	1.253	7.18
110 m	0.1580	142998	8.559	1.240	1.03	1.255	7.17

Table 7.2: KC-numbers,  $A_{33}^{corr}$  and drag coefficients for load case O.2

Depth	Heave Plate			Corner Column		Pontoon	
	KC	$A_{33}^{corr}$ [kg]	$C_D$	KC	$C_D$	KC	$C_D$
50 m	0.3359	246923	5.803	1.446	0.90	0.515	5.15
80 m	0.3382	248372	5.784	1.353	0.96	0.594	5.15
110 m	0.3382	248354	5.787	1.323	0.99	0.603	5.06



Table 7.3: KC-numbers,  $A_{33}^{corr}$  and drag coefficients for load case M.1

Depth	Heave Plate			Corner Column		Pontoon	
	KC	$A_{33}^{corr}$ [kg]	$C_D$	KC	$C_D$	KC	$C_D$
50 m	0.098	100950	10.86	0.540	2.008	0.182	12.25
80 m	0.098	101005	10.86	0.519	2.048	0.179	12.30
110 m	0.1038	104501	10.48	0.5247	2.037	0.191	12.01

Table 7.4: KC-numbers,  $A_{33}^{corr}$  and drag coefficients for load case M.2

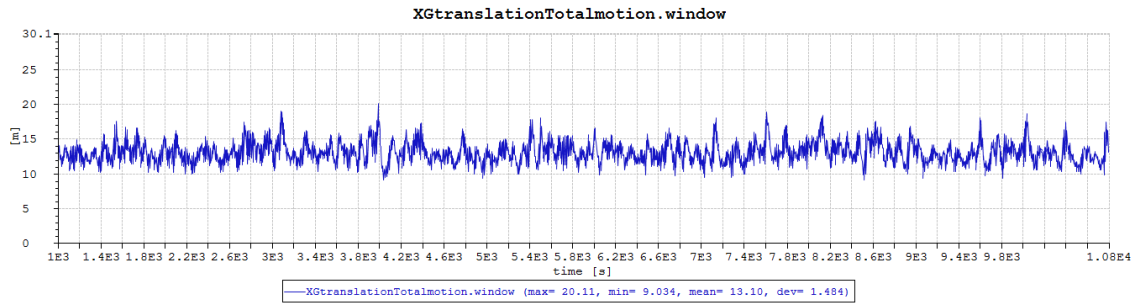
Depth	Heave Plate			Corner Column		Pontoon	
	KC	$A_{33}^{corr}$ [kg]	$C_D$	KC	$C_D$	KC	$C_D$
50 m	0.2140	171798	7.07	1.099	1.19	0.3957	7.667
80 m	0.2243	178135	6.9161	1.033	1.26	0.405	7.52
110 m	0.2353	184840	6.767	1.04	1.25	0.427	6.77

Table 7.5: KC-numbers,  $A_{33}^{corr}$  and drag coefficients for load case E.1 and E.2

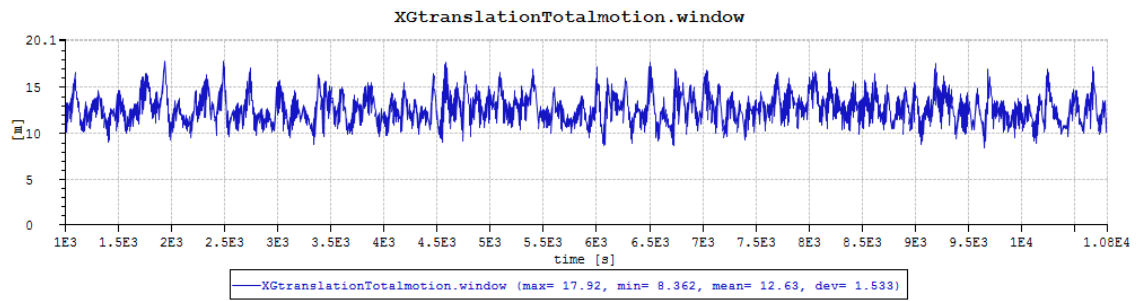
Depth	Heave Plate			Corner Column		Pontoon	
	KC	$A_{33}^{corr}$ [kg]	$C_D$	KC	$C_D$	KC	$C_D$
50 m [E.2]	0.2911	219240	6.16	1.538	0.852	0.534	5.771
80 m [E.1]	0.6337	432915	4.52	2.240	0.6926	1.085	2.96
110 m [E.1]	0.557	384702	4.75	2.173	0.694	0.991	4.753

### 7.3 Time Series

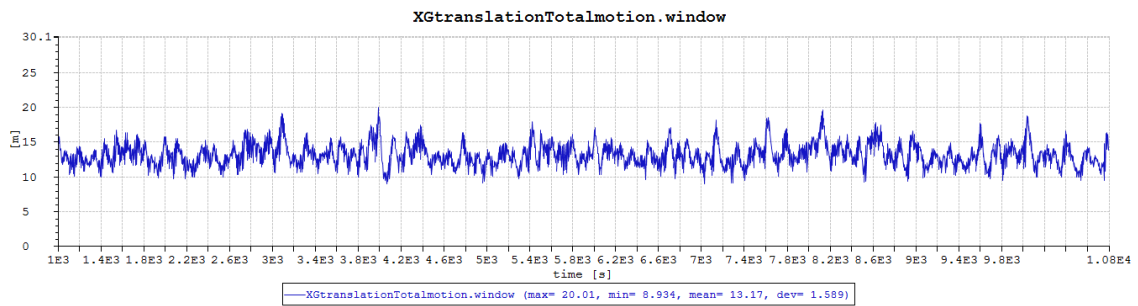
For illustrative reasons, the time-series of surge and pitch response are included in this section. The power output time-series are also presented, as these illustrate a large difference in the wind turbine performance between the two wind speeds. They M.1 and O.1 power output generally reflect the time-series of power output in the M.2 and O.2 load cases.



(a) 50 m

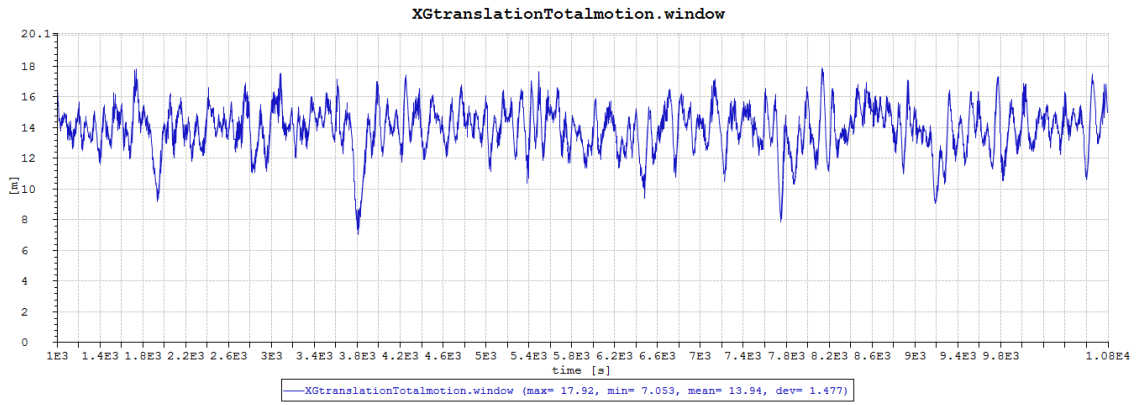


(b) 80 m

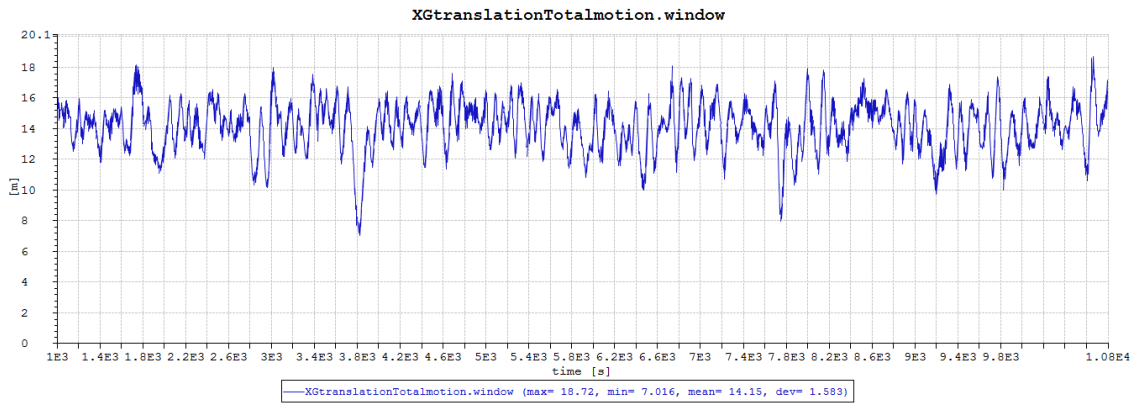


(c) 110 m

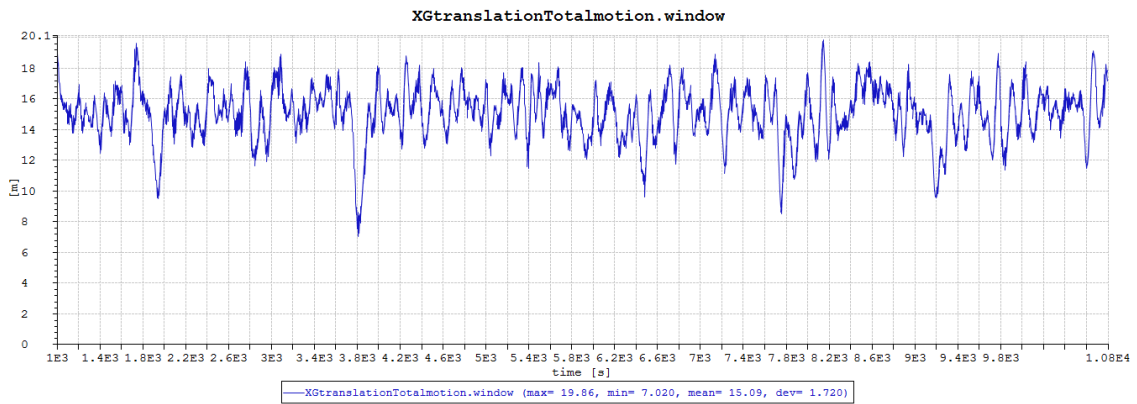
Figure 7.2: Surge response time-series for load case O.1



(a) 50 m

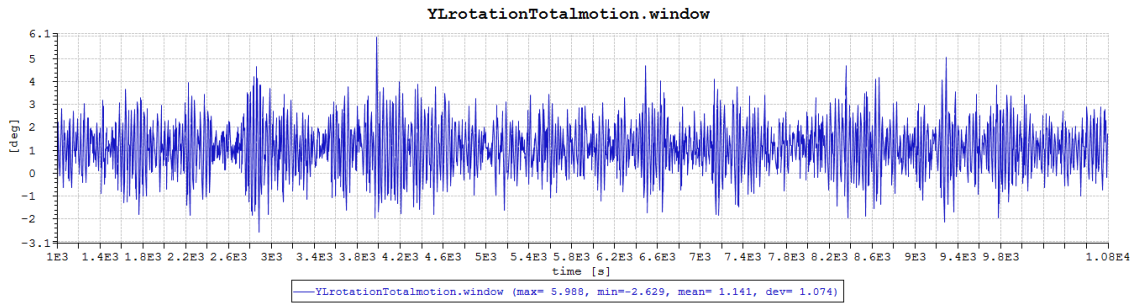


(b) 80 m

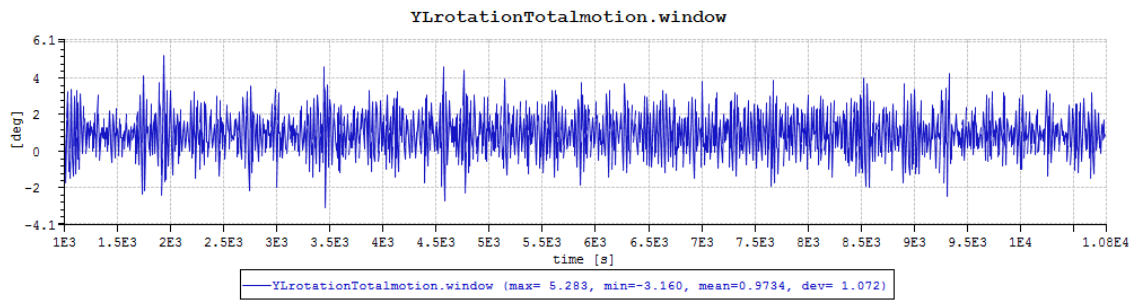


(c) 110 m

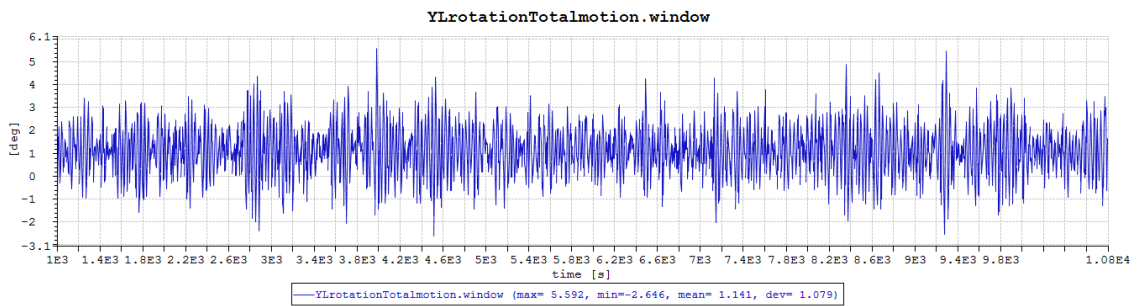
Figure 7.3: Surge response time-series for load case M.1



(a) 50 m

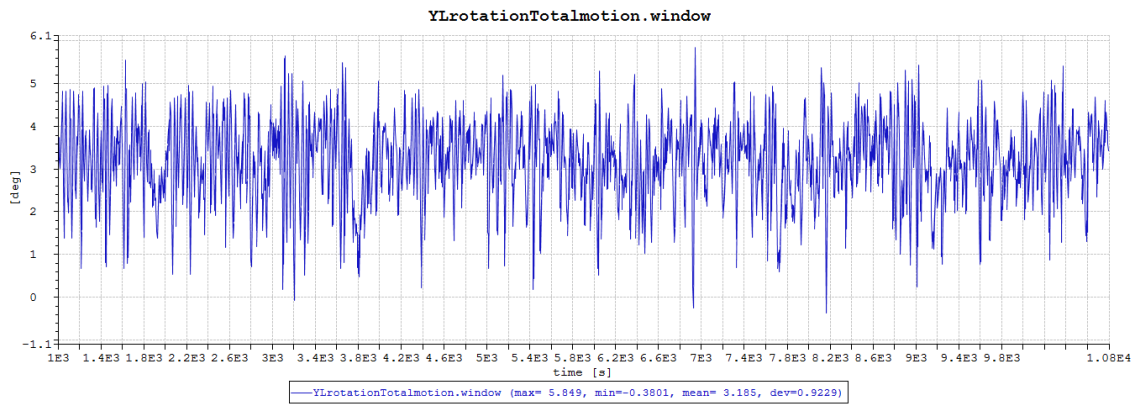


(b) 80 m

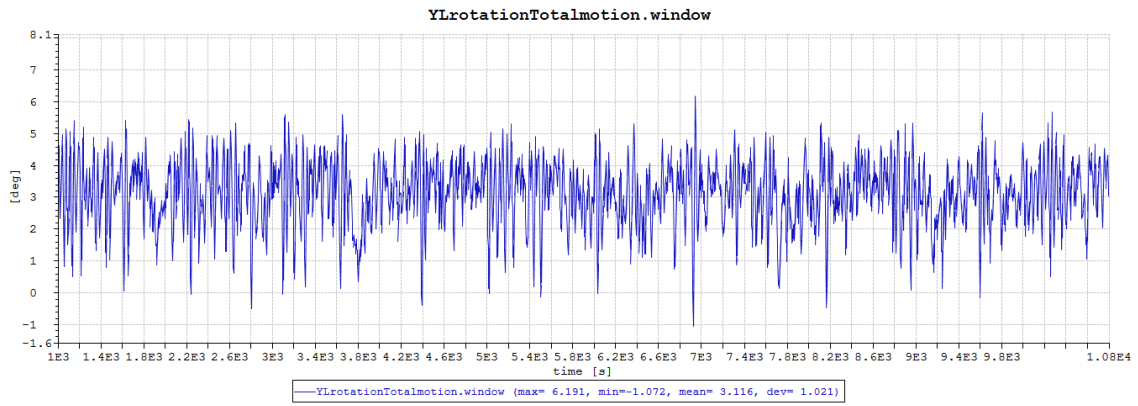


(c) 110 m

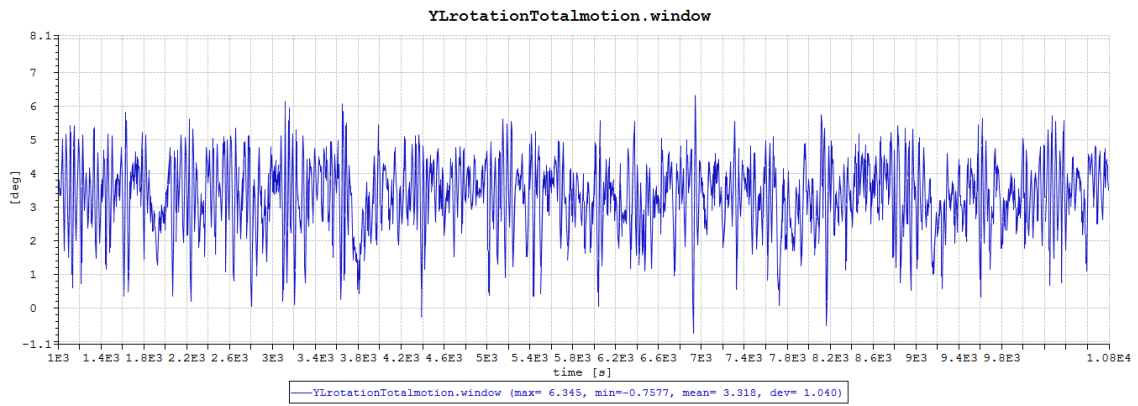
Figure 7.4: Pitch response time-series for load case O.1



(a) 50 m



(b) 80 m



(c) 110 m

Figure 7.5: Pitch response time-series for load case M.1

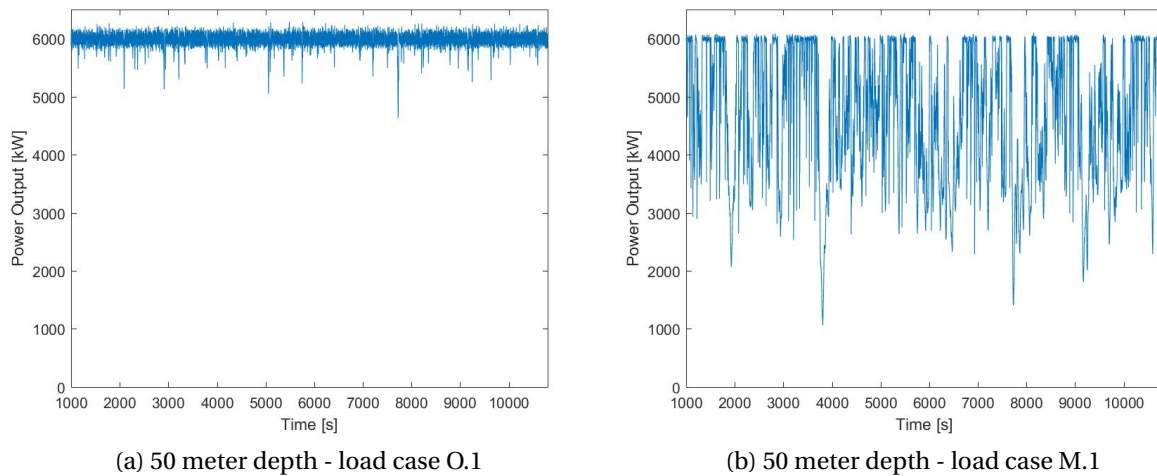


Figure 7.6: Power output for load cases O.1 and M.1

## 7.4 Model Behaviour in Intermediate Water Range

It was decided to present a statistical representation of the FWT response in order to analyze the water depth effects. Therefore, the standard deviation of surge, heave and pitch motion are presented in this section, in addition to the standard deviation of the wind turbine output. The first 1000 seconds of the sea state was taken out of the time-series, in order to allow for start-up time for the turbine. In addition to the standard deviation of the FWT motions, the max and min surge, pitch and heave position during the time-series are presented. Some trends were seen in the response in tables 7.6 and 7.7. In load cases M.1 and M.2, when the wind speeds were generally lower than the rated speed of the turbine, the turbine response was smaller in all DOF's as the water depth decreased. In case M.1, this was evidenced by a 9.6 % and 12.6 % difference in heave and pitch deviations, respectively. For case M.2, a load case characterized by higher waves, the differences were even more evident. In this case, the surge, heave and pitch standard deviations had a difference of 11.3 %, 22.4 % and 14.25 %, respectively, when comparing the results of the 50 m location and 110 m location. The surge and pitch deviations increased with water depth. This was also the case in heave. However, the differences between the response at 80 and 110 metres are small compared to the difference between 50 and 80 metres.

The opposite relation in surge and pitch was observed in load case O.2 and E.1. For load case O.2, which is defined by the 5<sup>th</sup>-percentile  $H_S$  at maximum operating wind speeds, the pitch and surge motions are larger in more shallow water. When assessing the results for the heave response, it was observed that the standard deviations decreased with water depth, as was the case in load cases M.1 and M.2.

In case E.1, the pitch response standard deviation at 80 metres was 4.5 % larger than at 110 metres. The differences were larger for surge and heave motions, with a 16.3 and 6.9 % difference, respectively. This was the only load case in which the heave motion was significantly larger in

Table 7.6: Standard deviation of FWT response

Case O.1				
Depth	Surge [m]	Heave [m]	Pitch [deg]	Turbine Power Output [kW]
50 m	1.4844	0.54509	1.0744	117.24
80 m	1.5334	0.6112	1.0741	114.06
110 m	1.5894	0.61371	1.0792	105.72
Case O.2				
Depth	Surge [m]	Heave [m]	Pitch [deg]	Turbine Power Output [kW]
50 m	2.1506	0.94797	1.619	122.24
80 m	2.0909	0.926	1.5882	117.05
110 m	2.0706	0.97398	1.5458	114.70
Case M.1				
Depth	Surge [m]	Heave [m]	Pitch [deg]	Turbine Power Output [kW]
50 m	1.4774	0.22205	0.92295	1159.7
80 m	1.5825	0.24343	1.0207	1153.8
110 m	1.7202	0.24337	1.0396	1154.2
Case M.2				
Depth	Surge [m]	Heave [m]	Pitch [deg]	Turbine Power Output [kW]
50 m	1.9054	0.505	1.035	1187.4
80 m	1.979	0.61599	1.156	1172.3
110 m	2.12	0.618	1.1825	1176.9
Case E.1/E.2				
Depth	Surge [m]	Heave [m]	Pitch [deg]	Turbine Power Output [kW]
50 m	1.9167	0.90591	2.1187	-
80 m	3.3335	1.9123	3.6526	-
110 m	2.8668	1.7875	3.494	-

the 80 meter location than the 110 meter location. The response for case E.2, which were assessed only for the location at 50 metres, was substantially smaller than the other extreme load case. The feasibility of the 6 MW OO-Star Wind Floater in depths around 50 metres should be viewed in light of this, as the lower environmental loads at such Northern Sea bathymetry implicate that the response generally would be smaller.

For load case O.1, the standard deviations of the FWT response in surge and heave increased with water depth. The FWT pitch motions showed roughly the same deviations. Thus, the surge and heave motions seemed to follow the same trends as the low wind speed cases.

Based on the operational load cases, the FWT heave response was smaller in more shallow water depths. The pitch motions decreased as the water depth decreased in the low wind speed load cases M.1 and M.2, while the opposite relation was seen in load cases O.2 and E.1. The surge motion followed the same trend. The wind turbine output was generally similar for each water depth within each load case. However, for the lower wind speed cases M.1 and M.2, the standard deviation was around ten times larger.



Table 7.7: Extreme values of FWT response

Case O.1				
Depth	Max/Min	Surge [m]	Heave [m]	Pitch [deg]
50 m	Max	20.111	2.2123	5.9878
	Min	9.0343	-1.7887	-2.629
80 m	Max	17.918	2.626	5.2829
	Min	8.362	-2.2821	-3.1599
110 m	Max	20.013	2.4251	5.592
	Min	8.9343	-1.8458	-2.6461
Case O.2				
Depth	Max/Min	Surge [m]	Heave [m]	Pitch [deg]
50 m	Max	21.133	3.5669	7.0112
	Min	6.1187	-4.2112	-4.622
80 m	Max	20.762	3.5329	6.885
	Min	5.7053	-3.0135	-5.4544
110 m	Max	22.04	4.0339	6.9964
	Min	6.8405	-3.8673	-4.1747
Case M.1				
Depth	Max/Min	Surge [m]	Heave [m]	Pitch [deg]
50 m	Max	17.919	0.75947	5.849
	Min	7.0526	-0.99257	-0.38014 2
80 m	Max	18.723	0.77311	6.1914
	Min	7.0164	-1.1356	-1.0719
110 m	Max	19.863	0.81772	6.3447
	Min	7.0204	-1.0528	-0.75772
Case M.2				
Depth	Max/Min	Surge [m]	Heave [m]	Pitch [deg]
50 m	Max	22.554	2.0476	6.719
	Min	6.052	-1.698	0.7269
80 m	Max	21.863	2.6393	6.727
	Min	7.3478	-2.3394	-1.418
110 m	Max	23.486	2.370	7.367
	Min	5.8904	-1.943	2.018
Case E.1/E.2				
Depth	Max/Min	Surge [m]	Heave [m]	Pitch [deg]
50 m	Max	28.768	2.728	13.009
	Min	15.718	-3.2253	-1.293
80 m	Max	40.117	7.5125	24.875
	Min	11.486	-6.8835	-3.9192
110 m	Max	47.93	6.7417	23.073
	Min	26.604	-7.0439	-2.5623

The maximum and minimum turbine motions was valuable in evaluating whether the FWT

was within its operating limits, as well as for evaluation in the ULS. The maximum surge at all operational states was within the linear mooring line behaviour for the depths of 80 and 110 metres, as seen in figure 6.1. For the 50 metre location, where the non-linear behaviour of the mooring line tension began at offsets  $\approx 18$  metres, non-linear behaviour was present in all operational load cases except M.1. This evidenced the mooring challenges in more shallow water, as explained in Section 5.7. Thus, it is noted that mooring design is a challenge in intermediate depth. It is recommended that further studies with a state-of-the-art mooring configuration should be carried out at all water depths.

In order to evaluate the ULS of the mooring design, the maximum surge position in the 50, 80 and 110 metre extreme cases were compared to the static tension in the mooring lines from figure 6.1. It was observed that the static tension at all water depths were within the breaking load of the mooring line material. It was therefore concluded that the proposed mooring system holds within the boundaries set in section 5.7. However, it should be noted that both fatigue life and dynamic tension in the mooring lines should be investigated for a full verification.

The maximum tilt in operational condition for the 6 MW OO Star was defined as  $6^\circ$  by Dr. Techn. Olav Olsen AS. This tilt angle was exceeded for every operational load case except case O.1 and the 50 m depth in location M.1. For regular joint distributions of wind speeds above rated speed, the turbine performance was expected to be within the operational limits, as the control system induced positive pitch damping (Figure 6.4). However, the large pitch motions at wind speeds below the rated wind could be problematic.

The blade-pitch control system utilized in this thesis was a modified version of a land-based control system. An alternative to ensure stable operation at low wind speeds could be to develop a control system with blade-pitch controlling also at wind speeds below the rated speed. As observed in the time-series of the turbine output in the M.1 load case (figure 7.3), there were several large drops in the turbine performance. This was also seen in the standard deviations of the turbine output, which were in the order of 10 times larger for M.1/M.2 when compared to the O.1/O.2 load cases. By aiming for a lower average output at wind speeds below rated speed, the control system could reduce the aerodynamic thrust and possibly reduce the turbine pitch motions to be within the operational limits.

## 7.5 Loads in Intermediate Water Range

In order to identify why the FWT response varied between the load cases and water depths, the hydrodynamic and aerodynamic loads on the turbine have been analyzed. These will be presented by their standard deviations in this section. Similar to the presentation of the turbine motions, the first 1000 seconds were taken out of the time-series. One trend that seemed quite stable was the small wave drift contribution. The standard deviation of the mean wave drift was around 1 % of the first order wave excitation in surge for all load cases. However, it was observed that the contribution from the mean wave drift forces were of the same order as the turbine thrust. Thus, they should be included in FWT analysis, even though the load contribution is small compared to e.g. first order wave excitation forces.

Table 7.8: Standard deviation of FWT loads - Case 0.1  
50 m

	Surge [kN]	Heave [kN]	Pitch [kNm]
1. Order Wave	7856.1	4517.6	108810
Wave Drift	72.2		
QTF	274.6	259.7	9587.7
Aerodynamic	91.77	-	4074.3

80 m

	Surge	Heave	Pitch
1. Order Wave	7622.3	4987.2	109830
Wave Drift	71.6		
QTF	249.91	255.6	8986
Aerodynamic	91.70	-	4110

50 m

	Surge	Heave	Pitch
1. Order Wave	7549.0	5072.2	110050
Wave Drift	70.2		
QTF	236.65	255.65	8769.1
Aerodynamic	91.00	-	4080

Table 7.8 present the loads for load case O.1. The difference frequency excitation forces increased with shallow water, which is in agreement with the discussion in Section 2.4. This trend was observed for both the surge, heave and pitch DOF. The first order excitation forces decreased with depth for the heave motion, while the opposite trend was observed in surge. The difference-frequency force contribution was less than 10 % of the first order in all water depths and DOFs. Although the first order excitation had significantly higher values when compared to the other force components, it was observed that the second-order difference frequency effects had a bigger standard deviation than the aerodynamic loads.

The excitation forces in pitch corresponded well with the standard deviation of the FWT pitch motion in case O.1. Neither force component were considered to change drastically between the water depths. This was reflected well in the response of the FWT, which were of a similar magnitude for all water depths in load case O.2.

A correlation between the first order excitation loads and the response was observed in heave. The response at the depth of 50 metres was smaller than at the two other water depths, whom experienced relatively similar loads and responses. In surge, the FWT motions were significantly smaller at the depth of 50 metres, while all surge force components increased as the water depth decreased.

Table 7.9: Standard deviation of FWT loads - Case 0.2  
50 m

	Surge [kN]	Heave [kN]	Pitch [kNm]
1. Order Wave	10481	4944.4e	132360
Wave Drift	79.331		
QTF	568.42	500.34	18303
Aerodynamic	98.44	-	4210
80 m			
	Surge [kN]	Heave [kN]	Pitch [kNm]
1. Order Wave	9993	5654.1	132810
Wave Drift	78.978		
QTF	435.02	410.5	15431
Aerodynamic	94.98	-	4180
110 m			
	Surge [kN]	Heave [kN]	Pitch [kNm]
1. Order Wave	9726.9	5848.2	131760
Wave Drift	76.794		
QTF	385.16	392.93	14182
Aerodynamic	95.51	-	4210

In case O.2, the difference frequency excitation forces had a significantly larger contribution to the FWT loads. The depth effects on the slow drift force contribution were evident, as there were a 47.5 %, 27.5 % and 29 % increase in the surge, heave and pitch diff.-freq.-excitation force, respectively. The higher peak period in this sea state was considered the most dominant factor for this, as it increased the number of low-frequency waves. The frequency-domain difference-frequency QTF show a clear dependency of depth for wave periods between 14 and 18 seconds (Figure 7.1). This trend was preserved in the time-domain analysis.

In pitch, the first order excitation forces and aerodynamic moment were relatively similar in each water depth. The pitch response, however, was generally larger as the water depth decreased. This was also the case for the difference-frequency excitation forces. Thus, it was concluded that the second-order forces was important for the pitch response. It should at this point be noted that the establishment of the difference-frequency QTF was shown to over-predict the pitch response in large wave periods. On the other hand, the study by You (2012) proved that numerical calculations of difference-frequency forces under-predict the results. The numerical accuracy of the procedure in this thesis should thus be further validated.

For the heave motion, the first order excitation force had a significantly lower standard deviation for the 50 meter load case (14.2 % when compared to the depth of 80 metres). The pitch first order excitation force in surge increased with decreasing water depth. In general, the first order excitation forces behave relatively similar from depth to depth in case O.1 and O.2.

Table 7.10: Standard deviation of FWT loads - Case M.1  
50 m

	Surge [kN]	Heave [kN]	Pitch [kNm]
1. Order Wave	3902.4	2467	58465
Wave Drift	28.059		
QTF	79.102	79.322	2751.9
Aerodynamic	112.95	-	1860
80 m			
	Surge [kN]	Heave [kN]	Pitch [kNm]
1. Order Wave	3807	2596.4	58586
Wave Drift	27.714		
QTF	75.025	79.004	2636.2
Aerodynamic	112.63	-	1870
110 m			
	Surge [kN]	Heave [kN]	Pitch [kNm]
1. Order Wave	3821.2	2630.4	59356
Wave Drift	27.431		
QTF	73.564	79.801	2628
Aerodynamic	112.37	-	1870

The difference-frequency excitation forces had a lower significance in load case M.1. In general, this was a more complex load picture to analyze, as the relative difference in pitch and surge first order excitation forces were small compared to the other cases. The second-order effects had a relatively small contribution to the total load case, with a standard deviation below 2.5 % for all DOFs and water depths.

The hydrodynamic forces in load cases M.1 and M.2 generally followed the same trends. There was an increase in the first order excitation force in heave and pitch from 50 m to 80 m, with the former having the largest deviations from depth to depth. The difference-frequency contribution was more significant in this load case when compared to M.1, as the second order pitch standard deviation was  $\approx 9\%$  of the first order excitation force.

Table 7.11: Standard deviation of FWT loads - Case M.2  
50 m

	Surge [kN]	Heave [kN]	Pitch [kNm]
1. Order Wave	7869.5	4516.2	108940
Wave Drift	72.439		
QTF	276.77	259.5	9616.6
Aerodynamic	118.66	-	1.91e+03
80 m			
	Surge [kN]	Heave [kN]	Pitch [kNm]
1. Order Wave	7635.6	4986	109960
Wave Drift	71.866		
QTF	251.79	255.45	9010.4
Aerodynamic	116.76	-	1910
110 m			
	Surge [kN]	Heave [kN]	Pitch [kNm]
1. Order Wave	7562.2	5070.8	110180
Wave Drift	70.435		
QTF	238.61	255.46	8795.5
Aerodynamic	116.50	-	1920

Table 7.12: Standard deviation of FWT loads - Case E.1/E.2  
50 m

	Surge [kN]	Heave [kN]	Pitch [kNm]
1. Order Wave	11602	7405.4	171810
Wave Drift	208.4		
QTF	632.66	604.82	21555
Aerodynamic	116.50	-	1.92e+03
80 m			
	Surge [kN]	Heave [kN]	Pitch [kNm]
1. Order Wave	15790	8069	200930
Wave Drift	156.56		
QTF	1379.9	1206.1	44437
Aerodynamic	272.72	-	2787
50 m			
	Surge [kN]	Heave [kN]	Pitch [kNm]
1. Order Wave	15194	8426.6	198080
Wave Drift	152.07		
QTF	1109	1042.9	39602
Aerodynamic	274.85	-	2789

In the extreme cases, the importance of difference-frequency loads at high first order periods were evident. In the 80 m location, the pitch second-order force had a significance of 22 % when compared to the first order excitation force. The slow-drift excitation force standard deviation

was also 13 % higher for the pitch motion at 80 metres, compared to the standard deviation at a depth of 110 metres.

It was still observed that the first order excitation forces in heave are considerably lower in the shallow water locations. This relation has been true for all load cases.

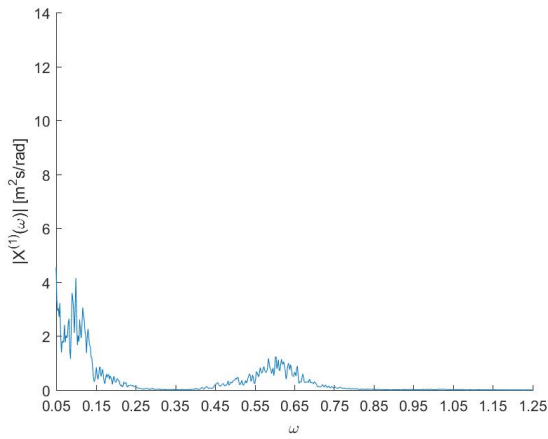


## 7.6 Global FWT Response Spectrum

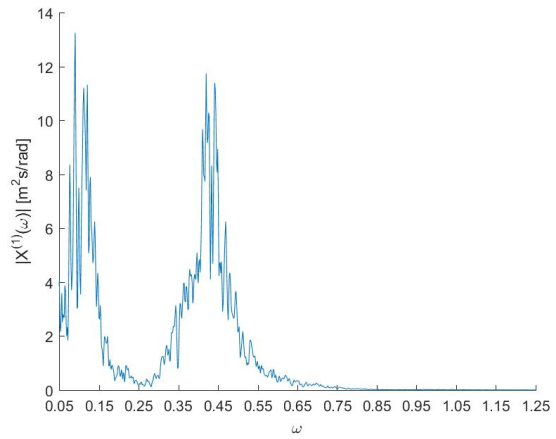
In order to assess the contribution from the aerodynamic and hydrodynamic loads, the power spectral density of the loads and FWT response are presented in this section. The spectral densities have been calculated using Welch's power spectral density estimator, which is a built-in Matlab function. The frequency of the peak response in heave and pitch are also presented. As the extreme load case was used to assess the ULS of the mooring configuration, the power spectral density of surge hydrodynamic loads and motions have been presented in this section. For the remaining cases, this information can be reviewed in Appendix C. Due to the big focus on heave plate performance throughout the thesis, it was decided to concentrate on this DOF in this discussion.

Additionally, the pitch response of the FWT has been a focus. As discussed in section 1.2, the fatigue life of components such as the tower shaft is sensitive to high pitch motions on a semi-submersible FWT. Because of this, smaller pitch response and lower deviations in this DOF are in the this discussion assumed to have a positive effect on the fatigue life of the FWT.

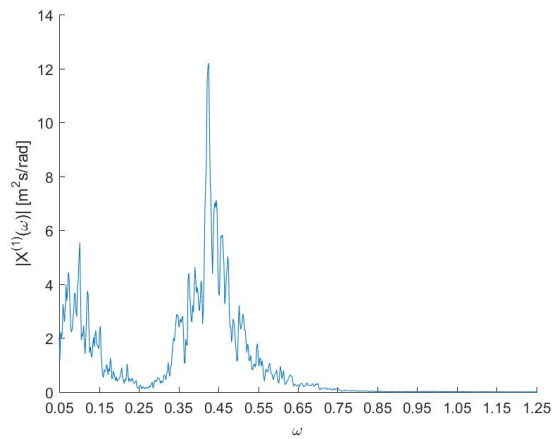
7.6.1 Case E



(a) 50 m

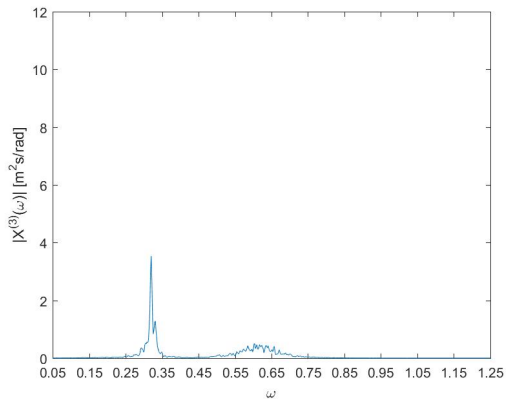


(b) 80 m

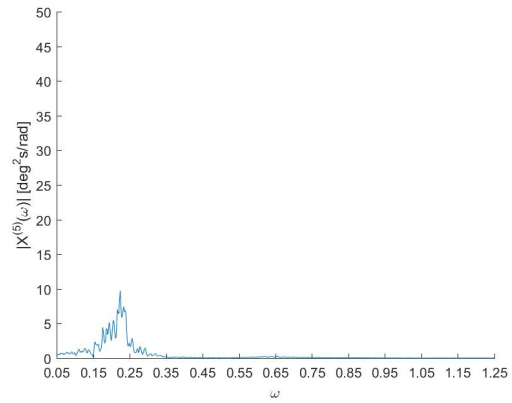


(c) 110 m

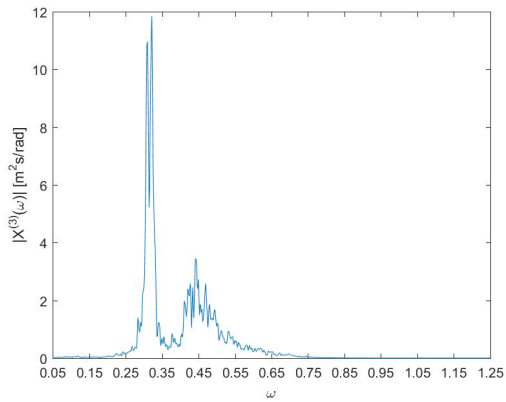
Figure 7.7: Surge response PSD, load case E.1/E.2



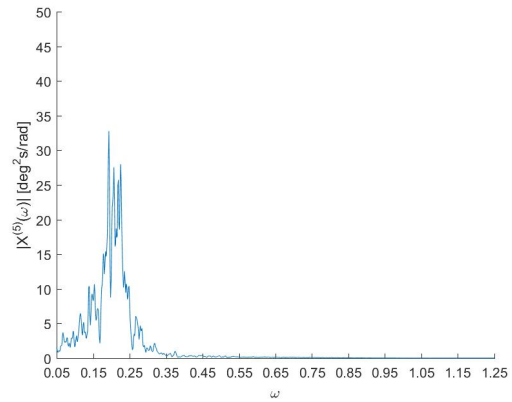
(a) 50 m



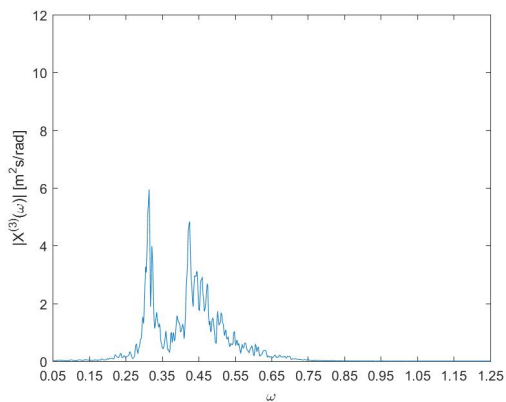
(b) 50 m



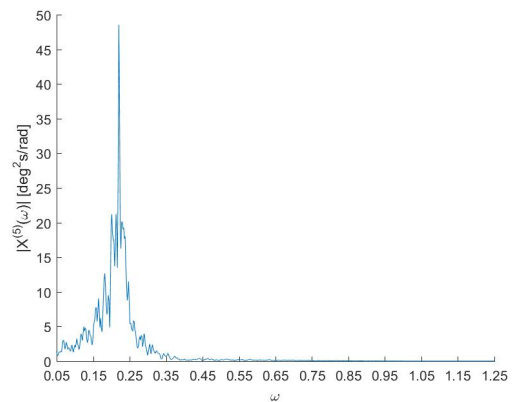
(c) 80 m



(d) 80 m



(e) 110 m



(f) 110 m

Figure 7.8: Heave and pitch response PSD, load case E.1/E.2

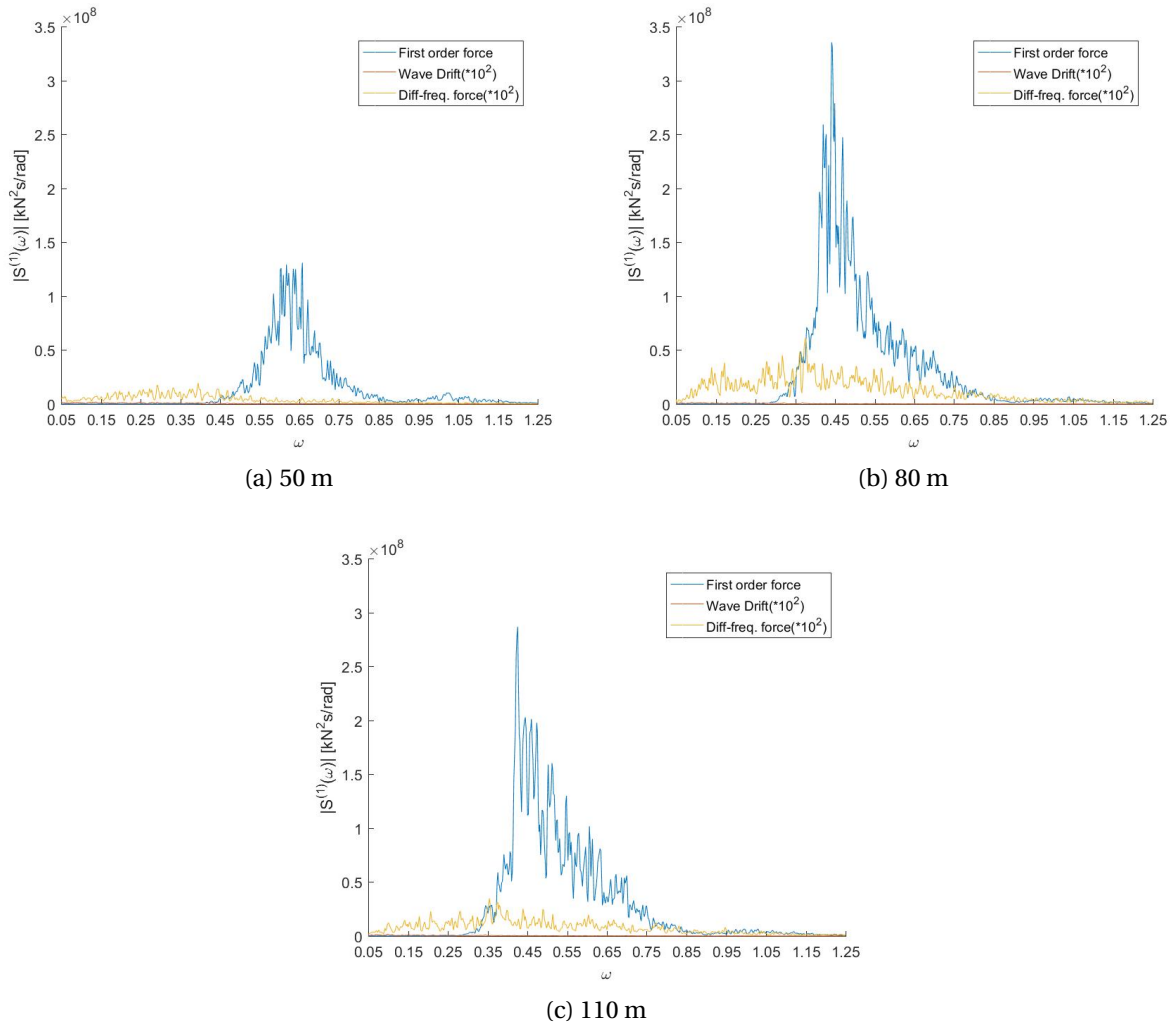


Figure 7.9: Surge first order, mean drift and difference Frequency loads, PSD for load case E.1/E.2

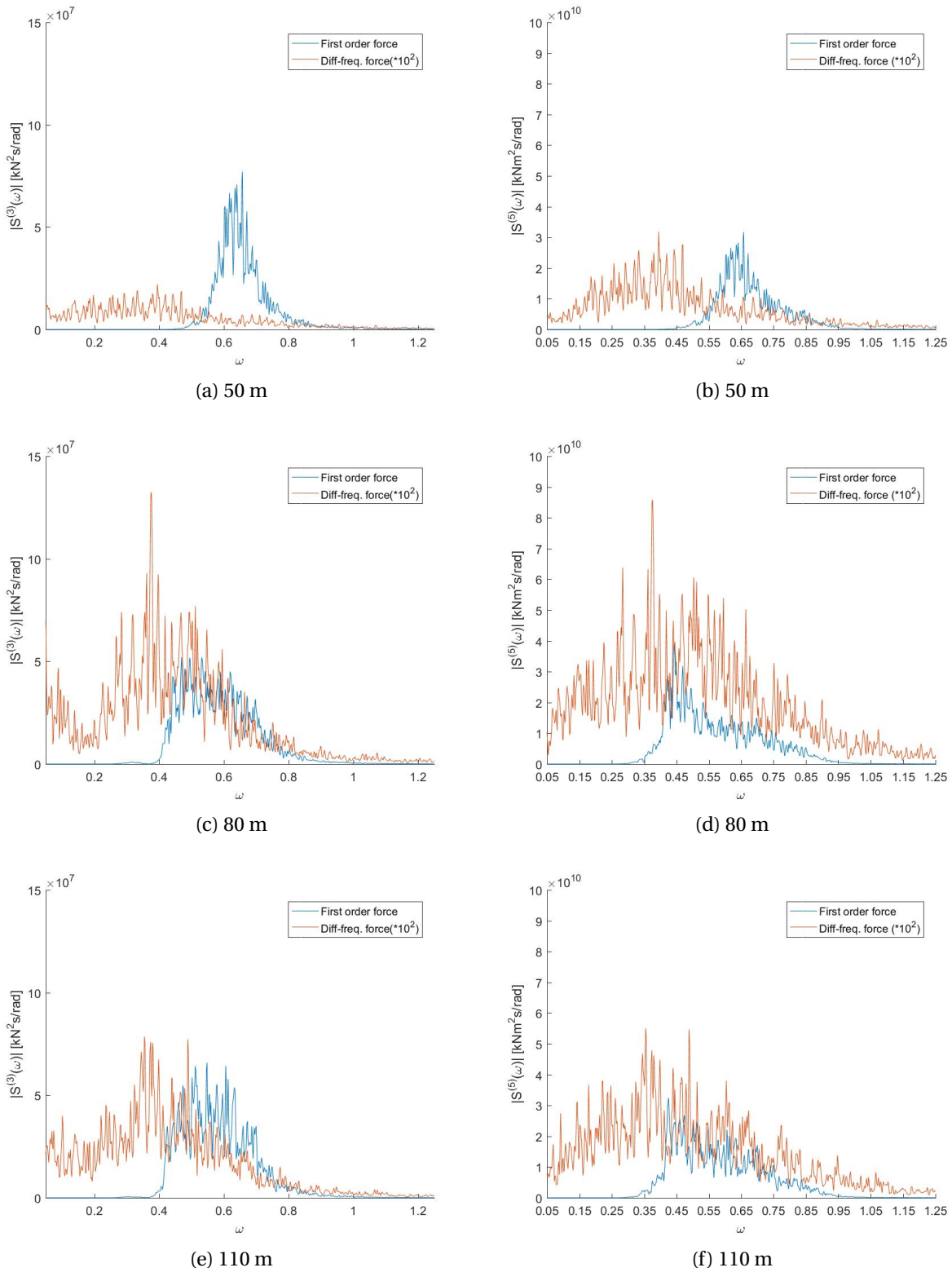


Figure 7.10: Have and pitch first order and difference-frequency loads, PSD for load case E.1/E.2

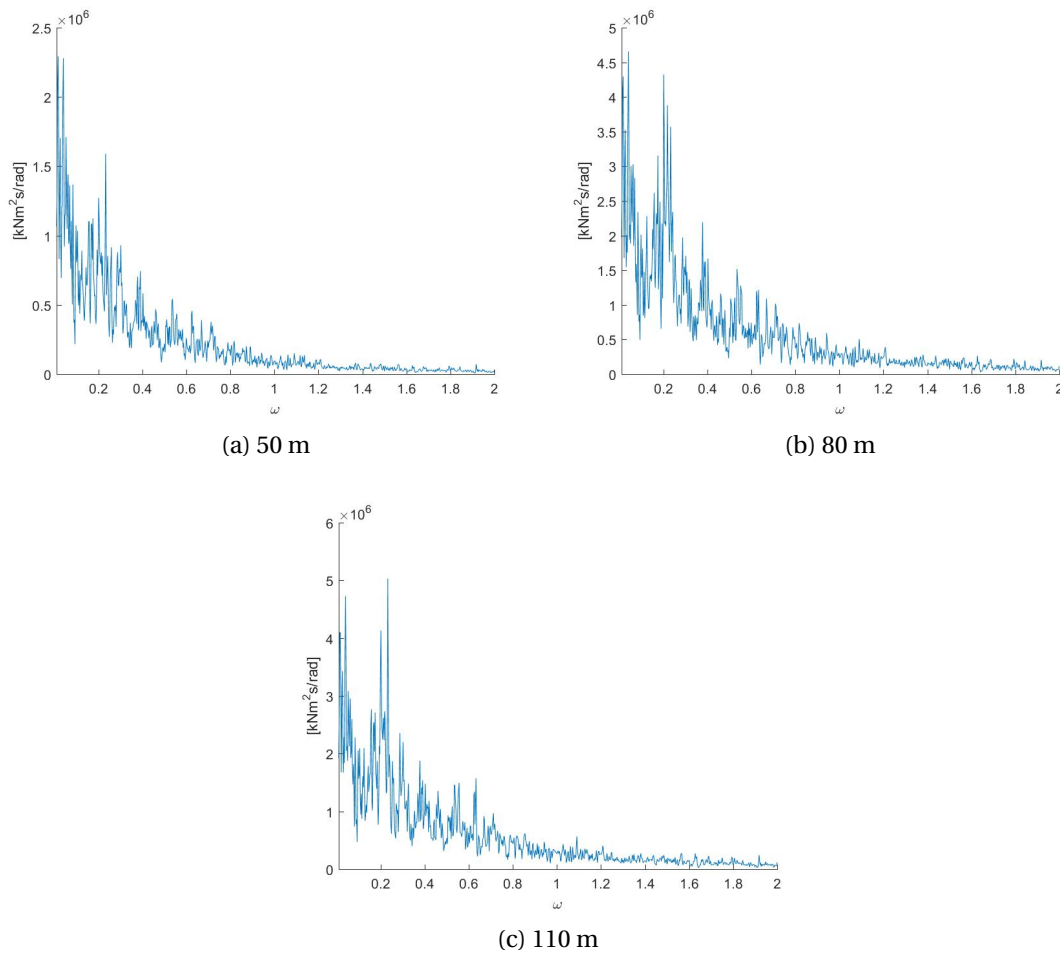


Figure 7.11: Aerodynamic pitch moment PSD, load case E.1/E.2

From investigating the power spectral densities of the hydrodynamic loads on the FWT, it was observed that the difference-frequency contribution can not be neglected. Figure 7.10 show that these second-order effects excite loads around the natural frequency in heave and pitch, in addition to having a considerable contribution in regular wave frequencies ( $> 10\%$  of the first order contribution).

The higher magnitude of difference-frequency excitation forces in more shallow water is illustrated in Figure 7.10. As the 50 meter location was subject to different extreme environmental loads, the relative values between the depths of 80 and 110 metres will be the main focus in this section. The power spectral density had higher values in the 80 meter case for all presented DOF's, which resulted in a more dense response around the natural frequency in surge and heave. In pitch, the FWT experienced larger maximum tilts which resulted in a higher peak around the natural frequency. However, the standard deviation of the response was larger also in this DOF. Because of this, it was concluded that the OO Star would experience larger ULS responses in 80 metres in all DOF's.

The power spectral densities illustrate that the difference-frequency excitation forces were

higher in all DOF's in 80 metres. This was considered to induce more resonance behaviour of the FWT, and the limited water depth are therefore concluded to present more difficult design parameters for the ULS. As it was previously discussed how numerical estimations under-predict the difference frequency forces in shallow water, it is concluded that depth effects on this force contribution have to be accounted for in an appropriate manner in the intermediate water range. Consequently, experiments and full scale model data are recommended to quantify the second-order forces in this range.

The FWT response at 50 metres was considerably smaller than the other locations. This was expected, as the most relevant North Sea location for this water depth comes with lower wind and wave data values. Even though the slow-drift motions were expected to increase in more shallow water, the geographic location of such water depths restricted the total motions. Therefore, based on these results, the OO-Star Wind Floater concept was considered more feasible at 50 metres as the wave loads at such sites excite forces of smaller magnitudes than e.g. the northern North Sea.

It was observed that the surge motion at 80 metres had a smaller maximum value than at 110 metres. However, the standard deviation was higher in this water depth, and the power spectral density was more dense, especially around the natural frequency in surge. This relation was attributed to the smaller suspended length of the mooring lines. In figure 7.9, the power spectral density of both the first order and difference-frequency excitation forces was higher in the 80 metre location, and this effect was considered to be the cause of the increased standard deviation of surge motions.

Based on the above discussion, the FWT motions in shallow water are more complex. This effect is considered to affect both fatigue life and cause more complex mooring design parameters. The results of this thesis indicate an increased contribution from difference-frequency excitation forces as the water depth decreases. It is also considered plausible that the numerical calculations under-estimate these second-order effects, and that the actual slow drift forces have a considerably higher contribution to the FWT response. Thus, further experimental testing is required to fully map out the response in the intermediate water depth range.

7.6.2 Case O1

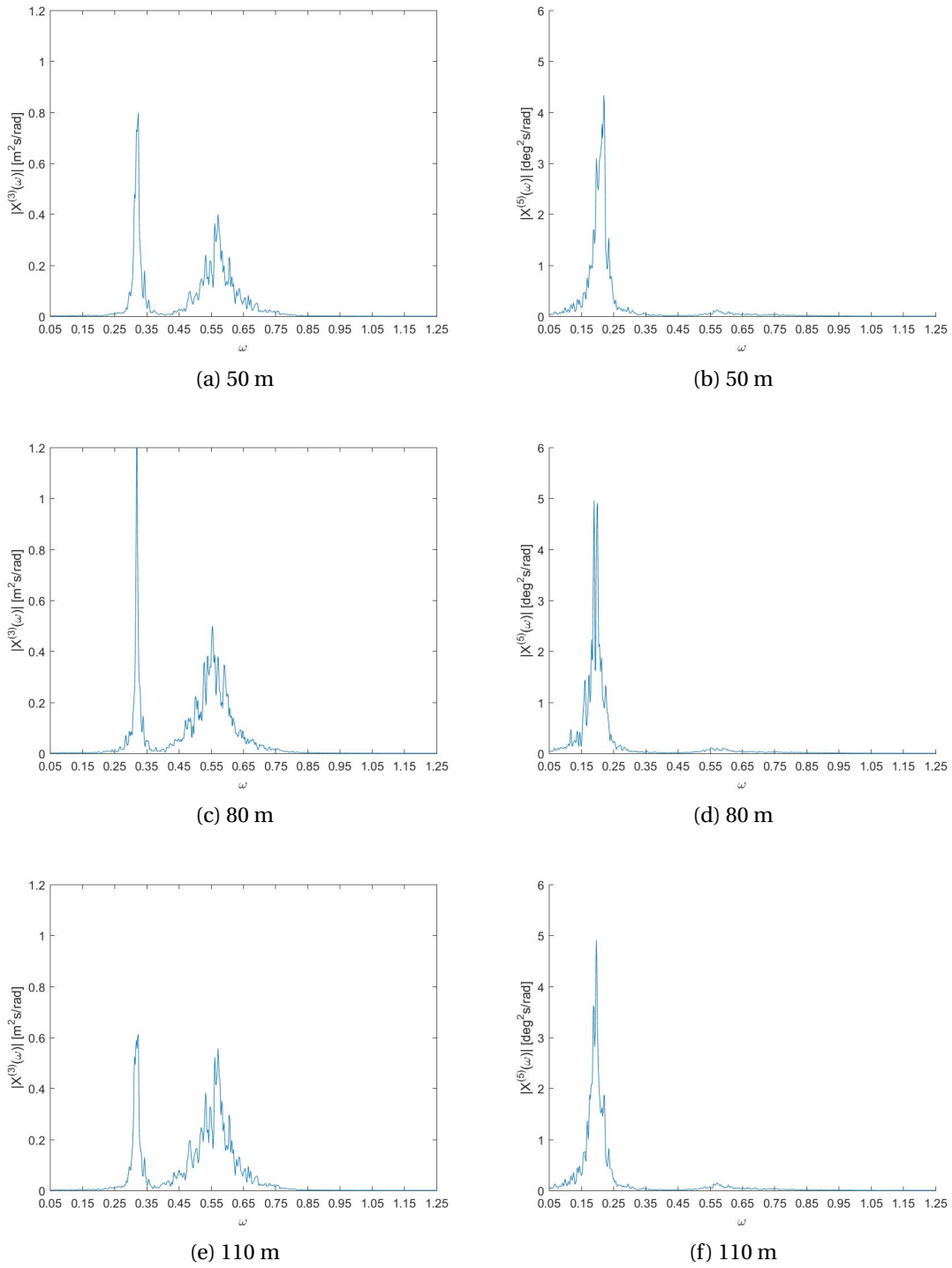


Figure 7.12: Heave and pitch response PSD, load case O.1



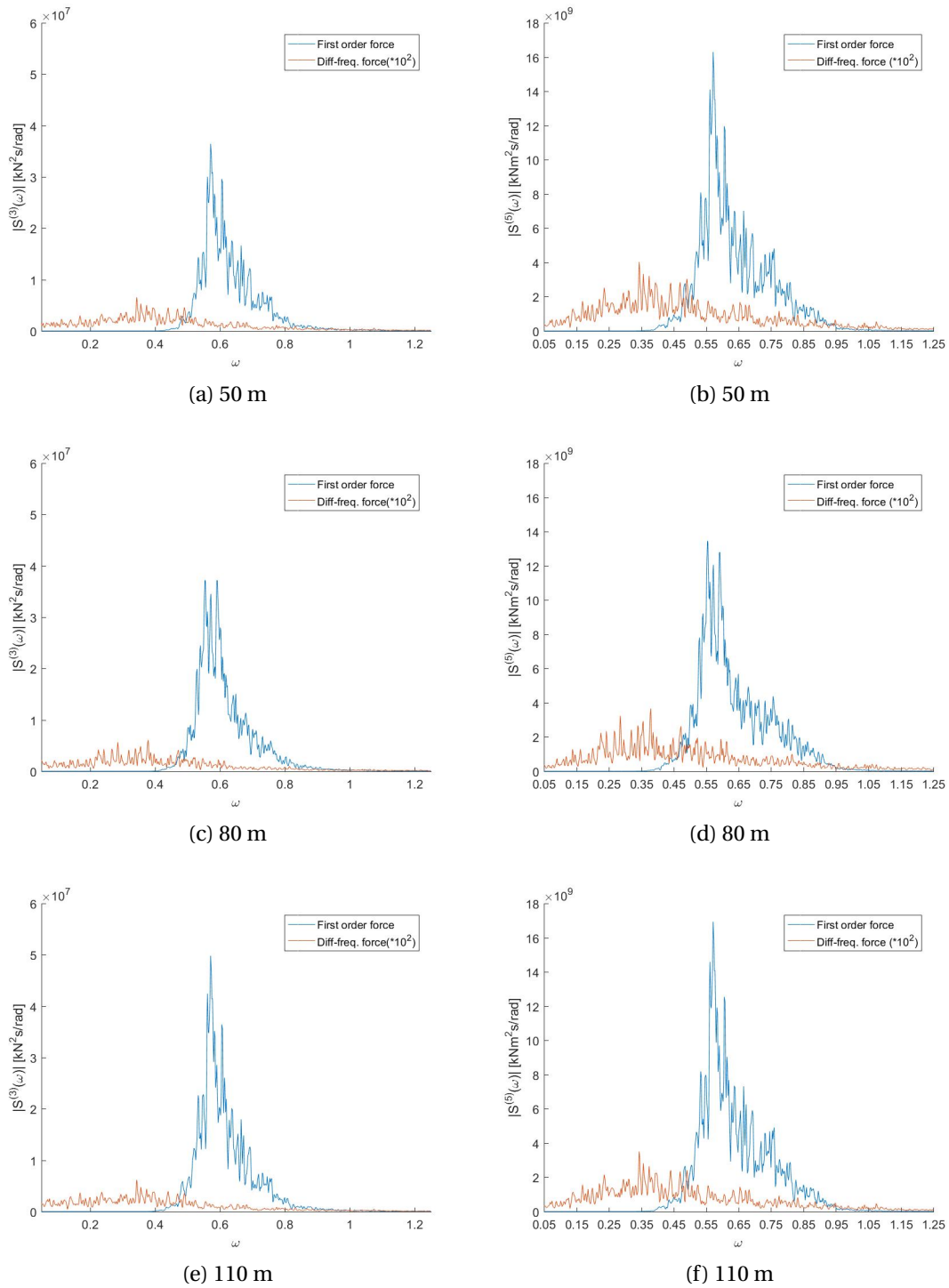


Figure 7.13: Pitch and heave first order and difference-frequency loads, PSD for load case O.1

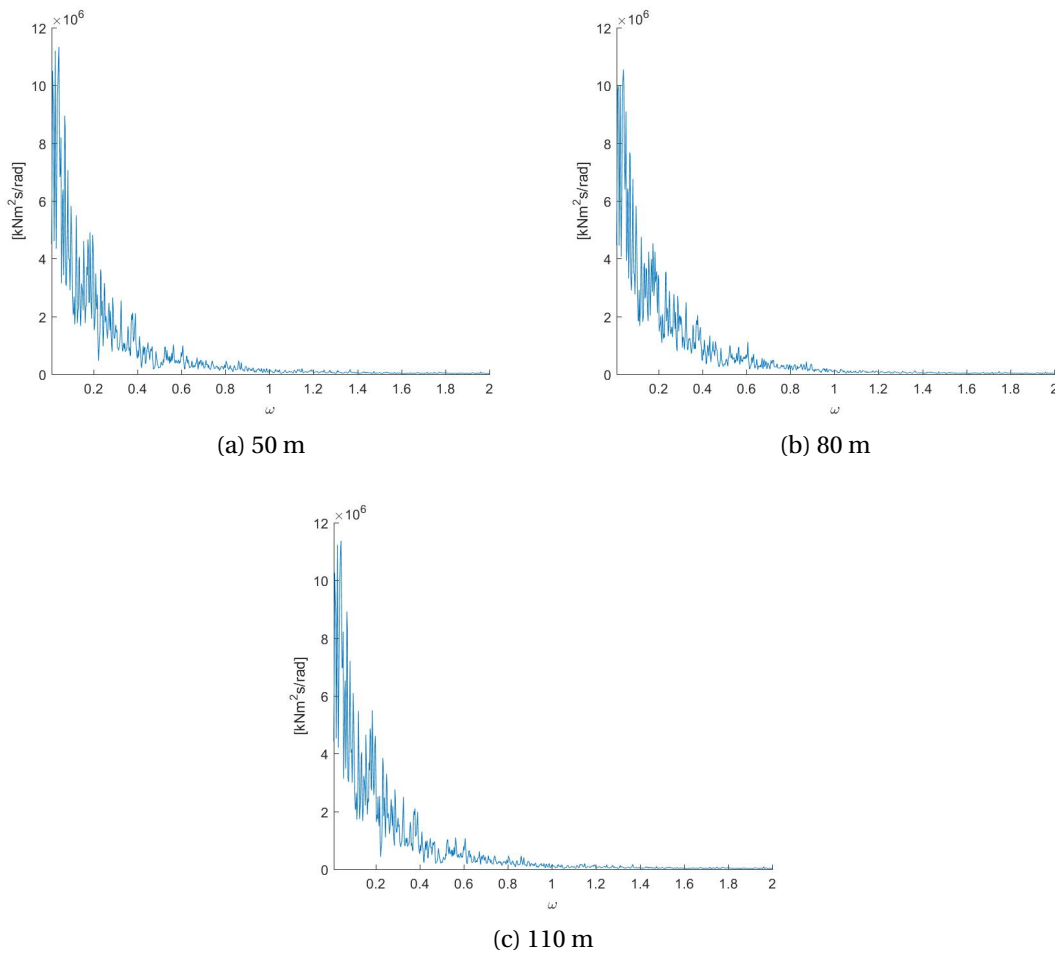
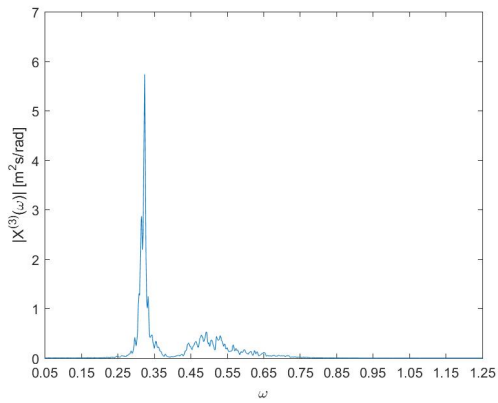


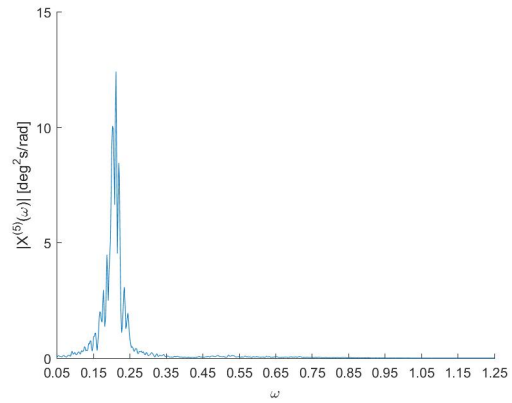
Figure 7.14: Aerodynamic pitch moment PSD, load case O.1

The standard deviations of pitch hydrodynamic loads and FWT motions was generally stable in load case 0.1. This notion was supported by the power spectral densities. For the heave motion, it was observed that the first order excitation loads were considerably higher in the 80 meter and 110 meter water depth. This relation is considered to be the governing reason for the relatively stable heave behaviour at the most shallow depth. It was also observed that the peak of the power spectral density were considerably higher at the location of 80 metres. This was due to a higher extreme measurement over the time series (Table 7.7).

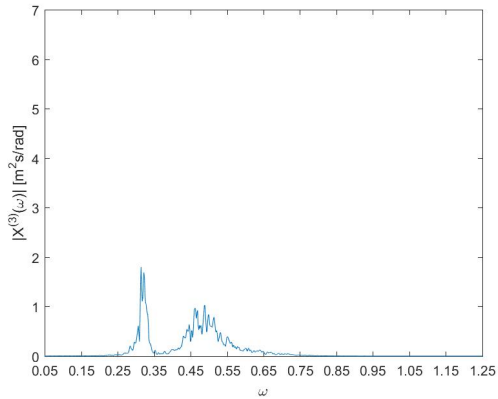
7.6.3 Case O2



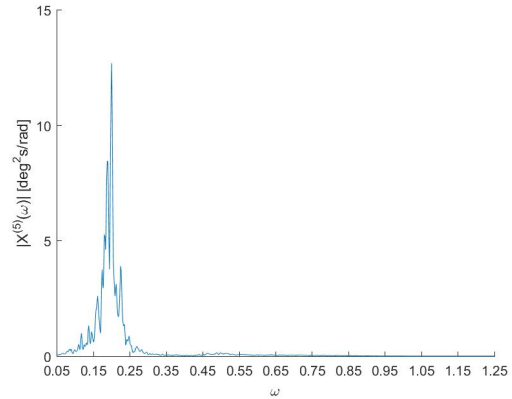
(a) 50 m



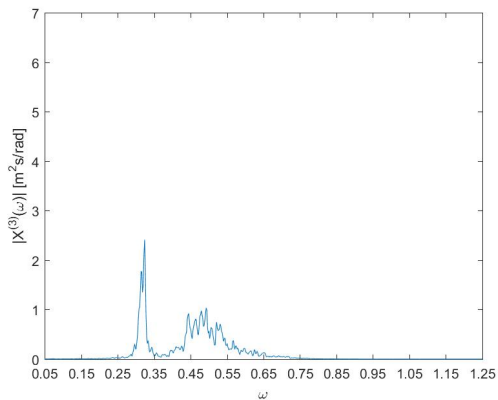
(b) 50 m



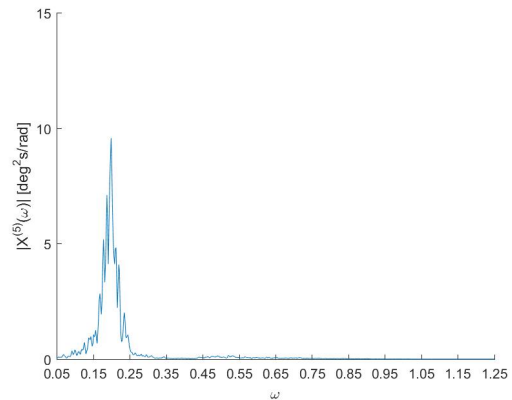
(c) 80 m



(d) 80 m



(e) 110 m



(f) 110 m

Figure 7.15: Heave and pitch response PSD, load case O.2

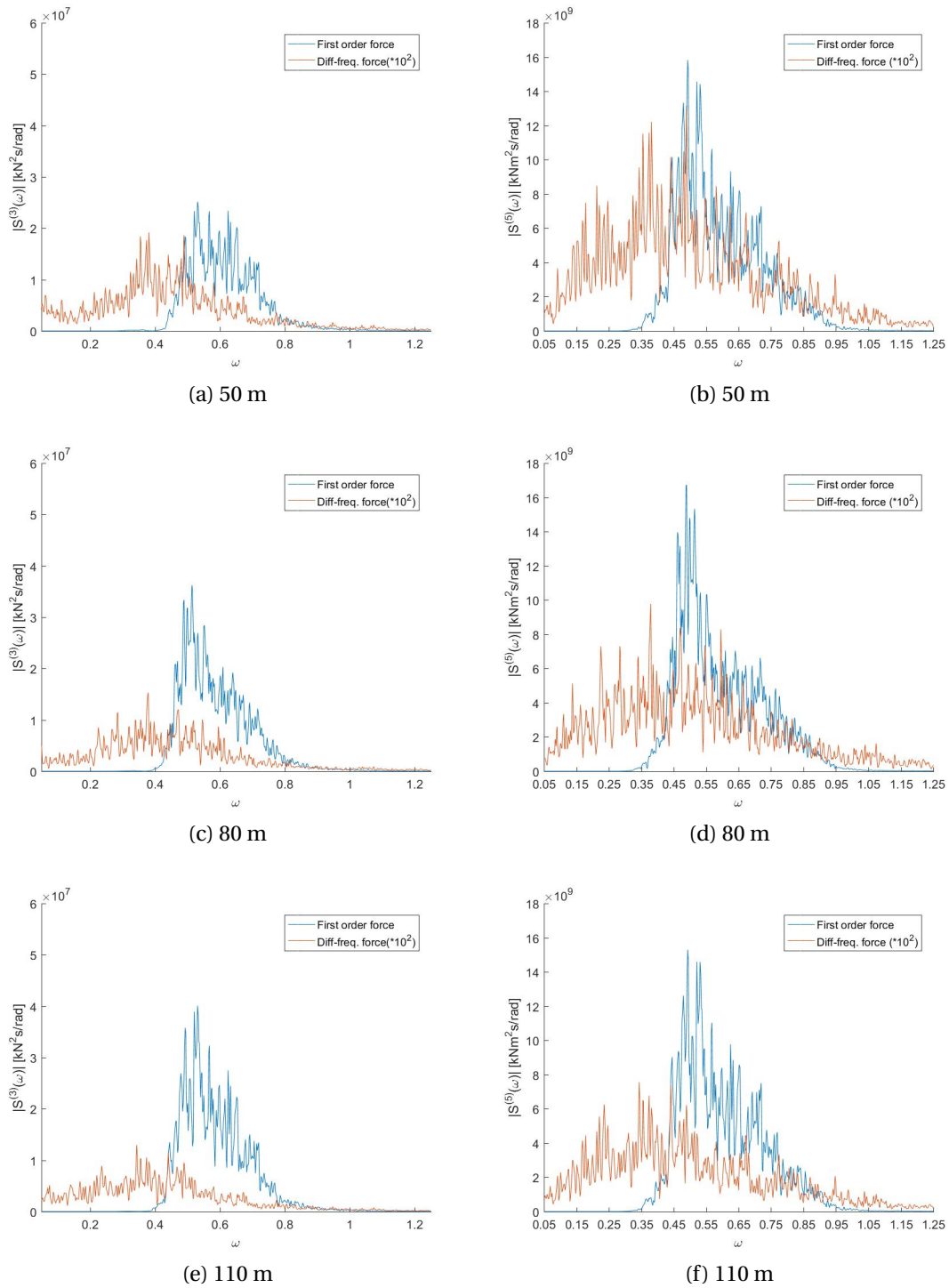


Figure 7.16: Pitch and heave first order and difference-frequency loads, PSD for load case O.2

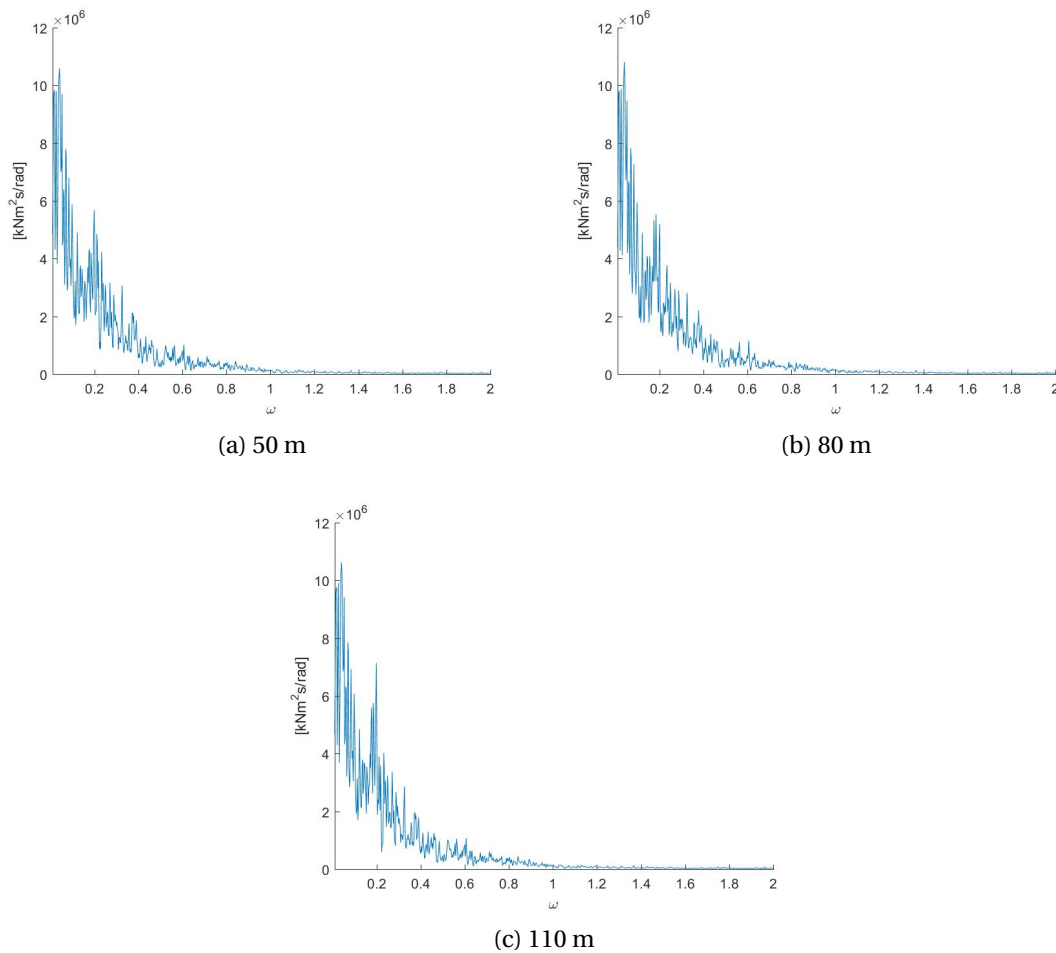


Figure 7.17: Aerodynamic pitch moment PSD, load case O.2

The peak wave period in load case O.2 was considerably higher than in load case O.1. Consequently, this load case included more high-period waves, which caused a higher contribution from slow drift forces. For the heave motion this resulted in higher extremes values, which was seen by the peak of the power spectral density 7.6.3. However, the trend of first order excitation forces in heave is still dominant, which result in generally more unstable behaviour at depths of 80 and 110 metres. Although the second-order hydrodynamic forces induced more resonance behaviour at 50 metres, the difference in first order excitation forces resulted in more stable behaviour at 50 metres.

In pitch, the first order excitation forces are relatively similar at the three water depths. The aerodynamic pitch moment does also stay within roughly the same values. However, the higher wave periods result in a considerably more dense difference-frequency power spectrum. This causes higher motions, both for extreme values and the standard deviation, which was also seen in the extreme case. Experiments, e.g. the findings of You (2012), indicate that numerical analysis can grossly under-estimate second-order effects for similar draft/depth-configurations as the 6 MW OO Star at 50 metres. Based on load cases O.2 and E.1, the FWT response in surge

and pitch are influenced by water depth. With the assumption that large standard deviations in surge and pitch leading to higher mooring and tower base fatigue loads, it is concluded that the design parameters of the OO-Star Wind Floater change over the intermediate water range.

7.6.4 Case M1

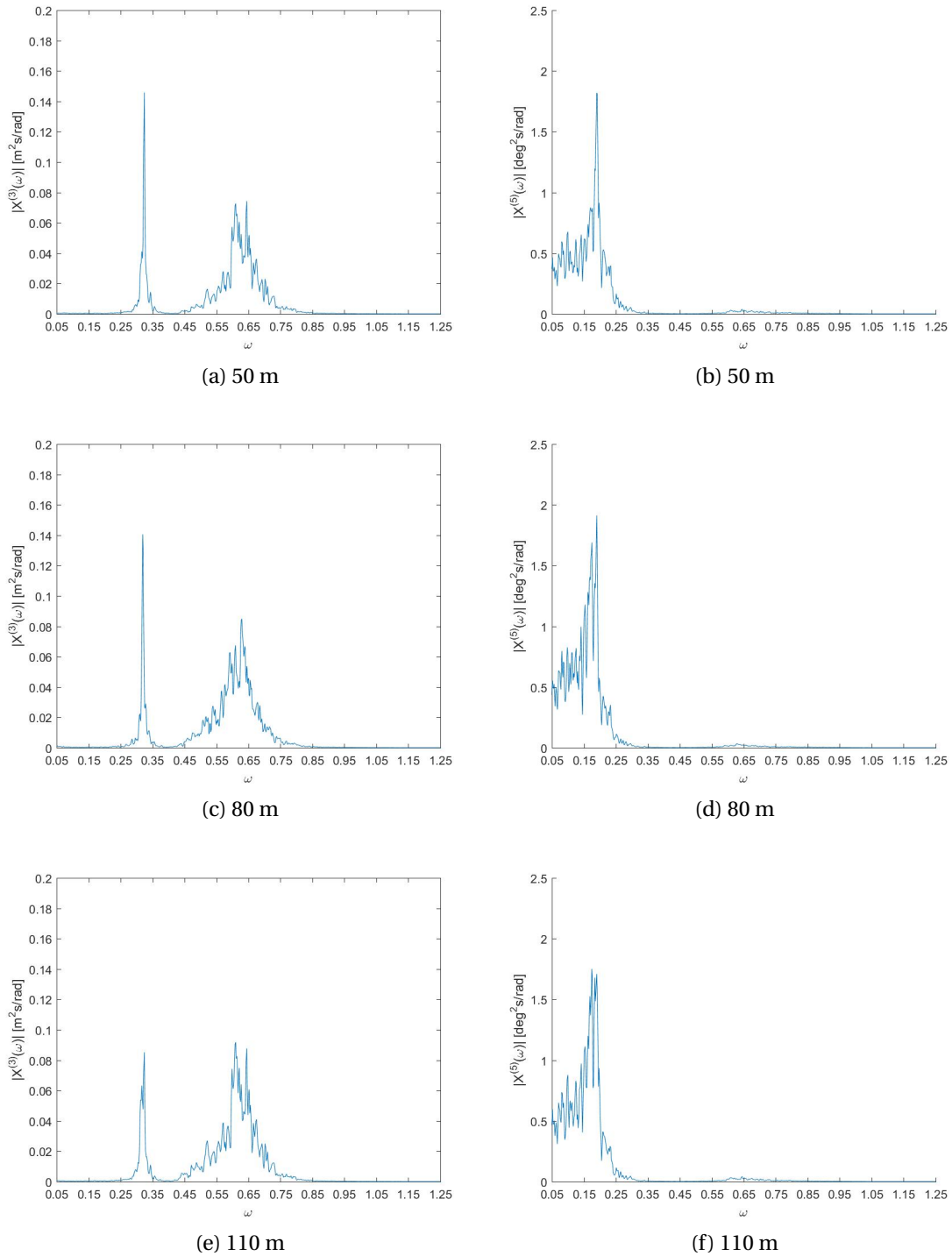


Figure 7.18: Heave and pitch response PSD, load case M.1

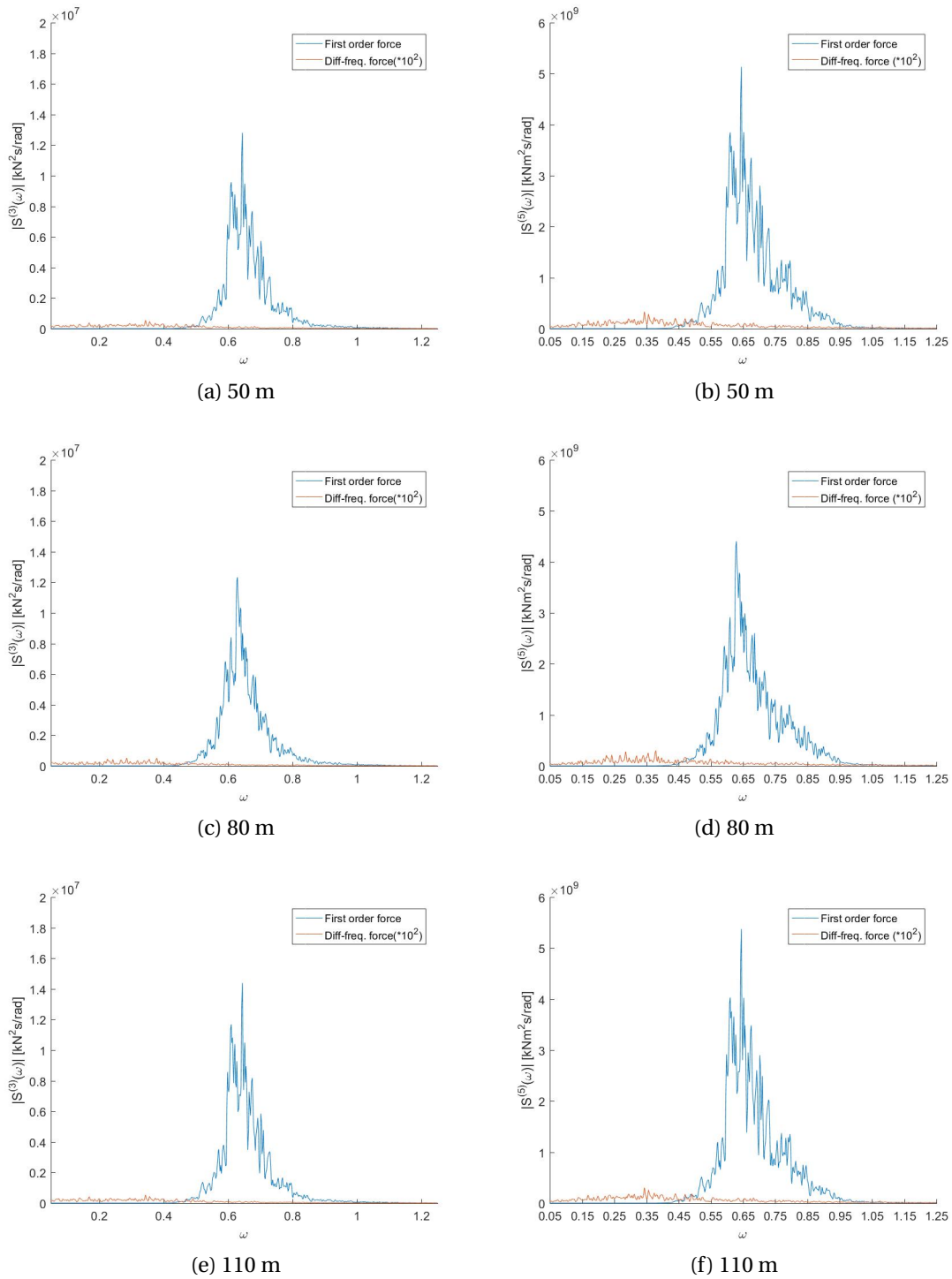


Figure 7.19: Pitch and heave first order and difference-frequency loads, PSD for load case M.1



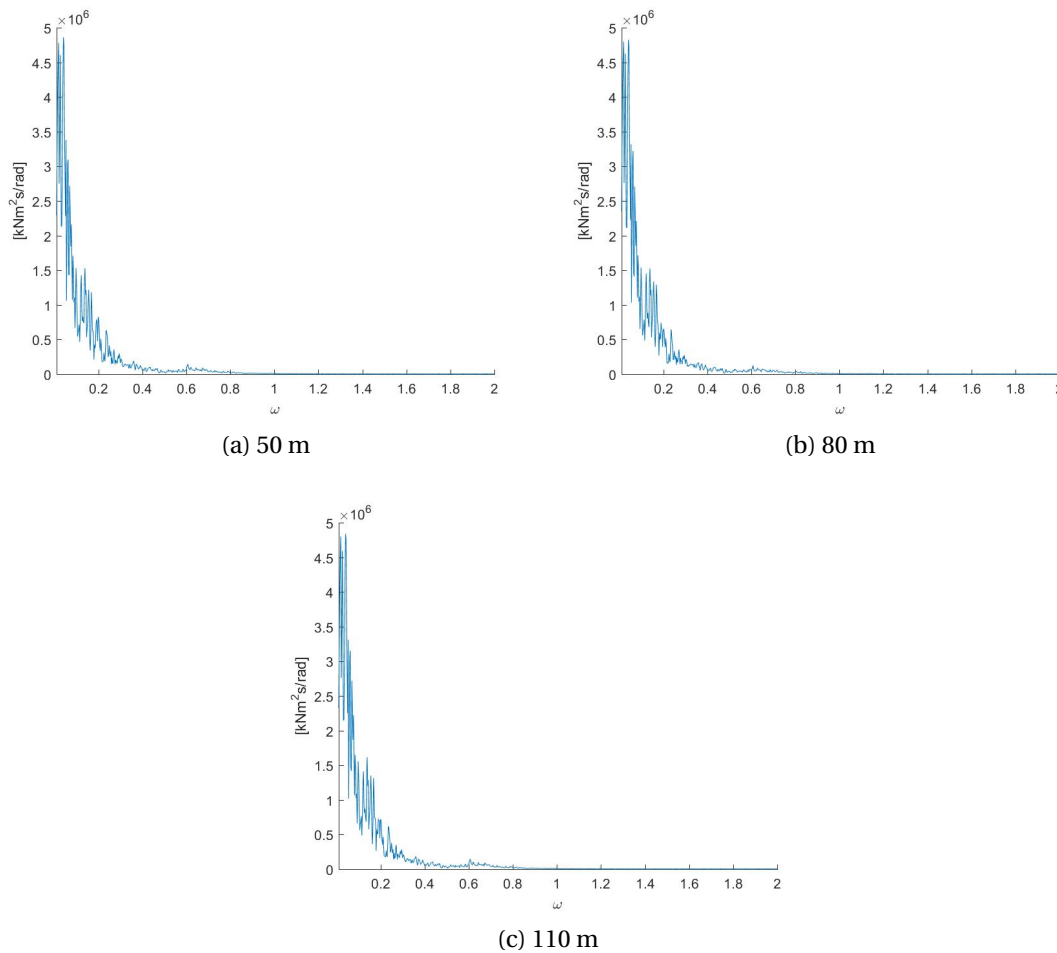


Figure 7.20: Aerodynamic pitch moment PSD, load case M.1

The surge (Appendix C) and pitch response of the FWT in load cases M.1 and M.2 were more stable with decreasing water depth. This contradicted the behaviour in load cases O.2 and E.1. In pitch, the response power spectral densities were concentrated around very low frequencies. This was reflected by the peak response frequencies (figure 7.6.4, which were higher than the natural periods from the free decay tests. Figure 7.6.4 showed that the wind moment in pitch was high in this frequency range, which is due to the erratic power output and subsequently aerodynamic forced on the wind turbine (Figure 7.3). However, the wind forces had approximately the same magnitude and standard deviation in pitch at all three water depths, which were also the same for first order excitation forces. Thus, neither of these force contributions explained the stable behaviour in more shallow water for the FWT.

The difference-frequency excitation forces did, as for every load case, increase with limited water depth. These forces also excite loads in the same frequency range as the wind forces. The stable behaviour in the 50 meter model could be due to two different causes:

- Lower pitch natural period for the numerical model at 50 metres, which would mean that the wind forces induce less resonance behaviour on the FWT.

- Hydrodynamic damping caused by difference-frequency excitation forces in the low frequency range.

7.6.5 Case M2

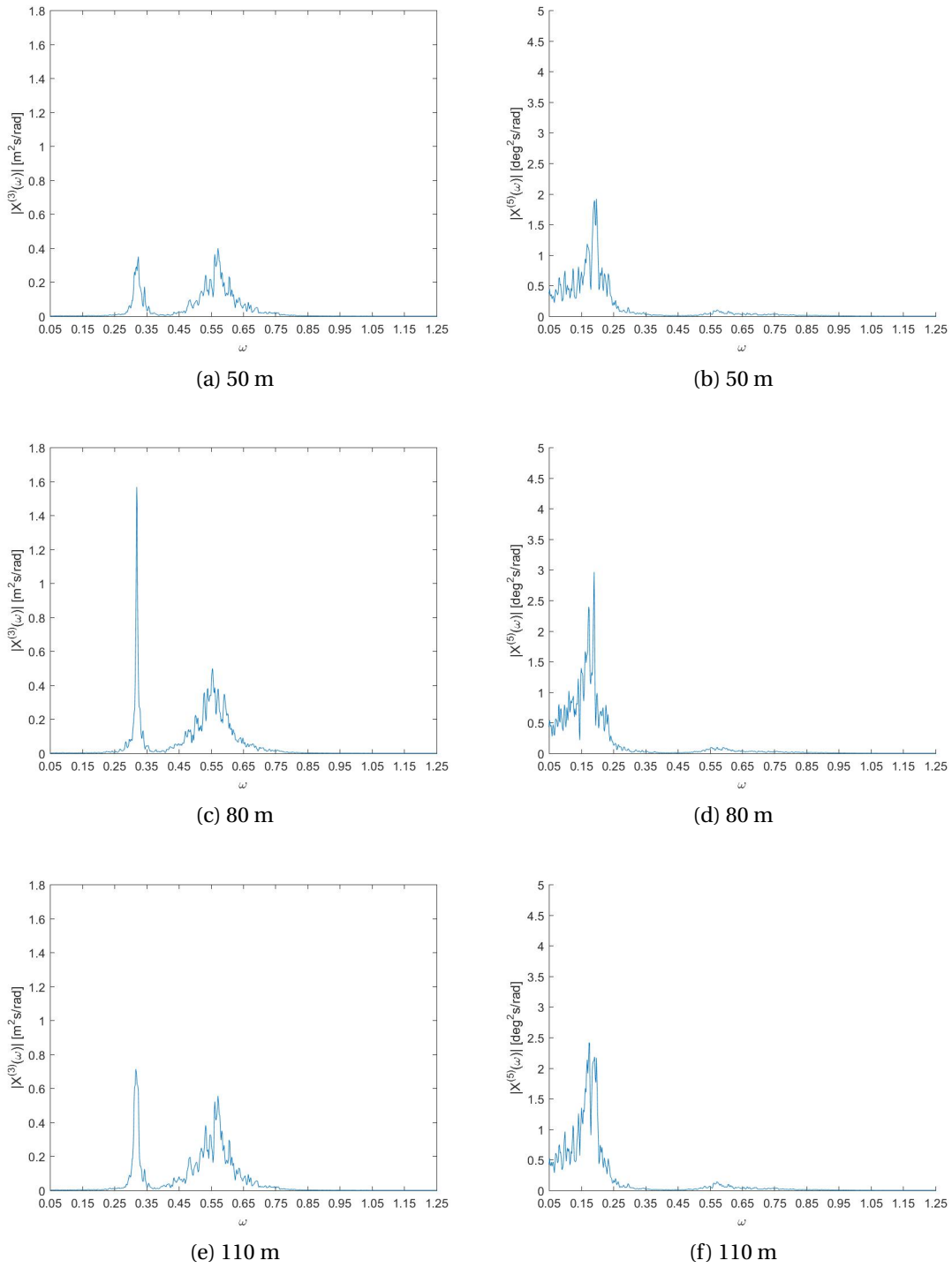


Figure 7.21: Heave and pitch response PSD, load case M.2

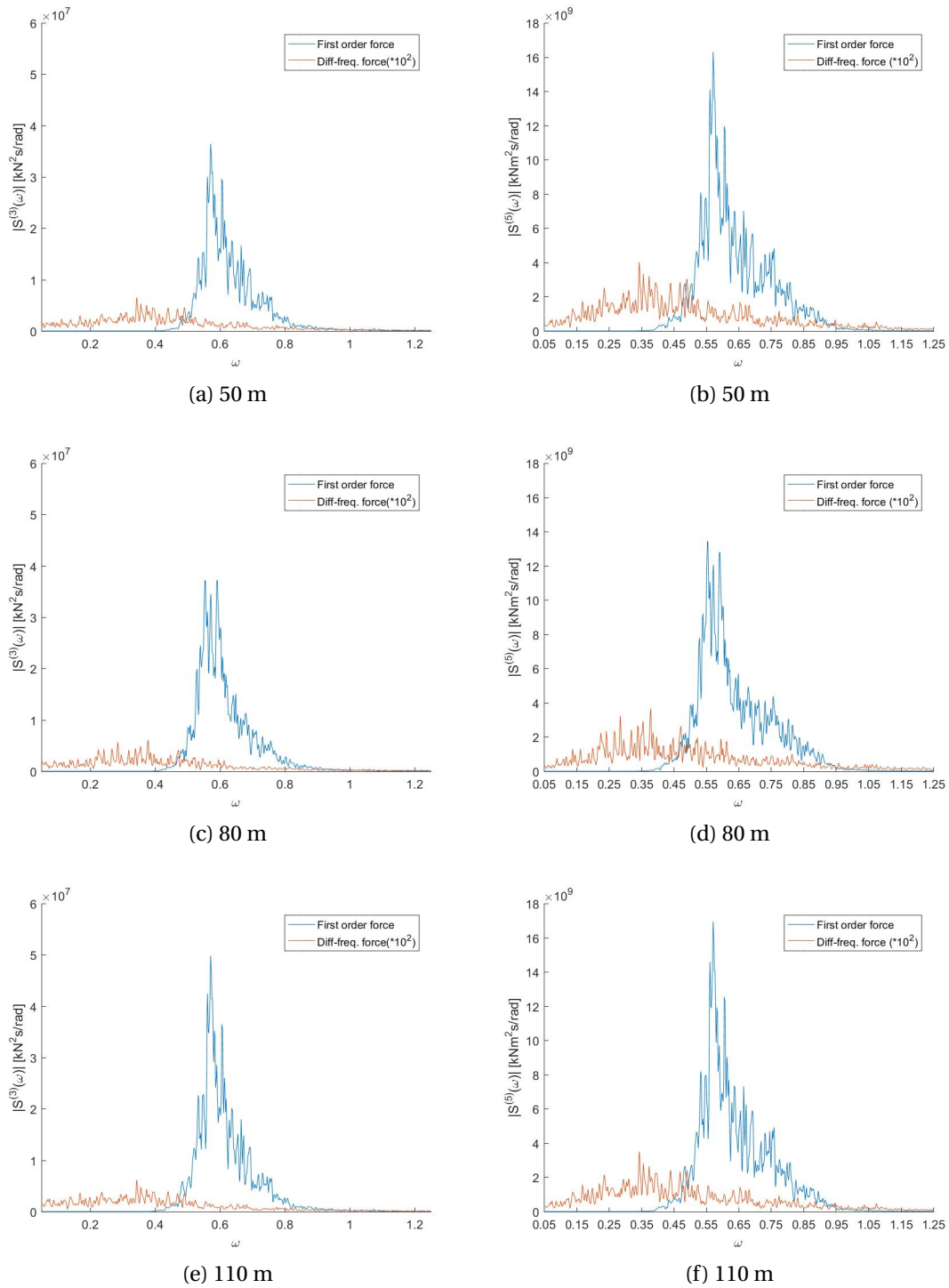


Figure 7.22: Pitch and heave first order and difference-frequency loads, PSD for load case M.2

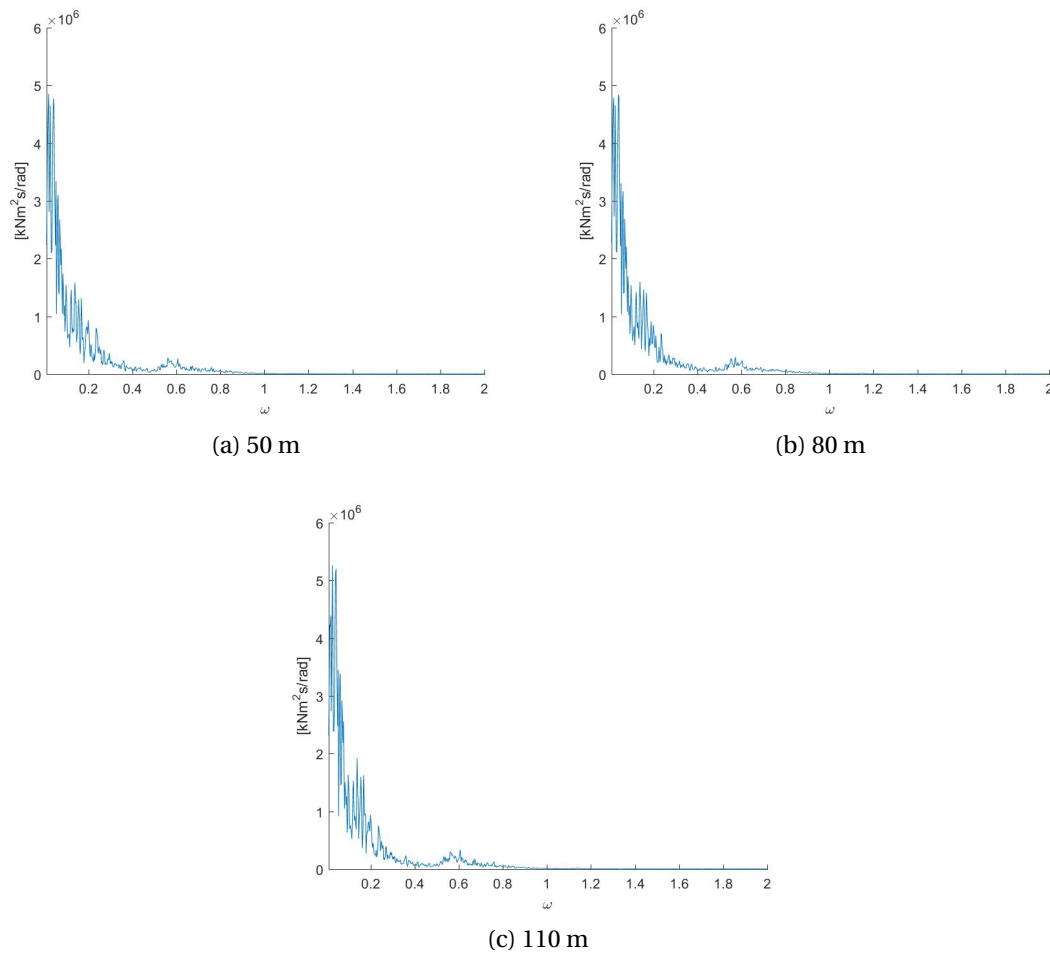


Figure 7.23: Aerodynamic pitch moment PSD, load case M.2

The pitch motions were larger for all water depths in load case M.2. In this case, the wind loads on the turbine were the same as in case M.1, while the hydrodynamic loads were larger and induced forces at higher wave periods. This supported the notion that the lower natural period in pitch excited less resonance motions in these wind speeds. It was therefore concluded that the large standard deviations in wind loads induced low-frequency motions on the turbine, which in return excited relatively unstable behaviour in pitch. In FWT design it is therefore recommended that specific control systems should be developed and implemented also in numerical design. Thus, by aiming for lower power output in low winds, it should be possible to increase the stability in numerical analysis.

The trend of higher first order excitation forces in heave for increasing water depth in the intermediate range was consistent for every load case. This effect has a bigger implication for the FWT response than the difference-frequency forces. The first order excitation forces was calculated in frequency-domain, and the model set-up was similar for each water depth. Thus, it is concluded that the lower excitation forces in heave at 50 metres were due to wave kinematics, and that the relation of higher first order excitation forces in heave would be consistent for e.g.

analysis carried out with state-of-the-art mooring designs.

The viscous coefficients were relatively similar for each water depth within a load case. Because of this, little discussion have been devoted on this subject. Upon close inspection of the power spectral densities, it was observed that the large correction for added mass in high energy sea states shifted the heave peak responses towards slightly lower frequencies. However, this effect was difficult to include graphically, and is thus mentioned as an indication that the added mass correction was higher for large waves, which were as expected. Further analysis and experimental results are therefore needed to validate the model utilized to establish viscous forces in this thesis.

# Chapter 8

## Parametric Heave Plate Study

In this chapter, the results from the conceptual heave plate study will be presented and discussed. The frequency-domain hydrodynamic analysis for the plates was carried out using first order potential theory. This was done as it was determined that the relative difference between the designs could be analyzed with reasonable accuracy without second-order effects (Section 5.8). However, some attention will be given to this topic in this section, as the results for the original design change due to the absence of difference-frequency excitation forces.

### 8.1 HydroD Natural Periods

In Section 5.8, three additional heave plate configurations were presented. As explained in this section, the frequency-domain hydrodynamic data for these configurations were implemented in the location at 80 metres for analysis. The mooring design was not altered. Because of this, it was considered excessive to carry out free decay tests for the new configurations. In order to illustrate the new natural periods for the numerical models, the results of the *Wadam*-analysis are presented.

Design	$T_{n3}$	$T_{n4}$	$T_{n5}$
1	19.720	28.724	28.722
2	19.073	27.561	27.552
3	20.329	29.331	29.335
4	19.830	28.981	28.987

Table 8.1: Natural periods for heave plate designs

## 8.2 KC

The KC-values determined through the iterative procedure explained in Section 5.6.1 are presented in this section. So is  $A_{33}^{corr}$ , as well as a representative selection of the drag coefficients used to implement the quadratic drag force contribution. As explained in Section 5.8, the relative velocity of the heave plates was taken at different drafts. Thus, the heave plate KC-value for Design 1 is of a smaller value than for the other designs.

Table 8.2: Kc-numbers  $A_{33}^{corr}$  and drag coefficients for load case O.1

Concept	Heave Plate			Corner Column		Pontoon	
	KC	$A_{33}^{corr}$ [kg]	$C_D$	KC	$C_D$	KC	$C_D$
Design 1	0.1580	142990	8.562	1.242	1.04	1.253	7.18
Design 2	0.2845	172545	4.36	1.09	1.20	0.427	7.18
Design 3	0.261	564019	15.68	1.02	1.27	0.392	7.73
Design 4	0.2817	242130	7.086	1.09	1.20	0.423	7.24

Table 8.3: KC-numbers  $A_{33}^{corr}$  and drag coefficients for load case M.1

Concept	Heave Plate			Corner Column		Pontoon	
	KC	$A_{33}^{corr}$ [kg]	$C_D$	KC	$C_D$	KC	$C_D$
Design 1	0.096	99453	11.038	0.515	2.056	0.176	12.39
Design 2	0.119	77525	4.408	0.514	2.058	0.179	12.33
Design 3	0.118	271921	15.58	0.514	2.058	0.177	12.38
Design 4	0.1177	128129	11.013	0.515	2.056	0.177	12.389

Table 8.4: KC-numbers  $A_{33}^{corr}$  and drag coefficients for load case E.1

Concept	Heave Plate			Corner Column		Pontoon	
	KC	$A_{33}^{corr}$ [kg]	$C_D$	KC	$C_D$	KC	$C_D$
Design 1	0.5756	396380	4.692	2.226	0.693	1.011	3.078
Design 2	0.6858	403113	2.569	2.24	0.693	1.0289	3.045
Design 3	0.6438	1342100	9.8324	2.228	0.693	0.9657	3.173
Design 4	0.6617	510010	5.0381	2.223	0.693	0.990	3.119

As presented in tables 8.2, 8.3 and 8.4, the correction for added mass are found to be substantially higher for case 3 than for the other designs. Additionally,  $A_{33}^{corr}$  for case 2 is higher than for the original design for high KC-values. This is due to the added flow separation of two heave plates, and is an evidence in the potential of such configurations. Due to the relative velocity, confident KC-values for two-plate configurations are difficult to obtain. It is recommended that further studies should be carried out to determine the effect of viscous forces in waves for such configurations.



### 8.3 Standard Deviations of Different Heave Plate Parameters

Table 8.5: Standard deviations for different heave plate parameters

Case O.1			
	Surge [m]	Heave [m]	Pitch [deg]
Case 1	1.3125	0.56818	0.7814
Case 2	1.3074	0.58728	0.75513
Case 3	1.2248	0.50217	0.7891
Case 4	1.3102	0.57202	0.78017
Case M.1			
	Surge [m]	Heave [m]	Pitch [deg]
Case 1	1.5572	0.22227	0.90975
Case 2	1.5422	0.23152	0.96664
Case 3	1.5361	0.22174	0.9886
Case 4	1.5443	0.22317	1.0066
Case E.1			
	Surge [m]	Heave [m]	Pitch [deg]
Case 1	2.841	1.619	2.4117
Case 2	2.8521	1.6937	2.3281
Case 3	2.7847	1.4898	2.4094
Case 4	2.824	1.562	2.4017

The standard deviation of the FWT behaviour indicate different characteristics for the conceptual heave plate designs. In surge, the differences were considered to be mainly due to the different mass of the structure. This changes the horizontal stiffness requirement presented in Section 5.7. Thus, the higher mass shifted the natural period in surge to a higher value. The lower standard deviation in surge was considered a favourable response characteristic, as it could increase fatigue life and present better design parameters for the mooring configuration and power cable.

As expected, the standard deviations in heave were largely different for the four cases. The results indicated that Design 3 generally had the least amount of heave motions, which is to be expected with the relatively large natural period and added mass correction. When compared to the original design (Design 1), its standard deviations in heave were 11.6 %, 2.3 % and 8.67 % lower for load cases O.1, M.1 and E.1, respectively.

Design 3 had the same configuration of column breadth, plate diameter and plate thickness as the original design, with the difference being an extra plate. Because of this, the local stresses in this design was assumed to be in the same order as in the original design. However, the relative velocity changes with the draft, as the wave particle velocity decreases with depth. Thus, the pressure on the additional heave plate will be higher, and structural analysis is needed to determine the implications this has for the structural integrity of the plate.

It was observed that Design 2 has the highest standard deviation in heave. The heave added mass for this design was considerably lower than for the other designs, as indicated by the natural period 8.1. More unexpected was the performance of design 4, which had higher deviations than the original design in the heave motion for load cases O.1 and M.1. The different behaviour in pitch for the four designs were more complex. No concept stood out consistently for all three load cases, and the responses are summarized in the following:

- In load case O.1 and E.1, the response of design 2 was the most stable, based on the standard deviations. The other 3 designs had relatively similar responses based on the same parameter.
- The results were different for load case M.1. The standard deviation of design 1 was 6.5 % lower than the second-lowest value. The trend in pitch motions between the other three designs were similar to the findings in load case O.1 and E.1.

The importance of difference-frequency excitation forces was observed by comparing the results of Design 1 to the findings in the previous chapter. The results were consistent in that the analysis without slow-drift motions yielded significantly lower response values. E.g., for load case O.1 the standard deviations in surge, heave and pitch were 16.8 %, 7.5 % and 37.46 %, respectively. The differences from Chapter 7 were even larger for load case E.1, where the respective motions increased with 17.3 %, 18.1 % and 51.5 %. These results underlined the importance of including a proper approach to modelling second-order effects in FWT analysis, with a particular importance in surge and pitch. Based on the discussion in Section 5.4.2, a Newman approximation would introduce a slight underestimation of this force contribution in surge. However, this is not the case for the pitch motion. Thus, a full QTF in pitch, based on second-order potential theory, is recommended for FWT analysis.

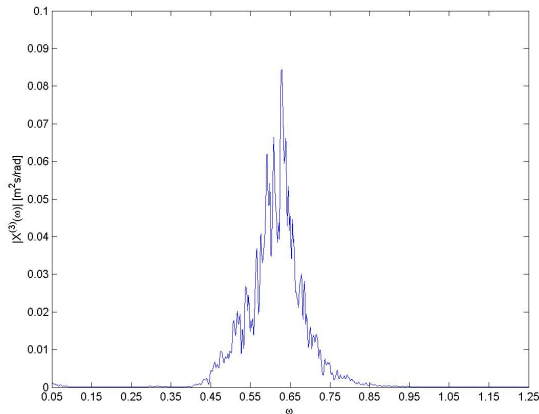
Table 8.6: Extreme values for different heave plate parameters

Case O.1				
Depth	Max/Min	Surge [m]	Heave [m]	Pitch [deg]
Case 1	Max	16.847	1.8125	3.5681
	Min	7.386	-1.925	-1.7996
Case 2	Max	16.773	1.8651	3.744
	Min	7.347	-1.8802	-1.719
Case 3	Max	15.302	1.5013	3.2581
	Min	7.8768	-1.6503	-1.5435
Case 4	Max	16.811	1.806	3.67
	Min	7.361	-1.9401	-1.785
Case M.1				
Depth	Max/Min	Surge [m]	Heave [m]	Pitch [deg]
Case 1	Max	18.24	0.60387	5.3763
	Min	6.4228	-0.85635	-0.62413
Case 2	Max	18.211	0.64231	5.6597
	Min	6.4012	-0.87469	-0.76967
Case 3	Max	18.132	0.60774	5.8634
	Min	6.3919	-0.83524	-1.0014
Case 4	Max	18.21	0.61041	5.9552
	Min	6.4188	-0.85157	-0.97081
Case E.1				
Depth	Max/Min	Surge [m]	Heave [m]	Pitch [deg]
Case 1	Max	36.902	4.804	17.668
	Min	16.425	-6.0562	1.0029
Case 2	Max	36.843	5.8055	16.88
	Min	16.358	-6.5959	0.47139
Case 3	Max	36.807	5.3435	17.106
	Min	16.303	-5.8597	1.101
Case 4	Max	36.89	4.575	17.432
	Min	16.408	-6.0549	1.0347

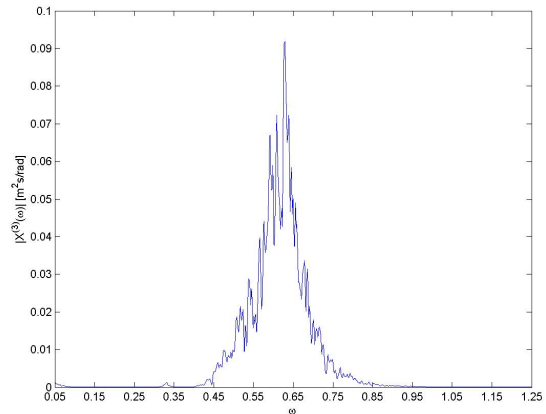
In the operating conditions of the FWT, the pitch motions were within the limit of 6° for all designs. However, this was not the case in the previous chapter. These results indicated that to fully establish the validity of the concepts, slow drift forces should be included in the hydrodynamic analysis. This was supported by the fact that the maximum surge motion for Design 1 was 3.215 metres smaller than the results presented in the previous Chapter. The maximum surge position and the tilt angle in operational state were within the limits set by the mooring material breaking load and tilt angle limit for all new heave plate designs. As mentioned, this should also be validated with difference-frequency forces included in the analysis.

## 8.4 Power Spectral Densities for Heave Plate Configurations

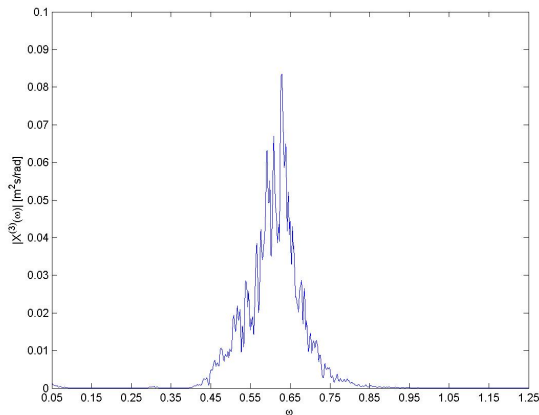
### 8.4.1 Case M1



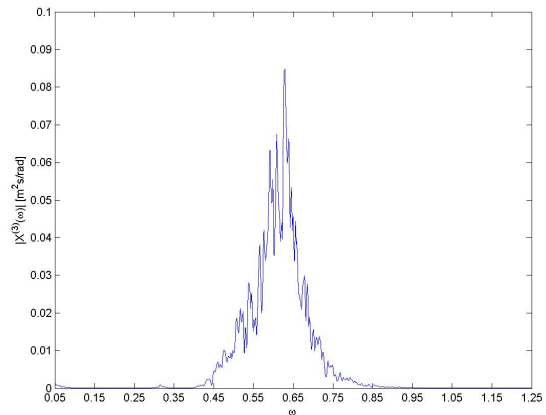
(a) Case 1



(b) Case 2

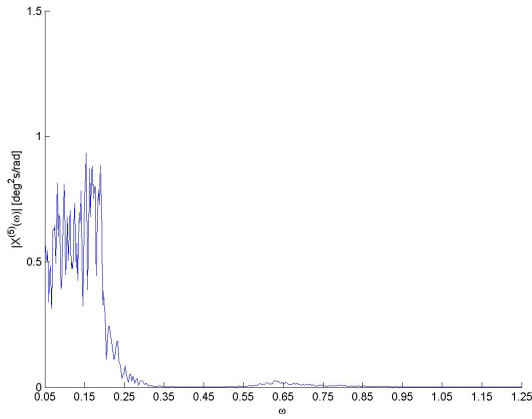


(c) Case 3

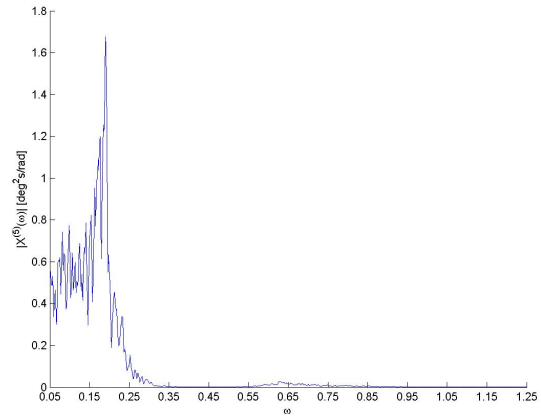


(d) Case 4

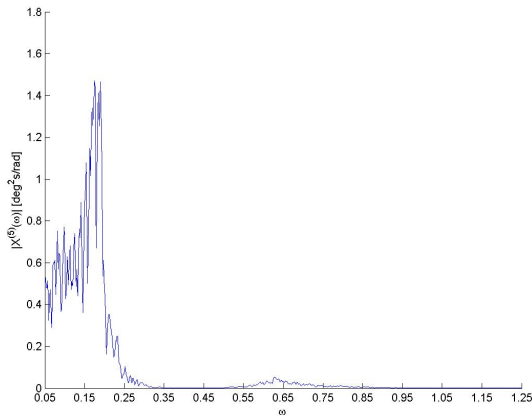
Figure 8.1: Heave PSD for different heave plate parameters, load case M.1



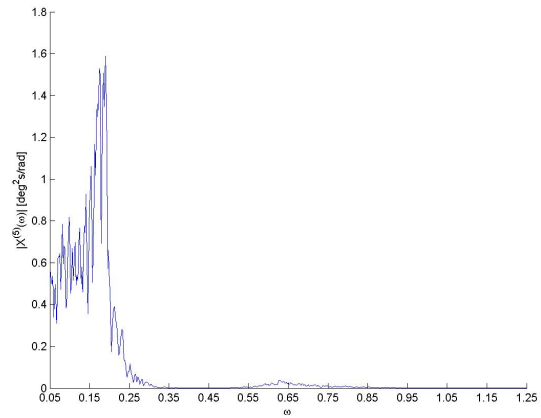
(a) Case 1



(b) Case 2

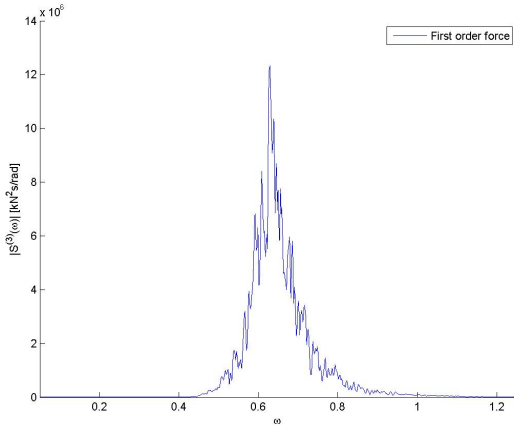


(c) Case 3

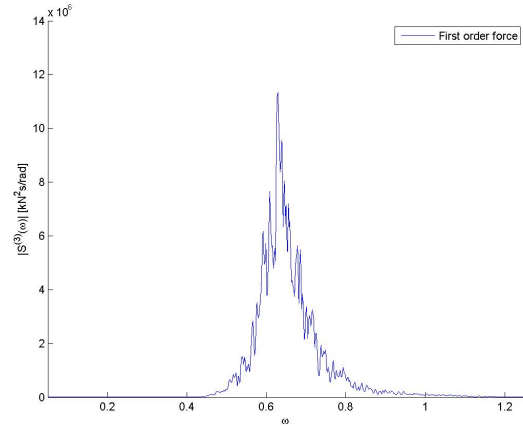


(d) Case 4

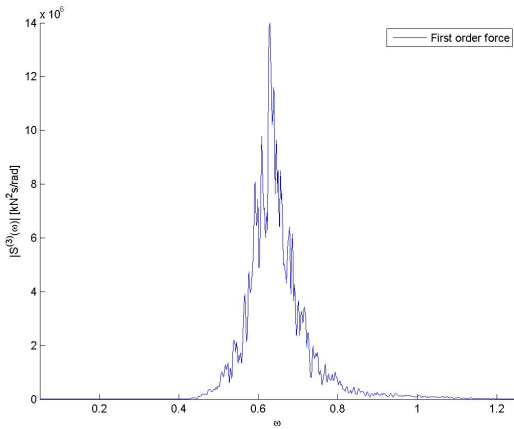
Figure 8.2: Pitch PSD for different heave plate parameters, load case M.1



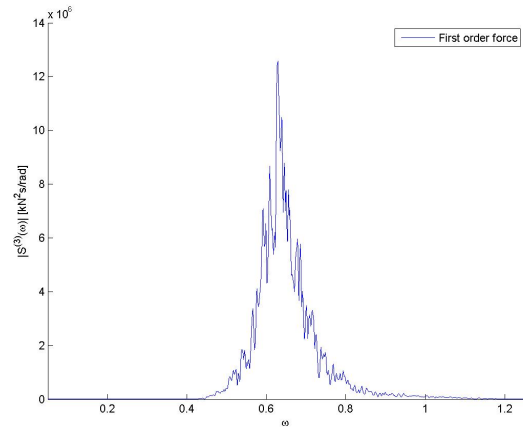
(a) Case 1



(b) Case 2

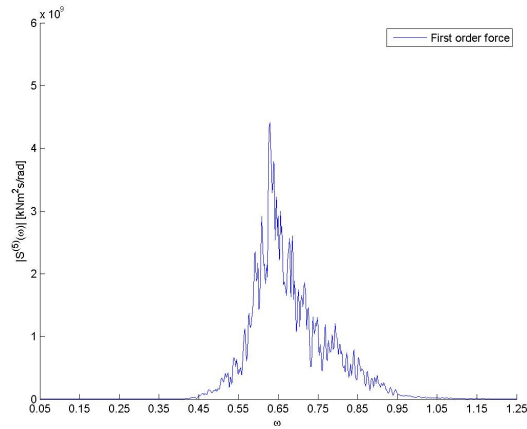


(c) Case 3

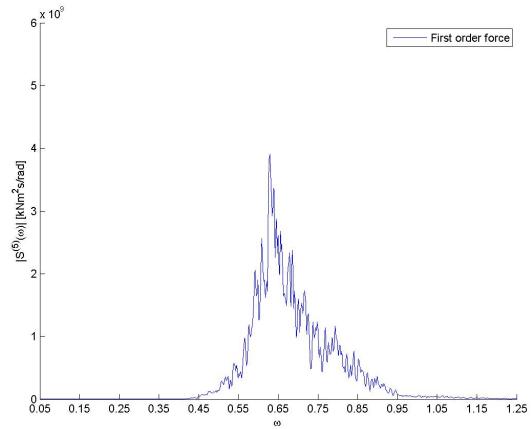


(d) Case 4

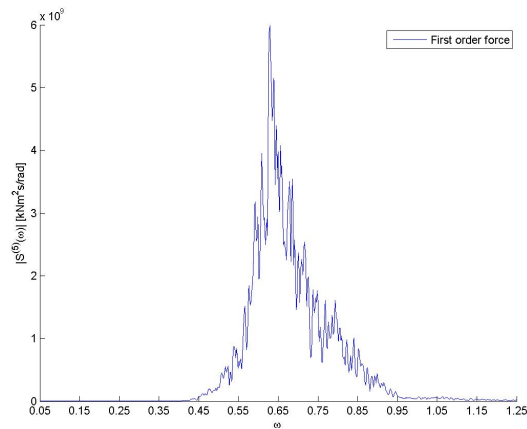
Figure 8.3: Heave first order excitation forces PSD - load case M.1



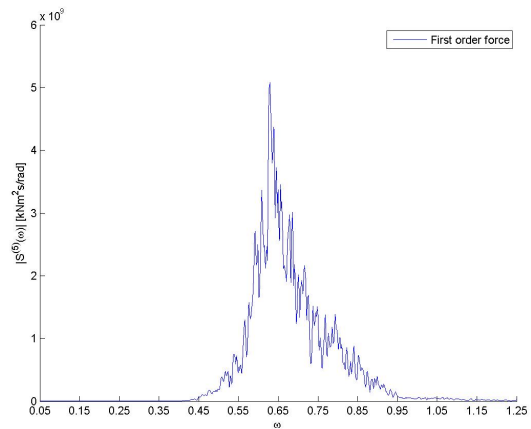
(a) Case 1



(b) Case 2

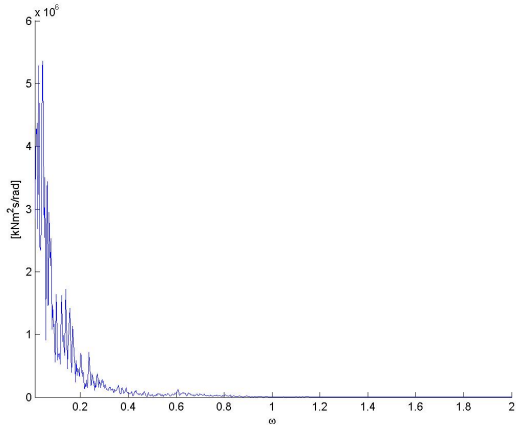


(c) Case 3

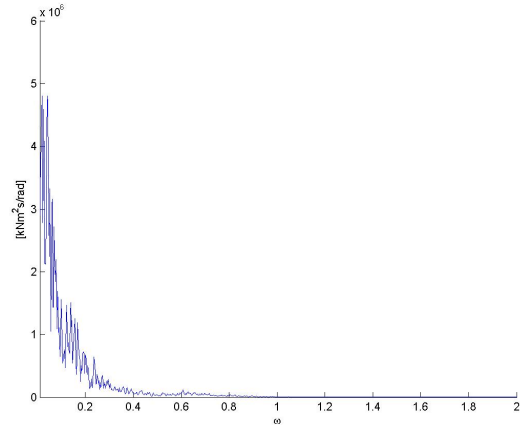


(d) Case 4

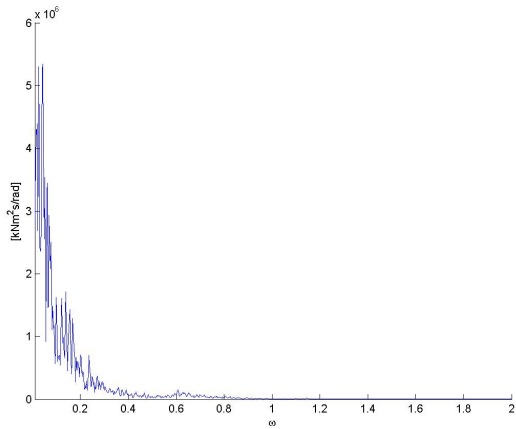
Figure 8.4: Pitch first order excitation forces PSD - load case M.1



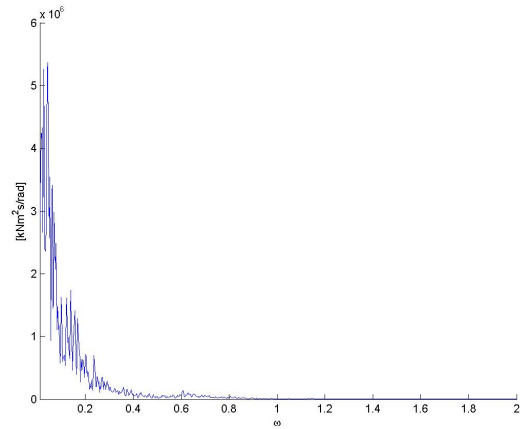
(a) Case 1



(b) Case 2



(c) Case 3



(d) Case 4

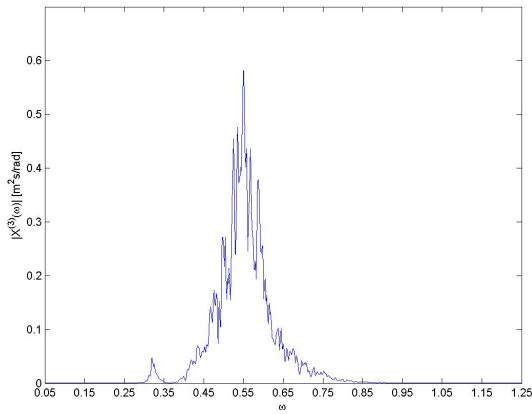
Figure 8.5: Aerodynamic pitch moment PSD - Case M.1



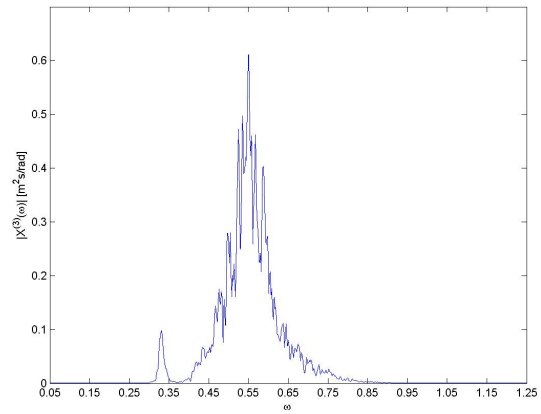
The pitch response in load case M.1 can be explained by the relatively large contribution from aerodynamic forces. Due to the large oscillations in the turbine torque and power output, the pitch moment due to wind induced large forces at low frequencies. This excited resonance oscillations around the natural period in pitch (Figure 8.4.1). Unexpectedly, this did not happen for Design 1, which had a lower natural frequency than for Design 2 and should have been more exposed to the low frequency wind loads. No good explanation for these results were found. It was therefore considered that the natural period of 28.772 seconds was simply a fortunate value in this load case, with few loads occurring around this frequency.

It was observed that there were no resonance behaviour in heave for either concept. The peak period of the sea state in load case M.1 was 9.98 s, and without the difference frequency effects, there were no waves that excited heave forces at the natural period in heave.

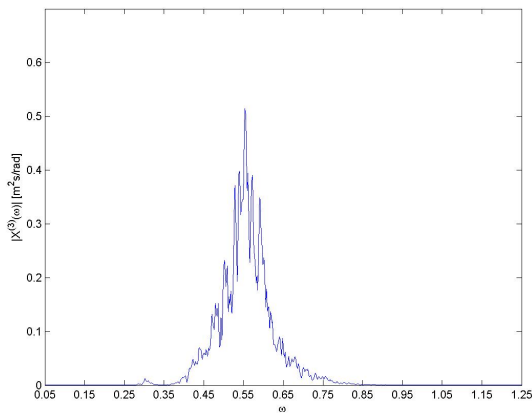
8.4.2 Case 01



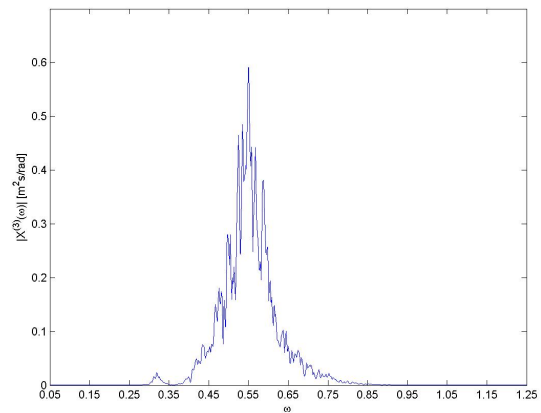
(a) Case 1



(b) Case 2

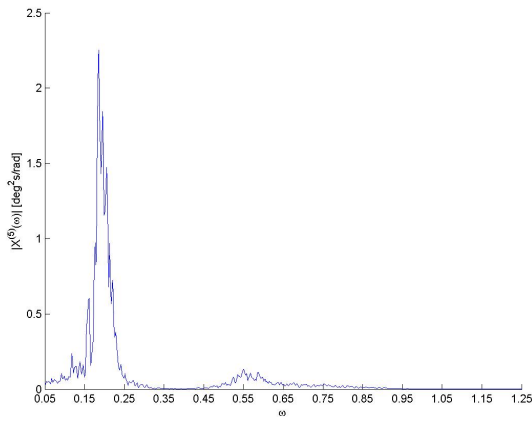


(c) Case 3

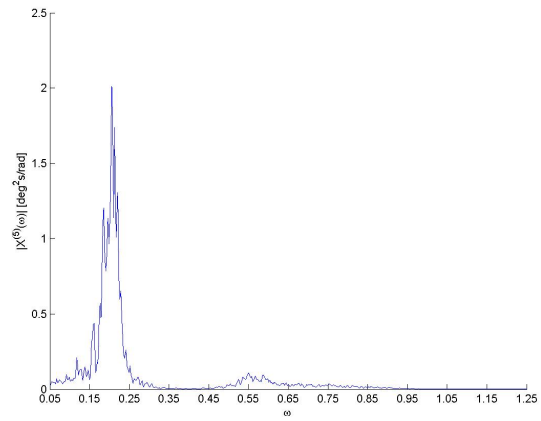


(d) Case 4

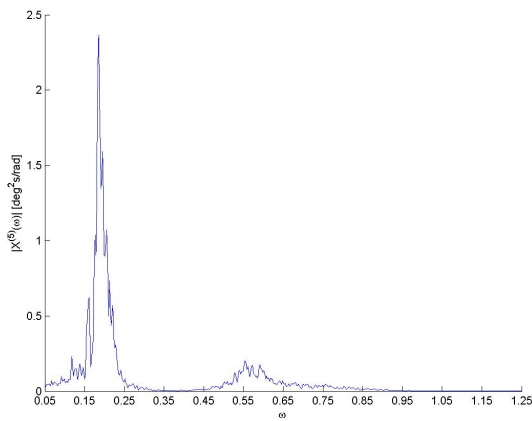
Figure 8.6: Heave PSD for different heave plate parameters, load case 0.1



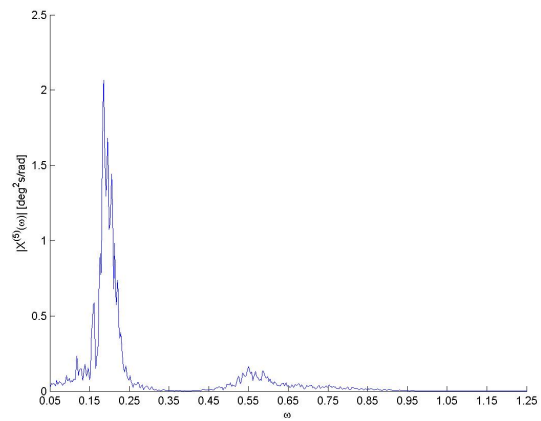
(a) Case 1



(b) Case 2

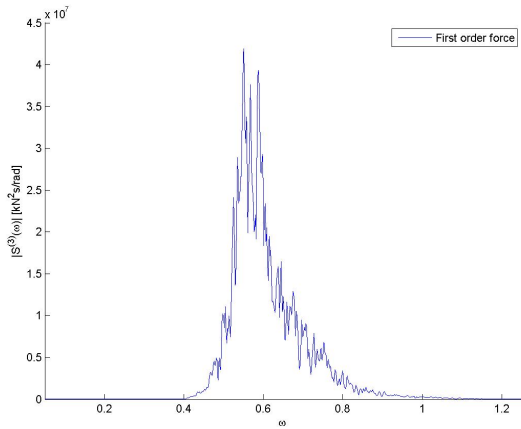


(c) Case 3

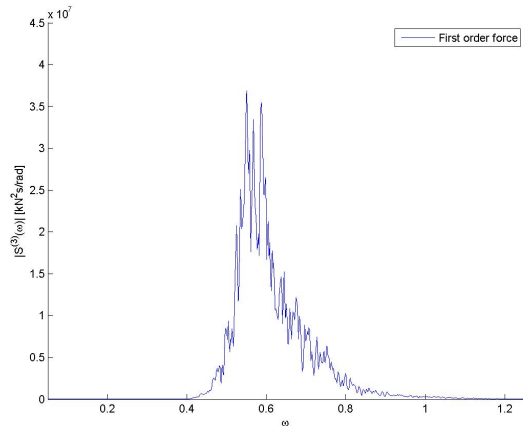


(d) Case 4

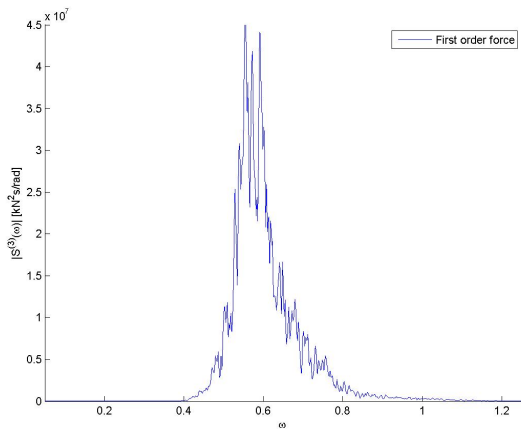
Figure 8.7: Pitch PSD for different heave plate parameters, load case M.1



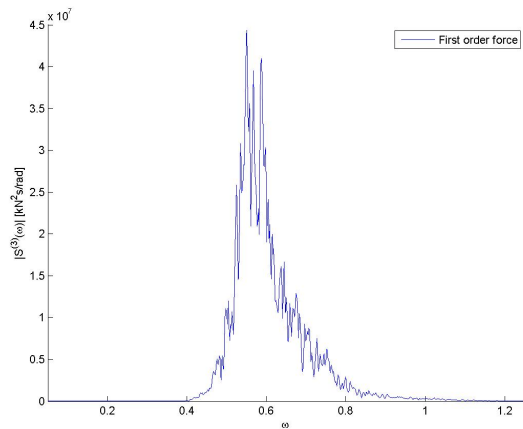
(a) Case 1



(b) Case 2

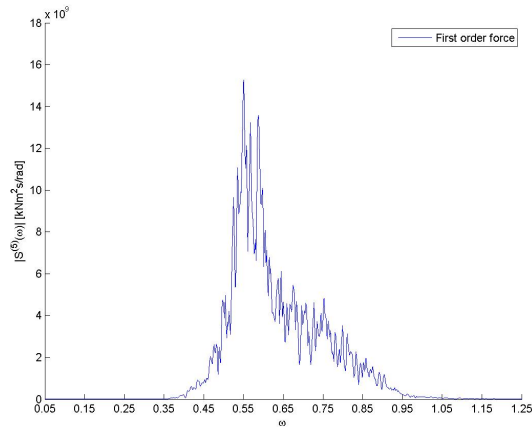


(c) Case 3

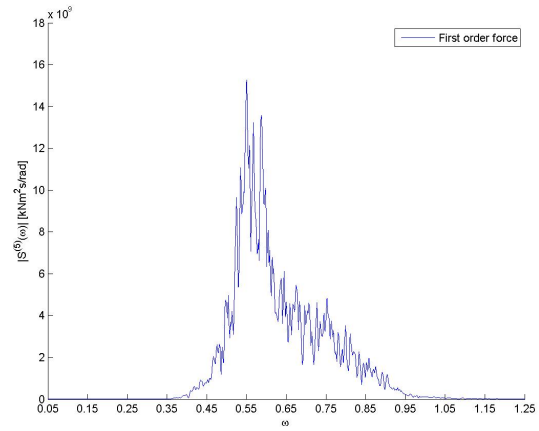


(d) Case 4

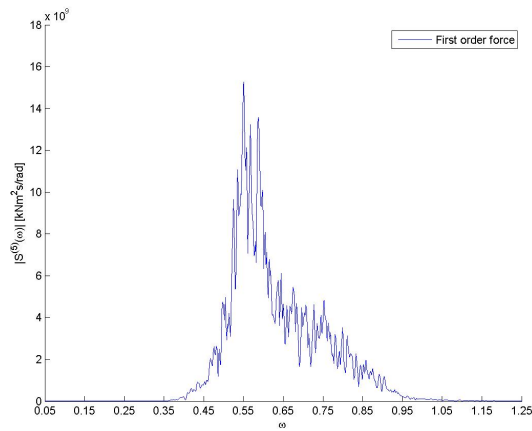
Figure 8.8: Heave first order excitation forces PSD - load case O.1



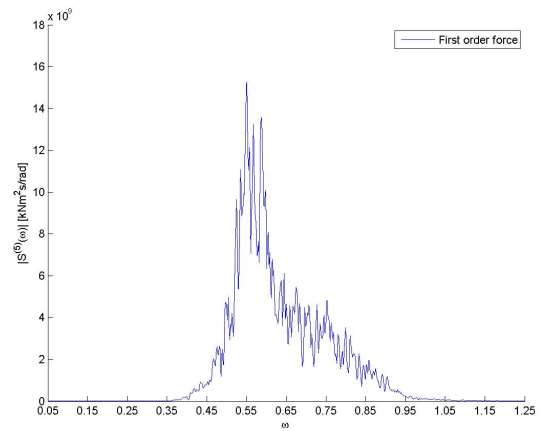
(a) Case 1



(b) Case 2

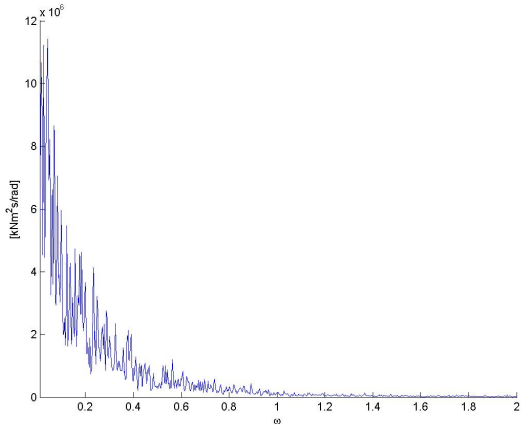


(c) Case 3

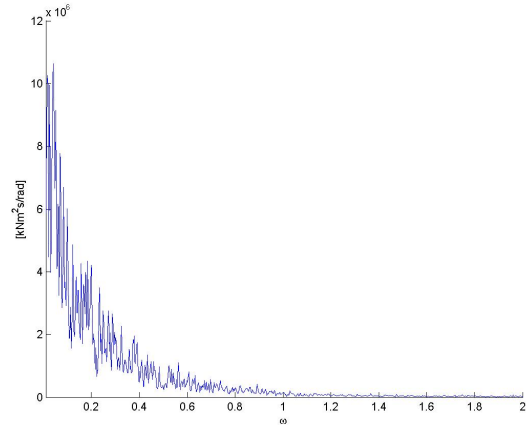


(d) Case 4

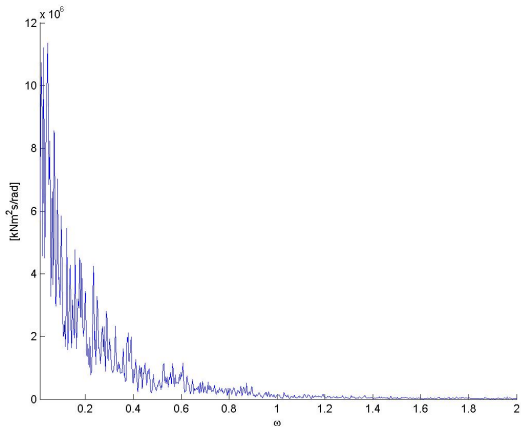
Figure 8.9: Pitch first order excitation forces PSD - load case M.1



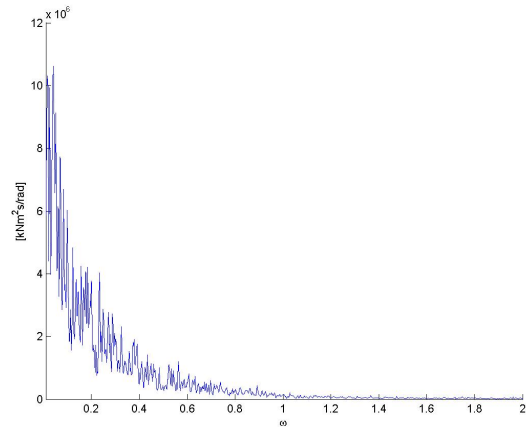
(a) Case 1



(b) Case 2



(c) Case 3



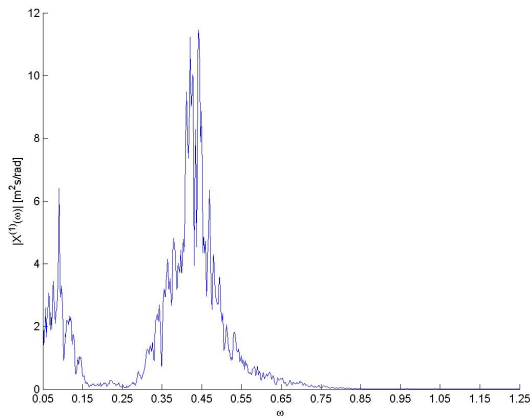
(d) Case 4

Figure 8.10: Aerodynamic pitch moment PSD - Case O.1

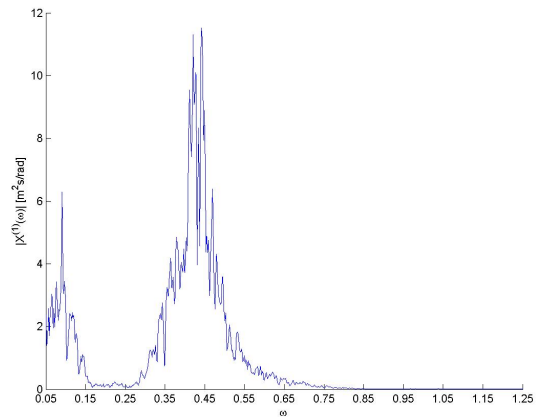
The pitch response in this load case were more expected. Higher natural periods in pitch corresponded to smaller standard deviations, with Design 3 experiencing the lowest standard deviations in pitch. Although the first order waves excited no loads around the natural period, their relative significance when compared to wind loads were high. Therefore, wind-wave coupling was more important for the response, and the designs with high natural periods in pitch had a lower standard deviation.

The sea state in load case O.1 contained more energy than M.1, and contained waves at higher periods. This was seen by the heave response, which contained responses around the natural period. When investigating the heave response power spectral density (Figure 8.4.2), it was possible to observe the shift in natural period due to added mass. Design 3 was characterized when compared to the other designs, which was attributed to the added damping of the heave plate configuration. However, this design also experienced higher excitation loads in heave, as seen by the first order excitation power spectral density. This was considered to be due to the higher wetted area of this design, as there was a bigger surface exposed to wave forces.

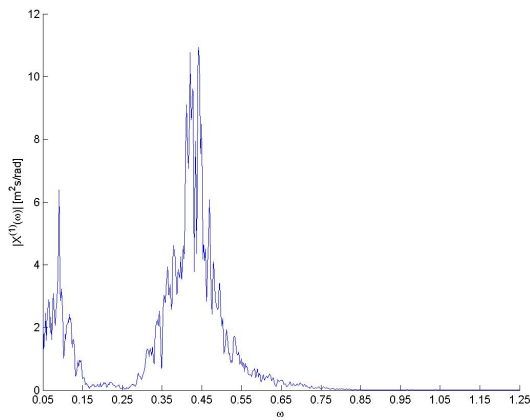
8.4.3 Case E.1



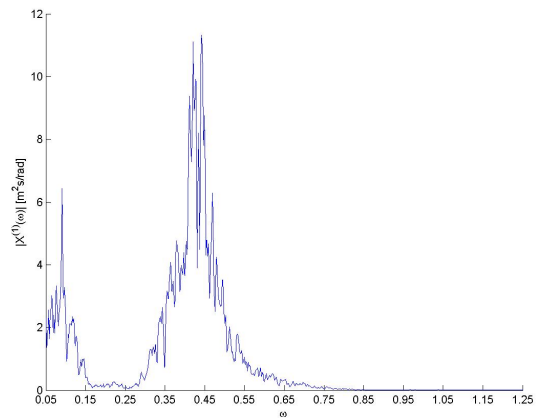
(a) Case 1



(b) Case 2



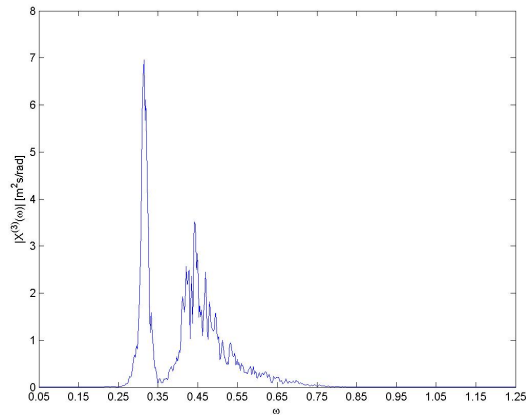
(c) Case 3



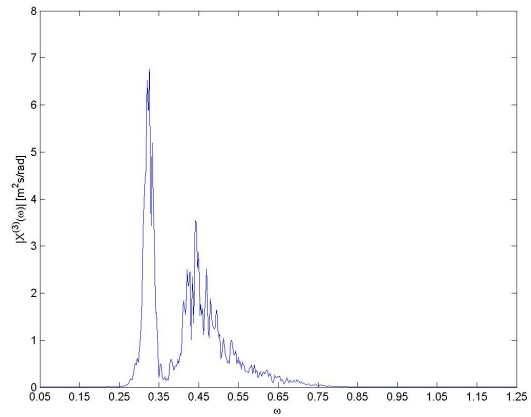
(d) Case 4

Figure 8.11: Surge PSD for different heave plate parameters, load case E.1

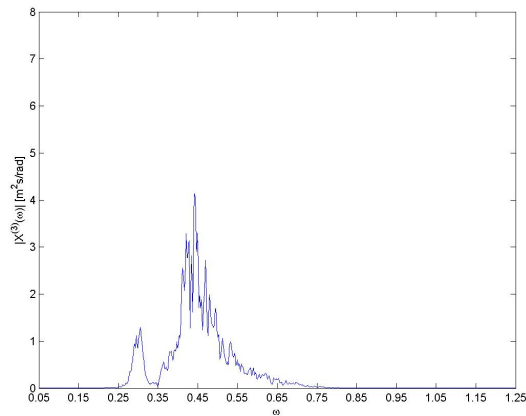




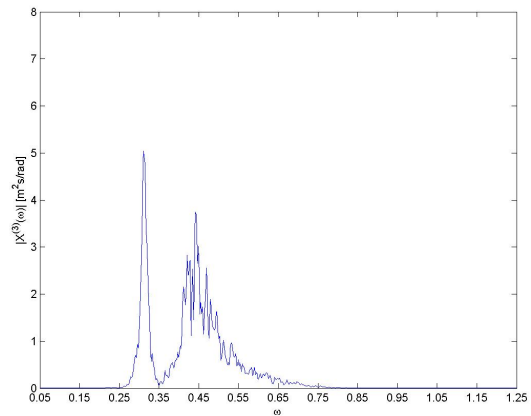
(a) Case 1



(b) Case 2

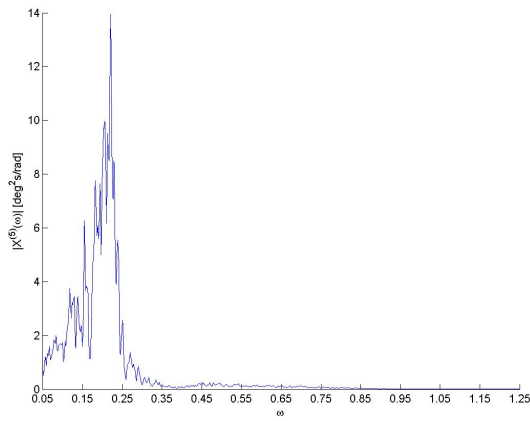


(c) Case 3

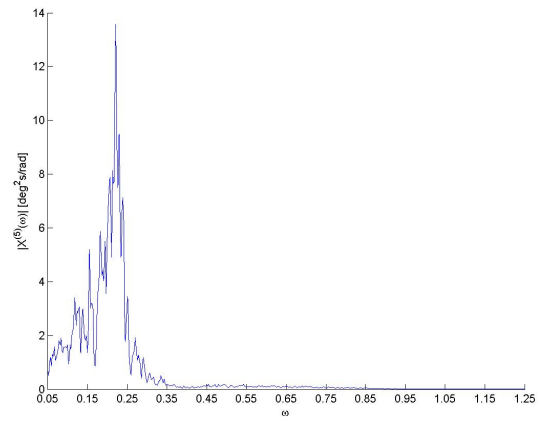


(d) Case 4

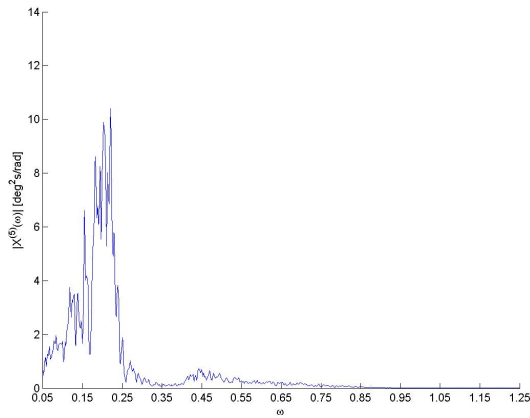
Figure 8.12: Heave PSD for different heave plate parameters, load case E.1



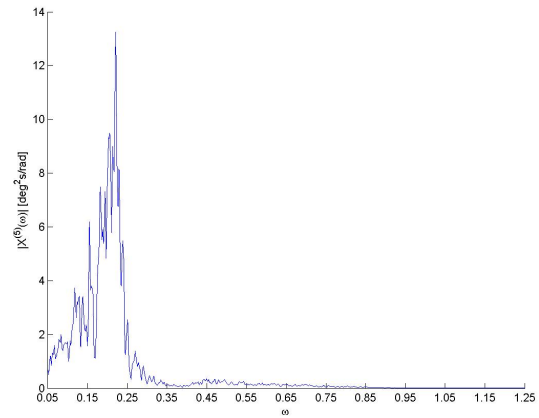
(a) Case 1



(b) Case 2

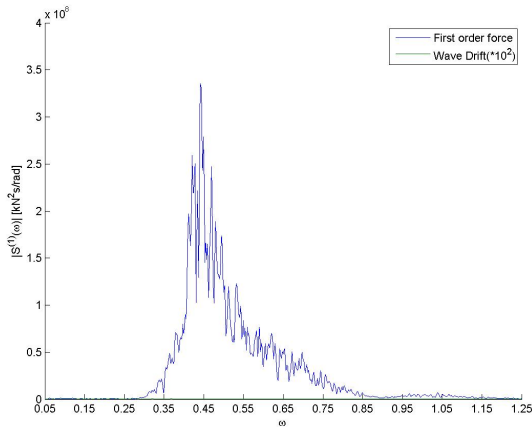


(c) Case 3

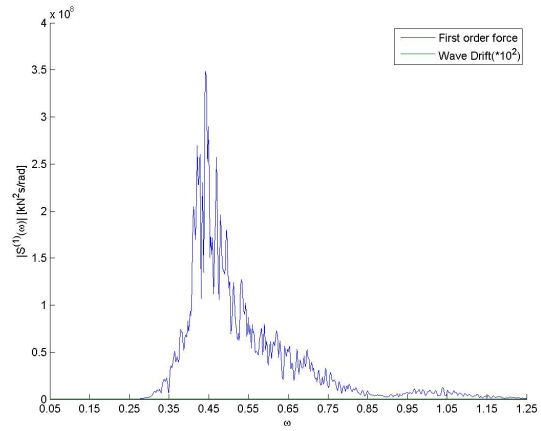


(d) Case 4

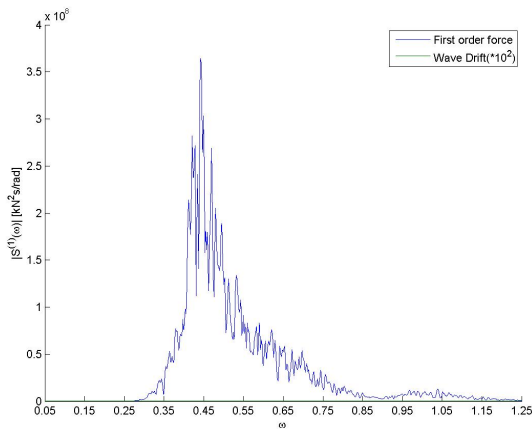
Figure 8.13: Pitch PSD for different heave plate parameters, load case M.1



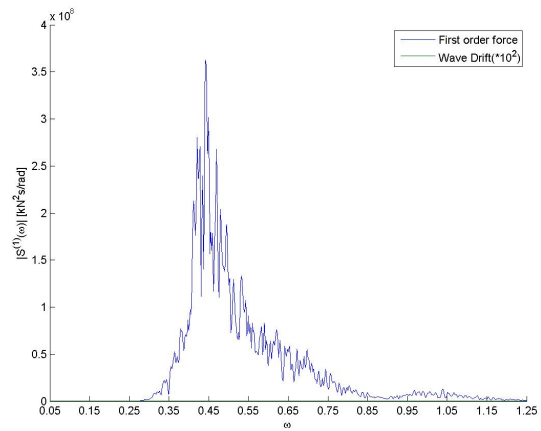
(a) Case 1



(b) Case 2

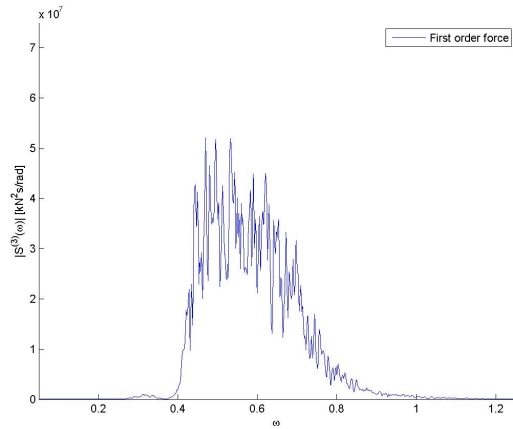


(c) Case 3

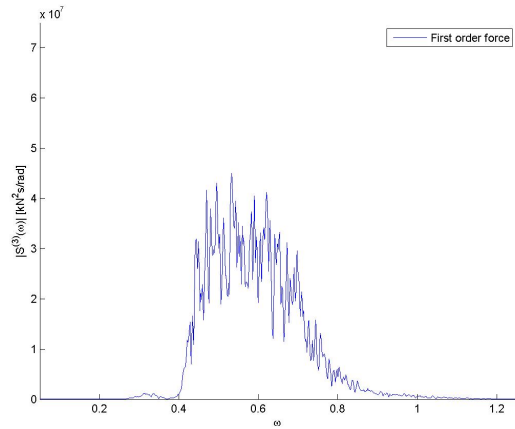


(d) Case 4

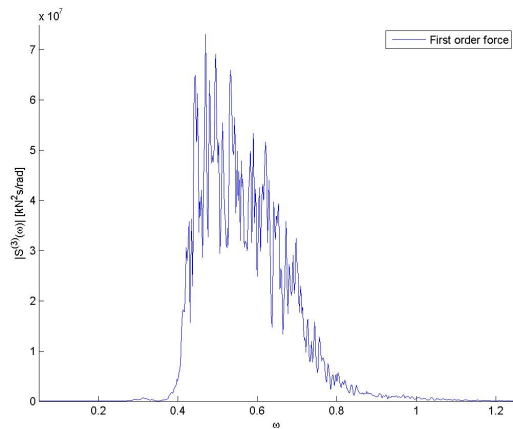
Figure 8.14: Surge first order excitation forces and mean wave drift PSD - load case E.1



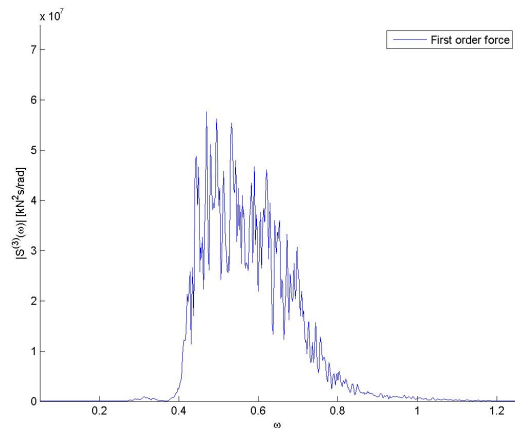
(a) Case 1



(b) Case 2

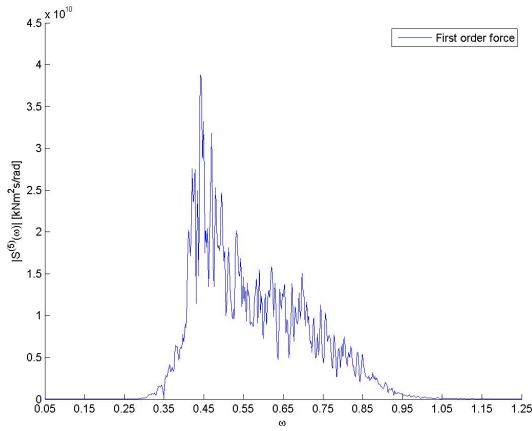


(c) Case 3

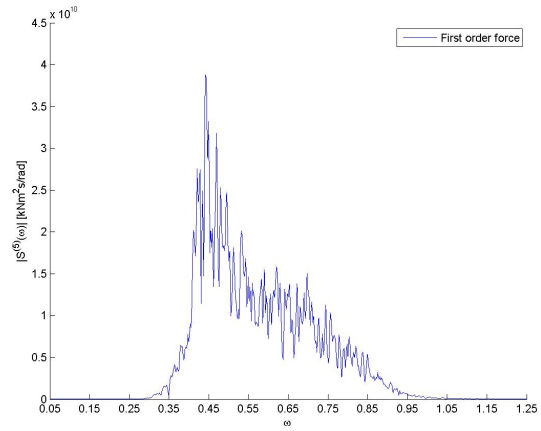


(d) Case 4

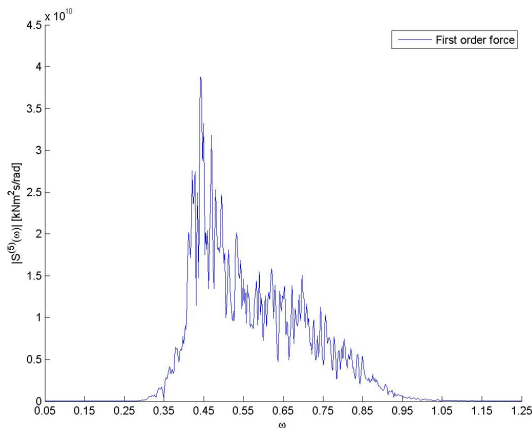
Figure 8.15: Heave first order excitation forces PSD - load case E.1



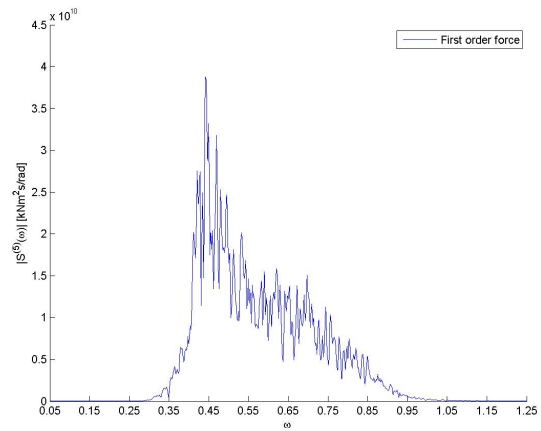
(a) Case 1



(b) Case 2

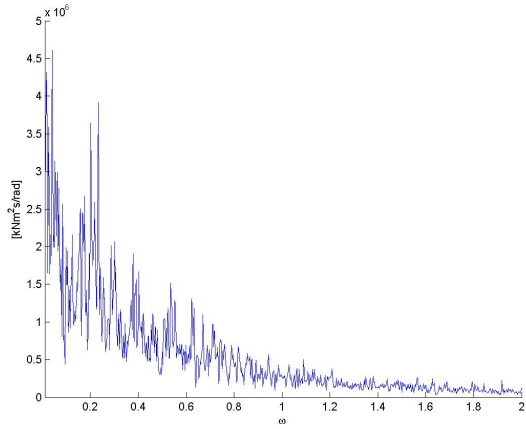


(c) Case 3

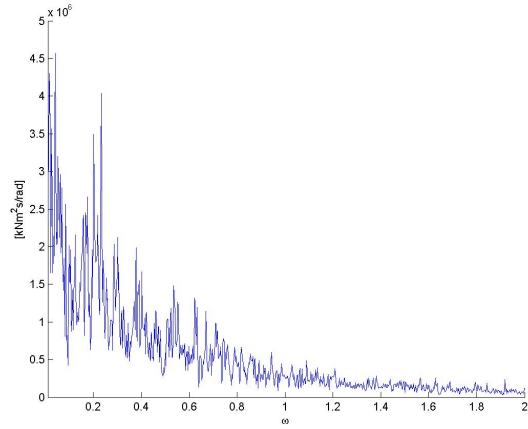


(d) Case 4

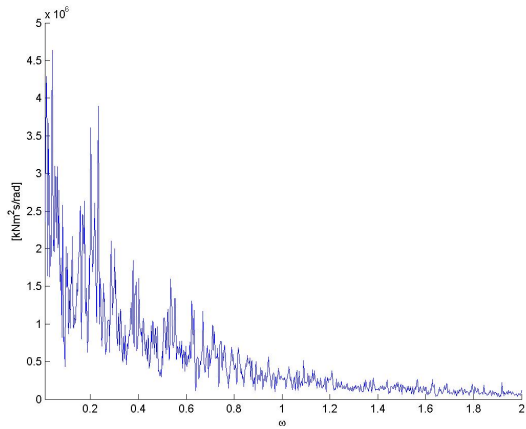
Figure 8.16: Pitch first order excitation forces PSD - load case E.1



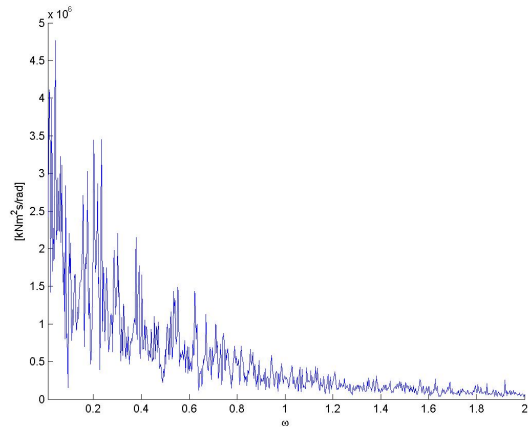
(a) Case 1



(b) Case 2



(c) Case 3



(d) Case 4

Figure 8.17: Aerodynamic pitch moment PSD - Case E.1

The extreme case response power spectral density illustrated a significant decrease in resonance behaviour, when compared to the intermediate water study. This was also the case for load case O.1 and to a lesser degree M.1. The trend was attributed to the absence of difference frequency excitation loads, and further supports the notion that these forces had a considerable contribution in the coupled analysis. A good approximation of slow drift forces are therefore needed to predict the FWT response in numerical analysis.

Consistent with the results in load case O.1, the excitation forces were higher for Design 3. Due to the higher loads, structural analysis will be needed to ensure the integrity of this design. However, Design 3 consistently had a smaller response than the other designs, with a less dense response spectrum around the natural frequency. Setting cost of material and production complexity aside, this design is therefore recommended. These factors have to be accounted for, as 163 tonnes of additional material are needed when compared to the original design. It is recommended that an analysis on the fatigue life and life cycle cost of energy for this heave plate design is carried out, to establish whether the more stable heave behaviour can lead to a more economically feasible concept.

High up-front production costs are already a factor that makes investors hesitant on FWT technology (Section 1.2). Therefore, it is recommended that double heave plate configurations with approximately the same displacement as the original design should be analyzed. The purpose of this is to take advantage of the added flow separation from two plates, while maintaining approximately the same cost of materials as for the original design of the 6 MW OO-Star Wind Floater studied in this thesis.

In order to confidently determined the added mass of the 6 MW OO Star heave plates, CFD and/or experimental analysis are required, and should be carried out. Finally, as mentioned in Section 2.1, the plate thickness should be assessed through structural analysis. Heave plates generally perform better with smaller thickness ratios and wider plates, and the structural integrity is therefore essential.





# Chapter 9

## Conclusion

Numerical models were set up at three different water depths. The models were analyzed in coupled time domain analysis, with environmental conditions corresponding to three North Sea locations in depths of 50, 80 and 110 metres. The numerical errors from the project thesis were addressed, and the wind turbine performance and mooring configuration were verified and discussed. The damping effect of heave plates were assessed through a literature study, and the findings were incorporated in the modelling process. Three new heave plate configurations were proposed for a parametric study and analyzed in coupled time-domain analysis.

The main observations in this master thesis are summarized in the following:

- Difference frequency excitation forces can not be neglected in intermediate water. For the pitch response in extreme conditions, the standard deviation of this force contribution was above 20 % compared to the first order force. The significance varied for each load case and degree of freedom, but it was concluded that they had a considerable effect on the FWT response.
- The response in time-domain analysis with and without second-order difference-frequency forces was compared in Chapter 8. Here, it was determined that the standard deviations of surge, heave and pitch responses were 17.3 %, 18.1 % and 51.5 % higher with the second order forces. It was consequently concluded that the difference-frequency excitation forces excited large resonance behaviour on the OO-Star Wind Floater, and that they have to be accounted for in semi-submersible FWT numerical analysis.
- The depth effects was evident for the difference frequency excitation forces in surge, heave and pitch. These forces consistently increased with decreasing water depth. For larger sea states, these depth effects had a significance for the response in surge and pitch. It was concluded that the OO-Star Wind Floater will be subject to larger surge and pitch responses in the intermediate water range, with the depth effects increasing for decreasing water depths.
- The first order excitation forces in heave increased with the water depth, with a significant

difference between the depths of 50 and 80 metres. As these results are directly based on a frequency-domain hydrodynamic analysis, the effect is considered to be due to the wave kinematics at the different depths.

- In the parametric study, Design 3 had the least amount of heave motions. This design contained two heave plates of equal geometry as the original design, with a spacing of 6 metres. In ULS, the standard deviation of the Design 3 heave response was 8.76 % lower than the original design. This concept also had a consistently lower surge response than the other concepts, while the pitch standard deviations were similar to the original design in load cases O.1 and E.1. Thus, based only on the hydrodynamic response, Design 3 was recommended.

## Recommendations for Further Work

Throughout the thesis work, some possible improvements to the numerical model were identified but never assessed due to time constraints. Based on the thesis work and findings in global time domain analysis, the subsequent areas was proposed for further work:

- One of the most challenging aspects of a FWT in intermediate water is the mooring configuration. This was not the scope of this thesis, and a relatively simple procedure was used to design the stationkeeping system. This was considered to have an effect on the FWT response, and further analysis with a state-of-the-art mooring configuration is required to fully map out the challenges of the OO-Star Wind Floater in intermediate water.
- The wind turbine control system used in this thesis is a modified version of a land-based turbine control system. This was observed to have an effect on the response, where the power output and thrust in below-rated wind speeds was unstable. It is therefore proposed to incorporate specialized control systems for FWT's, in order to have a more stable aerodynamic thrust in below-rated wind speeds and consequently reduce the pitch motions.
- Previous studies have shown that numerical analysis under-predict the difference-frequency excitation forces in shallow water. In this thesis, the frequency-range used to establish a quadratic transfer function for this effect is shown to over-predict the contribution in for low first order wave frequencies. For higher frequencies, the effect is over-predicted. Because of these uncertainties, it is recommended to carry out model tests on the 6 MW OO-Star Wind Floater to identify the numerical error for the difference-frequency excitation forces.
- The structural response of the proposed heave plates need to be assessed. This has to be done to validate the new designs, as well as to optimize the plate thickness and diameter.

- It is recommended that further analysis are carried out for heave plate designs with two or more plates. This is recommended in order to assess whether the added inertia effects of designing two smaller plates per cylinder can lead to more favorable response characteristics than for one large plate. Thus, it is recommended that further parametric investigations should be carried out with double heave plate configurations with column breadth/diameter ratios in the range between 1.25 and 1.5.
- A CFD and/or experimental study should be carried out to determine the KC-dependent added mass and damping of the OO Star 6 MW heave plates.
- A full cost and FLS analysis are recommended for Design 3, in order to determine whether the lower heave and surge motions can make the 6 MW OO-Star Wind Floater more economically feasible, despite the higher material costs and more complex production on the Design.



# Bibliography

- Antonutti, R., Peyrard, C., Johanning, L., Incecik, A., and Ingram, D. (2014). An investigation of the effects of wind-induced inclination on floating wind turbine dynamics: heave plate excursion. *Ocean Engineering*, 91:208–217.
- Arai, S. et al. (1995). Forces and circulation of horizontal cylinders submerged in regular waves. In *The Fifth International Offshore and Polar Engineering Conference*. International Society of Offshore and Polar Engineers.
- Arapogianni, A., Genachte, A.-B., Ochagavia, R. M., Vergara, J., Castell, D., Tsouroukdissian, A. R., Korbijn, J., Bolleman, N., Huera-Huarte, F., Schuon, F., et al. (2013). Deep water: The next step for offshore wind energy. *European Wind Energy Association (EWEA), Brussels, Belgium, ISBN*, pages 978–2.
- Bachynski, E. (2016). Lecture notes in integrated analysis of offshore wind turbine installations.
- Bachynski, E. E., Etemaddar, M., Kvittem, M. I., Luan, C., and Moan, T. (2013). Dynamic analysis of floating wind turbines during pitch actuator fault, grid loss, and shutdown. *Energy Procedia*, 35:210–222.
- Bailey, H., Brookes, K. L., and Thompson, P. M. (2014). Assessing environmental impacts of offshore wind farms: lessons learned and recommendations for the future. *Aquatic biosystems*, 10(1):8.
- Bayati, I., Jonkman, J., Robertson, A., and Platt, A. (2014). The effects of second-order hydrodynamics on a semisubmersible floating offshore wind turbine. In *Journal of Physics: Conference Series*, volume 524, page 012094. IOP Publishing.
- Blue H Engineering (2016). *About Blue H Engineering*.
- Borg, H. M., Mirzaei, M., and Bredmose, H. (2015). Qualification of innovative floating substructures for 10mw wind turbines and water depths greater than 50m. *DTU Wind Energy Report E*, 101.
- Carrington, D. (2014). Drifting off the coast of portugal, the frontrunner in the global race for floating windfarms. *The Guardian*.

- Castro-Santos, L., Filgueira-Vizoso, A., Carral-Couce, L., and Formoso, J. Á. F. (2016). Economic feasibility of floating offshore wind farms. *Energy*, 112:868–882.
- Chaney, K., Eggers, A. J., Moriarty, P. J., and Holley, W. E. (2001). Skewed wake induction effects on thrust distribution on small wind turbine rotors. *Journal of solar energy engineering*, 123(4):290–295.
- Chen, H., Moan, T., and Verhoeven, H. (2008). Safety of dynamic positioning operations on mobile offshore drilling units. *Reliability Engineering & System Safety*, 93(7):1072–1090.
- Corbetta, G. (2015). Wind energy scenarios for 2030. Technical report, The European Wind Energy Association.
- Cordle, A., Jonkman, J., et al. (2011). State of the art in floating wind turbine design tools. In *The Twenty-first International Offshore and Polar Engineering Conference*. International Society of Offshore and Polar Engineers.
- Council, G. W. E. (2017). Global wind statistics 2016.
- Cruz, J. and Atcheson, M. (2016). *Floating Offshore Wind Energy: The Next Generation of Wind Energy*. Springer.
- Cummins, W. (1962). The impulse response function and ship motions. Technical report, DTIC Document.
- DNV (2010). Environmental conditions and environmental loads -c205. *Recommended Practice*.
- DNV (2016). Loads and site conditions for wind turbines. *Recommended Practice*.
- DNV-GL (2013). Sesam user manual, genie v6. 4. *Concept design and analysis of offshore structures*. Det Norsk Veritas.
- Dr. Techn. Olav Olsen (2016). *OO-Star Wind Floater (pat.)*.
- Eik, K. J. and Nygaard, E. (2003). Statfjord late life metocean design basis. Technical report, Statoil.
- Faltinsen, O. (1993). *Sea loads on ships and offshore structures*, volume 1. Cambridge university press.
- Fylling, I., Larsen, C., Sødahl, N., Ormberg, H., Engseth, A., Passano, E., and Holthe, K. (1995). Riflex theory manual. *SINTEF report no. STF70 F, 95219:53*.
- Glauert, H. (1983). *The elements of aerofoil and airscrew theory*. Cambridge University Press.
- Gueydon, S., Duarte, T., and Jonkman, J. (2014). Comparison of second-order loads on a semisubmersible floating wind turbine. In *ASME 2014 33rd International Conference on Ocean, Offshore and Arctic Engineering*, pages V09AT09A024–V09AT09A024. American Society of Mechanical Engineers.

- Hansen, M. H., Hansen, A. D., Larsen, T. J., Øye, S., Sørensen, P., and Fuglsang, P. (2005). Control design for a pitch-regulated, variable speed wind turbine. Technical report.
- Hasselmann, K., Barnett, T., Bouws, E., Carlson, H., Cartwright, D., Enke, K., Ewing, J., Gienapp, H., Hasselmann, D., Kruseman, P., et al. (1973). Measurements of wind-wave growth and swell decay during the joint north sea wave project (jonswap). Technical report, Deutches Hydrographisches Institut.
- Ho, A. and Mbistrova, A. (2016). The european offshore wind industry key trends and statistics 1st half 2016. Technical report, The European Wind Energy Association.
- Ho, A., Mbistrova, A., and Corbetta, G. (2016). The european offshore wind industry - key trends and statistics 2015. Technical report, The European Wind Energy Association.
- IEC et al. (2009). Iec 61400-3. *Wind Turbines-Part, 3*.
- Ishihara, T., Phuc, P., and Sukegawa, H. (2007). A numerical study on the dynamic response of a floating offshore wind turbine system due to resonance and nonlinear wave. In *European Offshore Wind Conference & Exhibition*.
- James, R. and Ros, M. C. (2015). Floating offshore wind: market and technology review. *The Carbon Trust, London Google Scholar*.
- Johannessen, K., Meling, T. S., Hayer, S., et al. (2001). Joint distribution for wind and waves in the northern north sea. In *The Eleventh International Offshore and Polar Engineering Conference*. International Society of Offshore and Polar Engineers.
- Jonkman, B. J. (2009). Turbsim user's guide: Version 1.50.
- Jonkman, J., Butterfield, S., Musial, W., and Scott, G. (2009). Definition of a 5-mw reference wind turbine for offshore system development. *National Renewable Energy Laboratory, Golden, CO, Technical Report No. NREL/TP-500-38060*.
- Jonkman, J. M. and Buhl Jr, M. L. (2007). Loads analysis of a floating offshore wind turbine using fully coupled simulation. In *Wind Power Conference and Exhibition, Los Angeles, CA*. Citeseer.
- Karimirad, M. and Michailides, C. (2015). Dynamic analysis of a braceless semisubmersible offshore wind turbine in operational conditions. *Energy Procedia*, 80:21–29.
- Kimball, R., Goupee, A., Coulling, A., and Dagher, H. (2012). Model test comparisons of tlp, spar-buoy and semi-submersible floating offshore wind turbine systems. In *Society of Naval Architects Marine Engineering Annual Meeting, Providence, RI, Oct*, pages 24–26.
- Kvittem, M. I. (2014). Modelling and response analysis for fatigue design of a semi-submersible wind turbine.
- Larsen Hirth, M. (2016). Anbefaler at statoil får flytte hywind til oljeplattformer. *Sysla Grønn*.

- Li, L., Gao, Z., and Moan, T. (2013). Joint environmental data at five european offshore sites for design of combined wind and wave energy devices. In *ASME 2013 32nd International Conference on Ocean, Offshore and Arctic Engineering*, pages V008T09A006–V008T09A006. American Society of Mechanical Engineers.
- Li, Y. and Lin, M. (2010). Hydrodynamic coefficients induced by waves and currents for submerged circular cylinder. *Procedia Engineering*, 4:253–261.
- Lopez-Pavon, C. and Souto-Iglesias, A. (2015). Hydrodynamic coefficients and pressure loads on heave plates for semi-submersible floating offshore wind turbines: A comparative analysis using large scale models. *Renewable Energy*, 81:864–881.
- Lopez-Pavon, C., Watai, R. A., Ruggeri, F., Simos, A. N., and Souto-Iglesias, A. (2015). Influence of wave induced second-order forces in semisubmersible fowt mooring design. *Journal of Offshore Mechanics and Arctic Engineering*, 137(3):031602.
- Maritime, G. (2015). Anchor manual 2015, the guide to anchoring.
- Martin, P. and Farina, L. (1997). Radiation of water waves by a heaving submerged horizontal disc. *Journal of Fluid Mechanics*, 337:365–379.
- Matha, D. (2010). Model development and loads analysis of an offshore wind turbine on a tension leg platform with a comparison to other floating turbine concepts: April 2009. Technical report, National Renewable Energy Laboratory (NREL), Golden, CO.
- Matha, D., Schlipf, M., Pereira, R., Jonkman, J., et al. (2011). Challenges in simulation of aerodynamics, hydrodynamics, and mooring-line dynamics of floating offshore wind turbines. In *The Twenty-first International Offshore and Polar Engineering Conference*. International Society of Offshore and Polar Engineers.
- Moccia, J. (2014). Wind energy scenarios for 2020. Technical report, The European Wind Energy Association.
- Moreno, J., Thiagarajan, K. P., Cameron, M., and Urbina, R. (2015). Added mass and damping of a column with heave plate oscillating in waves.
- Myhr, A., Bjerkseter, C., Ågotnes, A., and Nygaard, T. A. (2014). Levelised cost of energy for offshore floating wind turbines in a life cycle perspective. *Renewable Energy*, 66:714 – 728.
- Neill, S. P., Hashemi, M. R., and Lewis, M. J. (2014). Optimal phasing of the european tidal stream resource using the greedy algorithm with penalty function. *Energy*, 73:997–1006.
- Nærum, E. S. (2016). Floating wind turbine in intermediate depth: Preliminary studies. Master's thesis, NTNU.
- Offshore Wind (2016). Principle power abandons windfloat project in oregon.



- Panofsky, H. A. and Dutton, J. (1984). Atmospheric turbulence: Models and methods for engineering applications, 397 pp.
- Patel, P. (2009). Floating wind turbines to be tested. *IEEE Spectrum*.
- Richard, M. (2016). Floating wind farms: Great concept, implausible economics. *Technology Review*.
- Robertson, A. N., Jonkman, J. M., et al. (2011). Loads analysis of several offshore floating wind turbine concepts. In *The Twenty-first International Offshore and Polar Engineering Conference*. International Society of Offshore and Polar Engineers.
- Robertson, A. N., Jonkman, J. M., Goupee, A. J., Coulling, A. J., Prowell, I., Browning, J., Masciola, M. D., and Molta, P. (2013). Summary of conclusions and recommendations drawn from the deepwind scaled floating offshore wind system test campaign. In *ASME 2013 32nd International Conference on Ocean, Offshore and Arctic Engineering*, pages V008T09A053–V008T09A053. American Society of Mechanical Engineers.
- Sandner, F., Amann, F., Azcona, J., Munduate, X., Bottasso, C., Campagnolo, F., and Robertson, A. (2015). Model building and scaled testing of 5mw and 10mw semi-submersible floating wind turbines. In *EERA DeepWind 2015 Conference (Trondheim, Norway)*.
- Statoil (2016). *Hywind Scotland Pilot Park*.
- Strahan, Z. (2014). History of wind turbines. *Renewable Energy World*.
- Sündermann, J. and Pohlmann, T. (2011). A brief analysis of north sea physics. *Oceanologia*, 53(3):663–689.
- Tao, L. and Cai, S. (2004). Heave motion suppression of a spar with a heave plate. *Ocean Engineering*, 31(5):669–692.
- Tao, L., Molin, B., Scolan, Y.-M., and Thiagarajan, K. (2007). Spacing effects on hydrodynamics of heave plates on offshore structures. *Journal of Fluids and structures*, 23(8):1119–1136.
- Torsethaugen, K., Haver, S., et al. (2004). Simplified double peak spectral model for ocean waves. In *The Fourteenth International Offshore and Polar Engineering Conference*. International Society of Offshore and Polar Engineers.
- Vengatesan, V., Varyani, K., Barltrop, N., et al. (1999). Wave-current forces on rectangular cylinder at low kc numbers. In *The Ninth International Offshore and Polar Engineering Conference*. International Society of Offshore and Polar Engineers.
- Veritas, D. N. (2010). Wadam user manual. *Det Norske Veritas*.
- Veritas, D. N. (2011). Modelling and analysis of marine operations. *Det Norske Veritas, tech. rep. DNV-RP-H103*.

Veritas, D. N. (2015). Dnv-os-e302: Offshore mooring chains.

Vryhof Anchors, B. (2010). Anchor manual 2010—the guide to anchoring. *AC Capelle a/d Yssel*.

Williams, M. O. et al. (2008). Wave mapping in uk waters. *Health and Safety Executive Res. Rep*, page 38.

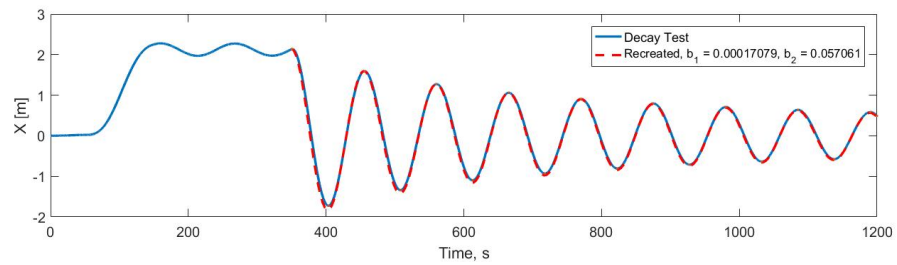
Xu, K. (2015). Design and analysis of mooring system for semi-submersible floating wind turbines in shallow water. Master's thesis, NTNU.

You, J. (2012). *Numerical studies on wave forces and moored ship motions in intermediate and shallow water*. PhD thesis, NTNU.

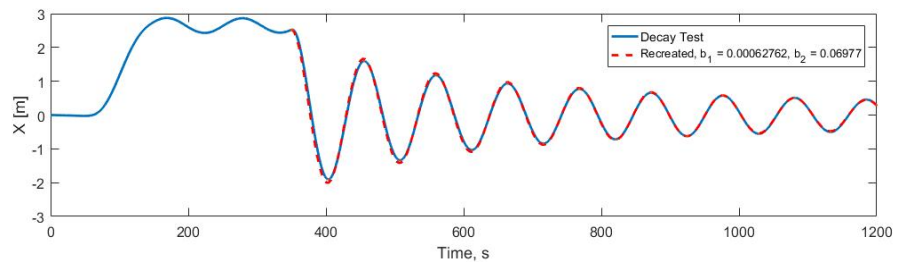
# Appendix A

## Free Decay

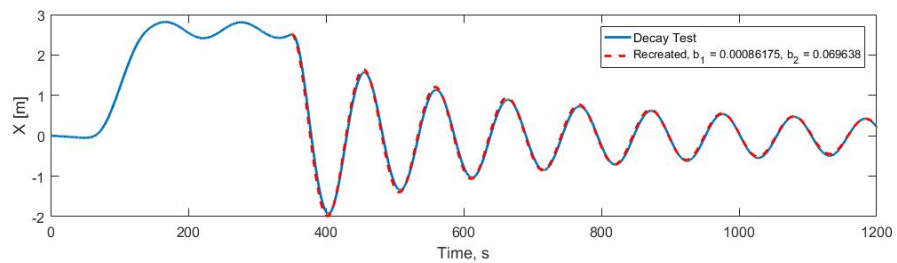
### A.1 Surge



(a) 50 m



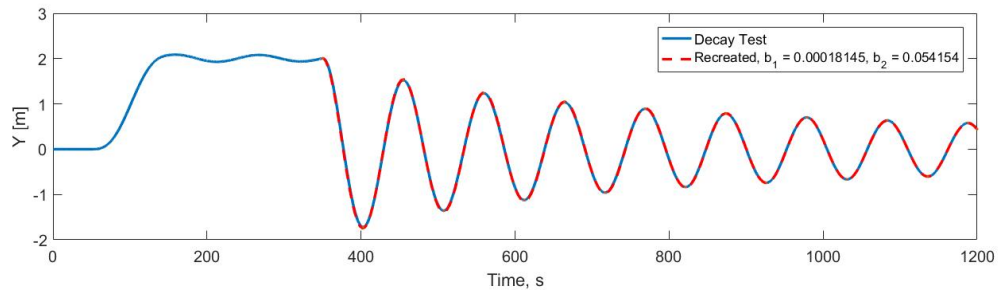
(b) 80 m



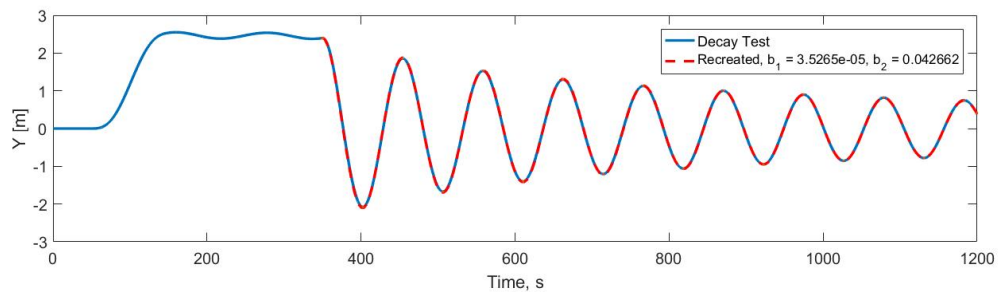
(c) 110 m

Figure A.1: Free decay tests in surge

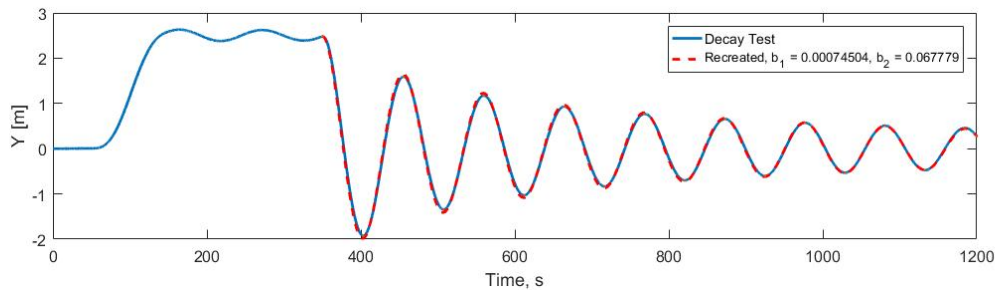
## A.2 Sway



(a) 50 m



(b) 80 m



(c) 110 m

Figure A.2: Free decay tests in sway

### A.3 Heave

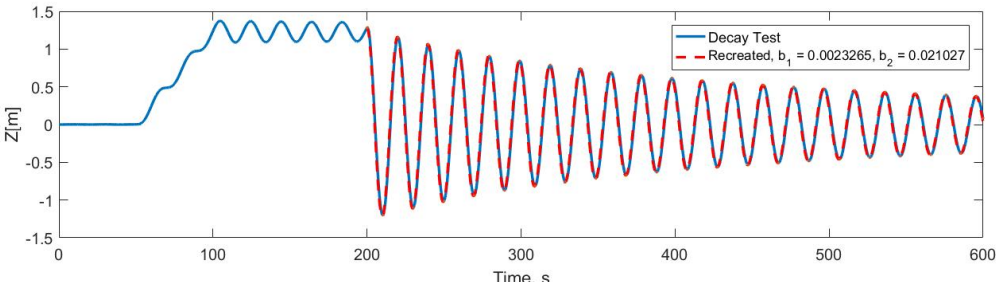
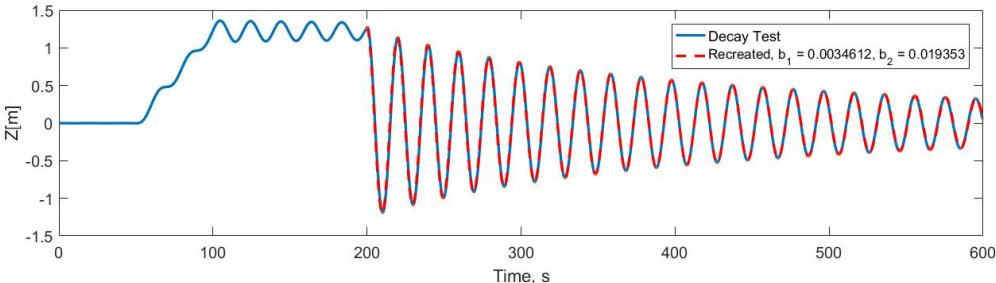
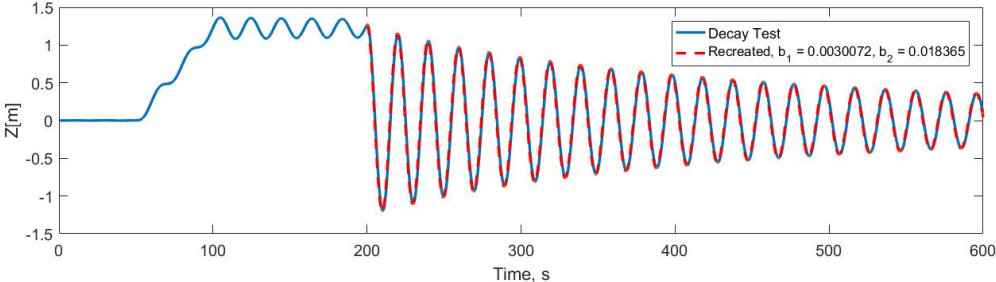
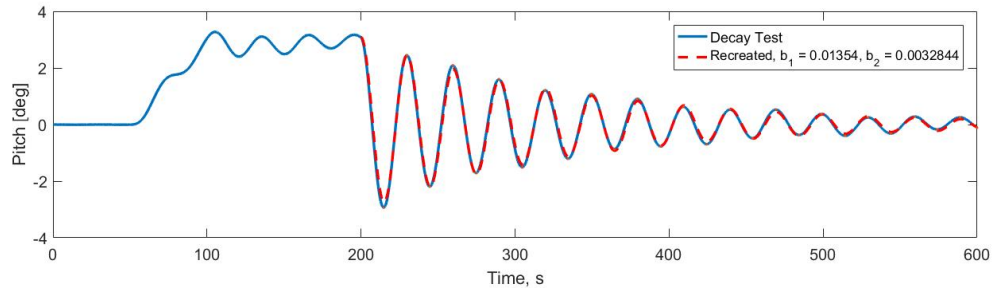
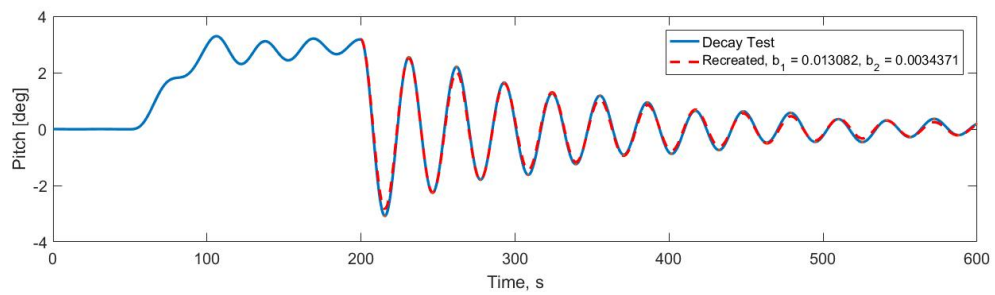


Figure A.3: Free decay tests in heave

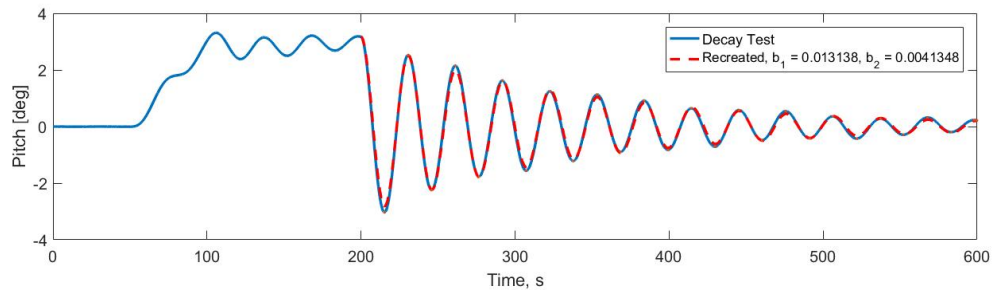
## A.4 Pitch



(a) 50 m



(b) 80 m

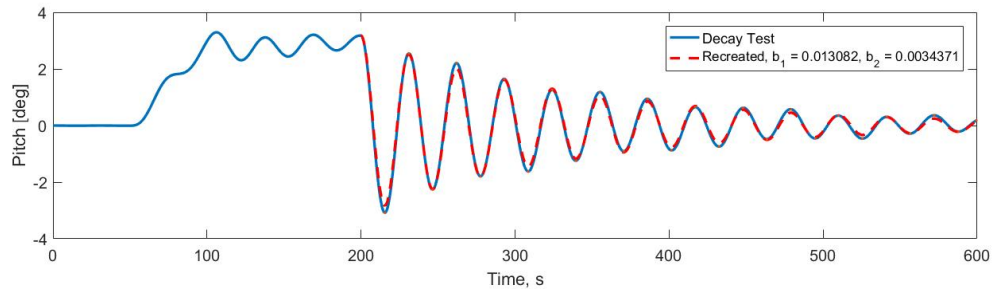


(c) 110 m

Figure A.4: Free decay tests in pitch

## A.5 Roll

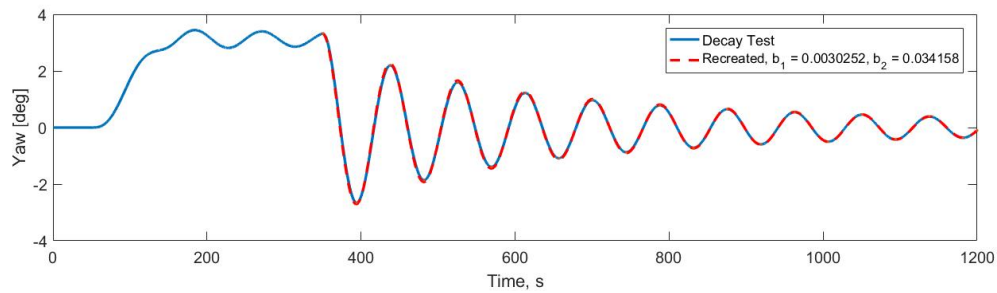
Only one free decay test were carried out for these DOF's, as the combination of the sway tests to describe the symmetry and the pitch free decay to describe the natural periods were considered sufficient.



(a) 110 m

Figure A.5: Free decay test in roll

## A.6 Yaw



(a) 110 m

Figure A.6: Free decay test in yaw





## **Appendix B**

### **Difference-Frequency Excitation Forces**

Due to the symmetry of the OO-Star Wind Floater, only the results for one half of the body are included. For the same reason, the sway and roll results have not been included, and the surge and pitch results are considered representative. The difference-frequency excitation forces are presented for different combinations of wave frequencies, and it is thus possible to deduct the accuracy of a Newman Approximation from the contour plots.

## B.1 50 m

### B.1.1 Surge

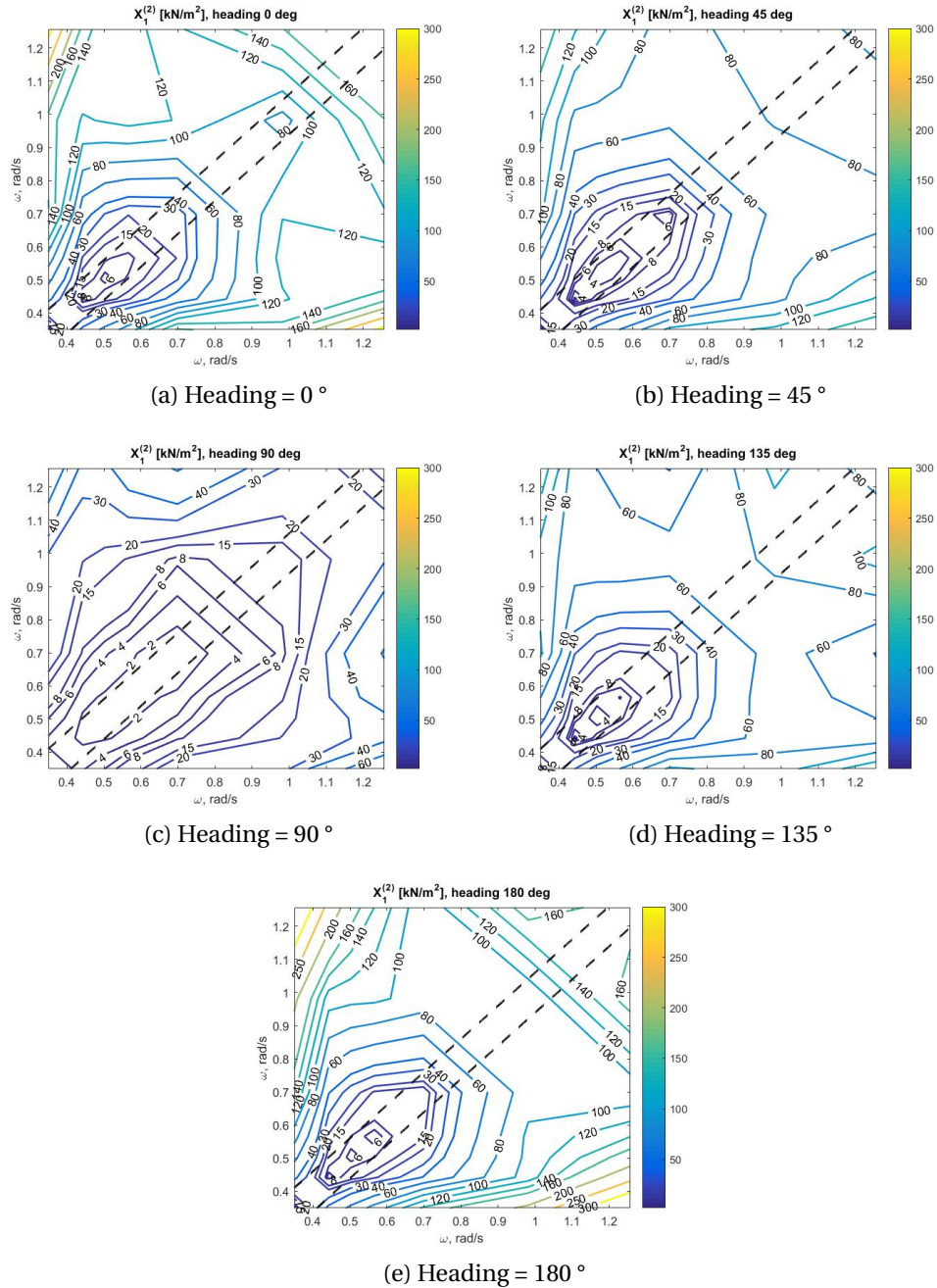


Figure B.1: Contour plots of surge difference-frequency excitation force at first-order wave frequencies

## B.1.2 Heave

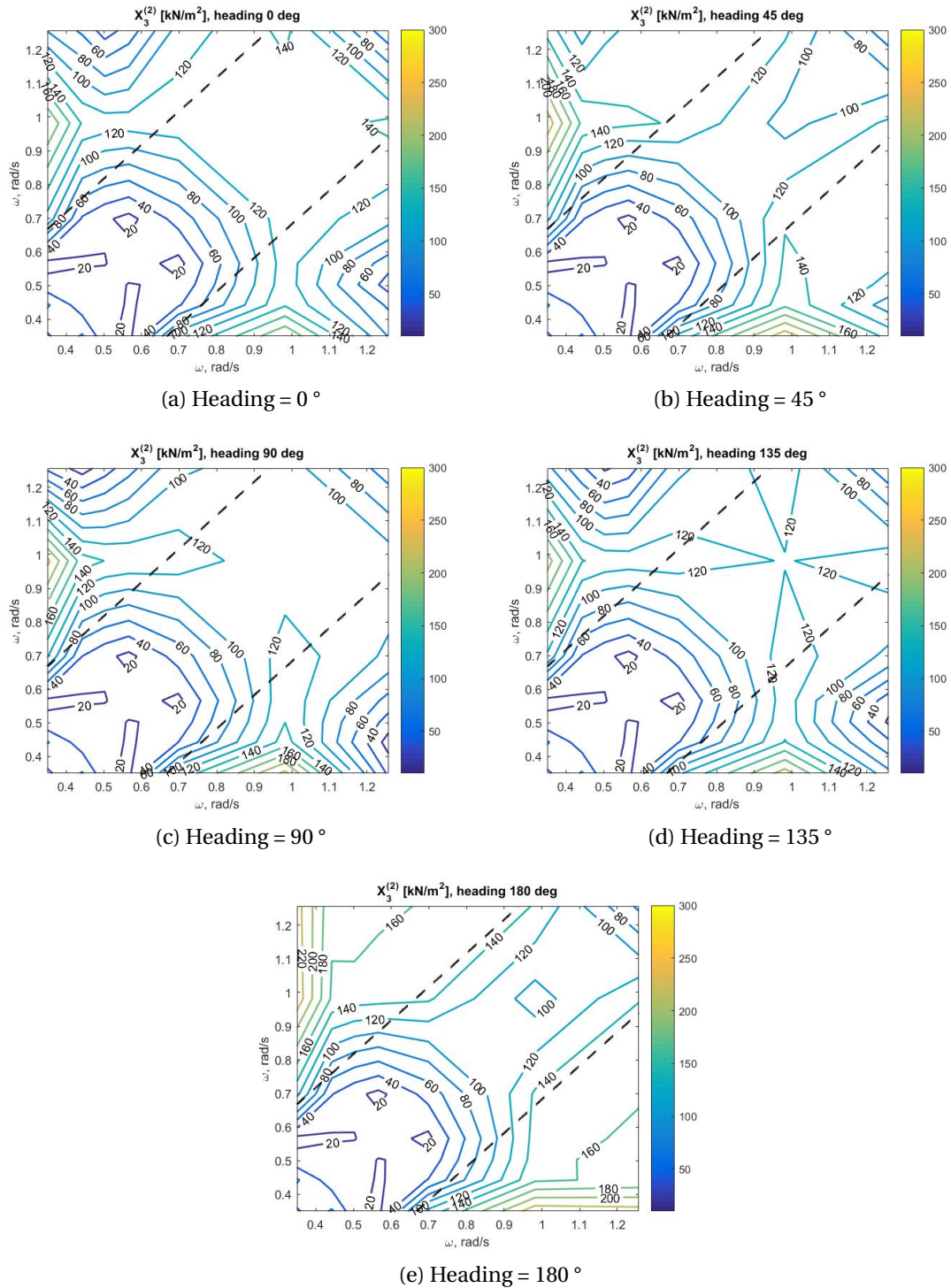


Figure B.2: Contour plots of heave difference-frequency excitation force at first-order wave frequencies

**B.1.3 Pitch**

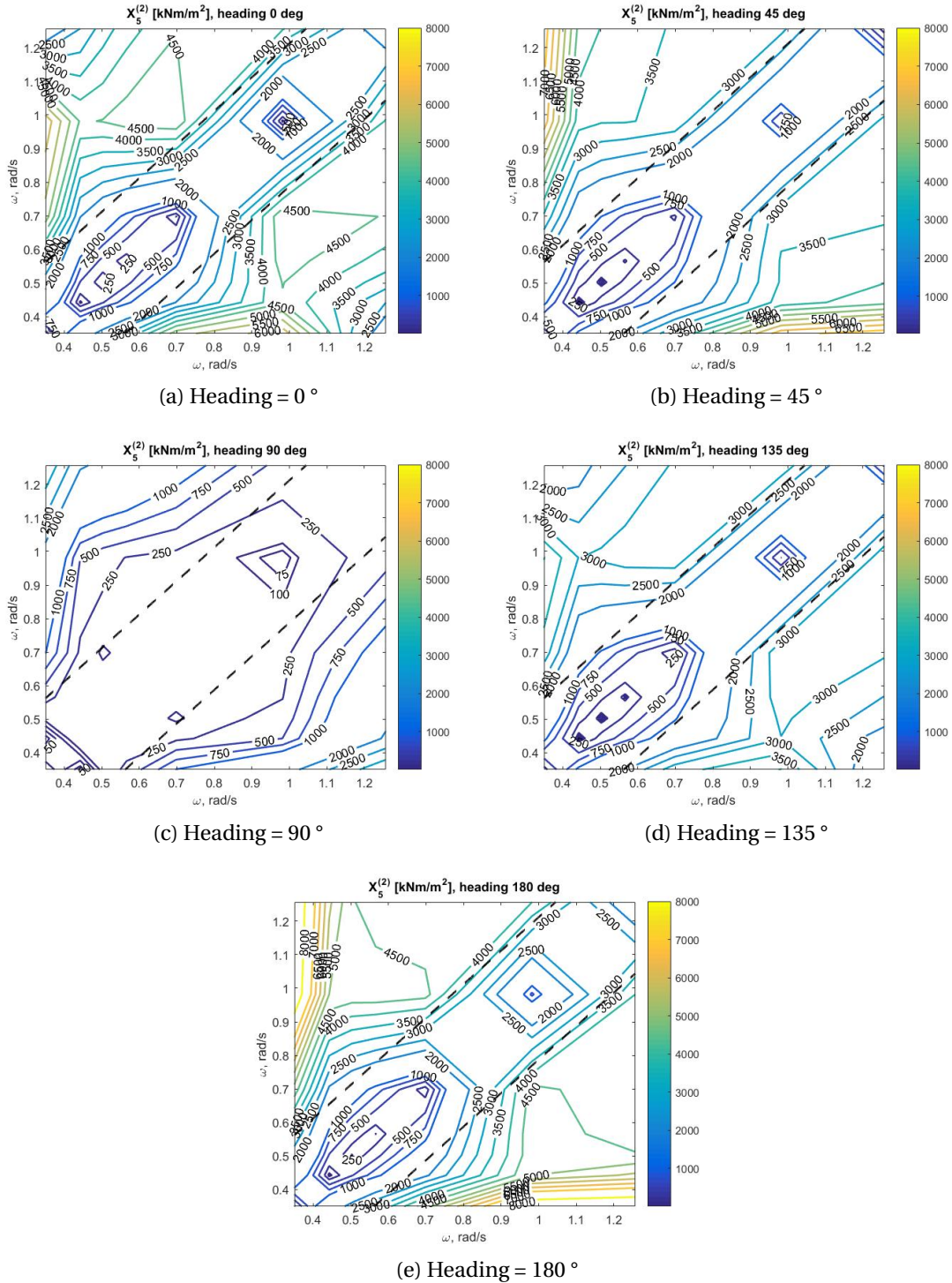


Figure B.3: Contour plots of pitch difference-frequency excitation force at first-order wave frequencies

**B.1.4 Yaw**

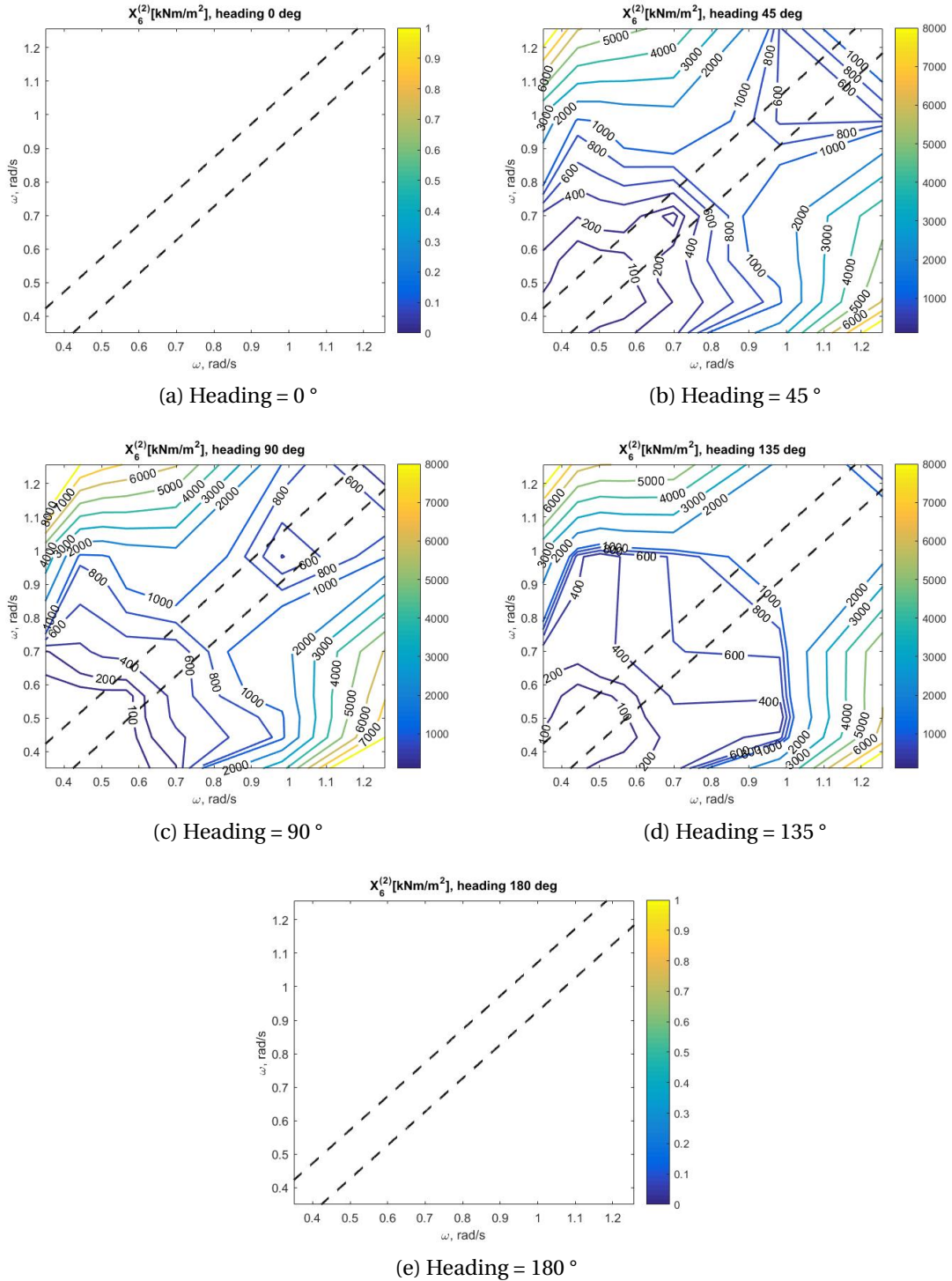


Figure B.4: Contour plots of yaw difference-frequency excitation force at first-order wave frequencies

## B.2 80 m

### B.2.1 Surge

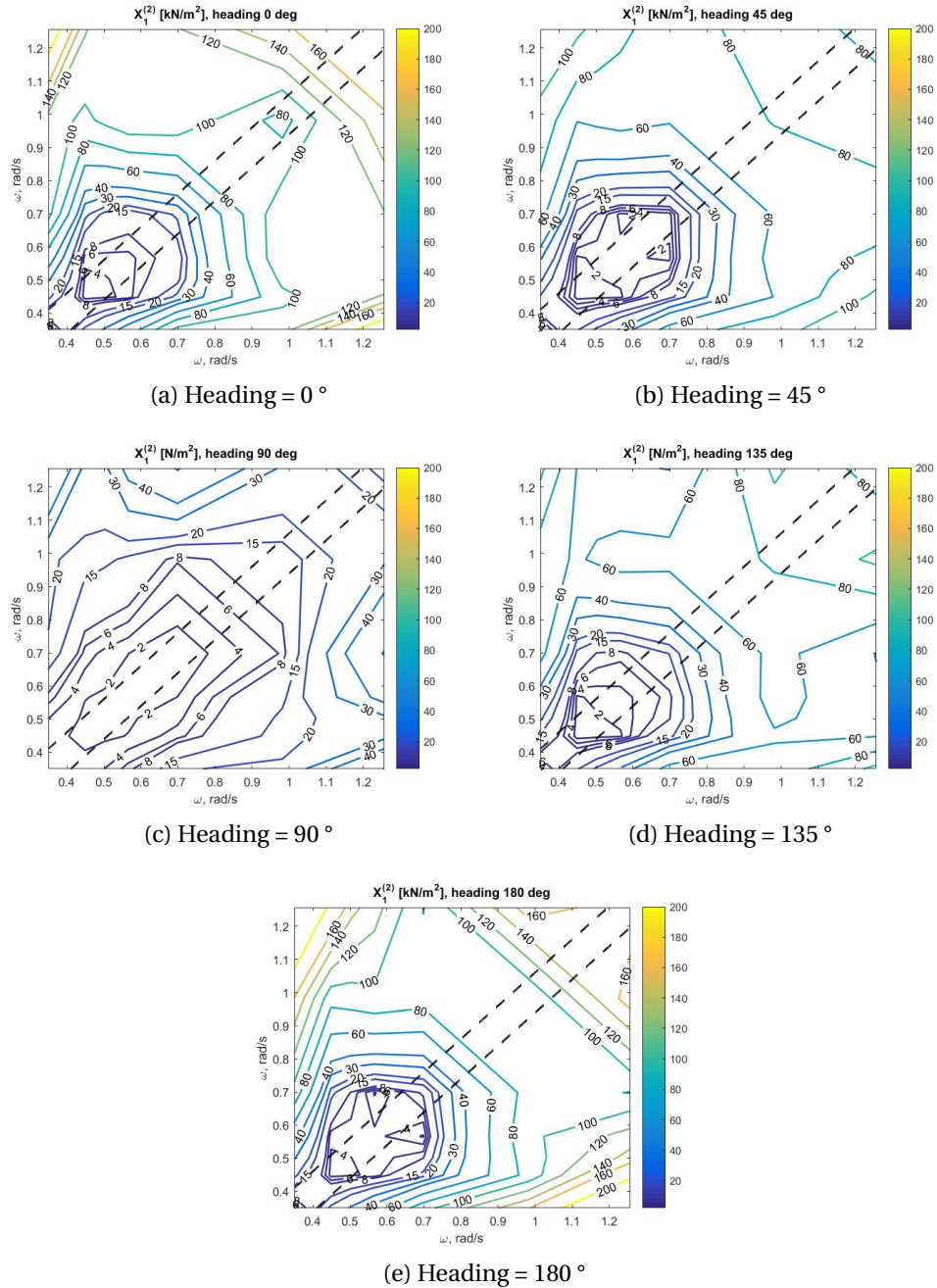


Figure B.5: Contour plots of surge difference-frequency excitation force at first-order wave frequencies

## B.2.2 Heave

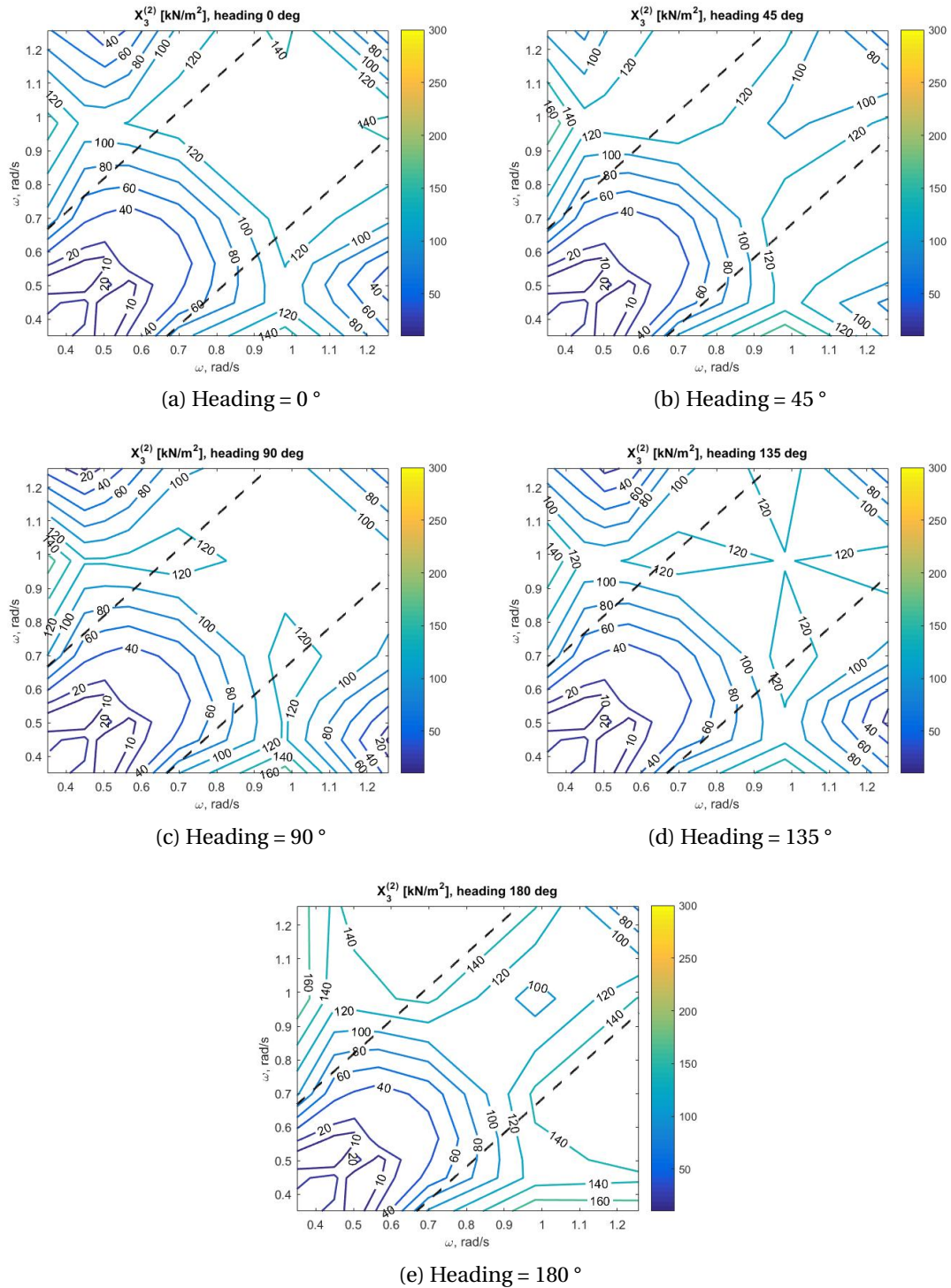


Figure B.6: Contour plots of heave difference-frequency excitation force at first-order wave frequencies

### B.2.3 Pitch

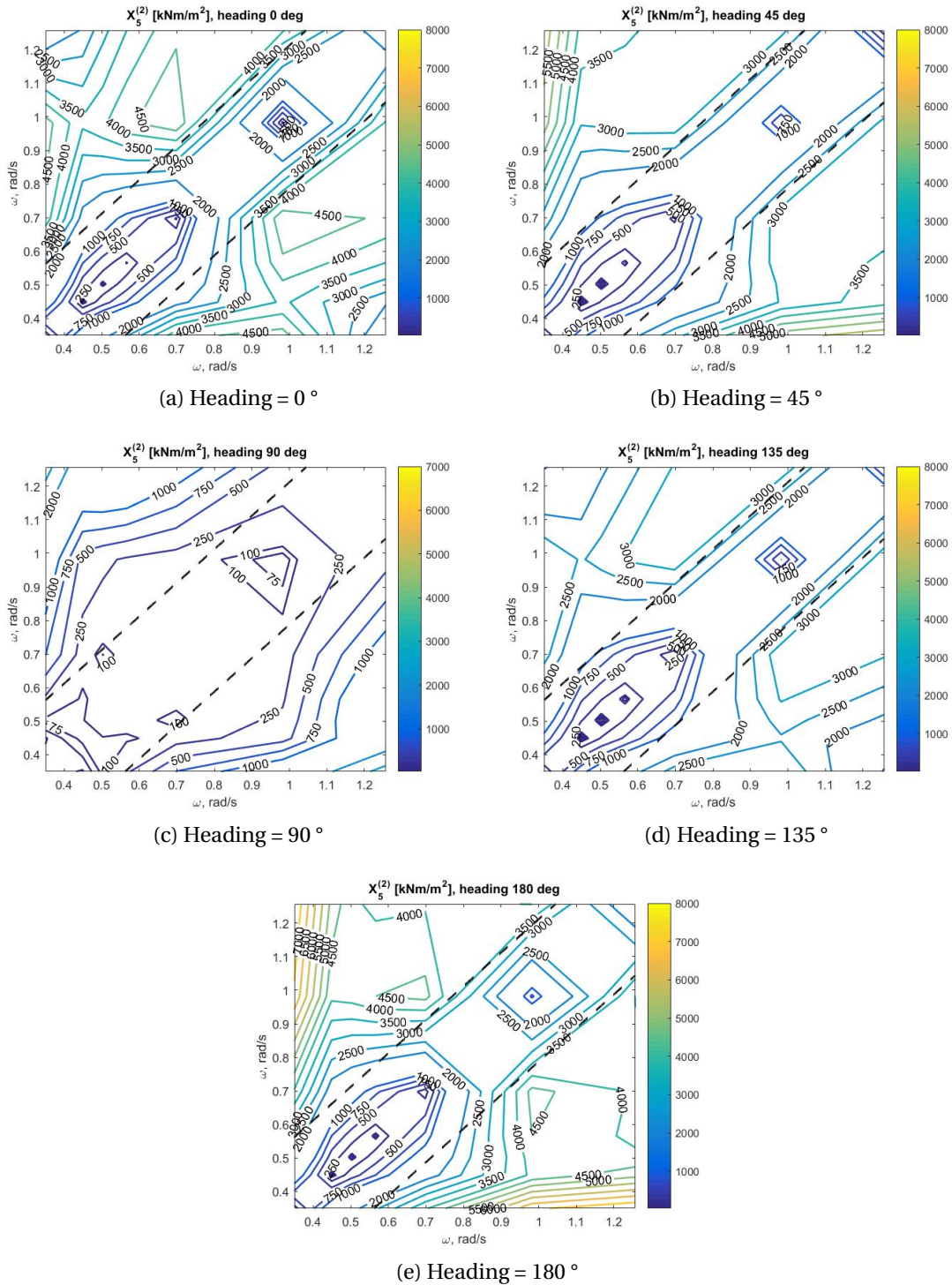


Figure B.7: Contour plots of pitch difference-frequency excitation force at first-order wave frequencies



**B.2.4 Yaw**

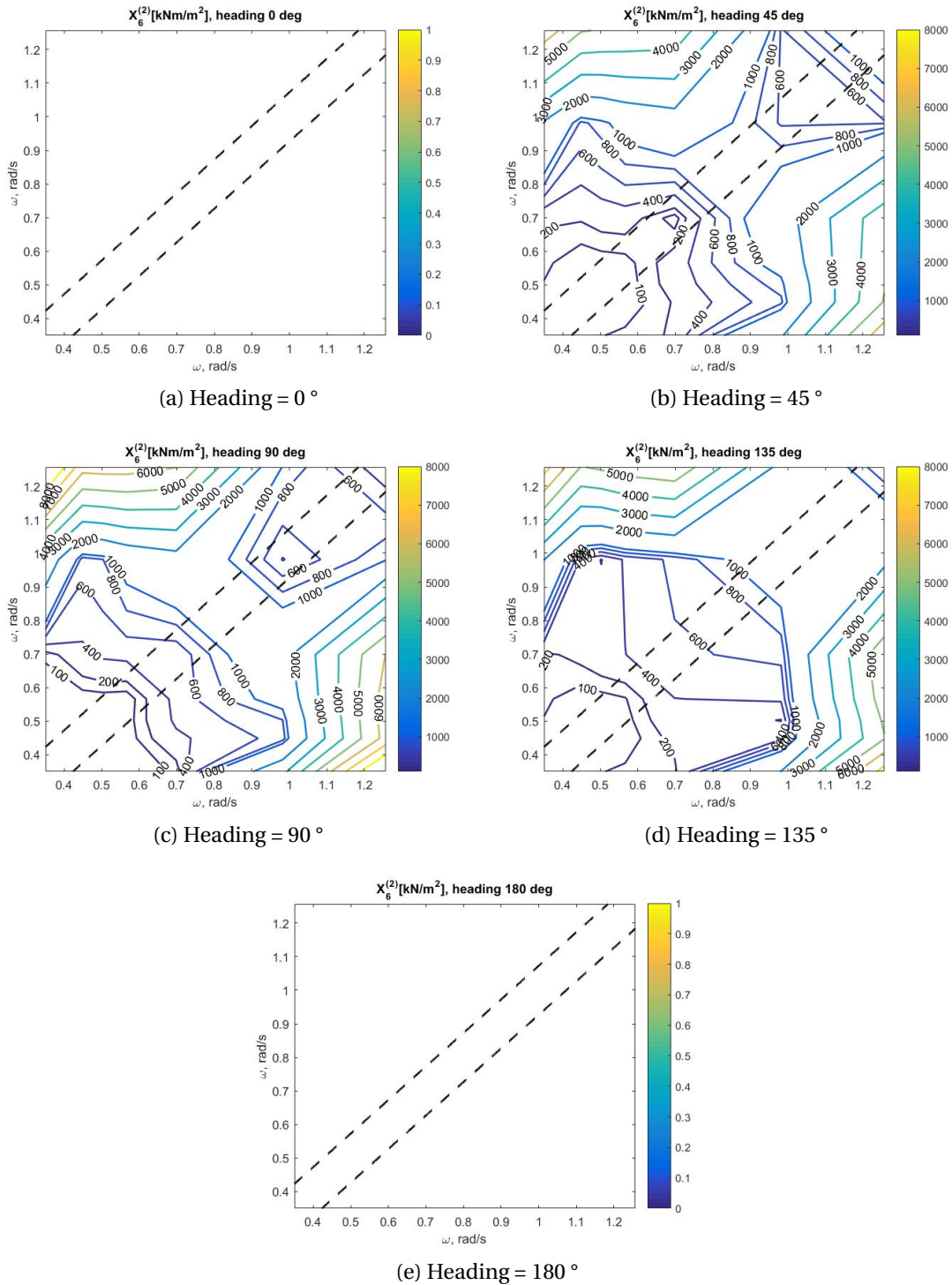


Figure B.8: Contour plots of yaw difference-frequency excitation force at first-order wave frequencies

### B.3 110 m

#### B.3.1 Surge

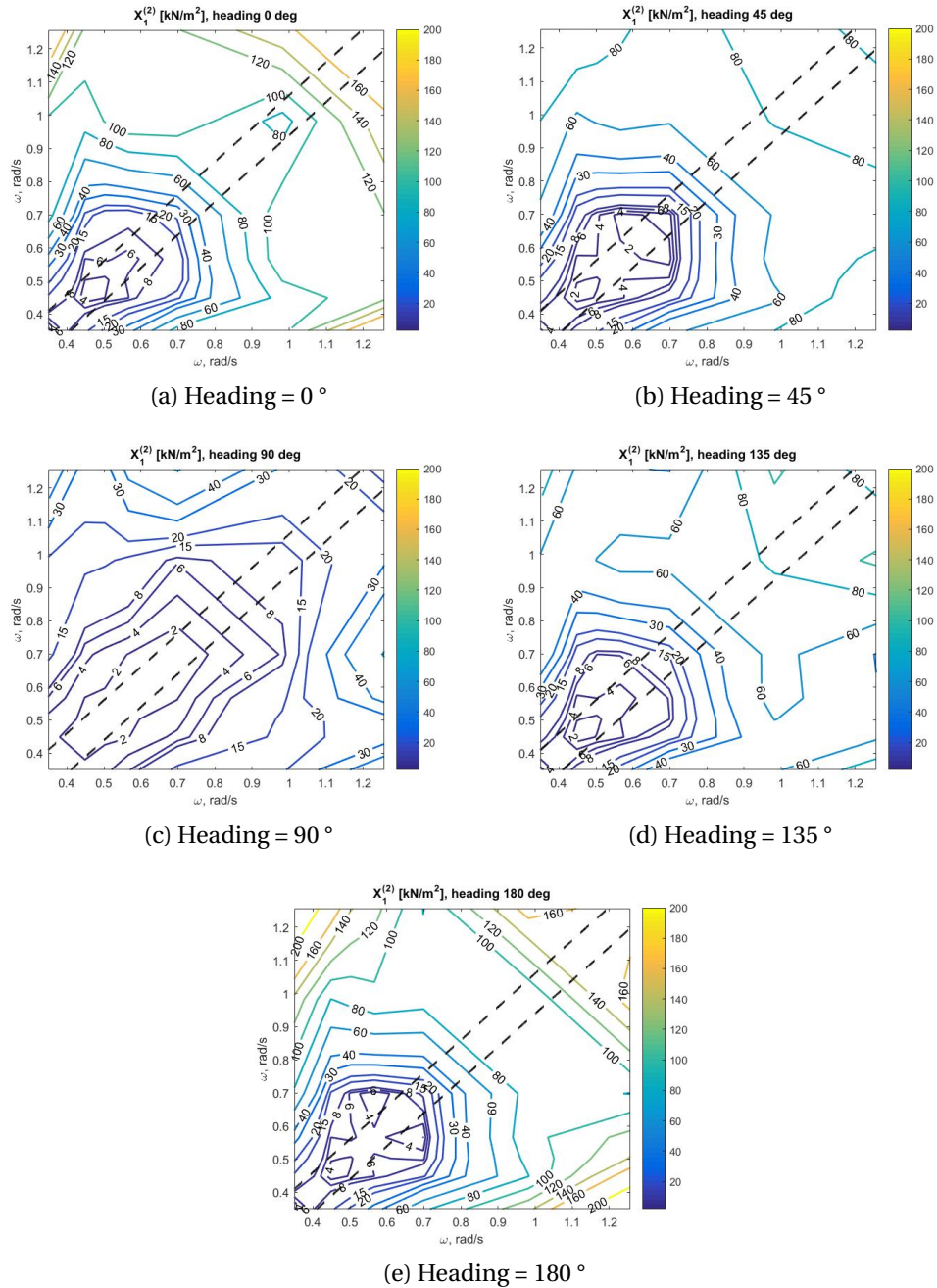


Figure B.9: Contour plots of surge difference-frequency excitation force at first-order wave frequencies

**B.3.2 Heave**

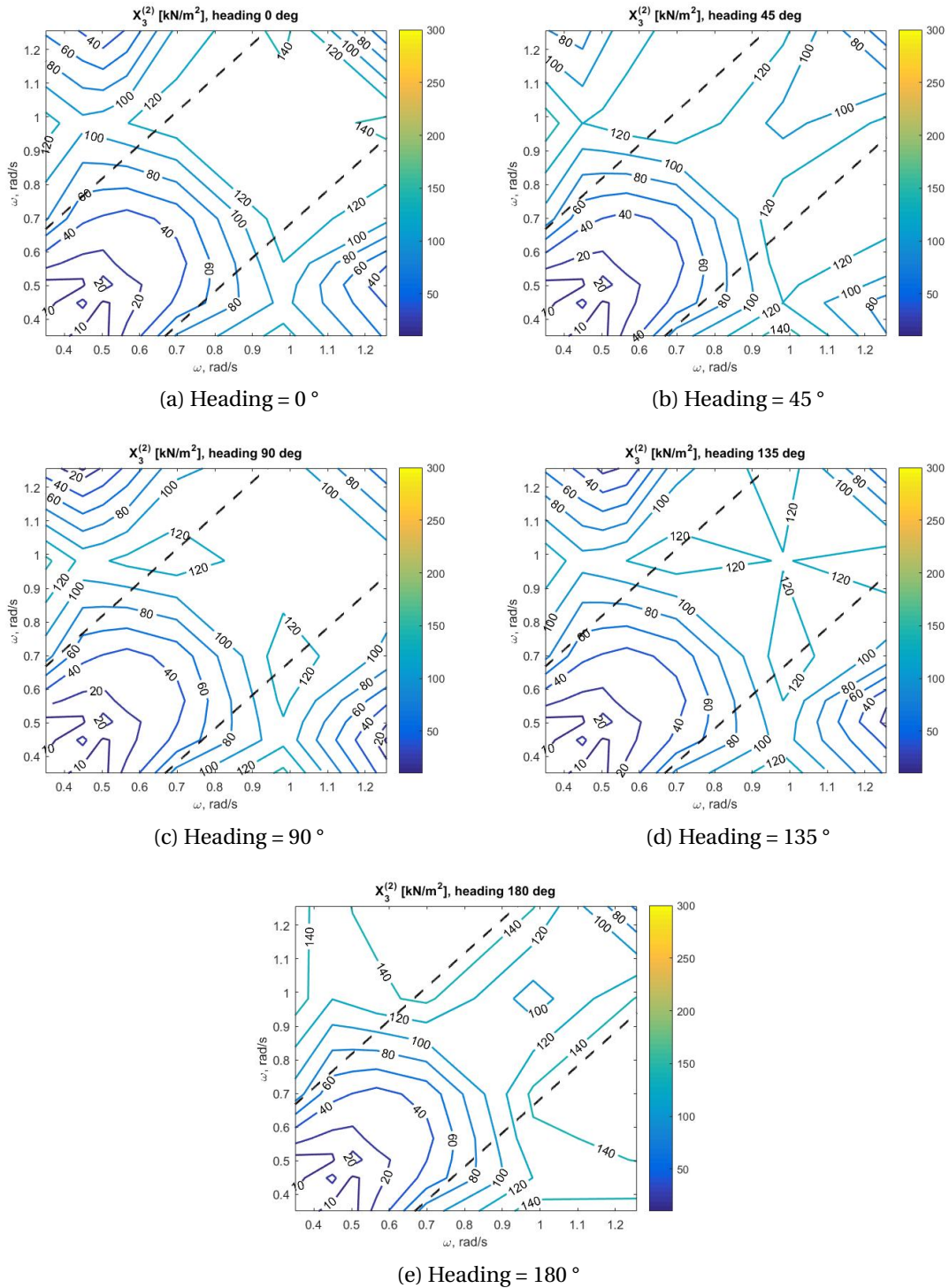


Figure B.10: Contour plots of heave difference-frequency excitation force at first-order wave frequencies

### B.3.3 Pitch

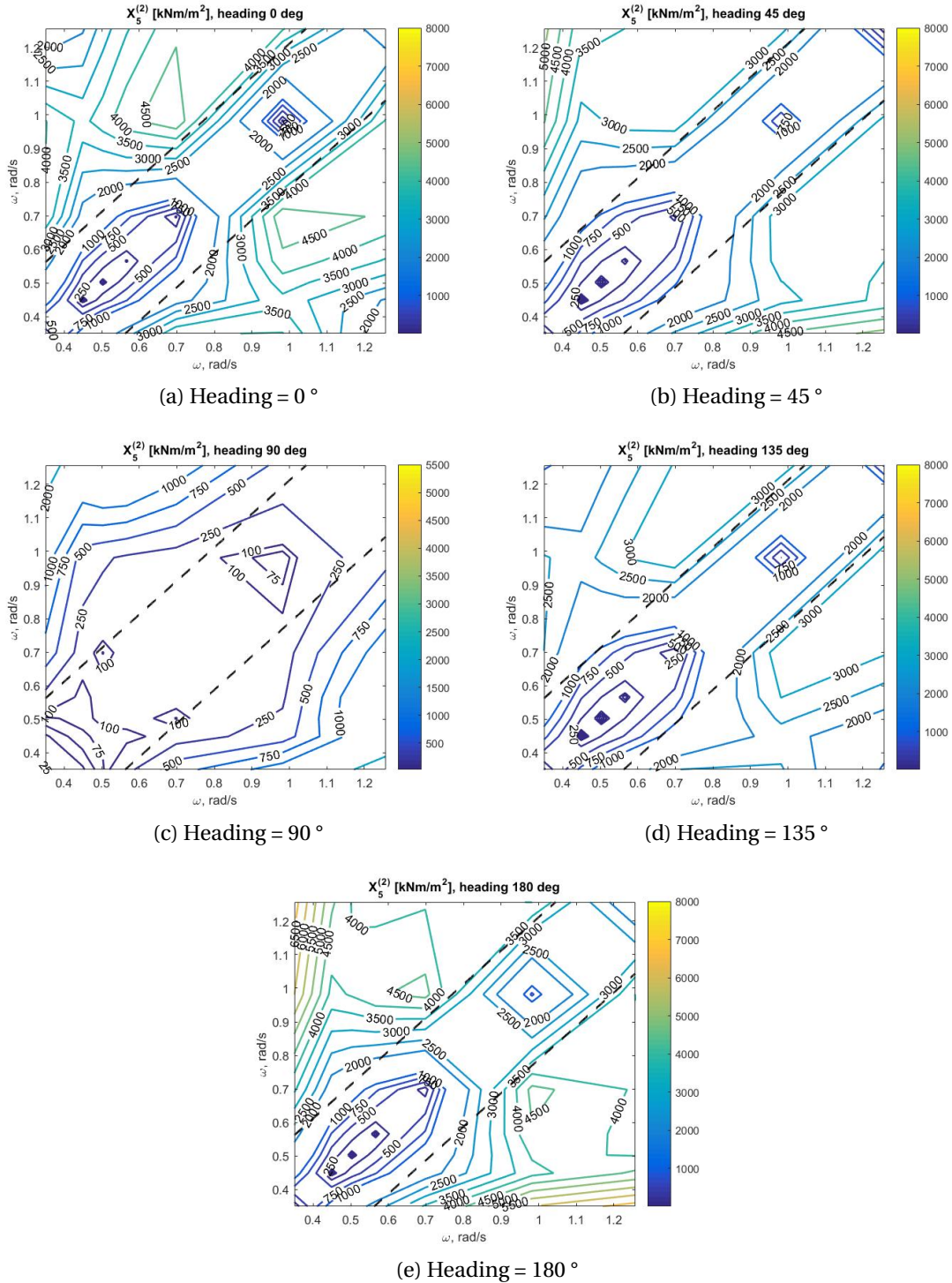


Figure B.11: Contour plots of pitch difference-frequency excitation force at first-order wave frequencies

**B.3.4 Yaw**

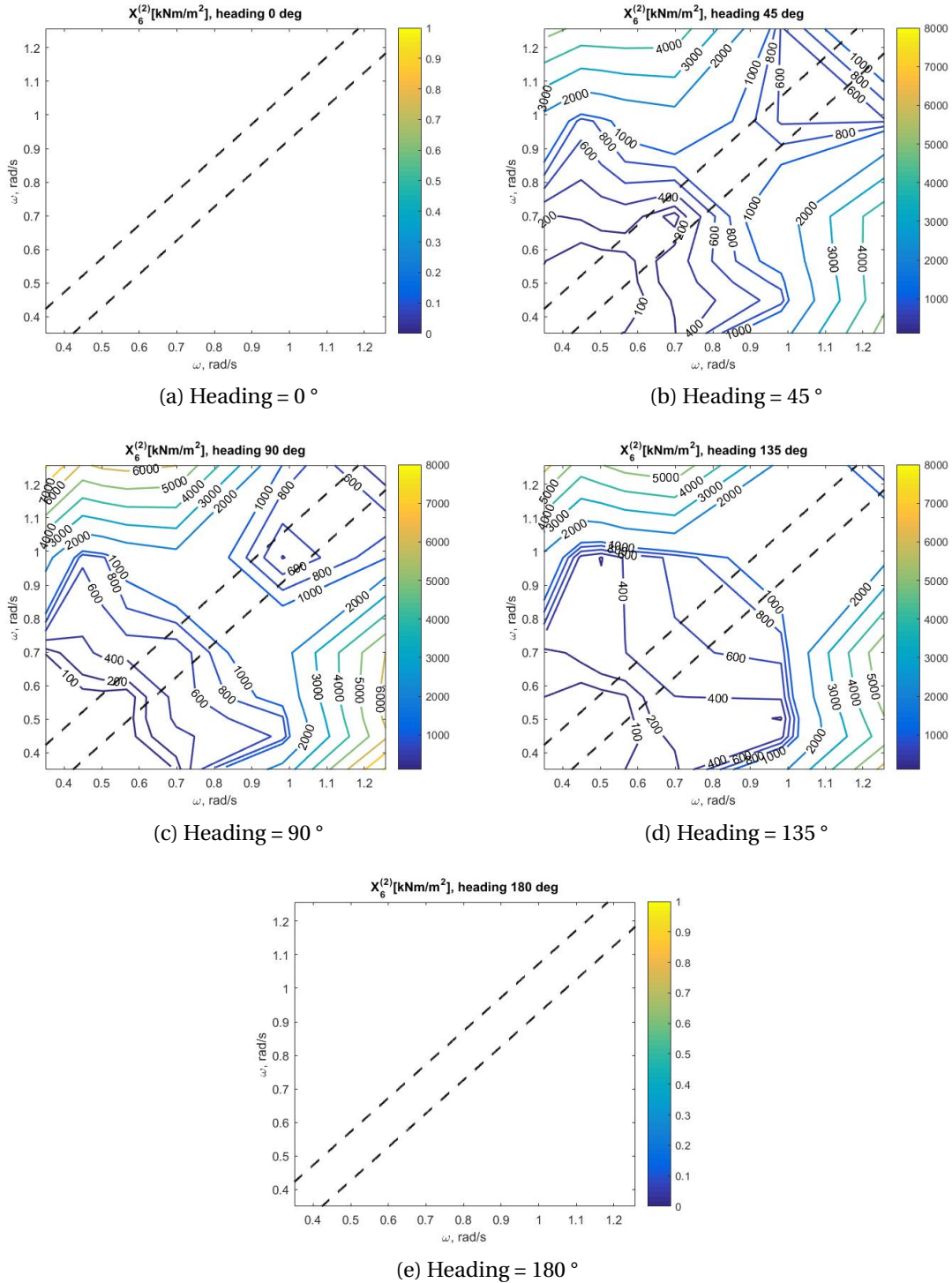


Figure B.12: Contour plots of yaw difference-frequency excitation force at first-order wave frequencies

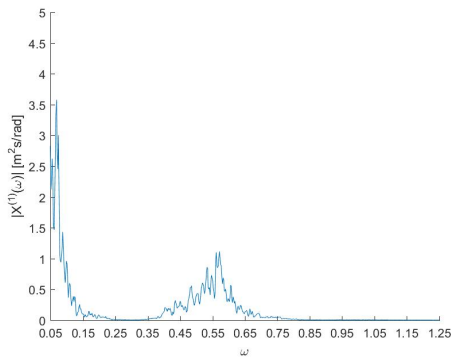


# Appendix C

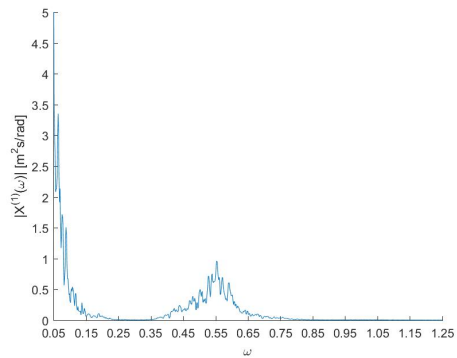
## FWT Time-Series and Spectrums

### C.1 Global FWT Motion Spectrum

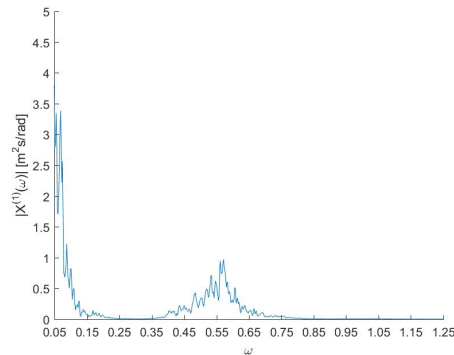
#### C.1.1 Case O1



(a) 50 m



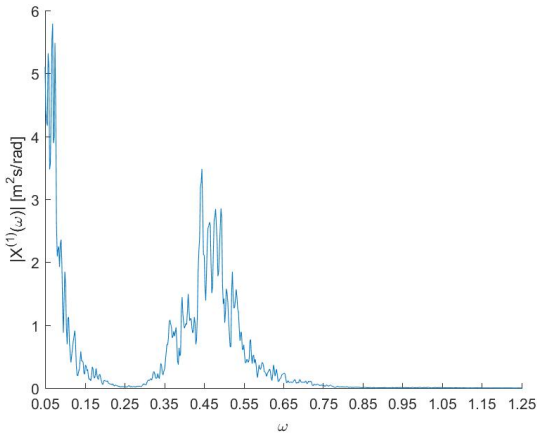
(b) 80 m



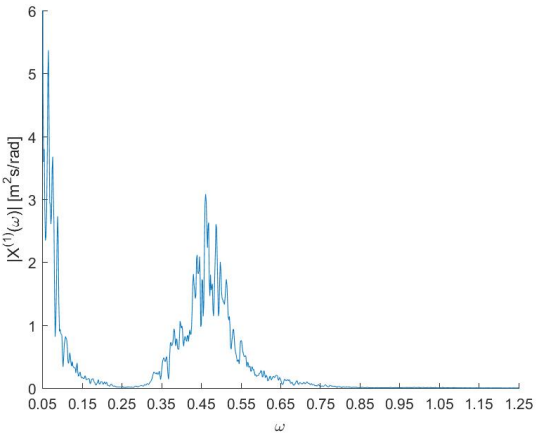
(c) 110 m

Figure C.1: FWT Surge response spectrum

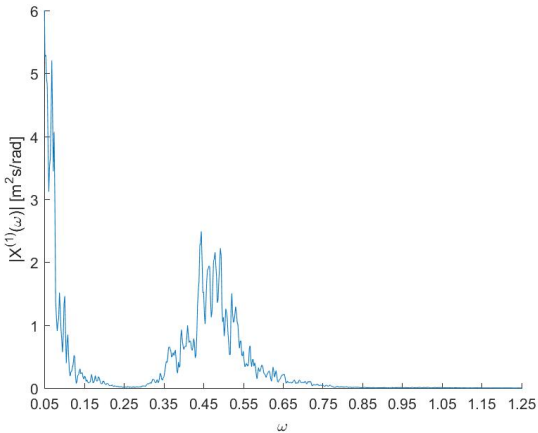
C.1.2 Case O2



(a) 50 m



(b) 80 m

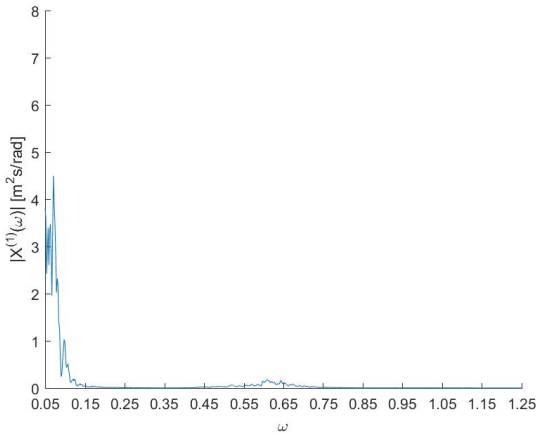


(c) 110 m

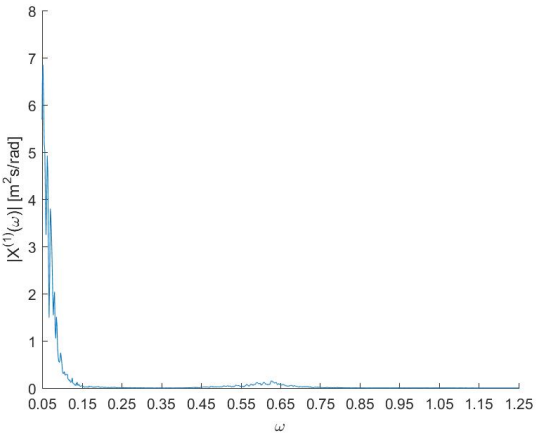
Figure C.2: FWT Surge response spectrum



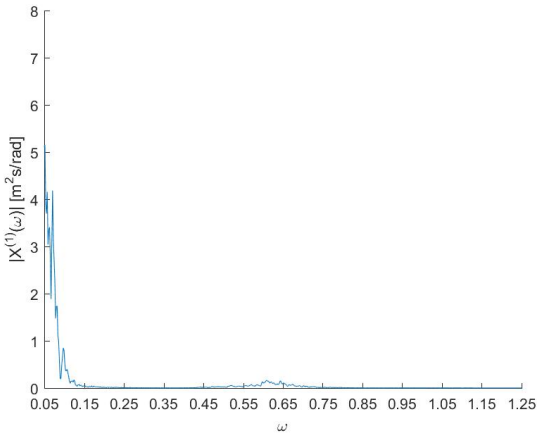
C.1.3 Case M1



(a) 50 m



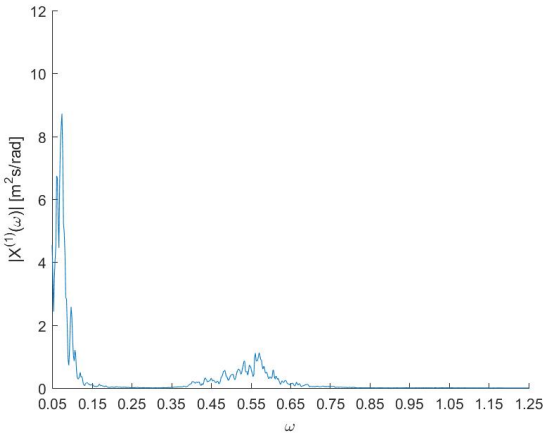
(b) 80 m



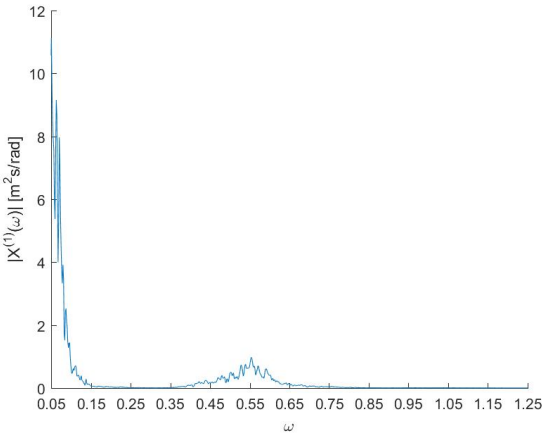
(c) 110 m

Figure C.3: FWT Surge response spectrum

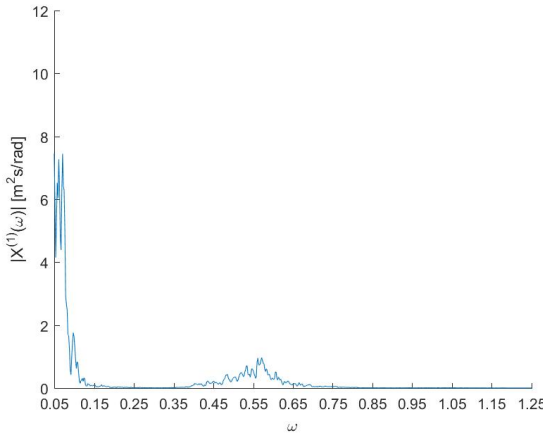
C.1.4 Case M2



(a) 50 m



(b) 80 m



(c) 110 m

Figure C.4: FWT Surge response spectrum

## C.2 Wave Loads in Time-Domain Simulation

### C.2.1 Case O1

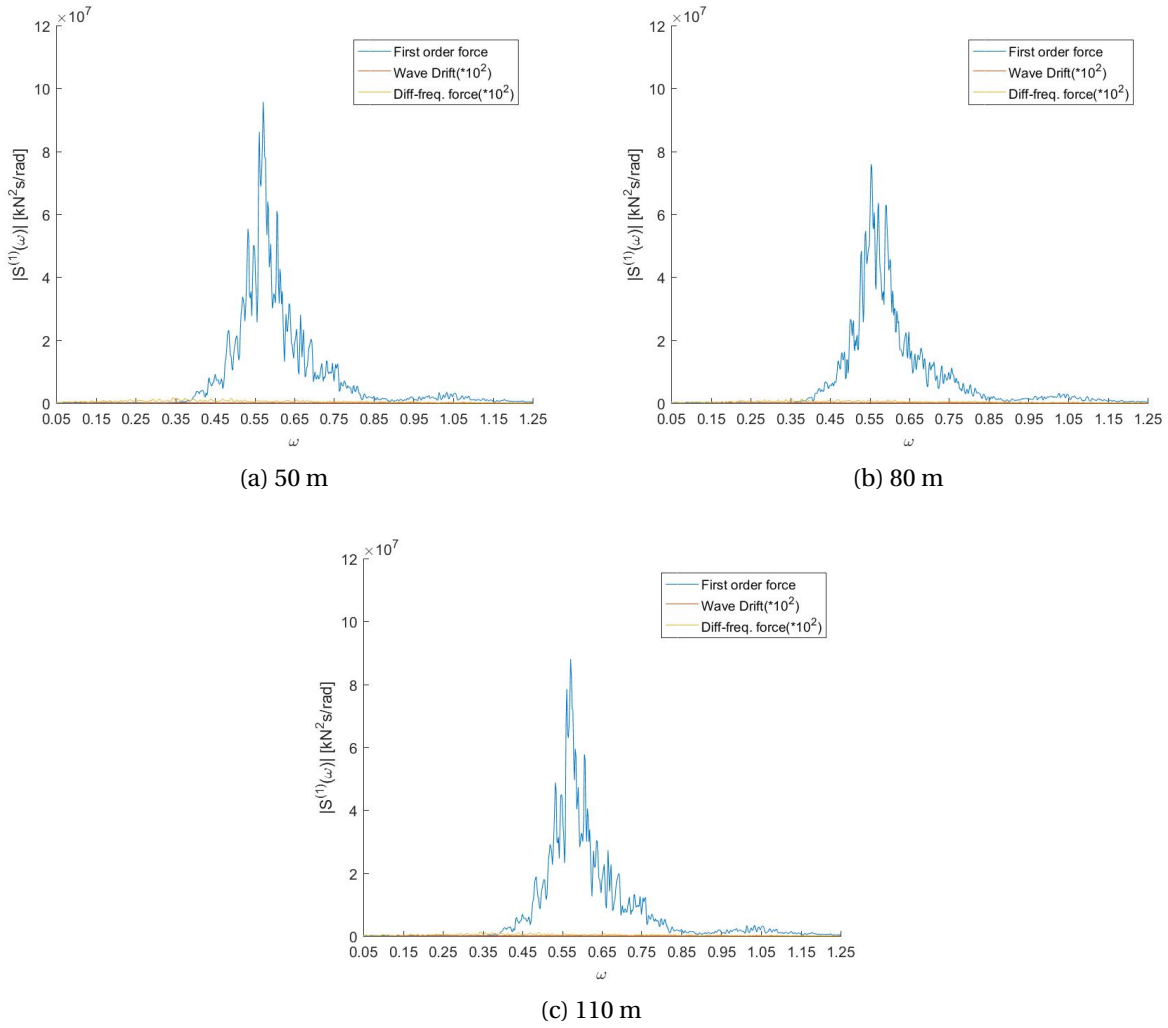
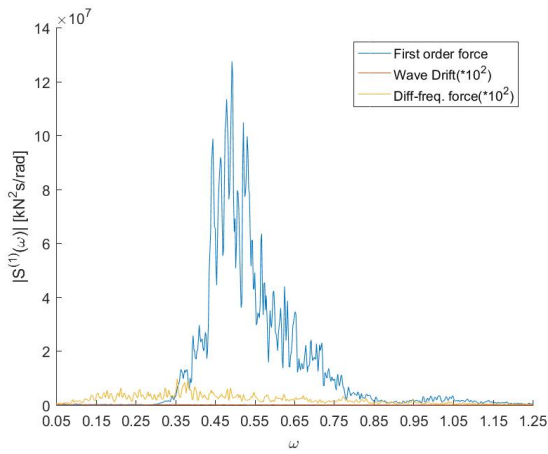
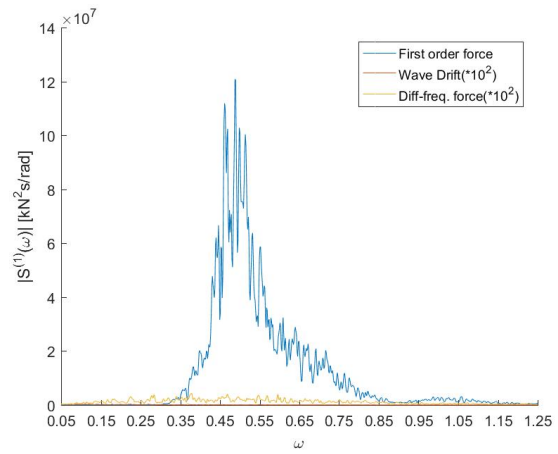


Figure C.5: FWT Surge First Order, Mean Drift and Difference Frequency Loads

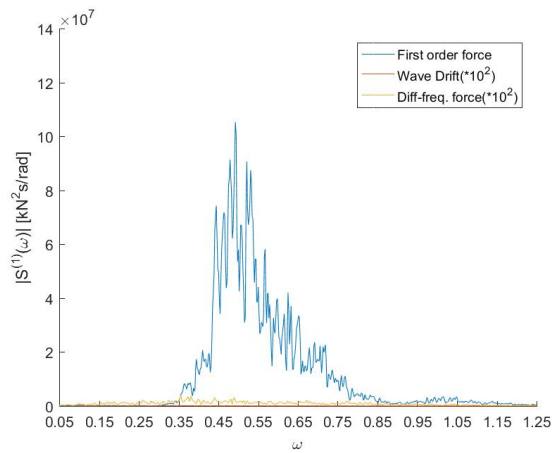
**C.2.2 Case O2**



(a) 50 m



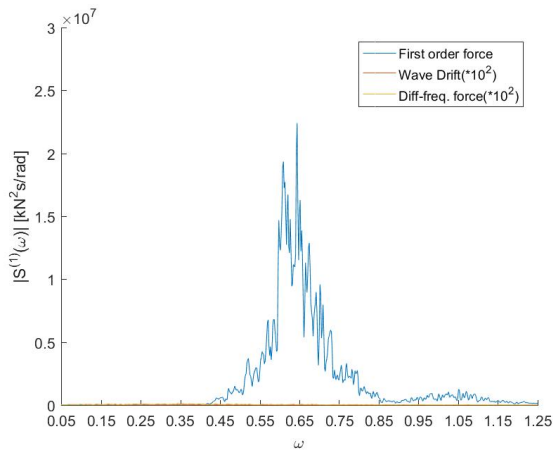
(b) 80 m



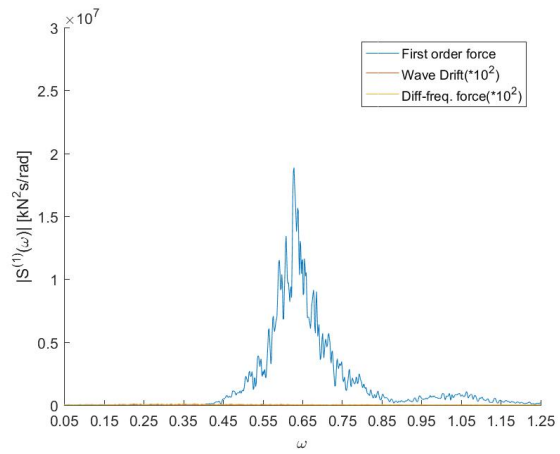
(c) 110 m

Figure C.6: FWT Surge First Order, Mean Drift and Difference Frequency Loads

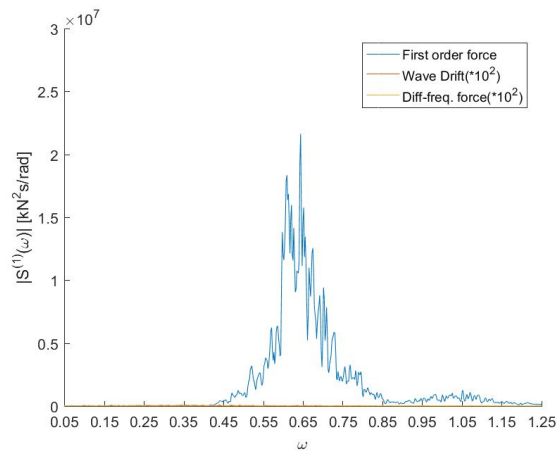
**C.2.3 Case M1**



(a) 50 m



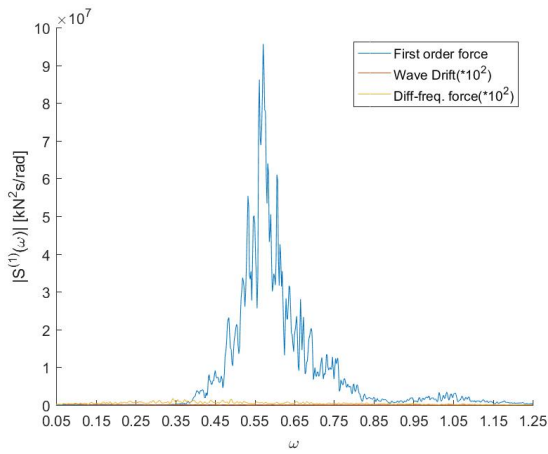
(b) 80 m



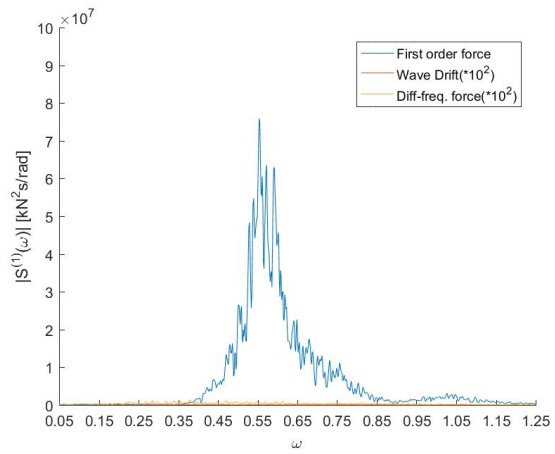
(c) 110 m

Figure C.7: FWT Surge First Order, Mean Drift and Difference Frequency Loads

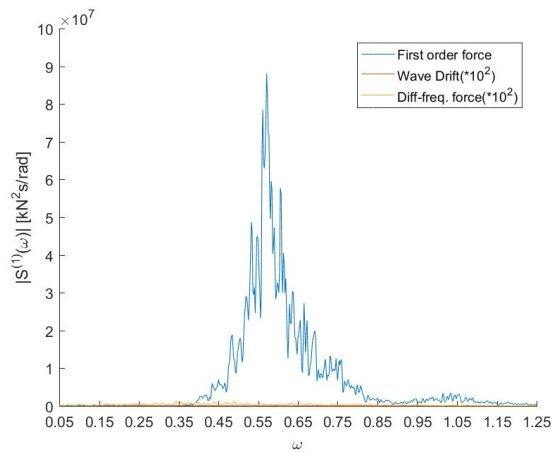
**C.2.4 Case M2**



(a) 50 m



(b) 80 m

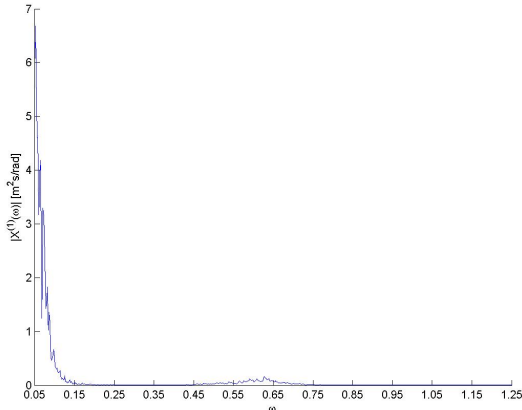


(c) 110 m

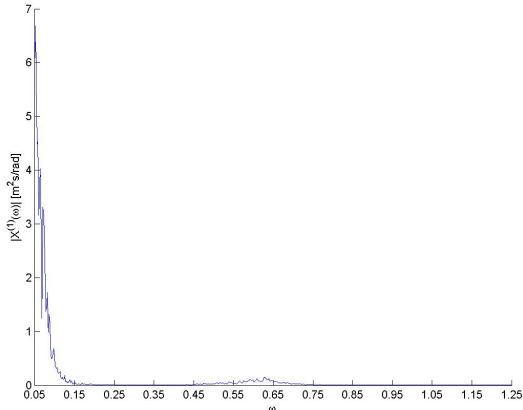
Figure C.8: FWT Surge First Order, Mean Drift and Difference Frequency Loads

### C.3 Heave Plate Parametric Study

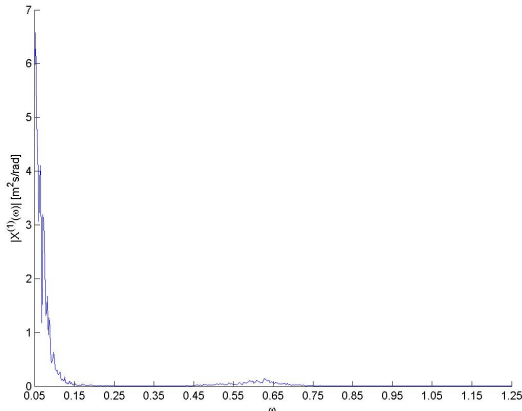
#### C.3.1 Case M1



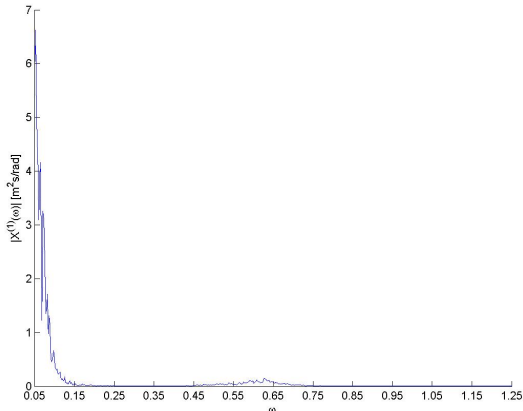
(a) Case 1



(b) Case 2



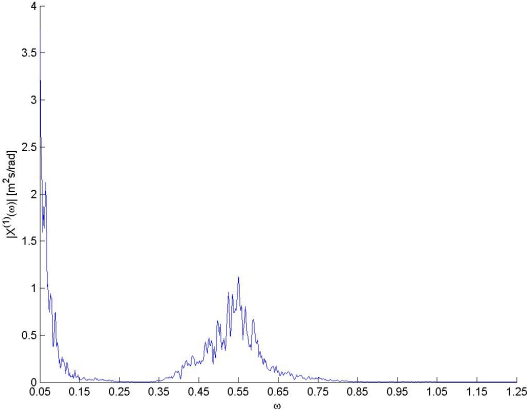
(c) Case 3



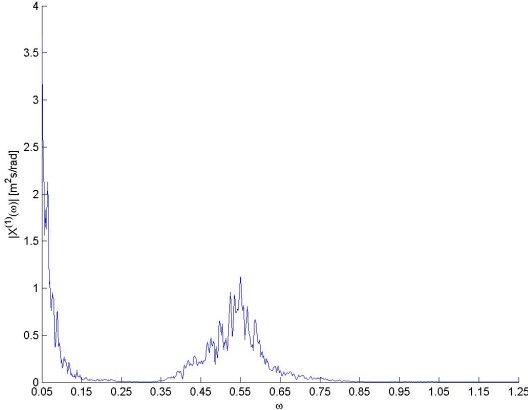
(d) Case 4

Figure C.9: FWT Surge response spectrum

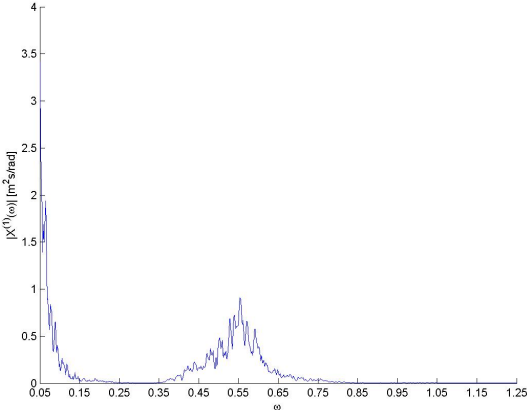
#### C.3.2 Case O1



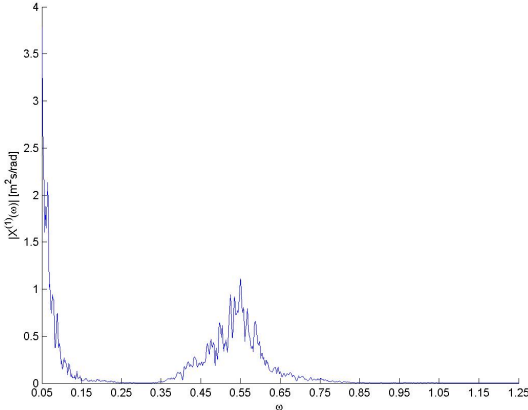
(a) Case 1



(b) Case 2



(c) Case 3



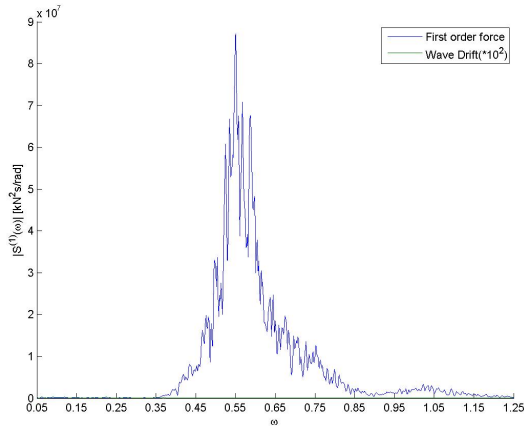
(d) Case 4

Figure C.10: FWT Surge response spectrum

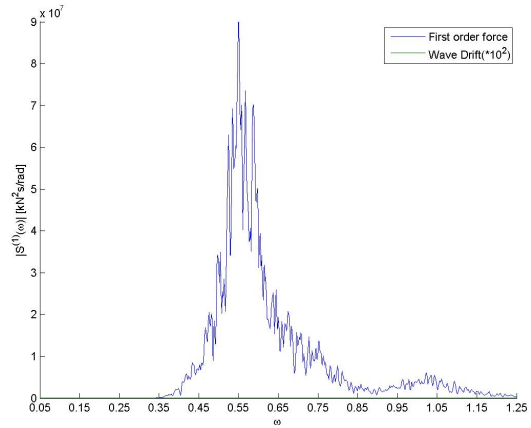


## C.4 Wave Loads in Time-Domain Simulation

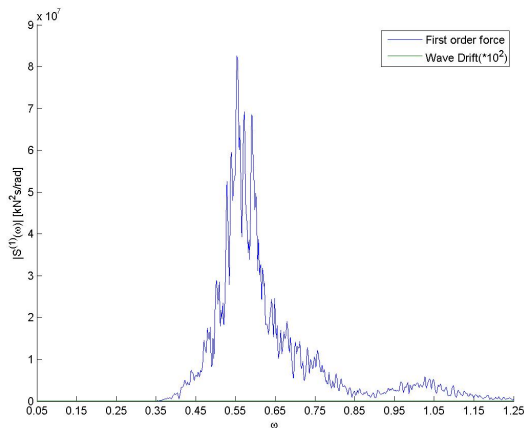
### C.4.1 Case M1



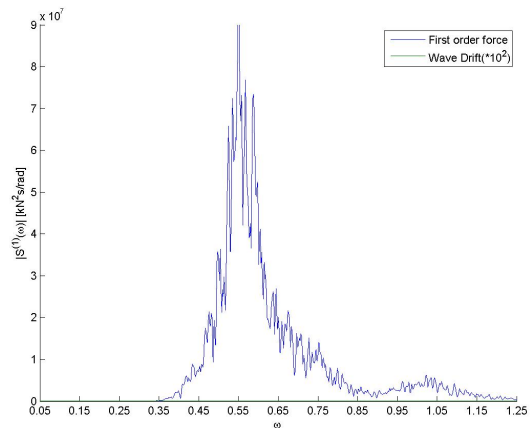
(a) Case 1



(b) Case 2



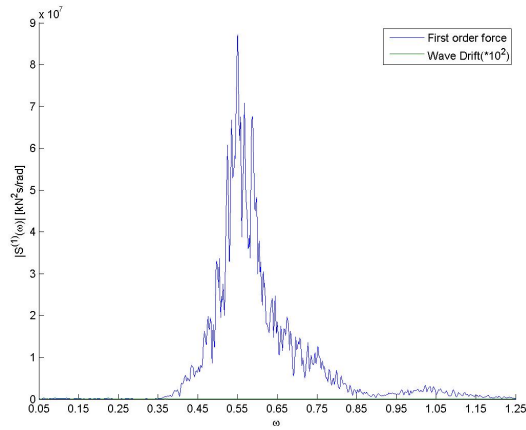
(c) Case 3



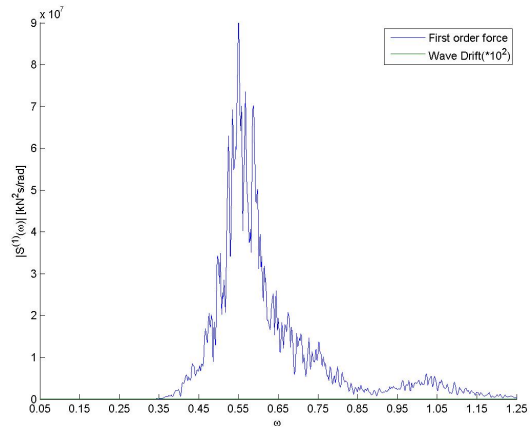
(d) Case 4

Figure C.11: FWT Surge First Order, Mean Drift Loads

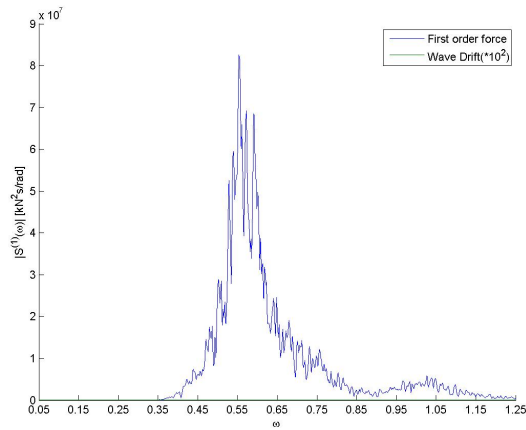
**C.4.2 Case O1**



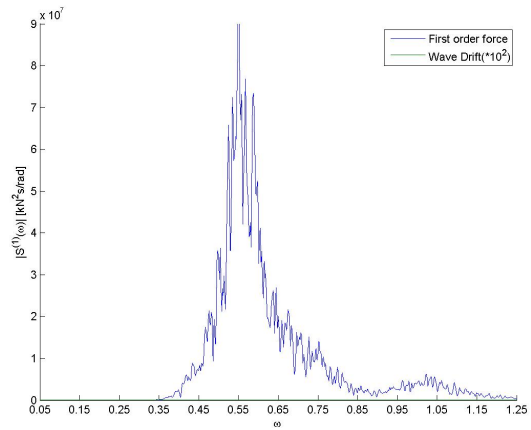
(a) Case 1



(b) Case 2



(c) Case 3

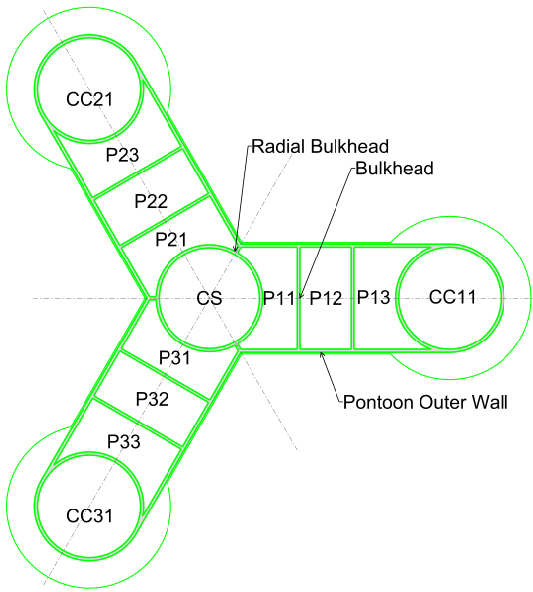


(d) Case 4

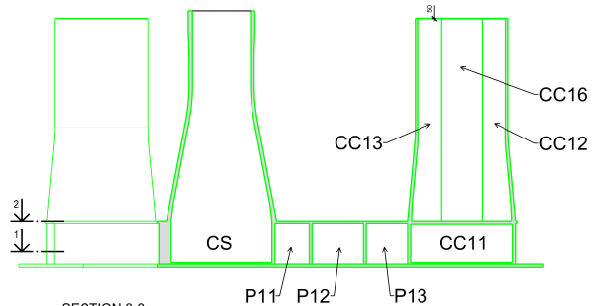
Figure C.12: FWT Surge First Order and Mean Drift Loads

# **Appendix D**

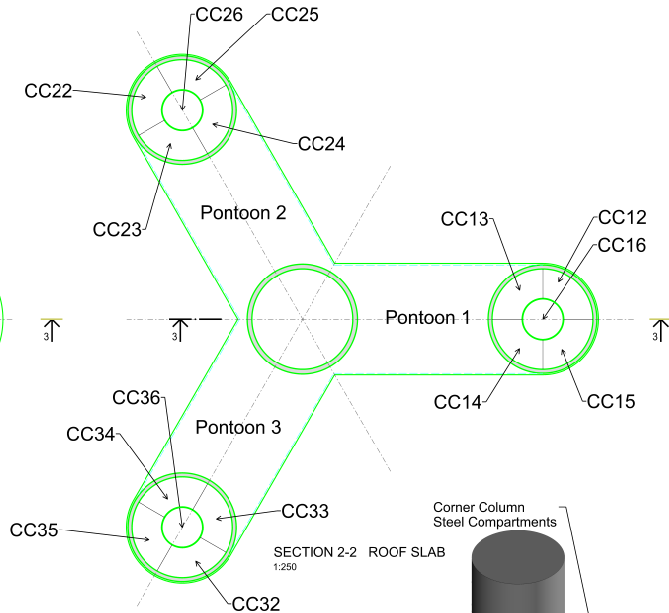
## **Structural Drawing 6 MW 00 Star**



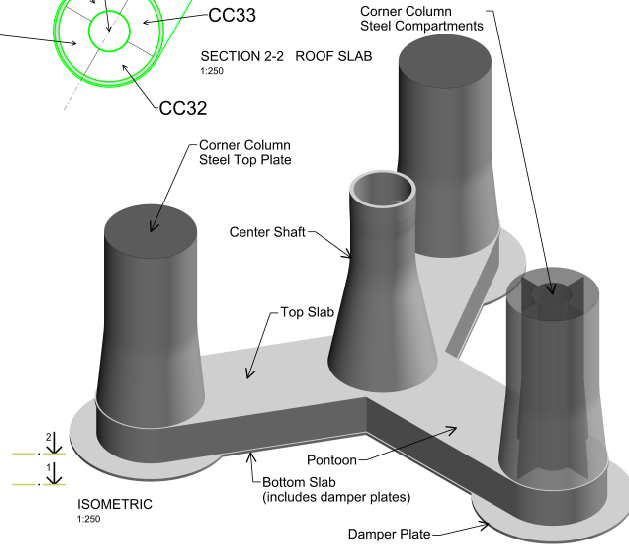
SECTION 1-1 PONTON  
1:250



SECTION 3-3  
1:250



SECTION 2-2 ROOF SLAB  
1:250



ISOMETRIC  
1:250



ISOMETRIC  
1:750

Rev.	Issue	Description	Design	Checked	Approved
01	14.10.14	ISSUE FOR INFORMATION			

 Dytech Olay Olsen Institute for Energy Technology	 Dytech Olay Olsen Structural and Marine Consulting Engineers P.O. Box 234, NO-2007 Sandness-Norway Tel: +47 7358 2000 E-mail: info@dytecholayolse.no	 Statoll The Research Council of Norway
--	--	---

RCN Proj. no: 225946 <b>CONCRETE SUBSTRUCTURE FOR          FLOATING OFFSHORE WIND TURBINES</b>			
14.10.14 Design	1:750 1:250 (A1)	<b>OO-STAR WIND FLOATER          CONCRETE FLOATER          NOMENCLATURE</b>	11802
006	01	11802	006 01